

Electronic Thesis and Dissertation Repository

12-17-2012 12:00 AM

Structural Insights into Group 14 Compounds from Solid-State NMR Spectroscopy

Margaret A. Hanson
The University of Western Ontario

Supervisor
Kim M. Baines
The University of Western Ontario Joint Supervisor
Yining Huang
The University of Western Ontario

Graduate Program in Chemistry
A thesis submitted in partial fulfillment of the requirements for the degree in Doctor of Philosophy
© Margaret A. Hanson 2012

Follow this and additional works at: <https://ir.lib.uwo.ca/etd>

Recommended Citation

Hanson, Margaret A., "Structural Insights into Group 14 Compounds from Solid-State NMR Spectroscopy" (2012). *Electronic Thesis and Dissertation Repository*. 1032.
<https://ir.lib.uwo.ca/etd/1032>

This Dissertation/Thesis is brought to you for free and open access by Scholarship@Western. It has been accepted for inclusion in Electronic Thesis and Dissertation Repository by an authorized administrator of Scholarship@Western. For more information, please contact wlsadmin@uwo.ca.

STRUCTURAL INSIGHTS INTO GROUP 14 COMPOUNDS FROM SOLID-STATE
NMR SPECTROSCOPY

(Spine title: Group 14 Structural Insights from SSNMR Spectroscopy)

(Thesis format: Integrated-Article)

By

Margaret A. Hanson

Graduate Program in Chemistry

A thesis submitted in partial fulfillment
of the requirements for the degree of
Doctor of Philosophy

The School of Graduate and Postdoctoral Studies
The University of Western Ontario
London, Ontario, Canada

© Margaret A. Hanson, 2012

THE UNIVERSITY OF WESTERN ONTARIO
School of Graduate and Postdoctoral Studies

CERTIFICATE OF EXAMINATION

Joint Supervisor

Dr. Kim M. Baines

Joint Supervisor

Dr. Yining Huang

Supervisory Committee

Dr. David Shoesmith

Examiners

Dr. T. K. Sham

Dr. Gary Shaw

Dr. Blaine A. Chronik

Dr. Glenn H. Penner

The thesis by

Margaret A. Hanson

entitled:

**Structural Insights into Group 14 Compounds from Solid-State NMR
Spectroscopy**

is accepted in partial fulfillment of the
requirements for the degree of
Doctor of Philosophy

Date

Chair of the Thesis Examination Board

Abstract

In this thesis, the potential utility of solid-state NMR spectroscopy to provide insights into the structure and bonding of organogermanium and tin compounds is examined.

Germanium-73 is an extremely challenging nucleus to examine due to multiple unfavourable NMR properties. However, the great utility of silicon-29 NMR spectroscopy suggests that ^{73}Ge could be a valuable tool for structural characterization.

Initial investigations focused on a series of simple organogermanes as benchmarks for future investigations. Compounds with known X-ray structures were used to determine an effective method for density functional theory calculations. That methodology was then further employed to propose structures for several less well characterized compounds.

^{73}Ge NMR spectroscopy was used, in conjunction with ^{35}Cl and ^{79}Br NMR spectroscopy, to characterize the novel germanium(I) halides, GeCl and GeBr . As the monohalides are amorphous, glasslike compounds, methods for structural characterization are limited.

Calculation of the NMR parameters for a series of model compounds was used to propose a structure.

^{35}Cl NMR spectroscopy was explored as a potential source of indirect information about germanium. There appears to be a relationship between the oxidation state at germanium and the shape of the ^{35}Cl NMR signal. Additionally, a correlation between the NMR parameters of germanium(II) chlorides and $\text{Ge}-\text{Cl}$ bond lengths was established.

^{119}Sn NMR spectroscopy is better developed than ^{73}Ge or ^{35}Cl NMR spectroscopy.

However, it is often difficult to obtain a ^{119}Sn signal in solution at moderate magnetic

fields. A series of cationic tin(II) cryptand complexes were examined in the solid state. The ^{119}Sn NMR parameters were used to describe the structure of a compound for which X-ray quality single crystals could not be grown. Additionally, several ambiguities about the bonding of a second compound were resolved.

Keywords

Cation

Chlorine-35

DFT

Germanium-73

Germanium(II)

Germylene

Organogermane

Solid-state NMR spectroscopy

Structure elucidation

Tin-119

Co-Authorship

Chapter 2 is based on a manuscript by Margaret Hanson, Andre Sutrisno, Victor Terskikh, Kim Baines and Yining Huang. Margaret Hanson was responsible for writing the manuscript. The majority of experimental work was performed by Margaret Hanson. X-ray crystallography performed by Guerman Popov. The ^{73}Ge NMR spectra for **2.4**, **2.9**, **2.10** and **2.15** were acquired by Victor Terskikh and interpreted by Margaret Hanson.

Chapter 5 is based on a manuscript by Jessica Avery, Margaret Hanson, Rolfe Herbert, Kamila Bladek, Paul Rugar, Israel Nowik, Yining Huang and Kim Baines. Margaret Hanson was responsible for writing the included portion of the manuscript. Compound **5.1** was synthesized by Paul Rugar. Compounds **5.8-5.11** were synthesized by Jessica Avery.

Acknowledgements

No work is ever created in a vacuum and this thesis is no exception. I must first and foremost thank both my supervisors, Kim Baines and Yining Huang. Their guidance has made me the chemist I am today, and this work could not have been completed without the considerable time they contributed. I must also thank my labmates in the Baines and Huang groups for all the sudden insights that came of our discussions and, more importantly, for five years of fun and friendship.

I am also indebted to all the Chemistry department staff. In particular, I must thank the NMR manager, Mat Willans. It seems I could never bring him a *normal* problem, but he always managed to get my experiments working again. Related to that, John Vanstone's near wizardlike skills with NMR probe repairs were invaluable. I thank Viktor Straverov for consultations on the finer points of computational chemistry and Doug Harsine for mass spectrometry.

Many people provided fascinating samples over the course of this work. I thank Christoph Marschner for providing a germylene phosphine complex and Krysten Hurni for dimesitylbis(trimethylsilyl)germanes. The germanium monohalides provided by Andreas Schnepf were a fascinating investigation. The cationic tin and germanium compounds provided by Jessica Avery and Paul Rugar proved to be far more exciting than I ever could have predicted when Jess first asked for NMR help.

I would not be here today without the love and support of my parents. In addition to always being encouraging me to pursue my scientific interests, they always emphasized that to succeed in science one must learn to write. I cannot thank them enough. My

siblings, Jennifer and Brian, were also a wonderful source of support. Without them I would not be completing the M. Hanson pair-a-docs.

Finally, I would never have been able to do this without my husband Ryan. His love and support have kept me going throughout all of this.

Table of Contents

CERTIFICATE OF EXAMINATION	ii
Abstract	iii
Keywords	v
Co-Authorship	vi
Acknowledgements	vii
Table of Contents	ix
List of Tables.....	xiv
List of Figures	xv
List of Schemes	xxiv
List of Abbreviations	xxv
Chapter 1 Introduction.....	1
1.1 Recent Advances in Group 14 Chemistry.....	1
1.1.1 Low Valent Species.....	3
1.1.2 Cationic Species	5
1.2 Introduction to Solid-State NMR Spectroscopy.....	6
1.2.1 Chemical Shielding Anisotropy	7
1.2.2 Quadrupolar Interaction.....	9
1.3 Techniques for Wideline NMR Spectroscopy	12
1.4 NMR Crystallography	14

1.5	Group 14 NMR Spectroscopy	15
1.5.1	Silicon-29	16
1.5.2	Tin-119	17
1.6	Germanium-73 NMR Spectroscopy	19
1.7	Chlorine-35 NMR Spectroscopy	21
1.8	Thesis Overview	23
1.9	Co-Authorship	25
1.10	References	26
Chapter 2	Solid-State ^{73}Ge NMR Spectroscopy of Simple Organogermanes	31
2.1	Introduction	31
2.2	Results and Discussion	37
2.2.1	Tetraorganogermanes	37
2.2.2	Mesitylgermanes	50
2.2.3	Tetrakis(trimethylsilyl)germane and tetra(tert-butoxy)germane.....	61
2.2.4	Dimesitylbis(trimethylsilyl)germane (2.9)	66
2.2.5	Compounds for which ^{73}Ge SSNMR Spectroscopy was Unsuccessful	71
2.3	Conclusion	75
2.4	Experimental	76
2.4.1	Materials	76
2.4.2	Solid-State NMR Spectroscopy	77

2.4.3	NMR Spectral Simulations	79
2.4.4	Theoretical Calculations	79
2.4.5	Differential Scanning Calorimetry	80
2.4.6	Single Crystal X-ray Diffraction	80
2.5	References	81
 Chapter 3 Characterization of Germanium Monohalides by Solid-State NMR		
Spectroscopy and Density Functional Theory Calculations		85
3.1	Introduction	85
3.2	Results and Discussion	87
3.2.1	Solid-State NMR Spectroscopy	88
3.2.2	Computational Investigations	95
3.3	Conclusions	102
3.4	Experimental	102
3.4.1	Materials	102
3.4.2	Solid-State NMR Spectroscopy	102
3.4.3	Spectral Simulations	103
3.4.4	Theoretical Calculations	103
3.5	References	103
 Chapter 4 Chlorine-35 SSNMR Spectroscopy as an Indirect Probe of Germanium		
Compounds		108

4.1	Introduction	108
4.2	Results.....	114
4.2.1	Solid-State NMR Spectroscopy	114
4.3	Discussion	123
4.3.1	Computational Investigation.....	127
4.4	Conclusions	141
4.5	Experimental	143
4.5.1	Materials	143
4.5.2	Solid-State NMR Spectroscopy	143
4.5.3	NMR Spectral Simulations	144
4.5.4	Theoretical Calculations	144
4.6	References.....	145
Chapter 5	Solid-State ^{119}Sn NMR Studies of Cationic Tin Cryptand Complexes	150
5.1	Introduction.....	150
5.2	Results and Discussion	155
5.2.1	Halide Complexes	155
5.2.2	Triflate Complex	168
5.2.3	Calculation of Isotropic Shifts	171
5.2.4	Natural Bond Order Calculations.....	172
5.2.5	Investigation of the Germanium Dication 5.1.....	175

5.3	Conclusions	177
5.4	Experimental	179
5.4.1	Materials	179
5.4.2	^{119}Sn SSNMR Spectroscopy	179
5.4.3	SSNMR Spectral Simulations	180
5.4.4	Theoretical Calculations	180
5.5	References	181
Chapter 6	Summary, Conclusions and Future Work.....	184
6.1	Summary	184
6.2	Future Work	187
6.3	Conclusions	189
6.4	References	191
Appendix 1:	Low Field ^{35}Cl SSNMR Data.....	193
Appendix 2:	Copyrighted Material and Permissions.....	195
Curriculum Vitae	199

List of Tables

Table 2.1 Summary of ^{73}Ge NMR spectroscopic and computational data for compounds 2.1-2.9 . In all simulations, the Euler angles $\alpha=\beta=\gamma=0$	38
Table 2.2 Selected crystallographic bond lengths and angles for $\text{Ge}(\text{p-MeO-C}_6\text{H}_4)_4$	43
Table 2.3 Summary of computational results for 2.1 using different model chemistries.	46
Table 2.4 Detailed ^{73}Ge SSNMR experimental conditions.....	78
Table 2.5 Crystallographic data for $\text{Ge}(\text{p-MeO-C}_6\text{H}_4)_4$	81
Table 3.1 NMR properties of ^{35}Cl , ^{73}Ge and ^{79}Br	87
Table 3.2 Summary of experimental SSNMR data of GeX $\text{X} = \text{Cl}, \text{Br}$	89
Table 3.3 Summary of computational results.....	95
Table 3.4 Solid-state NMR acquisition parameters.....	103
Table 4.1 Summary of experimental ^{35}Cl SSNMR parameters.....	115
Table 4.2 Assessment of computational methodology using 4.1	130
Table 4.3 Effect of basis set on germanium on calculated ^{73}Ge C_Q value.....	132
Table 4.4 Summary of computational ^{35}Cl NMR parameters compounds 4.2-4.9 . ^a	133
Table 4.5 ^{35}Cl SSNMR acquisition parameters for 4.1-4.9	144
Table 5.1 Experimental ^{119}Sn SSNMR parameters for crown ether and glyme complexes of tin(II). ⁵	152
Table 5.2 Spectral ^{119}Sn SSNMR parameters of 5.8-5.11 and various stannates.....	156
Table 5.3 Summary of natural bond order calculations and natural population analysis. ^a	173
Table 5.4 Experimental ^{119}Sn acquisition parameters.....	180

List of Figures

- Figure 1.1** Comparison of the interaction of H₂ with A) a multiply bonded main group species and B) a transition metal complex.....3
- Figure 1.2** Effect of CSA parameters on SSNMR spectrum lineshape. A) Varying span with a constant skew of 0. B) Varying skew with a constant span of 300 ppm.....8
- Figure 1.3** CSA lineshapes with varying skew under MAS conditions with a spin rate less than the spectral breadth. The isotropic shift is indicated by the dashed line.9
- Figure 1.4** Effect of quadrupolar parameters on SSNMR lineshape of ³⁵Cl (I=3/2) at 21.1 T. A) Varying η_Q with a constant $C_Q = 3$ MHz. B) Varying C_Q with a constant η_Q of 0. .11
- Figure 2.1** Germanes examined in this study. **2.1** Ge(p-Me-C₆H₄)₄ **2.2** Ge(p-MeO-C₆H₄)₄ **2.3** tetraphenylgermane (GePh₄) **2.4** tetrabenzylgermane (Ge(CH₂Ph)₄) **2.5** tetra(tert-butoxy)germane (Ge(OtBu)₄) **2.6** tetrakis(trimethylsilyl)germane (Ge(SiMe₃)₄) **2.7** dimesitylgermane (Mes₂GeH₂) **2.8** trimesitylgermane (Mes₃GeH) **2.9** bis(trimethylsilyl)dimesitylgermane (Mes₂Ge(SiMe₃)₂).36
- Figure 2.2** ⁷³Ge SSNMR spectra of compounds **2.1-2.4** at 21.1 T. Dotted traces represent simulations using parameters from Table 2.1. A) MAS (5 kHz) and B) static spectra of Ge(p-Me-C₆H₅)₄. C) MAS (5 kHz) spectrum of Ge(p-MeO-C₆H₅)₄. D) MAS (4 kHz) and E) static spectra of GePh₄. F) MAS (5 kHz) and G) static spectra of Ge(CH₂Ph)₄.....41
- Figure 2.3** Simulation breakdown of A) Ge(p-MeC₆H₄)₄ and B) Ge(CH₂Ph)₄ showing the individual contributions of CSA (dash-dot line), EFG (dashed line), and the two combined (dotted line).42
- Figure 2.4** Relationship between experimental and calculated values of C_Q (⁷³Ge) for compounds **2.1-2.4**. The solid line represents the ideal 1:1 correlation between

experiment and theory. Hydrogen positions were optimized at the TPSS/6-31G* level.....	47
Figure 2.5 Relationship between A) experimental C_Q and average Ge–C bond length. The sign of C_Q was assumed to be the same as the calculated value. B) experimental C_Q and angular distortion C) experimental C_Q and Hammett constants D) isotropic shift and Hammett constants.	48
Figure 2.6 Relationship between A) calculated C_Q and Ge–C bond length and B) calculated C_Q and angular distortion. All calculations were performed at the TPSS/6-311+G** level.	50
Figure 2.7 ^{73}Ge SSNMR spectra of compounds 2.7 and 2.8 at 21.1 T. Dotted traces represent simulations using parameters from Table 2.1 as discussed in the text. Dashed traces show the individual contributions to the total simulation. A) MAS (5 kHz) and B) static spectra of Mes_2GeH_2 . C) MAS (5 kHz) and D) static spectra of Mes_3GeH	51
Figure 2.8 Comparison between experimental spectrum of a stationary sample of Mes_3GeH (solid line) and that predicted computationally from the X-ray structure (dashed line).	53
Figure 2.9 Relationship between calculated C_Q value for Mes_3GeH and A) C–Ge–C bond angle. The geometry optimized value is a notable outlier. B) Ge–H bond length C) all Ge–C bond lengths D) one Ge–C bond length with the others held at their optimized value.....	55
Figure 2.10 Relationship between calculated η_Q value and one Ge–C bond length in Mes_3GeH	56

Figure 2.11 Selected ^{13}C CPMAS SSNMR spectra at 9.4 T. A) Mes_3GeH B) Mes_2GeH_2 C) $\text{Ge}(\text{SiMe}_3)_4$ D) $\text{Ge}(\text{OtBu})_4$ E) $\text{Mes}_2\text{Ge}(\text{SiMe}_3)_2$ MAS spinning speed was 8 kHz in A, B and C and 10 kHz in D and E.....	57
Figure 2.12 A) The stereographic structure of an untwisted metallane is shown above and its Newman projection below. B) In order to minimize interactions between ortho substituents, the aryl rings twist into a propeller geometry as shown above. The Newman projection below demonstrates the effect of this twisting on the dihedral angles α and β	59
Figure 2.13 Relationship between the calculated C_Q value for Mes_2GeH_2 and A) Ge–C bond lengths, B) Ge–H bond lengths, C) H–Ge–H bond angle, and D) C–Ge–C bond angle.....	61
Figure 2.14 ^{29}Si CPMAS spectrum of $\text{Ge}(\text{SiMe}_3)_4$ at 9.4 T.....	62
Figure 2.15 Differential scanning calorimetry plot of $\text{Ge}(\text{SiMe}_3)_4$ showing a solid-solid phase transition at $-34.6\text{ }^\circ\text{C}$	63
Figure 2.16 Variable temperature ^{29}Si SSNMR spectra of $\text{Ge}(\text{SiMe}_3)_4$ at 9.4 T.	64
Figure 2.17 ^{73}Ge SSNMR spectra of compounds 2.5 , 2.6 and 2.9 at 21.1 T. Dotted traces represent simulations using parameters from Table 2.1. A) MAS (5 kHz) and B) static spectra of $\text{Ge}(\text{OtBu})_4$. C) MAS (5 kHz) and D) static spectra of $\text{Ge}(\text{SiMe}_3)_4$. E) Static WURST-CPMG spectrum of $\text{Mes}_2\text{Ge}(\text{SiMe}_3)_2$	66
Figure 2.18 Relationship between the calculated C_Q value for $\text{Mes}_2\text{Ge}(\text{SiMe}_3)_2$ and A) Ge–C bond lengths, B) Ge–Si bond lengths, C) C-Ge-C angle, and D) Si-Ge-Si angle. ...	68

Figure 2.19 Relationship between the calculated η_Q value for $\text{Mes}_2\text{Ge}(\text{SiMe}_3)_2$ and A) Ge–C bond lengths, B) Ge–Si bond lengths, C) C–Ge–C bond angle, and D) Si–Ge–Si bond angle.	69
Figure 2.20 ^{29}Si CPMAS spectrum of $\text{Mes}_2\text{Ge}(\text{SiMe}_3)_2$ at 9.4 T showing two distinct silicon resonances for the trimethylsilyl groups.	70
Figure 2.21 Compounds for which a ^{73}Ge SSNMR signal was not observed.	71
Figure 2.22 ^{29}Si CPMAS NMR spectrum of the germylene complex 2.15 at 9.4 T.	74
Figure 2.23 ^{31}P MAS ($\nu_{\text{rot}} = 10$ kHz) spectrum of 2.15 at 9.4 T. The spectrum was acquired over 16 transients with a 30 second pulse delay.	75
Figure 3.1 Raman spectrum of GeBr.	88
Figure 3.2 ^{73}Ge static echo NMR spectrum of GeCl. The spectrum was acquired overnight in 245670 transients with a 0.25 s recycle delay and an 8 ms acquisition time. The simulated fit is indicated by the solid trace.	90
Figure 3.3 ^{35}Cl quadrupolar echo spectrum of GeCl at 21.1 T. The spectrum was acquired in 20480 transients with a recycle delay of 0.5 and an acquisition time of 16 ms. The simulated fit is indicated by a solid line.	92
Figure 3.4 ^{79}Br quadrupolar echo spectrum of GeBr at 21.1 T. The spectrum was acquired over 20480 transients with a recycle delay of 0.25 s and an acquisition time of 1 ms. The simulated fit is indicated by a solid line.	93
Figure 3.5 ^{73}Ge quadrupolar echo spectrum of GeBr at 21.1 T. The spectrum was acquired over 276480 transients with a 0.25 s recycle delay and an 8 ms acquisition time. The simulated fit is indicated by a solid line.	94
Figure 3.6 Clusters featuring chlorine in a terminal environment.	97

Figure 3.7 Computational clusters featuring chlorine in a bridging environment.	98
Figure 3.8 Clusters for calculations involving tetrahedral chlorine.	99
Figure 3.9 Relationships between A) Ge–Ge bond length B) Ge–Cl bond length and C) the ratio between the two bond lengths and the calculated value of C_Q for ^{73}Ge	101
Figure 4.1 Germanium and tin chlorides examined in this study.	111
Figure 4.2 X-ray structures of compounds 4.1-4.6 and 4.9 showing the long range interactions between chlorine and germanium in 4.1, 4.2, 4.4 and 4.5	112
Figure 4.3 A) Individual ^{35}Cl static QCPMG subspectra (offset= 100 kHz) and co-added spectrum of $\text{GeCl}_2\cdot\text{dioxane}$. B) Individual static WURST-QCPMG subspectra (no offset, but opposite sweep directions) and coadded spectrum. of $\text{GeCl}_2\cdot\text{dioxane}$ at 21.1 T. The dashed trace indicates the empirical simulation accounting for only the EFG interaction. The dotted trace indicates the simulation including CSA.	116
Figure 4.4 Static ^{35}Cl WURST-QCPMG spectra of 4.2 (top) and 4.3 (bottom) at 21.1 T. Dotted traces indicate empirical simulations. An impurity of the hydrochloride salt of the carbene is indicated by an asterisk.	118
Figure 4.5 Static ^{35}Cl WURST-QCPMG spectra of 4.4 and 4.5 at 21.1 T. The dotted traces indicate empirical simulations. Both spectra exhibit partial satellite transitions, visible as lower intensity spikelets along the baseline.	119
Figure 4.6 ^{73}Ge SSNMR spectrum of 4.5 at 21.1 T after overnight acquisition.	120
Figure 4.7 Static ^{35}Cl WURST-QCPMG spectrum of [benzo-15-crown-5 GeCl][OTf](4.6) at 21.1 T. The dotted trace indicates the analytical simulation.	121
Figure 4.8 Static ^{35}Cl WURST-QCPMG spectra of 4.7 (top) and 4.8 (bottom) at 21.1 T. The dotted traces indicated analytical simulations.	122

Figure 4.9 ^{35}Cl WURST-QCPMG spectrum of $[[2.2.2]\text{SnCl}][\text{SnCl}_3]$ (4.9) at 21.1 T. The dashed trace indicates the analytical simulation.....	123
Figure 4.10 Relationship between quadrupolar coupling constant and germanium oxidation state.....	124
Figure 4.11 A) Relationship between ^{35}Cl quadrupolar coupling constant and crystallographically-determined Ge-Cl bond lengths. The solid line indicates a line of best fit ($y=111x^2-592x+802$, $R^2=0.90$). B) Relationship between ^{35}Cl quadrupolar coupling constant and crystallographically determined D-Ge-Cl angle for the germanium(II) series. C) Relationship between ^{35}Cl quadrupolar coupling constant and D-Ge-Cl angle excluding $\text{GeCl}_2\cdot\text{dioxane}$ and including geometry optimized structures of 4.7 and 4.8 . The solid line indicates a line of best fit ($y=1.43x-108.6$, $R^2=0.94$).	126
Figure 4.12 Clusters employed in the calculation of the ^{35}Cl NMR parameters for $\text{GeCl}_2\cdot\text{dioxane}$ in Gaussian 09. The chlorine centre for which the parameters were determined is indicated with a circle.	129
Figure 4.13 Relationship between calculated ^{35}Cl C_Q value and A) Ge-Cl bond length. The solid line indicates a line of best fit ($y = 13.8x+11.9$, $R^2=0.99$) B) C-Ge-Cl angle. The solid line indicates a line of best fit ($y = 0.01x^2-2x+147$, $R^2=0.99$).	136
Figure 4.14 Agreement between calculated and experimental C_Q values. The solid line represents an ideal 1:1 correlation, while the dashed line represents a line of best fit ($y = 0.87x+6.7$, $R^2=0.95$).	138
Figure 4.15 Orientation of the V_{33} component for compounds 4.1-4.6 calculated at the TPSS/6-311+G** level. Hydrogen atoms have been omitted for clarity.	139

Figure 4.16 Orientation of the V_{33} component for compounds 4.7-4.9 . Compounds 4.7 and 4.8 were geometry optimized at the TPSS/6-31G* level. Hydrogen atoms and the SnCl_3^- anion were omitted for clarity.....	140
Figure 5.1 A germanium cryptand complex and examples of macrocyclic tin complexes. Counterions are ^-OTf , with the exception of 5.5 for which the counterion is SnCl_3^-	151
Figure 5.2 X-ray structures of A) $[\text{CryptSnCl}][\text{SnCl}_3]$ and B) $[\text{CryptSnBr}][\text{SnBr}_3]$. Anions and hydrogen atoms have been omitted for clarity.	153
Figure 5.3 X-ray structure of the triflate complex showing two distinct tin sites.	154
Figure 5.4 A) Static ^{119}Sn WURST-CPMG spectrum of 5.8 at 9.4 T. The solid trace indicates the simulated spectrum. B) ^{119}Sn MAS spectrum ($\nu_{\text{rot}} = 17$ kHz) of 5.8 at 9.4 T. The solid dots indicate the isotropic shifts of the signals.	157
Figure 5.5 A) Static ^{119}Sn WURST-CPMG spectrum of $[\text{NBu}_4][\text{SnCl}_3]$ at 9.4 T. The solid trace indicates the simulated spectrum. An impurity of SnCl_2 is marked with an asterisk. B) ^{119}Sn MAS spectrum at 9.4 T ($\nu_{\text{rot}} = 15.4$ kHz).	158
Figure 5.6 A) Static ^{119}Sn WURST-CPMG spectrum of 5.9 at 9.4 T. The solid trace indicates the simulated spectrum. B) ^{119}Sn MAS spectrum at 9.4 T ($\nu_{\text{rot}} = 15.5$ kHz).....	160
Figure 5.7 ^{119}Sn MAS spectrum of $[\text{NBu}_4][\text{SnBr}_3]$ at 9.4 T ($\nu_{\text{rot}} = 15.5$ kHz).	161
Figure 5.8 Static ^{119}Sn WURST-CPMG spectrum of 5.10 at 9.4 T. The solid trace indicates the simulated spectrum.	163
Figure 5.9 Static ^{119}Sn WURST-CPMG spectrum of $[\text{NBu}_4][\text{SnI}_3]$ at 9.4 T. The solid trace indicates the simulated spectrum. An impurity of SnI_2 is indicated with an asterisk.	163

Figure 5.10 Static ^{119}Sn WURST-CPMG spectrum at 9.4 T of 5.10' prepared from SnCl_2 via halogen exchange. The solid trace indicates the simulated spectrum.	164
Figure 5.11 Static ^{119}Sn WURST-CPMG spectrum of $[\text{NBu}_4][\text{SnCl}_2]$ at 9.4 T. The solid trace indicates the simulated spectrum.	165
Figure 5.12 Simulation of the ^{119}Sn spectrum of 5.10' using parameters from multiple cations and anions.	166
Figure 5.13 A) Static ^{119}Sn spin echo spectrum of 5.11 at 9.4 T. The solid trace indicates the simulated spectrum. B) ^{119}Sn MAS spectrum ($\nu_{\text{rot}} = 16$ kHz) of 5.11 at 9.4 T.	169
Figure 5.14 ^{19}F MAS spectrum ($\nu_{\text{rot}} = 10$ kHz) of 5.5 at 9.4 T. Isotropic shifts are designated with solid dots, while the asterisks indicate spinning sidebands.	170
Figure 5.15 Comparison between the experimental ^{119}Sn static spectrum of 5.11 and the calculated spectrum based on the X-ray structure (dash-dot line). The monocationic site is shown by the dashed line and the dicationic site by the dotted line.	171
Figure 5.16 Experimental vs. Calculated ^{119}Sn SSNMR isotropic shifts for complexes 5.8-5.11 . The solid line indicates a 1:1 correlation between theory and experiment while the dashed line represents the line of best fit.	172
Figure 5.17 ^{13}C CPMAS spectrum at 21.1 T of A) 5.1 precipitated from THF B) 5.1 recrystallized from CH_3CN	176
Figure 5.18 Static ^{73}Ge WURST-QCPMG spectrum of 5.1 at 21.1 T.	177
Figure A1.1 Partial ^{35}Cl WURST-QCPMG spectrum of methyl-substituted NHC complex 4.2 at 9.4 T. * indicates an impurity of the hydrochloride salt of the carbene while # indicates a spectrometer artefact.	193
Figure A1.2 Partial ^{35}Cl WURST-QCPMG spectrum of 4.4 at 9.4 T.	193

Figure A1.3 ^{35}Cl WURST-QCPMG spectrum of 4.5 at 9.4T.	194
Figure A1.4 Partial ^{35}Cl WURST-QCPMG spectrum of 4.7 at 9.4 T.	194

List of Schemes

Scheme 1.1 Catalytic reaction of a low valent germanium hydride with carbon dioxide...4	4
Scheme 1.2 Synthesis of the first isolable germanium cation.5	5
Scheme 5.1 Synthesis of tin cryptand derivatives.....153	153

List of Abbreviations

Å = Angstrom

ADF = Amsterdam Density Functional

B3LYP = Becke's hybrid exchange-correlation DFT functional

Bu = butyl

*t*Bu = *tert*-butyl

C = Celcius

Calc'd = calculated

CIF = crystallographic information file

cm⁻¹ = reciprocal centimetre

CP = cross polarization

CPMAS = cross polarized magic angle spinning

CPMG = Carr-Purcell-Meiboom-Gill

Crypt = cryptand[2.2.2]

C_Q = quadrupolar coupling constant

CSA = chemical shielding anisotropy

DFT = density functional theory

DI = distortion index

DSC = differential scanning calorimetry

EFG = electric field gradient

ESI-MS = electrospray ionization mass spectrometry

Et = ethyl

Exp = experimental

FWHH = full width at half height

GIAO = gauge-including atomic orbitals

HOMO = highest occupied molecular orbital

HMBC = heteronuclear multiple bond coherence

HSQC = heteronuclear single quantum coherence

Hz = hertz

kHz = kilohertz

kJ = kilojoule

LanL2DZ = Dunning/Huzinaga double zeta on first row, Los Alamos effective core potential plus double zeta on Na-La, Hf-Bi

LUMO = lowest unoccupied molecular orbital

MAS = magic angle spinning

mb = millibarn

Me = methyl

Mes = mesityl = 2,4,6-trimethylphenyl

MHz = megahertz

ms = millisecond

n. a. = not applicable

n. o. = not observed

NBO = Natural Bond Orbital

NHC = *N*-heterocyclic carbene

nm = nanometre

NMR = nuclear magnetic resonance

NPA = Natural Population Analysis

Opt = optimized

OTf = triflate = O_3SCF_3

PBE1PBE = the pure functional of Perdew, Becke and Ernzerhof as made into a hybrid
by Adamo

Ph = phenyl

*i*Pr = isopropyl

ppm = parts per million

Q = quadrupole moment

Q4ZP = quadruple zeta plus polarization

QCPMG = quadrupolar Carr-Purcell-Meiboom-Gill

RF = radio frequency

RHF = restricted Hartree-Fock

s = second

SSNMR = solid-state nuclear magnetic resonance

T = Tesla

T2ZP = triple zeta doubly polarized

THF = tetrahydrofuran

TPSSTPSS = the exchange and correlation functionals of Tao, Perdew, Staroverov and
Scuseria

VT = variable temperature

WBI = Wiberg bond index

WURST = Wideband Uniform Rate Smooth Truncation

ZORA = Zeroth Order Regular Approximation

γ = gyromagnetic ratio

δ_{iso} = isotropic shift

η_Q = quadrupolar asymmetry parameter

κ = skew

ν_{rot} = spinning rate

Ω = span

Chapter 1 Introduction

1.1 Recent Advances in Group 14 Chemistry

Early group 14 chemistry was dominated by the chemistry of carbon. Studies of the heavier members of the group focused largely on comparisons to traditional organic chemistry. This is particularly true for the metalloids, silicon and germanium. The heaviest members, tin and lead, had more distinct early chemistries due to their status as metals as well as a stable +2 oxidation state.

The heavier group 14 elements, particularly silicon and germanium, do exhibit considerable similarities to analogous carbon compounds. Notably, the alkane equivalents of all group 14 elements possess similar properties. However, the E–C bond is weaker than a C–C bond. This difference was exploited in synthetic organic chemistry. Organotin compounds, in particular, proved to be very useful reagents in C–C bond forming coupling reactions,¹ but other group 14 compounds are often capable of similar reactivity. While the germanium equivalents are generally more expensive, they offer the advantage of decreased toxicity when compared to the more popular stannanes. Unlike alkanes, organotin hydrides exhibit extensive radical chemistry.²

Several notable differences quickly became apparent in the case of multiply bonded species. While carbon dioxide is a gas, the dioxides of the heavier elements are solids made up of a network of E–O single bonds as the double bonds are unstable.³ Early attempts to synthesize multiply bonded silicon and germanium species focused on the carbon analogy and attempting to disprove the so called “double bond rule”.³ After the successful isolation of stable tetrylles⁴⁻⁶ and ditetrylles,^{7,8} the chemistry of these

species again focused on comparison to carbon chemistry. The heavier species are considerably more reactive due to the weaker π bonds. As one descends group 14, the doubly bonded species resemble alkenes less, with the electron density being localized into zwitterionic species or diradicaloids. The frontier orbitals in the less traditional bonding schemes are very close in energy, much like the d-orbitals of transition metals.⁹

More recent developments in heavy group 14 chemistry have focused less on the chemistry of carbon, taking inspiration instead from the rich chemistry of transition metals.⁹ Many attempts to synthesize heavy equivalents of simple carbon compounds resulted in species possessing transition metal like properties such as open coordination sites (whether due to low valency or frustrated Lewis pairs), paramagnetism and stable diradicaloids. The comparisons to transition metals were based on energetic arguments, notably the small HOMO- LUMO gaps of the multiply bonded species, which could be compared to the closely spaced d-orbitals of transition metals. More important is the actual reactivity of these compounds. Transition metal complexes are often used to activate various small molecules. This chemistry was not often examined for heavy main group compounds. The first example of H_2 activation was the addition of molecular hydrogen across the triple bond of a digermene.¹⁰ This reactivity is unknown in the absence of a transition metal catalyst in alkyne chemistry. The interaction of the H_2 σ orbital with the π bonding and unoccupied non-bonding orbital of the digermene closely mirrors the same interaction with the frontier d orbitals of transition metal complexes for hydrogen activation (Figure 1.1). The exploration of this new view of main group compounds has led to a renaissance in main group chemistry.¹¹

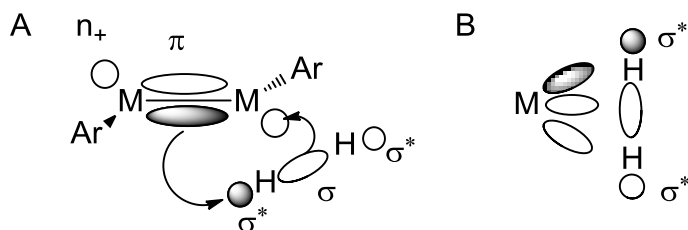


Figure 1.1 Comparison of the interaction of H₂ with A) a multiply bonded main group species and B) a transition metal complex

1.1.1 Low Valent Species

While the chemistry of carbenes is extensive, the +4 oxidation state is by far the most stable for carbon. As one descends group 14, the +2 oxidation state becomes increasingly stable due to the inert pair effect, with tin(II) and lead(II) species being considerably more readily isolated than carbenes, silylenes and germylenes. The isolation of the lighter species can be approached in three ways:¹²⁻¹⁵ 1) kinetic stabilization with bulky ligands (Chart 1.1 A) 2) electronic stabilization with an intramolecular donor (either an adjacent π donor analogous to N-heterocyclic carbenes (Chart 1.1 B) or a tethered σ donor (Chart 1.1C)) and 3) electronic stabilization with an intermolecular donor (Chart 1.1 D). The two former methods are more extensively developed, with intermolecular stabilization being a recent area of interest.¹⁶⁻¹⁹

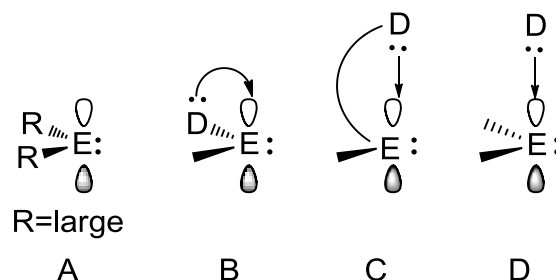
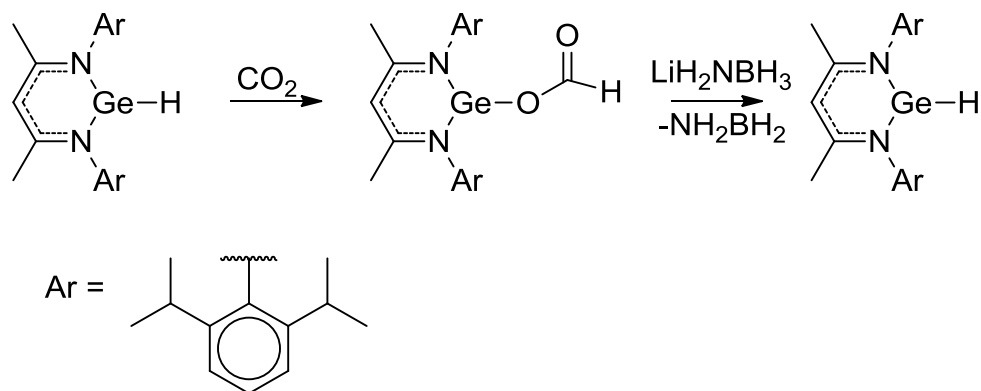


Chart 1.1 Stabilization of light group 14 compounds in the +2 oxidation state (E=C, Si, Ge).

The reactivity of the group 14 hydrides in the +4 oxidation state has been well studied due to their utility in organic synthesis.² Again, the tin compounds have been most extensively examined due to their utility in radical reactions, but germanium hydrides have also been used in cases where the rate constant for the germanium derivative was better suited to the reaction. Low valent group 14 hydrides posed a more considerable synthetic challenge as hydrogen does not provide the steric bulk or electronic requirements needed to stabilize the +2 oxidation state.²⁰ However, once the relevant compounds were synthesized, they were found to insert cleanly into carbon dioxide without an additional catalyst (Scheme 1.1). The addition of LiH_2NBH_3 regenerates the original germanium hydride, rendering the entire reaction catalytic. Achieving small molecule activation *without* the use of expensive transition metals is a highly desirable outcome, especially in terms of carbon sequestering.

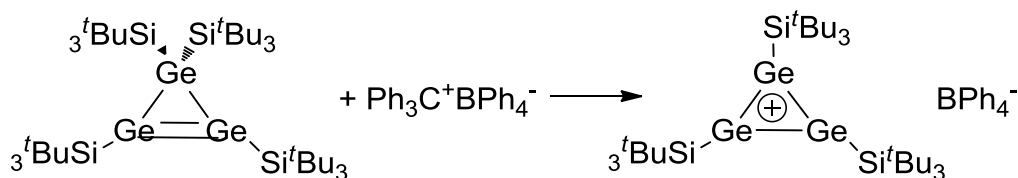


Scheme 1.1 Catalytic reaction of a low valent germanium hydride with carbon dioxide.

A notable extension of the traditional chemistry of the tetravalent hydrides was the discovery that the low valent hydrides perform hydrogermylation reactions, a well established reaction of germanium(IV) hydrides, without the use of traditional transition metal catalyst.

1.1.2 Cationic Species

The analogy to transition metal chemistry provided a new avenue of investigation for main group cations. Cationic species of group 14 have long been of interest because of the direct analogy to carbenium ions and the synthetic challenge they presented.²¹ While ions of the heavier, less electronegative members of group 14 should, in theory, be more stable than carbenium ions, the larger atomic radius and longer bonds led to facile interactions with either the solvent or counterion, mitigating the cationic character on the actual metalloid centre. The first reported example of an unambiguous group 14 cation was a germanium analogue of the cyclopropylcarbenium ion.²² Through the use of bulky, electron donating tri-*tert*-butylsilyl groups and a weakly coordinating tetraphenylborate anion, it was possible to isolate the cationic species free from any significant interactions (Scheme 1.2). The strategies of great steric bulk, non-coordinating solvent and weakly coordinating anions have proven to be generally effective for the isolation of group 14 cations.^{21,23-25}



Scheme 1.2 *Synthesis of the first isolable germanium cation.*

In 2008, silylium ions ceased to be mere laboratory curiosities when a silylium-carborane species was shown to defluorinate fluoralkanes, a notoriously challenging process of great environmental interest.²⁶ Regeneration of the silylium ion rendered the process catalytic, improving the potential for application.

These exciting reactivity trends are inextricably linked to the unusual structures of the low valent and charged compounds. A thorough understanding of the structure of novel compounds is necessary to understand their reactivity. As more unusual bonding modes emerge, there is an increasing need for new tools to understand structure.

In the cases of silicon and tin compounds, NMR spectroscopy in both the solid and solution states has played a critical role in the characterization of new compounds.²⁷⁻³⁰

The ability to directly study the reactive centre in novel group 14 compounds is extremely useful as the most dramatic changes take place there, rather than at the organic ligands. The development of organogermanium chemistry has lagged behind that of silicon and tin. While there are many factors at play, the lack of the same convenient NMR techniques available for the rest of group 14 has contributed to the delay.

1.2 Introduction to Solid-State NMR Spectroscopy

Solution state nuclear magnetic resonance (NMR) spectroscopy is the most valuable diagnostic technique in synthetic chemistry. While the most commonly studied nuclei in synthetic organic chemistry are ^1H and ^{13}C , multinuclear NMR spectroscopy is invaluable in synthetic inorganic chemistry. Generally, more information can be obtained by directly probing the relevant nucleus than through indirect examination of the attached ligands.

While solution state experiments are relatively routine, additional electronic and structural information can be obtained by solid-state NMR (SSNMR) spectroscopy. In the solid state, anisotropic interactions dependent on the orientation of the molecule within the magnetic field are observed. Rapid molecular tumbling in solution averages

anisotropic interactions to their isotropic value. Due to the absence of averaging, solid-state experiments exhibit broader signals and generally require longer acquisition times.

Solid-state NMR spectroscopy is particularly useful in materials which lack the long range order required for X-ray diffraction.³¹ Even in the case of systems which do diffract, NMR spectroscopy can provide complementary information by examining shorter range interactions. Additionally, empirical relationships between NMR spectroscopic data and structural metrics provided by X-ray crystallography can be used to provide insight into the structure of an unknown compound through comparison to related systems. In these endeavours, *ab initio* calculations of NMR spectroscopic parameters can provide a useful support, if reliable computational methods exist for the nucleus of interest.

The most commonly studied anisotropic interactions in SSNMR spectroscopy are dipolar coupling, chemical shielding anisotropy (CSA) and the quadrupolar interaction. Of these, CSA and the quadrupolar interaction are considered in this study. The compounds examined in this work do not feature NMR active nuclei in sufficient proximity to each other to give rise to dipolar coupling, with the exception of ^1H , which was decoupled in all cases for ease of acquisition.

1.2.1 Chemical Shielding Anisotropy

CSA is the orientation dependence of the chemical shielding at a nucleus. It is a three component tensor which is described here using the Herzfeld-Berger convention. Using this convention, the shape of the line is described by the isotropic shift (δ_{iso}), span (Ω) and

skew (κ). The isotropic shift corresponds to the average shift observed in solution, while Ω reflects the overall breadth of the signal and κ the lineshape.

$$\delta_{iso} = \frac{\delta_{11} + \delta_{22} + \delta_{33}}{3} \quad (1)$$

$$\Omega = \delta_{11} - \delta_{33} \quad (2)$$

$$\kappa = \frac{3(\delta_{22} - \delta_{iso})}{\delta_{11} - \delta_{33}} \quad (3)$$

δ_{nn} are the individual components of the tensor with magnitudes defined as $\delta_{11} > \delta_{22} > \delta_{33}$.

A skew value of +/-1, with the greatest intensity on one end of the spectrum, indicates an axially symmetric environment at the nucleus of interest while a symmetric spectrum with a skew value of 0 indicates spherical symmetry (Figure 1.2). A larger span indicates a greater orientation dependence of the nuclear shielding.

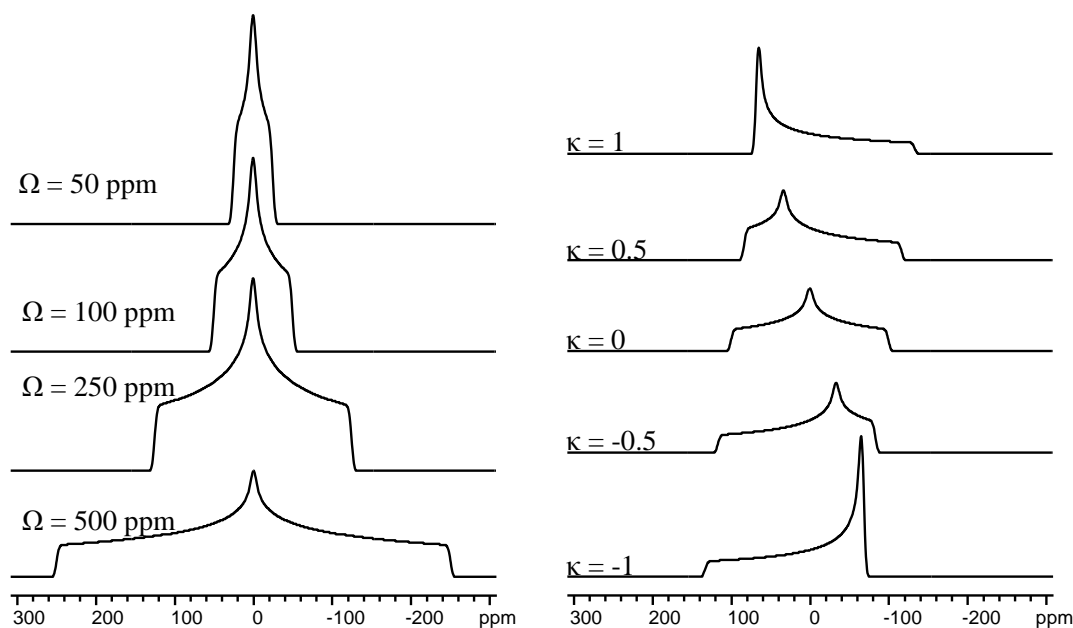


Figure 1.2 Effect of CSA parameters on SSNMR spectrum lineshape. A) Varying span with a constant skew of 0. B) Varying skew with a constant span of 300 ppm.

When a solid sample is rotated, it acquires a modulation factor dependent on angles.³² The factor can be described using a second order Legendre polynomial, $\frac{1}{2}(3 \cos^2\theta - 1)$. This term becomes zero when $\theta = 54.74^\circ$, thereby cancelling out the anisotropic interactions through what is known as magic angle spinning (MAS). With sufficiently rapid spinning, the signal becomes a single sharp line at the isotropic shift. However, to completely average out anisotropic interactions, the spinning rate must exceed the breadth of the static signal. At slower speeds, the signal is instead broken down into a series of spinning sidebands separated from the isotropic shift by the spinning rate (Figure 1.3). Acquisition of the spectrum at two different spinning rates is required to determine which peak is the isotropic shift.

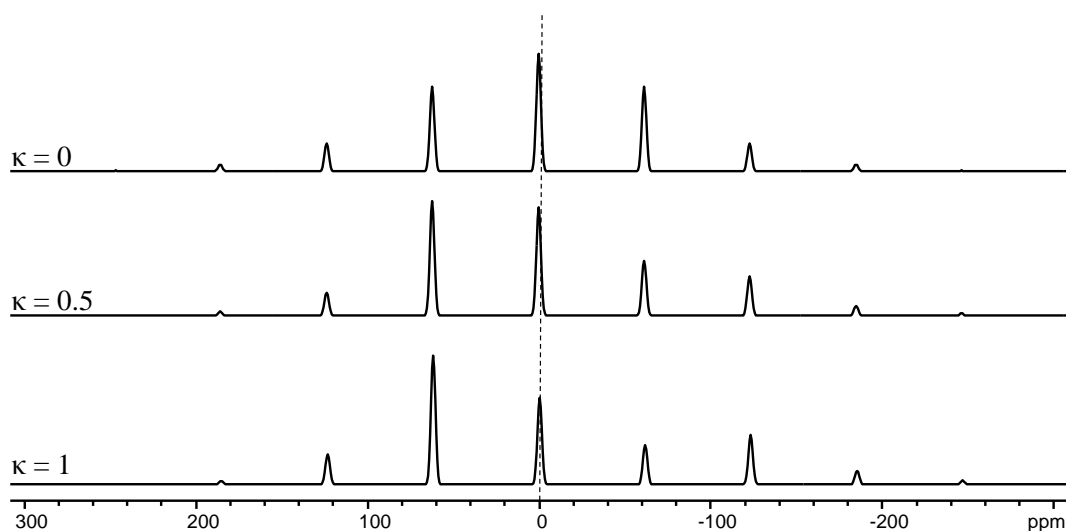


Figure 1.3 CSA lineshapes with varying skew under MAS conditions with a spin rate less than the spectral breadth. The isotropic shift is indicated by the dashed line.

1.2.2 Quadrupolar Interaction

In nuclei with a spin greater than $\frac{1}{2}$, the dominant anisotropic interaction is generally the quadrupolar interaction.³³ In the absence of perfect spherical symmetry, there is a distribution of electron density around the nucleus known as the electric field gradient

(EFG). In quadrupolar nuclei, the uneven distribution of charge within the nucleus will interact with the EFG, leading to broader lines. The exact extent of this broadening depends on the quadrupole moment of the nucleus. In quadrupolar nuclei, there are 2I allowed transitions. However, generally only the central ($-1/2 \rightarrow +1/2$) transition is observed for half integer nuclei as the satellite transitions give rise to extremely broad transitions that are also off resonance, and thus, not readily detected. The different transitions differ in energy due to the quadrupolar interaction which can be viewed as a perturbation of the Zeeman interaction.³⁴ The central transition is not affected by first order quadrupolar distortion. However, second order quadrupolar interactions still cause complex lineshapes. EFG-based lineshapes are described in terms of the quadrupolar coupling constant (C_Q) and the quadrupolar asymmetry parameter (η_Q). These are defined as:

$$C_Q = \frac{eV_{zz}Q}{h} \quad (4)$$

$$\eta_Q = \frac{V_{xx} - V_{yy}}{rV_{zz}} \quad (5)$$

where e is the charge of an electron, Q is the quadrupolar moment of the nucleus of interest, h is Planck's constant and V_{mn} are the eigenvalues of the electric field gradient (EFG) tensor. The magnitudes of the components are defined as $V_{zz} > V_{yy} > V_{xx}$.

C_Q describes the overall breadth of the spectrum and is most strongly influenced by the overall strength of the electric field gradient tensor and in a perfectly symmetrical environment would be equal to zero. This parameter is extremely sensitive to the environment around the nucleus. While it is a complex dependence, it is often possible to

form structural correlations to specific elements such as bond lengths or coordination numbers within a series of related compounds.³³ The asymmetry parameter reflects the symmetry at the nucleus, with $\eta_Q = 0$ indicating an axially symmetric (C_3 or higher) environment and yielding a spectrum where the major discontinuities are found at the edges of the spectrum (Figure 1.4). Decreased symmetry causes the discontinuities to move toward the centre of the spectrum.

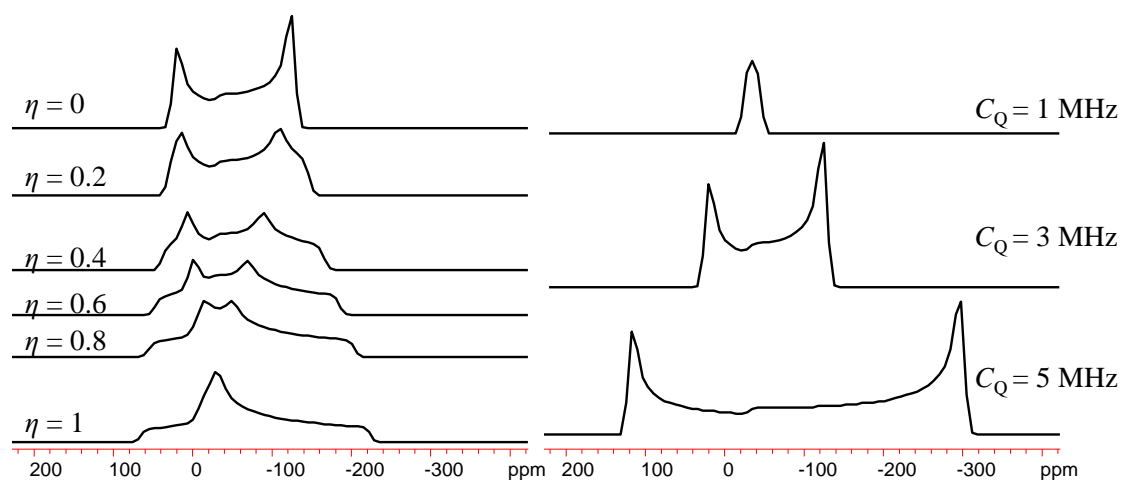


Figure 1.4 Effect of quadrupolar parameters on SSNMR lineshape of ^{35}Cl ($I=3/2$) at 21.1 T. A) Varying η_Q with a constant $C_Q = 3$ MHz. B) Varying C_Q with a constant η_Q of 0.

In general, quadrupolar interaction dominates over CSA when present. However, as the effect of CSA on linewidth is proportional to field strength and the effect of the quadrupolar interaction is inversely proportional, at sufficiently high magnetic field it is possible to observe both in the same spectrum. In the absence of symmetry elements dictating the orientation of tensor components, the two tensors are not necessarily coincident.³⁵ The two tensors offer insight into different properties, as the interactions which affect shielding are much more localized than those that impact the quadrupolar interaction.

While first order quadrupolar interactions are averaged out by MAS, the second order quadrupolar interaction exhibits a more complex angular dependence than CSA or dipolar coupling. As a second order interaction, it depends instead on the fourth order Legendre polynomial, $1/8(35\cos^4\theta-30\cos^2\theta+3)$, which cannot be canceled at the same angle as the second order polynomial. In the case of nuclei with spin greater than $1/2$, even infinite speed MAS would not completely average out the quadrupolar broadening. However, there will still be some reduction of linewidth. This is particularly useful in cases where the CSA and EFG are of comparable magnitudes as it allows for determination of the quadrupolar parameters independently, which can then be held constant and the CSA parameters determined from a static spectrum.³⁵

1.3 Techniques for Wideline NMR Spectroscopy

One of the greatest challenges when performing solid-state NMR spectroscopy on quadrupolar nuclei is the extreme breadth of the signals. This leads to two problems: a reduction in the signal-to-noise ratio and technical difficulties associated with excitation of such a broad signal.

Both these problems can be combatted to a degree through the use of higher magnetic fields. The signal-to-noise ratio is enhanced due to the inherently improved sensitivity. More importantly, the effect of the quadrupolar interaction on linewidth is inversely proportional to field strength. While the excitation profile of an RF pulse is not affected by field strength, the overall signal is narrower at higher fields.

One of the most commonly used techniques for enhancement of broad signals is the Quadrupolar Carr-Purcell-Meiboom-Gill (QCPMG) sequence.³⁶ The sequence consists of

a standard spin echo experiment, but rather than allowing the magnetization to decay normally after the initial refocusing pulse, it is repeatedly refocused. Signal decay is thus only from the true T_2 rather than the magnetic field inhomogeneity-induced T_2^* .

Additionally, when the echo train is Fourier transformed, the broad signal is collected into a series of spikelets, greatly enhancing the signal-to-noise ratio. However, due to the use of hard pulses, the excitation profile is often insufficient for excitation of the full linewidth, especially in the case of nuclei with a large quadrupole moment. This problem can be overcome through frequency-stepping, where a series of spectra are collected at evenly spaced transmitter frequencies. The individual subspectra are then Fourier transformed and added together in the frequency domain to give the complete lineshape. As the probe must be manually tuned to each frequency, this is an extremely labour intensive approach to the acquisition of broad spectra.

In recent years, several variations on the QCPMG sequence have been developed to further increase its utility.^{37,38} The use of shaped pulses which do not employ a consistent frequency or amplitude can significantly alter the excitation profile. One popular variation employs adiabatic Wideband Uniform Rate Smooth Truncation (WURST) pulses to improve the excitation profile.^{39,40} A WURST-80 pulse is employed for initial excitation and then a series of identical pulses is used to refocus the signal. While frequency-stepping may still be required for particularly wide signals, the number of subspectra is greatly reduced, which allows for a significant reduction in acquisition time. While there is some loss in the signal-to-noise ratio using WURST pulses due to the longer pulse lengths, the improved excitation profile makes it the preferred pulse sequence for signals exceeding the excitation profile of a simple RF pulse in breadth.

Although initially developed for quadrupolar nuclei, the same pulse sequence can also be used for spin $\frac{1}{2}$ nuclei with large chemical shielding anisotropies.⁴¹

1.4 NMR Crystallography

NMR spectroscopy provides a powerful complement to X-ray diffraction methods. The ability to obtain specific structural information was recognized early in the development of SSNMR spectroscopy when Pake determined the distance between the hydrogen atoms of $\text{CaSO}_4 \cdot 2\text{H}_2\text{O}$ to be 1.58 Å from the dipolar coupling interaction.⁴² This was particularly notable as at the time (1948), it was extremely difficult to detect hydrogen atoms by X-ray diffraction. Indeed, NMR spectroscopy is most facile for the lighter elements, while diffraction methods excel with heavier elements, making them excellent complements to each other.

More recently, with advances in both NMR and computational techniques, the possibilities for determining crystallographic information from spectroscopic data have greatly increased, leading to the rise of the term NMR crystallography. NMR parameters are all highly sensitive to the local symmetry about the nucleus. If the molecule is found to have local symmetry, the number of possible space groups can thus be narrowed down considerably to only those which contain the relevant Wyckoff sites.⁴³ In the case of molecular compounds, the number of resonances observed will depend on the number of molecules within the asymmetric unit of the unit cell. Due to the inherent sensitivity of NMR tensors to local geometry, the parameters for a proposed structure can be calculated to determine whether it is a realistic possibility.

Where diffraction is sensitive to long range order, NMR spectroscopy is sensitive to the short range interactions. This can be useful for determining the individual configurations within a disordered crystal. Where the diffraction data will reveal only the average environment, the NMR line shape will show contributions from each individual local environment, with the exception of fast exchange between sites.⁴⁴ This allows for the distinction between static and dynamic disorder in a crystal structure.

Solid-state NMR spectroscopy is a powerful complement as it makes it possible to circumvent some of the limitations of diffraction.⁴⁵ Notably, it is not necessary to obtain X-ray quality single crystals in order to study a compound by SSNMR spectroscopy. NMR experiments are most commonly carried out on polycrystalline samples for which it is only possible to obtain powder diffraction data. Additionally, it is also possible to examine amorphous materials which do not diffract at all. Finally, elements with similar atomic numbers such as nitrogen and oxygen can be difficult to differentiate in diffraction data. However, the two nuclei resonate at distinct frequencies. Additionally, the effect on nearby nuclei is also distinctive, allowing for clarification of ambiguous structure. Even in those cases where the X-ray structure is unambiguous, SSNMR spectroscopy can be used to ascertain that the single crystal obtained does in fact accurately represent the structure of the bulk sample.

1.5 Group 14 NMR Spectroscopy

Carbon, silicon, tin and lead all possess at least one spin $\frac{1}{2}$ isotope. NMR spectroscopy, in both the solid and solution states, has proven to be an invaluable diagnostic tool. To examine the new forms of transition metal-like reactivity, the ability to directly examine the reactive metal or metalloid center has been invaluable.

1.5.1 Silicon-29

^{29}Si NMR spectroscopy is a common and useful characterization technique.²⁹ Silicon has several favourable NMR properties: spin of $\frac{1}{2}$ and a Larmor frequency of 79.44 MHz at 9.4 T. The major challenges of this nucleus are the low (4.6%) natural abundance and the long T_1 relaxation times. In solution, it is generally preferable to use indirect detection experiments. In the solid state, cross polarized experiments are preferred when there are hydrogen atoms in reasonable proximity to silicon. By transferring magnetization from the more sensitive ^1H nuclei, it is possible to overcome both the lower gyromagnetic ratio and long relaxation times. The success of ^{29}Si SSNMR spectroscopy was a major factor to the development of SSNMR spectroscopy as an important technique in materials chemistry.⁴⁶ ^{29}Si SSNMR spectra are generally well resolved as the CSA tends to be relatively small even in low symmetry environments, allowing it to be readily averaged under MAS conditions. Static spectra are employed for additional structural insight, particularly in systems with sites of similar isotropic shifts but different CSA tensors.

Due to the accessibility of ^{29}Si NMR spectroscopy, extensive relationships between chemical environment and chemical shift have been developed.²⁹ Chemical shifts range from 600 to -400 ppm relative to SiMe_4 at 0 ppm. The overall trends in the relationship between multiple bonding and coordination number are similar to those seen for ^{13}C . Generally, deshielded signals are observed for low coordinate species such as silylenes and uncomplexed cationic systems. The most shielded signals are those of hypercoordinate silicon species.

In the solid state, a large number of studies have focused on inorganic silicate materials.⁴⁶

While the first coordination sphere of silicon in these materials is filled by oxygen,

extensive relationships between the isotropic shift and the *second* coordination sphere have been determined. Additionally, there has been considerable interest in the relationship between chemical shift and the Si–O bond length or the O–Si–O bond angle. Within groups of related materials, reasonable correlations have been found; however, when the relationship is generalized to all silicate materials, there is considerably more scatter, reducing the utility of the correlation.

One particularly notable example with respect to the employment of SSNMR spectroscopy as a diagnostic technique in *organosilicon* chemistry is the use of ^{29}Si spectroscopy to characterize a series disilenes.⁴⁷ The nature of the double bond was, at the time, highly controversial. Examination of the CSA tensor revealed considerable anisotropy, consistent with a true π bond.

In this work, ^{29}Si SSNMR spectroscopy is primarily used as an additional source of structural data along with ^{13}C SSNMR spectroscopy.

1.5.2 Tin-119

Tin possesses three NMR active isotopes (^{115}Sn , ^{117}Sn and ^{119}Sn), all of which are spin $\frac{1}{2}$.³⁰ Of these, ^{115}Sn is very rarely studied due to its extremely low (0.59%) natural abundance. The other two NMR active isotopes are much more amenable to NMR spectroscopy with higher natural abundance and high gyromagnetic ratios. Due to the slightly higher abundance and gyromagnetic ratio, ^{119}Sn (8.54% abundant, 149.1 MHz at 9.4 T) is the most frequently studied nucleus, but ^{117}Sn (7.67% abundant, 142.5 MHz at 9.4 T) NMR spectroscopy is feasible when circumstances require it. Much like silicon,

indirect detection experiments are generally preferred in the solution state²⁷ and cross polarization for solid samples when feasible, due to long T_1 relaxation times.

¹¹⁹Sn has a wide chemical shift range, from 4000 to -2500 ppm relative to SnMe₄ at 0 ppm. Due to this range, the isotropic shift is very sensitive to small changes in structure, making ¹¹⁹Sn NMR an extremely valuable characterization technique. Additionally, as is common for heavier spin ½ nuclei, tin compounds are subject to considerable chemical shielding anisotropy, giving rise to broad powder patterns and providing the potential for additional structural insight, although this does also pose some degree of challenge in collecting spectral data. The span of this interaction is equally sensitive to structural features, including the oxidation state of tin.²⁸

Solid-state NMR experiments makes it possible to link solution state data to crystallographic information as well as providing evidence for differences in structure between the two states.³⁰ Intermolecular interactions, while generally weak in solution, can have a dramatic impact on a solid-state lineshape. Additionally, tin frequently adopts a higher coordination number in the condensed phase, causing a shift to lower frequencies.

CSA relaxation is the dominant mode of T₂ relaxation for ¹¹⁹Sn in solution at moderate (> 5.97 T) magnetic fields. As B₀ increases, ¹¹⁹Sn signals become increasingly broadened. In the case of highly anisotropic environments, this may make solution state spectroscopy extremely challenging while solid-state experiments remain feasible.^{48,49}

In many lighter nuclei, *ab initio* calculations have provided a valuable complement to NMR spectroscopy. However, until recently, there had been little success in reproducing

experimental tin shielding parameters computationally.³⁰ Due to the relatively large atomic number, relativistic effects can have a substantial effect on the calculated parameters.⁵⁰ While good agreement can be achieved without including these effects when tin is bound only to light elements, the situation changes considerably when heavy atoms are involved. In the case of SnI₄, the spin orbit term accounts for a difference of over 2500 ppm in comparison to non-relativistic calculations. The use of the Zeroth Order Relativistic Approximation (ZORA) and all electron basis sets specifically tailored to the method allows for the inclusion of the spin orbit term, and thus, accurate computation of ¹¹⁹Sn chemical shielding.

1.6 Germanium-73 NMR Spectroscopy

Where ²⁹Si and ¹¹⁹Sn NMR spectroscopy have been invaluable tools for the investigation of organosilicon and organotin chemistry,^{28-30,51} investigation of organogermanium systems has often been more challenging as germanium NMR spectroscopy is considerably more poorly developed. Germanium possesses only one NMR active isotope, ⁷³Ge, which exhibits multiple unfavourable properties.⁵² It has a low natural abundance (7.76%), though the natural abundance is comparable to ²⁹Si (4.5%). Were the low natural abundance the only unfavourable property, ⁷³Ge NMR spectroscopy would still be extremely feasible. However, unlike the spin 1/2 ²⁹Si, ⁷³Ge is quadrupolar with a spin of 9/2 and a moderate quadrupole moment of -196 mb.⁵³ The greatest challenge is the low gyromagnetic ratio of ⁷³Ge, which, at $0.9332 \times 10^7 \text{ radT}^{-1}\text{s}^{-1}$ (corresponding to a Larmor frequency of only 31.4 MHz at 21.1 T), is among the lowest in the periodic table.⁵⁴

Low gyromagnetic ratio nuclei are inherently challenging to study as the sensitivity of a nucleus per spin is proportional to γ^3 .³¹ In the solid state, the sensitivity of quadrupolar nuclei is further diminished by the distribution of the magnetization across multiple spin levels. As only the central $-1/2 \rightarrow +1/2$ transition is typically observed, the remaining sensitivity is lost. The overall receptivity of a nucleus is thus defined as (natural abundance * γ^3)/(I(I+1)). The combination of unfavourable NMR properties for ^{73}Ge leads to a receptivity of only 0.644 relative to ^{13}C .

While the magnetic moment of ^{73}Ge was first reported in 1953,⁵⁵ the first ^{73}Ge chemical shifts were not reported until the 1970s.⁵⁶ Early studies largely focused on tetrasubstituted systems as any degree of quadrupolar broadening made observation of the signals extremely difficult using the instrumentation of the day. While solution state studies remain limited, there has been sufficient data acquired to determine that ^{73}Ge chemical shifts follow the same general trends observed for ^{29}Si and ^{119}Sn chemical shifts.⁵² While germanium chemical shifts exhibit a complex environmental dependence, within related classes of compounds it has been possible to draw linear correlations between ^{73}Ge shifts and those of the analogous silicon and tin systems.

Due to these challenges, solid-state studies of ^{73}Ge NMR spectroscopy have been even more limited than solution state studies. The earliest solid-state investigation of ^{73}Ge was undertaken in 1999 on single crystals of elemental germanium.⁵⁷

A limited number of studies on organogermanes have previously been carried out at moderate (300 MHz) field.⁵⁸⁻⁶⁰ These studies focused almost exclusively on highly symmetrical systems, though spectra were obtained for two compounds with similar but

non-identical substituents on germanium. With the exception of the highest symmetry examples, data acquisition required very long experiment times, on the order of weeks. Such experiment times are not practical for a diagnostic tool in synthetic chemistry.

More recently, studies using ultra-high (21.1 T) magnetic fields on inorganic germanates have proven more feasible.^{61,62} Using the QCPMG pulse sequence, it was possible to obtain spectra with a sufficiently high signal-to-noise ratio to extract quadrupolar parameters via spectral simulation in a reasonable time frame. In order to simulate a spectrum, the individual discontinuities must be clearly defined to assess their agreement with a simulated line. In a study of germanium halides,⁶³ ^{73}Ge and ^{35}Cl SSNMR spectroscopy were used in combination with density functional theory (DFT) calculations to determine that the structure of GeCl_2 was more likely to resemble that of GeI_2 than GeBr_2 as had been previously proposed.

1.7 Chlorine-35 NMR Spectroscopy

Due to the multiple unfavourable properties of ^{73}Ge , even with the use of sensitivity enhancement pulse sequence and ultrahigh magnetic fields, ^{73}Ge NMR spectroscopy is not always expected to be feasible. Thus, obtaining indirect information about germanium via the substituent is likely to remain a necessity. As chlorine is a frequently used substituent in synthetic germanium chemistry,⁶⁴ ^{35}Cl is an attractive spectroscopic target.

All the halogens possess at least one NMR active isotope.⁶⁵ However, with the exception of fluorine, they have only been the subject of limited studies. While ^{19}F is a spin $\frac{1}{2}$ nuclei, the remaining halogens are quadrupolar. Additionally, they possess large quadrupole moments leading to extremely wide signals. Of the quadrupolar halogens,

^{35}Cl and ^{37}Cl have the smallest quadrupole moments, though at -81.65 mb and -64.35 mb , respectively, they are still considered to be large. However, the quadrupole moments of ^{79}Br (313 mb), ^{81}Br (261.5 mb) and ^{127}I (-710 mb) are considerably larger.

Other than the large quadrupole moments, the quadrupolar halogens possess favourable NMR properties. While both isotopes of chlorine are considered low gamma (gyromagnetic ratio less than one tenth that of ^1H), they are only narrowly so, with Larmor frequencies of 88.18 MHz (^{35}Cl) and 73.40 MHz (^{37}Cl) at 21.1 T (900 MHz for ^1H). Additionally, the natural abundances are very favourable at 75.78% (^{35}Cl) and 24.22% (^{37}Cl). Due to the somewhat higher gyromagnetic ratio and considerably higher natural abundance, ^{35}Cl is the preferred isotope despite the somewhat larger quadrupole moment. ^{37}Cl NMR spectroscopy is also feasible and can be used to verify the spectral parameters determined for ^{35}Cl .

Due to the large quadrupole moment, the majority of early investigations into ^{35}Cl SSNMR spectroscopy focused on ionic salts with chlorine situated on a site of cubic symmetry.⁶⁶ While this simplifies spectral acquisition, the majority of chlorine-containing compounds feature chlorine in a site of much lower symmetry. Covalently-bound chlorine is typically found in a terminal position. In recent years, the availability of ultrahigh field ($>18.8\text{ T}$) spectrometers has greatly improved the accessibility of this nucleus. ^{35}Cl NMR spectroscopy has also benefitted from the development of pulse sequences specifically for the acquisition of extremely broad lines. This has made it possible to study organic chlorides with covalently bound chlorine.⁶⁷

Through the use of techniques designed for ultrawide line NMR spectroscopy, several systems of synthetic interest have been studied. In a study of metallocene complexes,⁶⁸ the quadrupolar coupling constant was found to be related to the M–Cl bond length. Through a combination of ³⁵Cl SSNMR spectroscopy and DFT calculations, insight was gained into the structure of Schwartz’s reagent (an important catalyst with an unknown structure).

DFT calculations have proven to be a highly useful complement to ³⁵Cl SSNMR spectroscopy. As much of the early work in this area has focused on ionic compounds, plane wave pseudopotential calculations have been widely used to account for long range order.⁶⁹ This has proven particularly useful for reproducing the value of C_Q .⁷⁰ From these calculations, it is possible to determine the sign of C_Q , information not available experimentally. Additionally, the orientations of the three EFG tensor components can potentially give insight into the bonding of a complex. Calculations can also be used to assign signals that are not immediately clear from symmetry alone via the relative magnitudes of predicted parameters.

1.8 Thesis Overview

This project is focused on the development of SSNMR spectroscopy as a technique for structural characterization of organogermanium compounds with a focus on novel germanium(II) and cationic species. While this is well established for ²⁹Si and ¹¹⁹Sn, ⁷³Ge NMR spectroscopy remains considerably less studied. Due to the inherent challenges in germanium NMR spectroscopy, ³⁵Cl will also be examined as a potential indirect probe of the structure at germanium.

In Chapter 2, a series of simple germanium(IV) compounds will be examined by ^{73}Ge SSNMR spectroscopy supported by ^{13}C and ^{29}Si SSNMR spectroscopy. While the ultimate goal is to be able to study low valent and cationic systems with potential catalytic applications, the study of simple benchmarks is an important starting point in the development of a diagnostic technique. Relationships between structural metrics and NMR parameters will be examined to gain insight into compounds without known structures. Finally, the scope of the technique will be examined from systems of ideal symmetry to lower symmetry systems which are more commonly encountered organogermanium chemistry.

In Chapter 3, the amorphous germanium(I) monohalides, GeCl and GeBr , will be examined through a combination of ^{35}Cl , ^{73}Ge and ^{79}Br SSNMR spectroscopy and computational techniques to obtain insight not available from other techniques into the structure of this novel non-crystalline material.

Chapter 4 examines the use of ^{35}Cl as an indirect probe of germanium environment. A series of germanium(II) and germanium(IV) complexes with varying chlorine environments will be examined to determine the sensitivity of ^{35}Cl parameters to changes at the attached germanium centre.

Chapter 5 will focus on a series of four cationic tin(II) complexes for which it was not possible to obtain ^{119}Sn spectra in solution. Two of these possess known crystal structures, which will be used to establish the spectroscopic parameters for comparison to a third for which single crystals could not be obtained. ^{119}Sn SSNMR spectroscopy will

also be used to offer insight into the correct interpretation of the crystal structure of a fourth complex.

Finally, overall conclusions will be presented in Chapter 6.

1.9 Co-Authorship

This work would not have been possible without the contributions of many individuals.

In Chapter 2, the ^{73}Ge SSNMR spectra at 21.1 T of **2.3**, **2.4**, **2.5**, **2.9**, **2.10**, **2.11** and **2.15** were acquired by Victor Terskikh. Andre Sutrisno provided considerable assistance in simulating the spectra. Compound **2.15** was provided by Christoph Marschner. The X-ray structure of **2.2** was acquired and solved by Guerman Popov.

In Chapter 3, GeCl and GeBr were provided by Andreas Schnepf, who also acquired the Raman spectrum of GeBr. The SSNMR spectra were acquired by Victor Terskikh.

In Chapter 4, the ^{35}Cl SSNMR spectra of **4.1-4.8** at 21.1 T were acquired by Victor Terskikh, along with the ^{73}Ge SSNMR spectra of **4.4** and **4.5**.

Finally, in Chapter 5, compound **5.1** was prepared by Paul Rupar and compounds **5.8-5.11** by Jessica Avery.

Spectral simulations were performed using Klaus Eichele's WSolids. In Chapter 3, Thomas Kemp's QuadFit was used to simulate spectra with a distribution of quadrupolar parameters. Gaussian 09 output files were analyzed using David Bryce's EFGShield. The WURST-QCPMG and WURST-CPMG pulse sequences were provided by Robert Schurko. Initial non-nucleus specific optimization of the WURST-QCPMG pulse sequence was performed by Andre Sutrisno.

1.10 References

- (1) Fouquet, E. In *The Chemistry of organic germanium, tin and lead compounds*; Rappoport, Z., Ed.; John Wiley and Sons: Chichester, **2002**; Vol. 2, p 1333.
- (2) Carland, M. W.; Schiesser, C. H. In *The Chemistry of organic germanium, tin and lead compounds*; Rappoport, Z., Ed.; John Wiley and Sons: Chichester, **2002**; Vol. 2, p 1401.
- (3) Pitzer, K. S. *J. Am. Chem. Soc.* **1948**, *70*, 2140.
- (4) Brook, A. G.; Abdesaken, F.; Gutekunst, G.; Kallury, R. K. *J. Chem. Soc., Chem. Commun.* **1981**.
- (5) Meyer, H.; Baum, G.; Massa, W.; Berndt, A. *Angew. Chem. Int. Ed.* **1987**, *26*.
- (6) Couret, C.; Escudie, J.; Satge, J.; Lazraq, M. *J. Am. Chem. Soc.* **1987**, *109*, 4411.
- (7) West, R.; Fink, M. J.; Michl, J. *Science* **1981**, *214*, 1343.
- (8) Hitchcock, P. B.; Lappert, M. F.; Miles, S. J.; Thorne, A. J. *J. Chem. Soc., Chem. Commun.* **1984**, 480.
- (9) Power, P. P. *Nature* **2010**, *463*, 171.
- (10) Power, P. P. *Organometallics* **2007**, *26*, 4362.
- (11) Arnold, J. *Dalton Trans.* **2008**, 4334.
- (12) Neumann, W. P. *Chem. Rev.* **1991**, *91*, 311.
- (13) Weidenbruch, M. *Eur. J. Inorg. Chem.* **1999**, 373.
- (14) Nagendran, S.; Roesky, H. W. *Organometallics* **2008**, *27*, 457.
- (15) Mizuhata, Y.; Sasamon, T.; Tokitoh, N. *Chem. Rev.* **2009**, *109*, 3479.
- (16) Rupar, P. A.; Jennings, M. C.; Ragogna, P. J.; Baines, K. M. *Organometallics* **2007**, *26*, 4109.

- (17) Rupar, P. A.; Jennings, M. C.; Baines, K. M. *Can. J. Chem.* **2007**, *85*, 141.
- (18) Rupar, P. A.; Jennings, M. C.; Baines, K. M. *Organometallics* **2008**, *27*, 5043.
- (19) Ruddy, A. J.; Rupar, P. A.; Bladek, K. J.; Allan, C. J.; Avery, J. C.; Baines, K. M. *Organometallics* **2010**, *29*, 1362.
- (20) Mandal, S. K.; Roesky, H. W. *Acc. Chem. Res.* **2012**, *25*, 298.
- (21) Lee, V. Y.; Sekiguchi, A. *Acc. Chem. Res.* **2007**, *40*, 410.
- (22) Sekiguchi, A.; Tsukamoto, M.; Ichinohe, M. *Science* **1997**, *275*, 60.
- (23) Sekiguchi, A.; Fukawa, T.; Lee, V. Y.; Nakamoto, K.; Ichinohe, M. *Angew. Chem. Int. Ed.* **2003**, *42*, 1143.
- (24) Lambert, J. B.; Lin, L.; Keinan, S.; Müller, T. *J. Am. Chem. Soc.* **2003**, *124*, 6022.
- (25) Lambert, J. B. In *Tin Chemistry: Fundamentals, Frontiers, and Applications*; Davies, A. G., Gielen, M., Pannel, K. H., Tiekink, E. R., Eds.; Wiley: West Sussex, **2008**, p 152.
- (26) Douvris, C.; Ozerov, O. V. *Science* **2008**, *321*, 1188.
- (27) Martins, J. C.; Biesemans, M.; Willem, R. *Prog. Nucl. Magn. Reson. Spectrosc.* **2000**, *36*, 271.
- (28) MacKenzie, K. J. D.; Smith, M. E. In *Multinuclear Solid-State NMR of Inorganic Materials*; MacKenzie, K. J. D., Smith, M. E., Eds.; Pergamon: Kidlington, **2002**, p 591.
- (29) Wrackmeyer, B. *Annu. Rep. NMR Spectrosc.* **2006**, *57*, 1.
- (30) Wrackmeyer, B. In *Tin Chemistry: Fundamentals, Frontiers, and Applications*; Davies, A. g., Gielen, M., Pannel, K. H., Tiekink, E. R., Eds.; Wiley: West Sussex, **2008**, p 17.

- (31) MacKenzie, K. J. D.; Smith, M. E. In *Multinuclear Solid-State NMR of Inorganic Materials*; MacKenzie, K. J. D., Smith, M. E., Eds.; Pergamon: Kidlington, **2002**, p 1.
- (32) MacKenzie, K. J. D.; Smith, M. E. In *Multinuclear Solid-State NMR of Inorganic Materials*; MacKenzie, K. J. D., Smith, M. E., Eds.; Pergamon: Kidlington, **2002**, p 23.
- (33) Ashbrook, S. E.; Duer, M. J. *Concepts Magn. Reson., Part A* **2006**, 28A, 183.
- (34) Bain, A. D.; Khasawneh, M. *Concepts Magn. Reson., Part A* **2004**, 22A, 69.
- (35) Bryce, D. L. In *NMR Crystallography*; Harris, R. K., Wasylshen, R. E., Duer, M. J., Eds.; John Wiley & Sons: Chichester, **2009**.
- (36) Larsen, F. H.; Jakobsen, H. J.; Ellis, P. D.; Nielsen, N. C. *J. Phys. Chem. A* **1997**, 101, 8597.
- (37) Siegel, R.; Nakashima, T. T.; Wasylshen, R. E. *J. Magn. Reson.* **2007**, 184, 85.
- (38) Schurko, R. W.; Hung, I.; Widdifield, C. M. *Chem. Phys. Lett.* **2003**, 379, 1.
- (39) O'Dell, L. A.; Schurko, R. W. *Chem. Phys. Lett.* **2008**, 464, 97.
- (40) O'Dell, L. A.; Rossini, A. J.; Schurko, R. W. *Chem. Phys. Lett.* **2009**, 468, 330.
- (41) MacGregor, A. W.; O'Dell, L. A.; Schurko, R. W. *J. Magn. Reson.* **2011**, 208, 103.
- (42) Pake, G. E. *J. Chem. Phys.* **1948**, 16, 327.
- (43) Taulelle, F. In *NMR Crystallography*; Harris, R. K., Wasylshen, R. E., Duer, M. J., Eds.; John Wiley & Sons: Chichester, **2009**, p 245.
- (44) Brouwer, D. H. In *NMR Crystallography*; Harris, R. K., Wasylshen, R. E., Duer, M. J., Eds.; John Wiley & Sons: Chichester, **2009**, p 263.

- (45) Harris, R. K. In *NMR Crystallography*; Harris, R. K., Wasylshen, R. E., Duer, M. J., Eds.; John Wiley & Sons: Chichester, **2009**, p 3.
- (46) MacKenzie, K. J. D.; Smith, M. E. In *Multinuclear Solid-State NMR of Inorganic Materials*; MacKenzie, K. J. D., Smith, M. E., Eds.; Pergamon: Kidlington, **2002**, p 201.
- (47) West, R.; Cavalieri, J. D.; Buffy, J. J.; Fry, C.; Zilm, K. W.; Duchamp, J. C.; Kira, M.; Iwamoto, T.; Müller, T.; Apeloig, Y. *J. Am. Chem. Soc.* **1997**, *119*, 4972.
- (48) Bandyopadhyay, R.; Cooper, B. F. T.; Rossini, A. J.; Schurko, R. W.; Macdonald, C. L. B. *J. Organomet. Chem.* **2010**, *695*, 1012.
- (49) Spikes, G. H.; Giuliani, J. R.; Augustine, M. P.; Nowik, I.; Herber, R. H.; Power, P. P. *Inorg. Chem.* **2006**, *45*, 9132.
- (50) Bagno, A.; Casello, G.; Saielli, G. *J. Chem. Theory Comput.* **2006**, *2*, 37.
- (51) Lippman, E. T.; Alla, M. A.; Pehk, T. J.; Engelhardt, G. *J. Am. Chem. Soc.* **1978**, *100*, 1929.
- (52) Liepins, E.; Zicmane, I.; Lukevics, E. *J. Organomet. Chem.* **1988**, *341*, 315.
- (53) Pykko, P. *Mol. Phys.* **2008**, *106*, 1965.
- (54) Takeuchi, Y.; Takayama, T. *Annu. Rep. NMR Spectrosc.* **2005**, *54*, 155.
- (55) Jeffries, C. D. *Phys. Rev.* **1953**, *92*, 1262.
- (56) Kidd, R. G.; Spinnye, H. G. *J. Am. Chem. Soc.* **1973**, *95*, 88.
- (57) Verkhovskii, S. V.; Yakubovskii, A. Y.; Trokiner, A.; Malkin, B. Z.; Saikin, S. K.; Ozhogin, V. I.; Tikhomirov, A. V.; Ananyever, A. V.; Gerashenko, A. P.; Piskunov, Y. V. *Appl. Magn. Reson.* **1999**, *17*, 557.

- (58) Takeuchi, Y.; Nishikawa, M.; Tanaka, K.; Takayama, T.; Imanari, M.; Deguchi, K.; Fujito, T.; Sugisaka, Y. *Chem. Commun.* **2000**, 687.
- (59) Takeuchi, Y.; Nishikawa, M.; Yamamoto, H. *Magn. Reson. Chem.* **2004**, *42*, 907.
- (60) Takeuchi, Y.; Nishikawa, M.; Hachiya, H.; Yamamoto, H. *Magn. Reson. Chem.* **2005**, *43*, 662.
- (61) Michaelis, V. K.; Aguiar, P. M.; Terskikh, V. V.; Kroeker, S. *Chem. Commun.* **2009**, 4660.
- (62) Michaelis, V. K.; Kroeker, S. *J. Phys. Chem. C* **2010**, *114*, 21736.
- (63) Greer, B. J.; Michaelis, V. K.; Terskikh, V. V.; Kroeker, S. *Can. J. Chem.* **2011**, *89*, 1118.
- (64) Levason, W.; Reid, G.; Zhang, W. *Coord. Chem. Rev.* **2011**, *255*, 1319.
- (65) Chapman, R. P.; Widdifield, C. M.; Bryce, D. L. *Prog. Nucl. Magn. Reson. Spectrosc.* **2009**, *55*, 215.
- (66) Widdifield, C. M.; Chapman, R. P.; Bryce, D. L. *Annu. Rep. NMR Spectrosc.* **2009**, *66*, 195.
- (67) Perras, F. A.; Bryce, D. L. *Angew. Chem. Int. Ed.* **2012**, *51*, 4227.
- (68) Rossini, A. J.; Mills, R. W.; Briscoe, G. A.; Norton, E. L.; Geier, S. J.; Hung, I.; Zheng, S.; Autschbach, J.; Schurko, R. W. *J. Am. Chem. Soc.* **2009**, *131*, 3317.
- (69) Charpentier, T. *Solid State Nucl. Magn. Reson.* **2011**, *40*, 1.
- (70) Bryce, D. L.; Bultz, E. B. *Chem.-Eur. J.* **2007**, *13*, 4786.

Chapter 2 Solid-State ^{73}Ge NMR Spectroscopy of Simple Organogermanes*

2.1 Introduction

^{29}Si nuclear magnetic resonance (NMR) spectroscopy has proven to be an invaluable tool for the structural characterization of organosilicon compounds, both in solution- and solid-states, offering insight beyond that available from ^1H and ^{13}C NMR spectroscopy.¹ Of particular utility is the ability to examine the actual nucleus of interest, Si, rather than relying on indirect information via organic substituents. Obtaining comparable information for germanium compounds is considerably more difficult due to the unfavourable properties of ^{73}Ge , the only NMR-active isotope of germanium.^{2,3} While ^{29}Si is a spin-1/2 nucleus, ^{73}Ge is quadrupolar, with a spin of 9/2 and a moderately large quadrupolar moment of -196 mb,⁴ leading to broad lines in the absence of ideal spherical symmetry. While the natural abundances of these nuclei are similar (4.5% for ^{29}Si and 7.7% for ^{73}Ge) the greatest challenge arises from the inherent lack of sensitivity due to the gyromagnetic ratio of ^{73}Ge , which, at $0.9332 \times 10^7 \text{ radT}^{-1}\text{s}^{-1}$, is among the lowest in the periodic table.

In recent years, there have been several developments that improved NMR accessibility of low γ nuclei. The increasing availability of ultrahigh field NMR spectrometers is particularly promising for ^{73}Ge NMR spectroscopy. Operating at very high magnetic field greatly enhances the sensitivity, which is particularly important for low gyromagnetic ratio nuclei. Solid-state NMR (SSNMR) line broadening due to quadrupolar interactions

* A version of this chapter has been published. Margaret A. Hanson, Andre Sutrisno, Victor V. Terskikh, Kim M. Baines, Yining Huang. Solid-State ^{73}Ge NMR Spectroscopy of Simple Organogermanes. *Chem.-Eur. J.* **2012**, *18*, 13770. Reproduced with permission from John Wiley and Sons.

is inversely proportional to the magnetic field strength, leading to narrower lines at higher fields. Additionally, performing NMR experiments at very high magnetic field allows the chemical shielding (CS) tensor, which provides invaluable information on bonding and structure, to be measured more accurately since the effect of chemical shielding anisotropy (CSA) on lineshape is directly proportional to field strength. At lower fields, the quadrupolar interaction tends to completely dominate over the CSA, while ultrahigh fields offer the potential to observe both, and thus, obtain additional structural insight. Sensitivity-enhancement techniques such as Quadrupolar Carr-Purcell-Meiboom-Gill (QCPMG)⁵ and related pulse sequences⁶⁻⁸ have proven valuable in increasing the signal-to-noise ratio of broad quadrupolar patterns. Recently, the incorporation of WURST pulses has further improved the excitation bandwidth of the QCPMG technique.⁷ As ⁷³Ge spectra are generally expected to be broad with poor signal-to-noise ratios even under favourable conditions, WURST-QCPMG has the potential to significantly ease their acquisition.

Due to the inherent challenges, ⁷³Ge SSNMR studies have, so far, been very limited. One of the earliest solid-state ⁷³Ge NMR investigations involved single crystals of elemental germanium.⁹ The large quadrupole moment of the ⁷³Ge nucleus was used to detect disorder induced by changes in the isotopic makeup of the single crystal. The first investigation of a substituted organogermanium center involved the symmetrically substituted GePh₄ and Ge(CH₂Ph)₄ under magic angle spinning (MAS) conditions.¹⁰ While the former compound gave a single sharp signal in a reasonable time-frame; the latter compound required extended acquisition times to acquire only a broad, featureless signal. The difference was attributed to the slightly different Ge–C bond lengths causing

deviation from ideal tetrahedral symmetry in $\text{Ge}(\text{CH}_2\text{Ph})_4$. Even with extended experiment times, the lineshapes were not sufficiently resolved to extract quadrupolar parameters, and thus, only a linewidth at half height and a peak maximum were reported. This report was followed in 2004 with a study of hexacoordinate germanes.¹¹ While several systems with differing ligands were examined, only signals from the symmetrical systems were observed in the solid state. A third study of organogermanes returned to tetra-coordinate systems.¹² The majority of the compounds studied were once again symmetrically substituted, but a few lower symmetry compounds were also included in the study. In general, the tetraaryl systems had distorted S_4 symmetry, resulting in broader lines than were observed for GePh_4 . Thus, longer experiment times were required, sometimes on the order of weeks. Although the less symmetrical systems generally did not give rise to signals, the ^{73}Ge SSNMR spectra of $\text{Ph}_2\text{Ge}(p\text{-C}_6\text{H}_4\text{Me})_2$ and $\text{Ph}_3\text{Ge}(p\text{-C}_6\text{H}_4\text{Me})$ revealed broad signals. This was the first indication that it might be feasible to study lower symmetry systems, though the long experiment times still presented a significant challenge at that time.

Due to the many unfavourable magnetic resonance properties of ^{73}Ge , ultrahigh magnetic fields are expected to be particularly beneficial. Germanium dioxide was the first material studied by ^{73}Ge SSNMR spectroscopy using a 21.1 T magnet.¹³ This work was later expanded to several different polymorphs of GeO_2 .¹⁴ Through the use of the QCPMG pulse sequence at ultrahigh field, it was possible to obtain sufficiently defined lineshapes to extract the quadrupolar parameters via spectral simulation. A comprehensive study of germanium oxide materials with different local structures about germanium, coordination environments and countercations was then conducted to

establish trends in the ^{73}Ge NMR parameters.¹⁵ In general, crystalline materials gave well-defined signals, while vitreous materials gave broad, featureless spectra. A similar situation was observed in the case of germanium selenide glasses,¹⁶ yielding only an average environment around germanium rather than the full range of structural information potentially available from SSNMR spectroscopy. Germanium SSNMR in conjunction with DFT calculations was also used to provide insight into the diverse structural environments in germanium di- and tetrahalides.¹⁷ In a recent communication, we examined GePh_4 and $\text{GeCl}_2\cdot\text{dioxane}$ at ultrahigh field.¹⁸ These two compounds are representative of the two extremes of ^{73}Ge SSNMR spectral data: $\text{GeCl}_2\cdot\text{dioxane}$ exhibited an extremely broad spectrum with a quadrupolar coupling constant (C_Q) of 44 MHz, the largest observed for ^{73}Ge by NMR spectroscopy to date. GePh_4 , on the other hand, exhibited a very small quadrupolar interaction, allowing for the first direct observation of CSA in a ^{73}Ge system.

In this work, we report a systematic investigation of the potential of ^{73}Ge SSNMR spectroscopy by examining simple organogermanium compounds with a range of substituents (Figure 2.1). The majority of these compounds are symmetrical tetra-substituted organogermanes. Specifically, we have investigated the ^{73}Ge SSNMR spectra of tetraarylgermanes including $\text{Ge}(p\text{-Me-C}_6\text{H}_4)_4$ (**2.1**), $\text{Ge}(p\text{-MeO-C}_6\text{H}_4)_4$ (**2.2**) and GePh_4 (**2.3**). While GePh_4 exhibits S_4 symmetry and thus a very small but non-zero EFG, $\text{Ge}(p\text{-Me-C}_6\text{H}_4)_4$ ¹⁹ exhibits a range of bond lengths and angles, which offers the potential to examine the sensitivity of quadrupolar and CSA parameters to small variations in structure. We also examined three other tetra-substituted germanes: tetrabenzylgermane¹⁰ (**2.4**), tetra(*tert*-butoxy)germane (**2.5**) and tetrakis(trimethylsilyl)germane (**2.6**). These are

prototypical examples of tetraalkyl, tetraalkoxy and tetrasilylgermanes, respectively, which will allow an investigation into the effect of different chemical environments on ^{73}Ge SSNMR parameters. While sites of tetrahedral symmetry are the most amenable to ^{73}Ge SSNMR spectroscopy, systems of chemical interest seldom meet this criterion. To determine the scope of the technique, our study included three less symmetrical germanes: dimesitylgermane (**2.7**), trimesitylgermane (**2.8**) and bis(trimethylsilyl)dimesitylgermane (**2.9**). Arylgermanes have previously been studied in the solution state, giving remarkably narrow spectra.²⁰ This makes them attractive targets for ^{73}Ge SSNMR. Mesityl groups were employed instead of phenyl groups as diphenylgermane is not a solid at room temperature. The inclusion of compound **2.9** allowed the investigation of whether the unusually narrow spectra were exclusive to the hydrogen substituted cases. Additionally, of the mesitylgermanes, only Mes_3GeH has a known, albeit disordered, crystal structure.²¹ In recent years, there has been an interest in using solid-state NMR spectroscopy as a complement to X-ray diffraction for structure determination,²² with the most relevant example for this work being examination of the structure of GeCl_2 through DFT calculation of ^{73}Ge and ^{35}Cl SSNMR parameters.¹⁷ Using a combination of ^{73}Ge SSNMR trends observed in the tetra-substituted systems with known crystal structures and computational modelling, we were able to obtain partial structural information on germanes **2.7-2.9**.

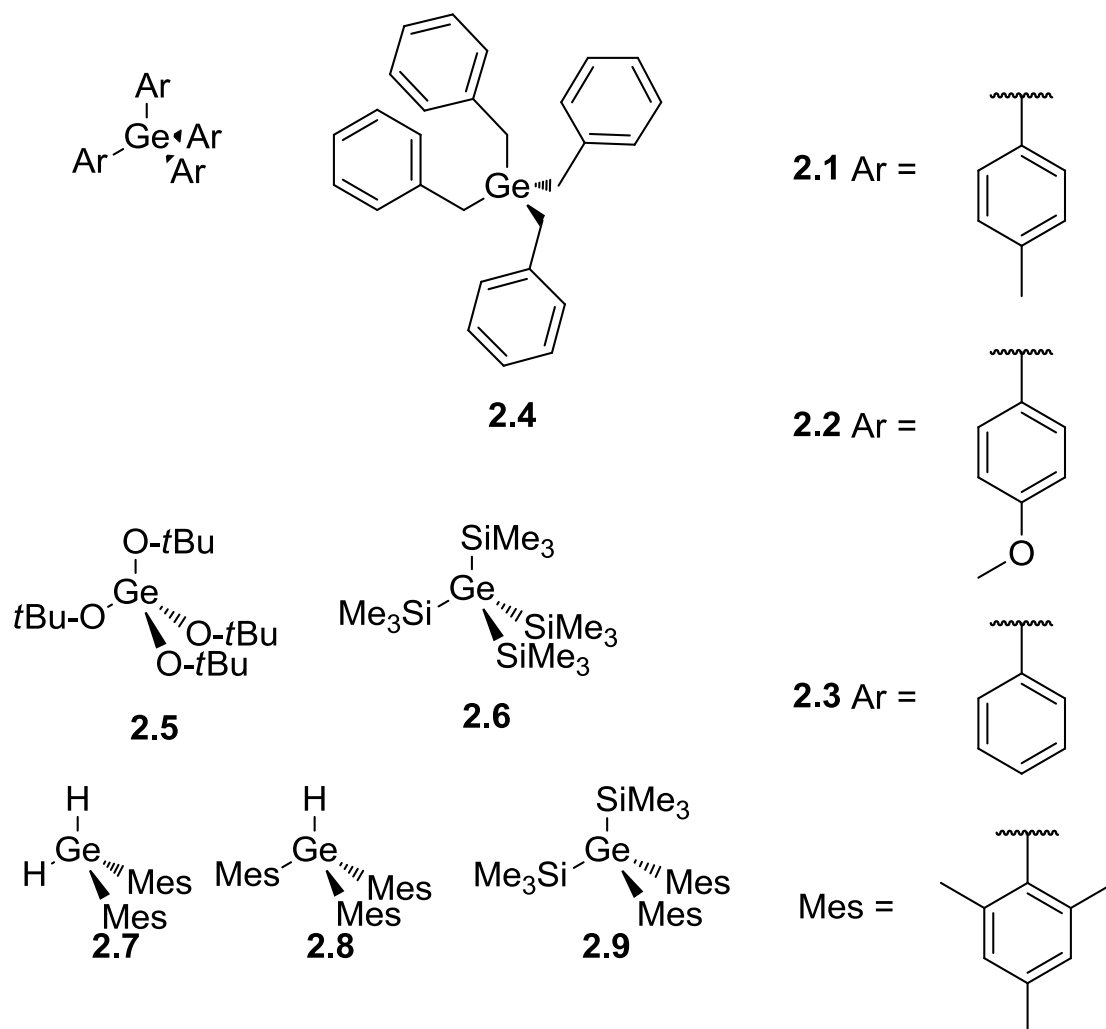


Figure 2.1 Germanes examined in this study. **2.1)** $Ge(p\text{-Me-C}_6\text{H}_4)_4$ **2.2)** $Ge(p\text{-MeO-C}_6\text{H}_4)_4$ **2.3)** tetraphenylgermane ($GePh_4$) **2.4)** tetrabenzylgermane ($Ge(CH_2Ph)_4$) **2.5)** tetra(*tert*-butoxy)germane ($Ge(OtBu)_4$) **2.6)** tetrakis(trimethylsilyl)germane ($Ge(SiMe_3)_4$) **2.7)** dimesitylgermane (Mes_2GeH_2) **2.8)** trimesitylgermane (Mes_3GeH) **2.9)** bis(trimethylsilyl)dimesitylgermane ($Mes_2Ge(SiMe_3)_2$).

2.2 Results and Discussion

2.2.1 Tetraorganogermanes

We first examined three tetraarylgermanes including $\text{Ge}(p\text{-Me-C}_6\text{H}_4)_4$, $\text{Ge}(p\text{-MeO-C}_6\text{H}_4)_4$ and GePh_4 as well as the tetraalkylgermane tetrabenzylgermane. The reasons for choosing these compounds are the following: (1) in all these compounds, Ge is tetrahedrally bound to four identical ligands, which should result in a reasonably small C_Q , making detection of a ^{73}Ge signal more feasible. (2) The crystal structures of these compounds are known, which allows us to examine the sensitivity of ^{73}Ge SSNMR parameters to the local environment. (3) For each compound, there is only one distinct Ge site in the unit cell, simplifying the spectral interpretation.

Table 2.1 Summary of ^{73}Ge NMR spectroscopic and computational data for compounds 2.1-2.9. In all simulations, the Euler angles $\alpha=\beta=\gamma=0$.

Structure		δ_{iso} (ppm)	δ solution (ppm)	C_Q^a (MHz)	η_Q^b	Ω^c (ppm)	κ^d
Ge(<i>p</i> -Me-C ₆ H ₄) ₄ (2.1)	Exp	-25(5)	-32.4 ¹²	3.9(2)	0.7(1)	30(10)	0.2(2)
	X-ray ^e	-50		3.7	0.8	35	-0.3
	Opt ^f	-50		3.9	0	12	-1
Ge(<i>p</i> -MeO-C ₆ H ₄) ₄ (2.2)	Exp	-	-11.3 ¹²	5.0(4)	0.9(2)	n.o. ^h	n.o. ^h
	X-ray ^e	20(10)	-27.1 ²³	3.0	0.7	n. a. ⁱ	n. a. ⁱ
	Opt ^f	-53		4.1	0.1	n. a. ⁱ	n. a. ⁱ
GePh ₄ (2.3)	Exp	-30(1)	-31.6 ¹²	0.5	0	30(3)	-1
	X-ray ^e	-55		1.2	0	49	-1
	Opt ^f	-50		3.8	0	14	-1
Ge(CH ₂ Ph) ₄ (2.4)	Exp	4.5(10)	---	2.5(2)	1.0(1)	60(10)	0.9(1)
	X-ray ^e	-5		-4.1	0.4	59	0.6
	Opt ^f	-11		-3.0	0.1	89	0.9
Ge(OtBu) ₄ (2.5)	Exp	≈ 0	---	n.a. ⁱ	-82(1)	≈ 0	n.a. ⁱ
Ge(SiMe ₃) ₄ (2.6)	Exp	≈ 0	---	n.a. ⁱ	-	≈ 0	n.a. ⁱ
Mes ₂ GeH ₂ (2.7)	Exp	-	---	2.3(1)	0.7(1)	100(10)	-
		181(5)					0.6(1)
	Opt ^f	-224		5.4	0.1	127	-0.2
Mes ₃ GeH (2.8)	Exp	-	---	2.9(2)	0.7(1)	50(10)	-
		120(5)					0.6(1)
	Opt ^f	-165		-4.6	0	116	-1
Mes ₂ Ge(SiMe ₃) ₂ (2.9)	Exp	-	---	24.7(3)	0.6(1)	n.o. ^h	n.o. ^h
		173(1)					
	Opt ^f	-204		-19.0	0.5	n. a. ⁱ	n. a. ⁱ
	Iterative ^g	-205		-24.5	0.5	n. a. ⁱ	n. a. ⁱ

^a $C_Q = \frac{eV_{zz}Q}{h}$ (Quadrupolar coupling constant) ^b $\eta = \frac{V_{xx}-V_{yy}}{V_{zz}}$ (Quadrupolar asymmetry parameter) ^c $\Omega = \delta_{11} - \delta_{33}$ (CSA span) ^d $\kappa = \frac{3(\delta_{22}-\delta_{iso})}{\delta_{11}-\delta_{33}}$ (CSA skew)

^e Calculated parameters using crystallographically determined geometry (hydrogen positions optimized at the TPSSTPSS/6-31G* level)

^f Calculated parameters using structure fully optimized at the TPSSTPSS/6-31G* level

^g *Calculated parameters using geometry obtained by systematic variation of structural metrics* ^h *n.o. = not observed* ⁱ *n.a. = not applicable*

Figure 2.2 shows the MAS and static spectra of **2.1-2.4** obtained at 21.1 T. The NMR tensor parameters extracted from spectral simulations are given in Table 2.1. The MAS spectrum of Ge(*p*-Me-C₆H₄)₄ (Figure 2.2A) exhibits a lineshape which is typical of half-integer quadrupolar nuclei experiencing residual second-order quadrupolar interaction under MAS conditions. The spectrum can be very well simulated by a single ⁷³Ge signal with $C_Q = 3.9$ MHz, $\eta_Q = 0.7$ and $\delta_{\text{iso}} = -25$ ppm. Observing one resonance is consistent with the crystal structure of this compound. The relatively small C_Q is indicative of a rather symmetric local environment around Ge. Indeed, an inspection of the crystal structure reveals that the variations in the Ge–C bond lengths are very small (within 0.016 Å). The deviations of the C-Ge-C bond angles from ideal tetrahedral angles are also rather small (i.e., the largest deviation is only $\sim 2^\circ$). The value of the asymmetry parameter is closer to one than zero, suggesting that the EFG is non-axial symmetric, which is consistent with the low Ge site symmetry (C_1). The ⁷³Ge isotropic shift of -25(5) ppm is in reasonable agreement with the previously reported value of -32.4 ppm given the reported linewidth and half-height of 400 Hz in that spectrum;¹² however, Takeuchi did not report lineshape information beyond the breadth of the line.¹² The static ⁷³Ge spectrum of Ge(*p*-Me-C₆H₄)₄ (Figure 2.2B) acquired at 21.1 T can be fit using the same set of EFG tensor parameters with the inclusion of a small CSA ($\Omega = 30$ and $\kappa = 0.2$). The individual contributions from the EFG and the CSA are shown in Figure 2.3. It is clear the second-order quadrupolar interaction dominates the spectrum. The presence of a small CSA is ambiguous at this point since the static spectrum was only acquired at one

field (an attempt to record a static spectrum at 9.4 T was unsuccessful); however, it was later confirmed by DFT calculations (see below).

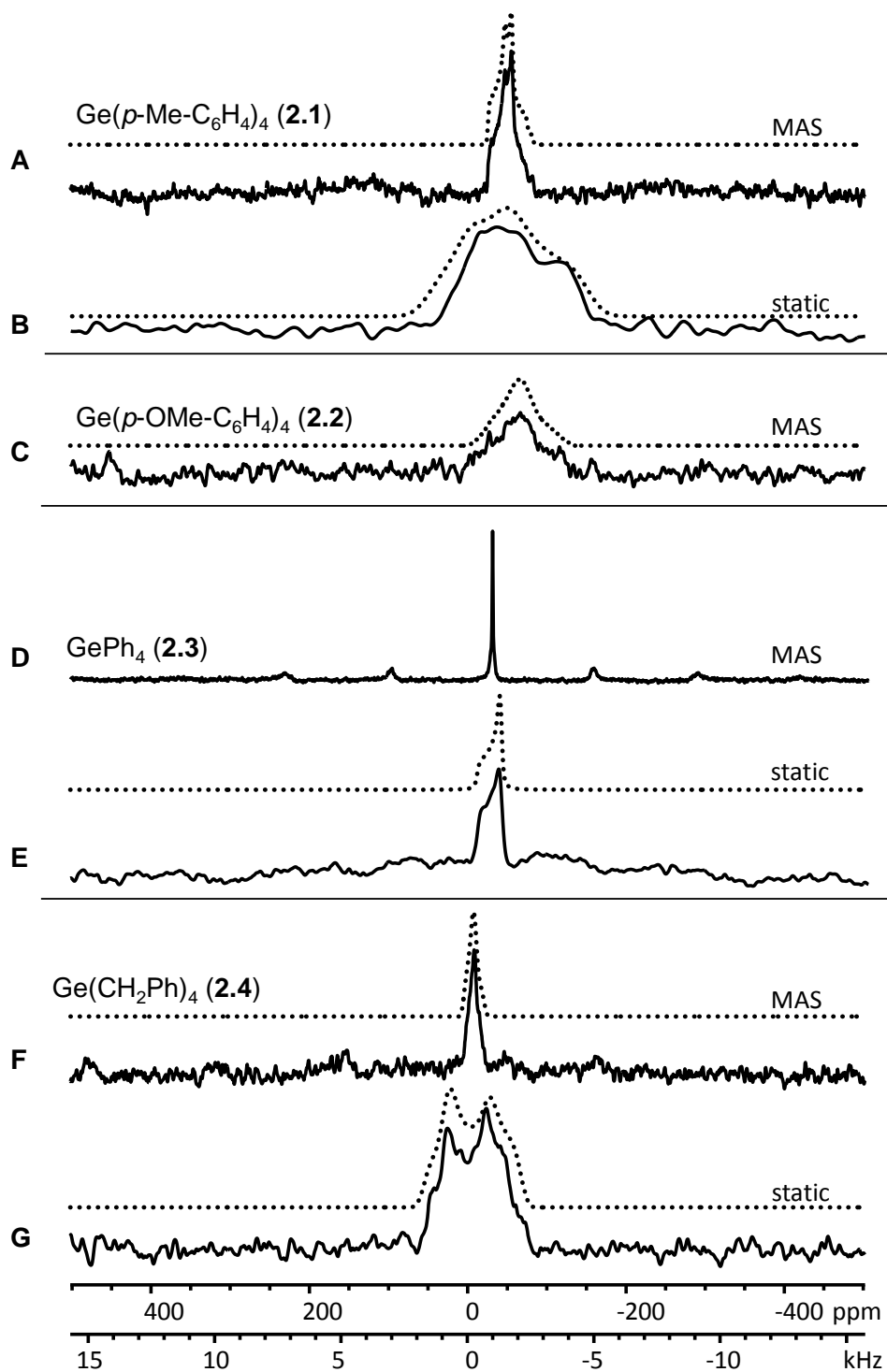


Figure 2.2 ^{73}Ge SSNMR spectra of compounds 2.1-2.4 at 21.1 T. Dotted traces represent simulations using parameters from Table 2.1. A) MAS (5 kHz) and B) static spectra of $\text{Ge}(p\text{-Me-C}_6\text{H}_5)_4$. C) MAS (5 kHz) spectrum of $\text{Ge}(p\text{-MeO-C}_6\text{H}_5)_4$. D) MAS (4 kHz) and E) static spectra of GePh_4 . F) MAS (5 kHz) and G) static spectra of $\text{Ge}(\text{CH}_2\text{Ph})_4$.

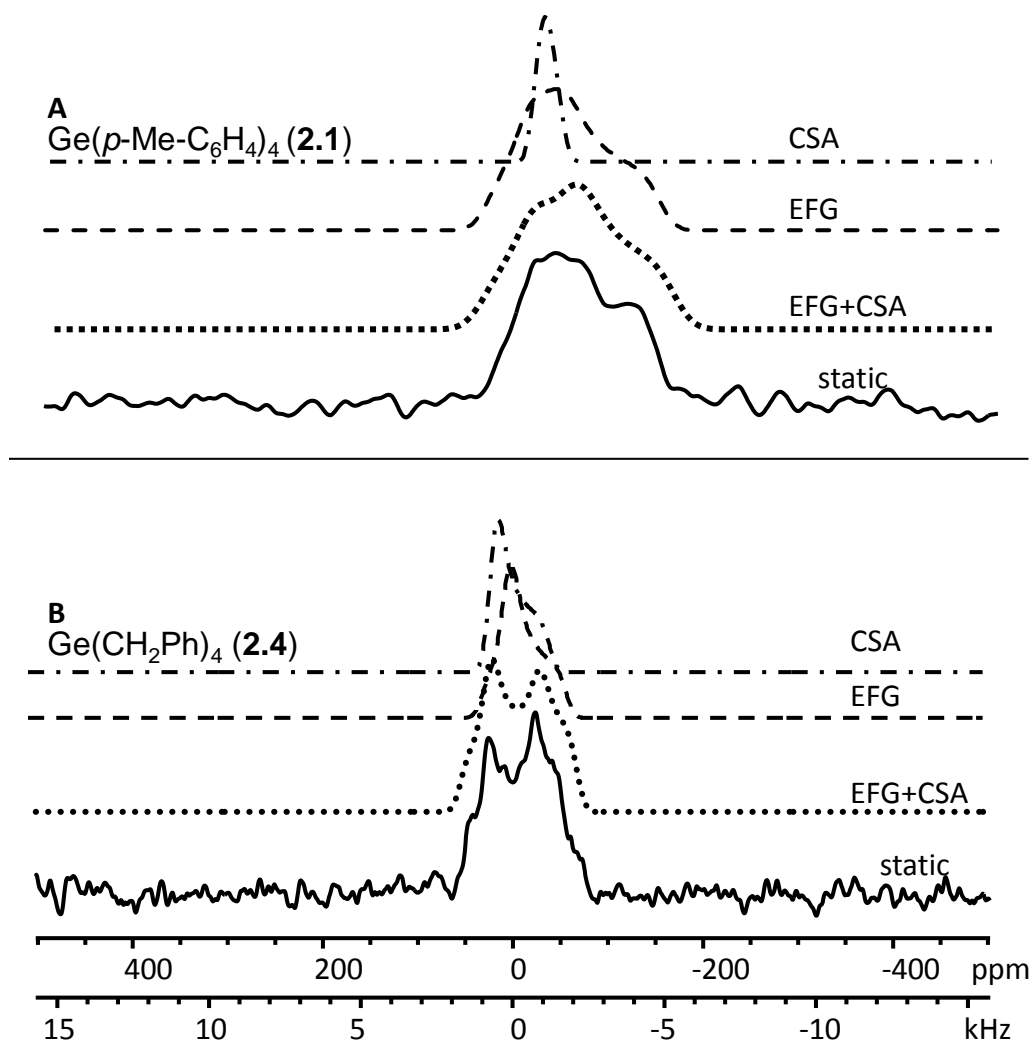


Figure 2.3 Simulation breakdown of A) $\text{Ge}(p\text{-MeC}_6\text{H}_4)_4$ and B) $\text{Ge}(\text{CH}_2\text{Ph})_4$ showing the individual contributions of CSA (dash-dot line), EFG (dashed line), and the two combined (dotted line).

The MAS spectrum of $\text{Ge}(p\text{-MeO-C}_6\text{H}_4)_4$ (2.2) is shown in Figure 2.2C. The signal-to-noise (S/N) ratio is still rather poor after 17 hours of acquisition. The spectral breadth is larger than that of $\text{Ge}(p\text{-Me-C}_6\text{H}_4)_4$. Simulations yielded the following EFG parameters: $C_Q = 5.0$ MHz, $\eta_Q = 0.9$ and $\delta_{\text{iso}} = -20$ ppm. The larger C_Q in $\text{Ge}(p\text{-MeO-C}_6\text{H}_4)_4$ suggests

that the distortion of local Ge geometric environment from tetrahedral symmetry must be larger compared to that in $\text{Ge}(p\text{-Me-C}_6\text{H}_4)_4$. As the X-ray structure of $\text{Ge}(p\text{-MeO-C}_6\text{H}_4)_4$ was not reported, single crystals were grown. As expected, the structure is a distorted tetrahedron, with C–Ge–C angles ranging from 107.4(1) to 111.2(1)°, Ge–C bond lengths ranging from 1.940(3) to 1.950(3) Å and there is no specific site symmetry at the germanium center (Table 2.2). The fact that the Ge–C distances found in $\text{Ge}(p\text{-MeO-C}_6\text{H}_4)_4$ are slightly shorter than those in $\text{Ge}(p\text{-Me-C}_6\text{H}_4)_4$ accounts for the larger C_Q of **2.2**. The value of $\eta_Q = 0.9$, is consistent with the low Ge site symmetry. The isotropic shift found for $\text{Ge}(p\text{-MeO-C}_6\text{H}_4)_4$ (-20 ppm) lies between the reported solution state values of -11.3 ppm reported by Takeuchi¹² and that reported by Yoder (-27.1 ppm).²³ We were unable to acquire a static spectrum at 21.1 T in a reasonable period of time, excluding the possibility of measuring the CSA.

Table 2.2 Selected crystallographic bond lengths and angles for $\text{Ge}(p\text{-MeO-C}_6\text{H}_4)_4$.

Ge–C Bond Lengths (Å)	C–Ge–C Bond Angles (°)
1.949(3)	107.4(1)
1.940(4)	111.2(1)
1.943(3)	110.7(1)
1.950(3)	108.3(1)
	109.9(1)
	109.2(1)

For GePh_4 (**2.3**), preliminary ^{73}Ge NMR results were reported in a communication.¹⁸ The MAS spectrum of **2.3** (Figure 2.2D) exhibits a very sharp single line, suggesting the quadrupolar interaction experienced by the Ge in this compound is very small. The EFG parameters determined from the static spectrum at 21.1 T were $C_Q \leq 0.5$ MHz and $\delta_{\text{iso}} = -30$ ppm. The very small, but non-zero C_Q can be attributed to the high site symmetry at

Ge. The striking feature of the static spectrum of GePh_4 (Figure 2.2E) is that the lineshape of the central transition is clearly dominated by a small but measurable CSA with $\Omega = 30$ and $\kappa = -1$. The skew value is consistent with the axial site symmetry. The reason why such a small CSA can be observed directly and accurately is the combination of a very small EFG and performing the NMR measurement at ultrahigh magnetic field because the effect second-order quadrupolar interaction on linewidth is scaled down linearly with magnetic field and the effect of CSA increases proportional to the strength of the field applied.

The MAS spectrum of $\text{Ge}(\text{CH}_2\text{Ph})_4$ (**2.4**) (Figure 2.2F) shows a single peak. Although very narrow (full width at half height (FWHM) = 400 Hz), the signal does exhibit a typical quadrupolar line-shape. The simulations yielded $C_Q = 2.5$ MHz, $\eta_Q = 1.0$ and $\delta_{\text{iso}} = 4.5$ ppm. The asymmetry parameter ($\eta_Q = 1.0$) indicates an absence of axial symmetry. This is consistent with the molecular structure in the solid state, where the Ge center is located at a general position with no specific site symmetry.²⁴ The Ge–C bond lengths in $\text{Ge}(\text{CH}_2\text{Ph})_4$ range from 1.946(6) to 1.973(6) Å and the C–Ge–C angles range from 106.9(3) to 110.7(3)°. The distortion from ideal tetrahedral local geometry results in a notable EFG. The C_Q value of $\text{Ge}(\text{CH}_2\text{Ph})_4$ is smaller than in both $\text{Ge}(p\text{-Me-C}_6\text{H}_4)_4$ and $\text{Ge}(p\text{-MeO-C}_6\text{H}_4)_4$, which can be rationalized by the fact that the Ge–C bond distances in $\text{Ge}(\text{CH}_2\text{Ph})_4$ are longer than those in $\text{Ge}(p\text{-Me-C}_6\text{H}_4)_4$ and $\text{Ge}(p\text{-MeO-C}_6\text{H}_4)_4$ while the symmetry is similar. The static spectrum of $\text{Ge}(\text{CH}_2\text{Ph})_4$ (Figure 2.2G) at 21.1 T exhibits a complex lineshape suggesting the presence of CSA. The simulation of the static spectrum indeed reveals the presence of the CSA with $\Omega = 60$ ppm and $\kappa = 0.9$, confirming that the observed spectrum contains contributions from both the quadrupolar

and chemical shift interactions. Although we were not able to obtain the static spectrum at a second (lower) field due to the low sensitivity, in this particular case, the existence of CSA is unambiguous. As shown in Figure 2.3B, the observed lineshape at 21.1 T definitely cannot be reproduced by using only the EFG parameters extracted from the MAS spectrum. Thus, $\text{Ge}(\text{CH}_2\text{Ph})_4$ is another example where the CSA is directly and unambiguously observed by experiment. The span is twice of that GePh_4 and the skew ($\kappa = 0.9$) is consistent with the non-axially symmetric environment around germanium observed in the molecular structure of the germane in the solid state.²⁴

To better understand the experimental results and to rationalize these results in light of available structural information, we carried out computational NMR studies. Previous computational studies of ^{73}Ge NMR parameters^{14,15,18,25} have made use of the plane wave pseudopotential method in the CASTEP program, which has proven to be an excellent method to predict NMR tensor parameters of crystalline solids.²⁶ However, the large ($> 1000 \text{ \AA}^3$) volumes of the unit cells of the structures in this study^{19,24} made this method practically unfeasible with available computational resources. Since the solids of all the compounds in this study contain discrete molecules rather than infinite framework materials, it is feasible to investigate these systems using first principles calculations in Gaussian 09.²⁷ In order to optimize the computational methodology, we tested the suitability of various computational methods and basis sets for predicting ^{73}Ge NMR tensor parameters. We first performed the calculations on $\text{Ge}(p\text{-Me-C}_6\text{H}_4)_4$ using restricted Hartree-Fock (RHF) and density functional theory (DFT) with several different functionals (B3LYP,²⁸ TPSSSTPSS,²⁹ PBE1PBE³⁰) and two basis sets (6-31G*, 6-311+G**). As the X-ray structure of $\text{Ge}(p\text{-Me-C}_6\text{H}_4)_4$ ¹⁹ did not include hydrogen atoms,

their assumed positions were added and optimized at the TPSSTPSS/6-31G* level. The results are summarized in Table 2.3.

Table 2.3 Summary of computational results for **2.1** using different model chemistries.

Entry	Method	Basis Set	C_Q (MHz)	η_Q	Ω (ppm)	κ
1	HF	6-31G*	2.2	0.5	67	0.7
2	B3LYP	6-31G*	2.3	0.9	76	0.6
3	PBE1PBE	6-31G*	2.2	0.9	76	0.6
4	TPSSTPSS	6-31G*	2.4	0.8	76	0.6
5	HF	6-311+G**	4.5	0.7	32	-0.2
6	B3LYP	6-311+G**	3.9	0.8	36	-0.3
7	PBE1PBE	6-311+G**	3.9	0.8	35	-0.3
8	TPSSTPSS	6-311+G**	3.7	0.7	35	-0.3
9	Experimental		3.9(2)	0.7(1)	30(10)	0.2(2)

Generally, when using the smaller 6-31G* basis set, the calculations significantly underestimated C_Q and overestimated the CS parameter (both span and skew) of Ge(*p*-Me-C₆H₄)₄ (Table 2.3, entries 1-4), regardless of the method and functional used. The agreements between the calculated and measured C_Q improve significantly when using a larger basis set of 6-311+G** (Table 2.3, entries 5-8). The calculations consistently yielded a small CSA ranging from 32 to 36 ppm independent of the method and the functional utilized, which is important given that the experimental results were obtained only at one magnetic field. Since the relatively recent TPSSTPSS²⁹ functional gave accuracies comparable to the other model chemistries employed in approximately half the computational time, this functional was utilized in this work as the preferred functional for subsequent calculations. The results of the calculations on compounds **2.2-2.4** are summarized in Table 2.1. Figure 2.4 shows that the agreement between experiment and theory for the C_Q values of **2.1-2.4** is reasonably good.

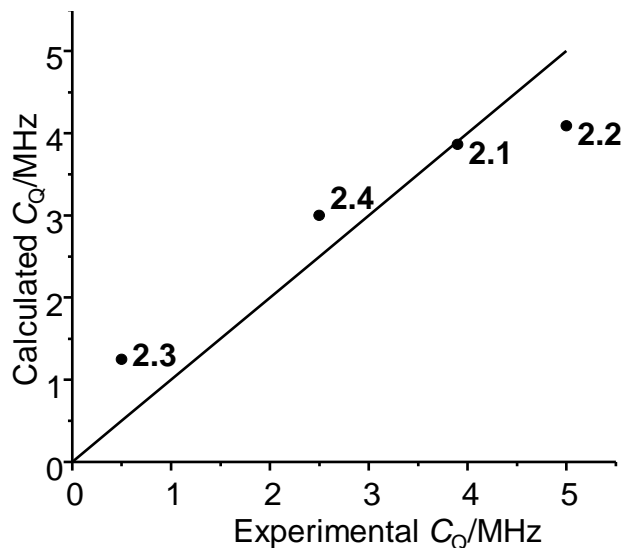


Figure 2.4 Relationship between experimental and calculated values of $C_Q(^{73}\text{Ge})$ for compounds 2.1-2.4. The solid line represents the ideal 1:1 correlation between experiment and theory. Hydrogen positions were optimized at the TPSS/6-31G* level.

Previous studies suggested that the magnitude of $C_Q(^{73}\text{Ge})$ of germanium oxides and halides can be related to the tetrahedral and octahedral distortion.¹⁵ As we are interested in ^{73}Ge SSNMR spectroscopy as a diagnostic tool for the structural characterization of organogermanium compounds, we also looked for correlations between the NMR parameters and structural features. In this work, the quadrupolar coupling constant was found to correlate reasonably to the average Ge–C bond length as determined by X-ray crystallography within sets of compounds with similar symmetries, with longer bonds yielding smaller quadrupolar interactions (hence small C_Q) in three tetraarylgermanes (Figure 2.5A). The experimental value observed for $\text{Ge}(\text{CH}_2\text{Ph})_4$ did not fit the observed trend. However, $\text{Ge}(\text{CH}_2\text{Ph})_4$ was the only case in which the calculated C_Q was negative. While it is not possible to determine the sign of C_Q from an NMR experiment, if it is assumed to be the same as the theoretical case, this point also becomes consistent with the larger trend (Figure 2.5A).

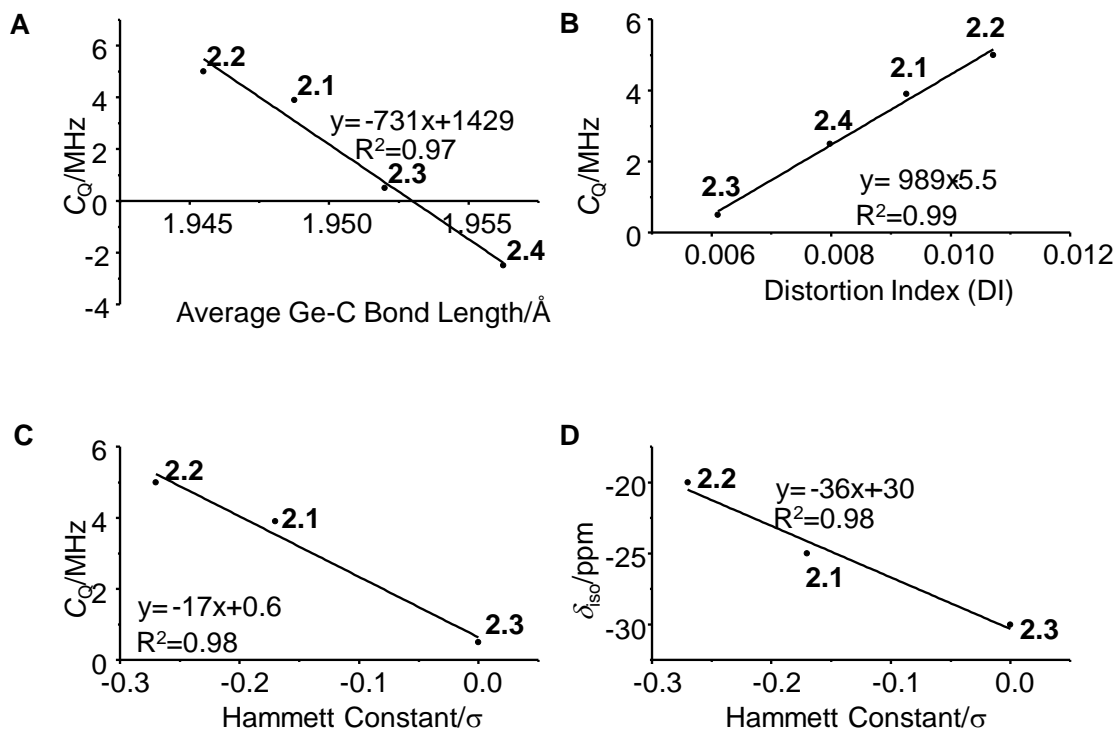


Figure 2.5 Relationship between A) experimental C_Q and average Ge–C bond length. The sign of C_Q was assumed to be the same as the calculated value. B) experimental C_Q and angular distortion C) experimental C_Q and Hammett constants D) isotropic shift and Hammett constants.

The influence of the magnitude of the C-Ge-C bond angles was also examined. The average angle did not correlate directly to any EFG parameter; however, the overall distortion from ideal tetrahedral angles, as quantified by the distortion index³¹ defined by

$$DI = \sum \frac{|\theta - \theta_i|}{6\theta_i}$$

where θ is the bond angle and θ_i is the ideal tetrahedral bond angle, 109.5° , was found to correlate with C_Q . A greater distortion from ideal tetrahedral symmetry led to larger magnitudes of C_Q in a linear fashion (Figure 2.5B). The distortion, being related to symmetry, is likely the dominant effect, while bond lengths come into play in cases of similar symmetry. Finally, trends in the NMR parameters of tetraarylgermanes were

examined in terms of pure electronic effects. Using standard Hammett constants, a linear correlation was found (Figure 2.5C), with more electron-rich germanes possessing larger C_Q values. The isotropic shifts of these compounds also correlate linearly in these compounds, with substituents with a more negative σ value having a larger deshielding effect at germanium (Figure 2.5D).

Due to the limited number of data points in this series, we further explored the validity of these empirical trends computationally. Starting from the experimental geometry of GePh_4 , one structural metric was systematically distorted. Compression of one Ge–C bond length led to an increase in the calculated value of C_Q (Figure 2.6A), in keeping with the trend observed experimentally (Figure 2.5A). Elongation of the same bond beyond the experimental value of 1.95 Å led to an increase in the magnitude of C_Q as the sign became negative. There did not appear to be any correlation between the bond length and the calculated value of η_Q . The effect of the magnitude of the C-Ge-C bond angles on C_Q and η_Q was also examined. A single angle was systematically varied. Consistent with experimental observations, the size of the angle did not correlate to any calculated parameters; however, when the effect of the angles was examined in terms of distortion from T_d symmetry using distortion index as a parameter, there was a linear correlation to C_Q (Figure 2.6B). There was, once again, no clear trend in η_Q . Overall, the theoretical calculations confirm the trends established using empirical correlations.

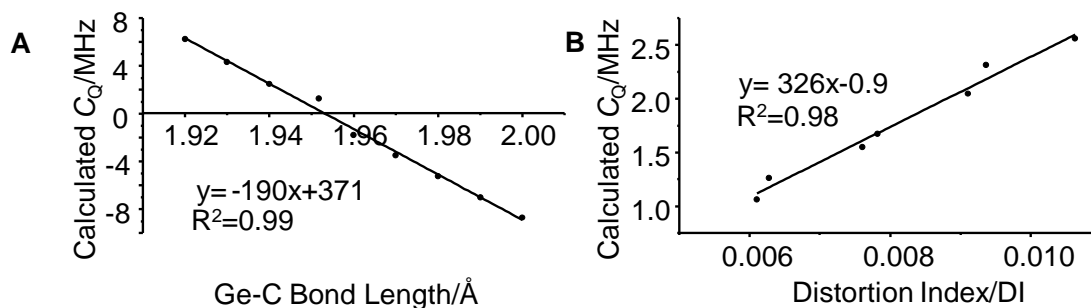


Figure 2.6 Relationship between A) calculated C_Q and Ge–C bond length and B) calculated C_Q and angular distortion. All calculations were performed at the TPSS/TPSS/6-311+G** level.

2.2.2 Mesitylgermanes

Mes₂GeH₂ (**2.7**) and Mes₃GeH (**2.8**) represent two systems whose structures are either unknown or poorly described. At 21.1 T, the ⁷³Ge MAS spectra (Figure 2.7A, C) of these two compounds with seemingly very asymmetric Ge environments exhibit surprisingly narrow signals (FWHH = 500 Hz and 700 Hz for Mes₂GeH₂ and Mes₃GeH, respectively) rather than the expected broad EFG-dominated pattern. While this is consistent with solution state results for phenylgermanes,²⁰ both cases remain inconsistent with the symmetry at germanium. The more shielded shift in Mes₂GeH₂ indicates that replacing aryl groups with hydride ligand increases the shielding at the germanium center, consistent with the established trends in ²⁹Si NMR spectroscopy.¹

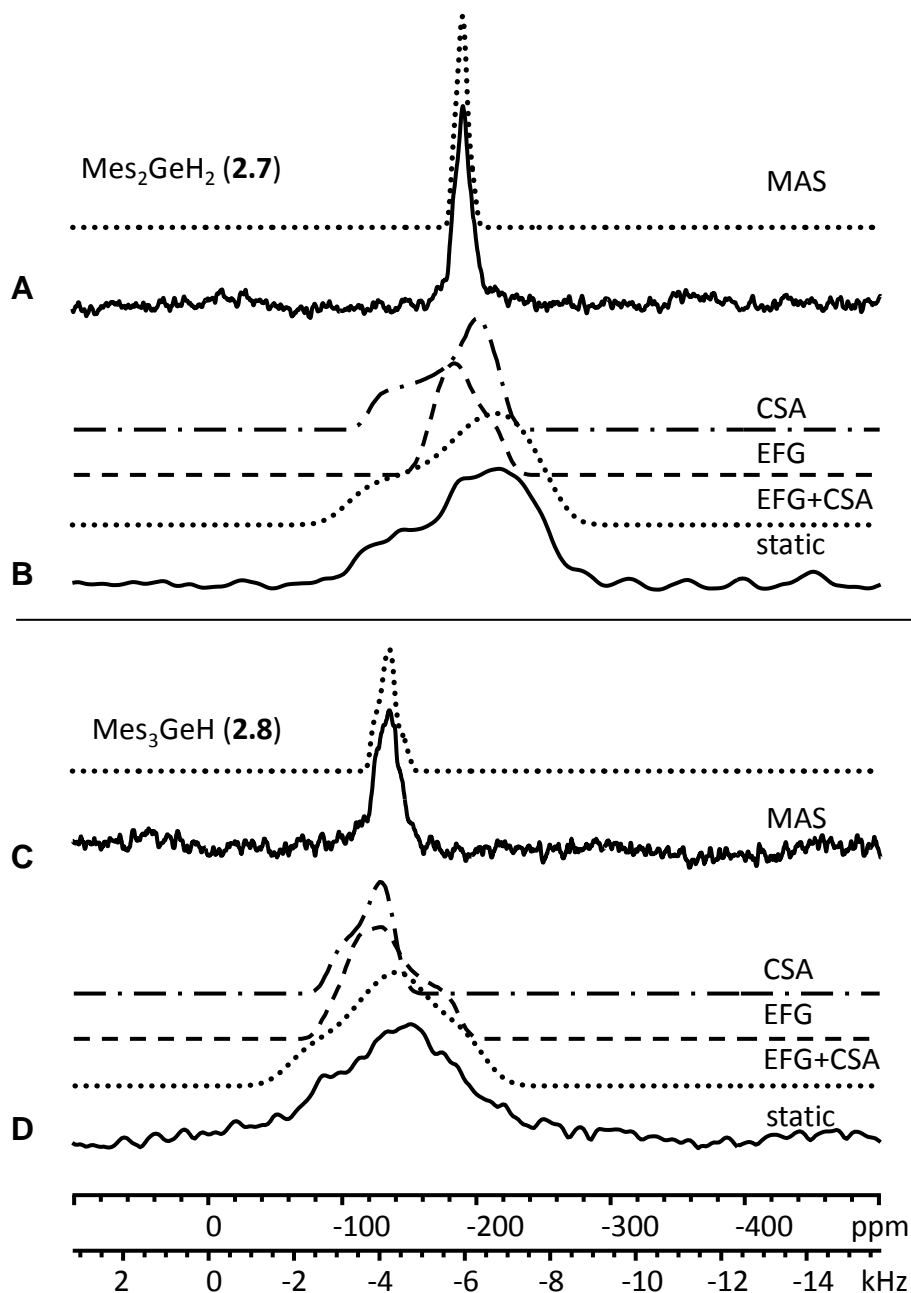


Figure 2.7 ^{73}Ge SSNMR spectra of compounds 2.7 and 2.8 at 21.1 T. Dotted traces represent simulations using parameters from Table 2.1 as discussed in the text. Dashed traces show the individual contributions to the total simulation. A) MAS (5 kHz) and B) static spectra of Mes_2GeH_2 . C) MAS (5 kHz) and D) static spectra of Mes_3GeH .

The EFG parameters of Mes_2GeH_2 extracted from spectral simulation are $\eta_Q = 0.7$ and $C_Q = 2.3$ MHz. The value of C_Q is much smaller than those of the tetraarylgermanes

examined in this study (Table 2.1). While the C_Q of Mes_3GeH (2.9 MHz) is larger than that of Mes_2GeH_2 , it is smaller than those of the *p*-substituted tetraarylgermanes **2.1** and **2.2**. The asymmetry parameter for Mes_3GeH is 0.7, indicating an absence of axial symmetry despite the possibility of a C_3 axis through the Ge–H bond. The static spectrum of Mes_2GeH_2 (Figure 2.7B) at 21.1 T cannot be reproduced by using only the EFG parameters obtained from the MAS spectrum alone. In fact, Figure 2.20B shows that the static spectrum is most likely dominated by the CSA interaction. Mes_2GeH_2 has a span of approximately 100 ppm, the largest ^{73}Ge CSA observed to date. The effect of CSA on the Mes_3GeH spectrum is more subtle, but as shown in Figure 2.20D, it is still required in order to better simulate the static lineshape. The span ($\Omega = 50$) of the CSA tensor of **2.8** is smaller than that of Mes_2GeH_2 . Mes_2GeH_2 and Mes_3GeH have skew values (-0.6 in both cases) indicating an absence of axial symmetry, consistent with the EFG observations.

A disordered crystal structure was reported for Mes_3GeH .²¹ Using the structural parameters reported in the literature, the DFT calculations predicted the following NMR parameters: $C_Q = 23.3$ MHz, $\eta_Q = 0.17$. The powder pattern, predicted based on the reported molecular structure, is dominated by the EFG and remarkably different from the experimentally measured spectrum (Figure 2.8), implying that the true molecular geometry in the solid state at room temperature differs from the one reported in the literature. The difference is unlikely to be due to extensive molecular motion, as the large size of the mesityl groups does not allow for rapid rotation even in solution.

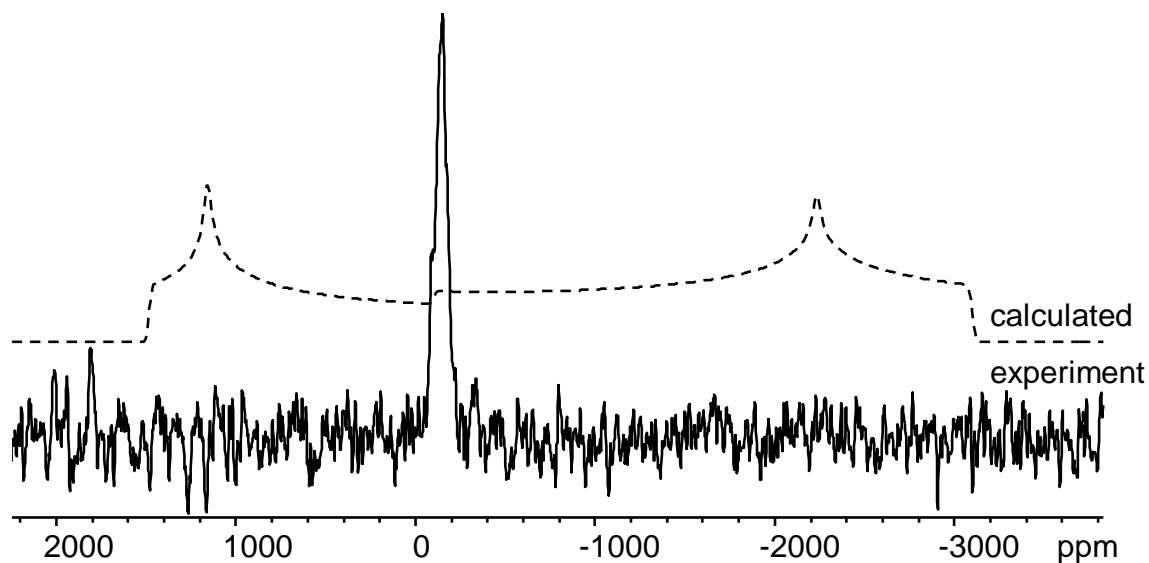


Figure 2.8 Comparison between experimental spectrum of a stationary sample of Mes_3GeH (solid line) and that predicted computationally from the X-ray structure (dashed line).

To understand why Mes_3GeH , a compound with a seemingly asymmetric environment around Ge, has a very small C_Q and to gain information on its true crystal structure, we carried out computational modelling to explore the effect of bond length and C–Ge–C angle on C_Q . The results are shown in Figure 2.9. Overall, the EFG tensor was considerably more sensitive to structural variation than the chemical shielding. The calculated isotropic shift consistently ranged from -165 to -166 ppm, while the calculated span was likewise consistent at 115 ppm. The structure of Mes_3GeH was first geometry optimized in Gaussian 09, yielding a structure with a C_Q value of 4.6 MHz. While this was in considerably better agreement with the experimental value, it still was greater than the measured value. The structural metrics were varied systematically in an attempt to obtain a better agreement. The optimized structure featured three equal C–Ge–C angles. Any slight alteration of one angle by more than 0.05° to either side of the geometry optimized value of 115.06° caused C_Q to increase dramatically to approximately 30 MHz

(Figure 2.9A). Between 115.00° and 115.09° , the calculated value of C_Q rose only slightly. Thus, the C-Ge-C angles were left unaltered in the final proposed structure. The Ge-H bond length had a substantial ($180 \text{ MHz}/\text{\AA}$) effect on the calculated C_Q (Figure 2.9B). Changing this metric from the optimized value rapidly increased C_Q well above the experimental value, and thus, the optimized value was also retained in the final structure. The most important variable for the determination of the final proposed structure was, thus, the Ge-C bond lengths. To minimize the number of variables, initial calculations altered all Ge-C bonds simultaneously. This yielded a linear trend, with a minimum value less than experiment (Figure 2.9C).

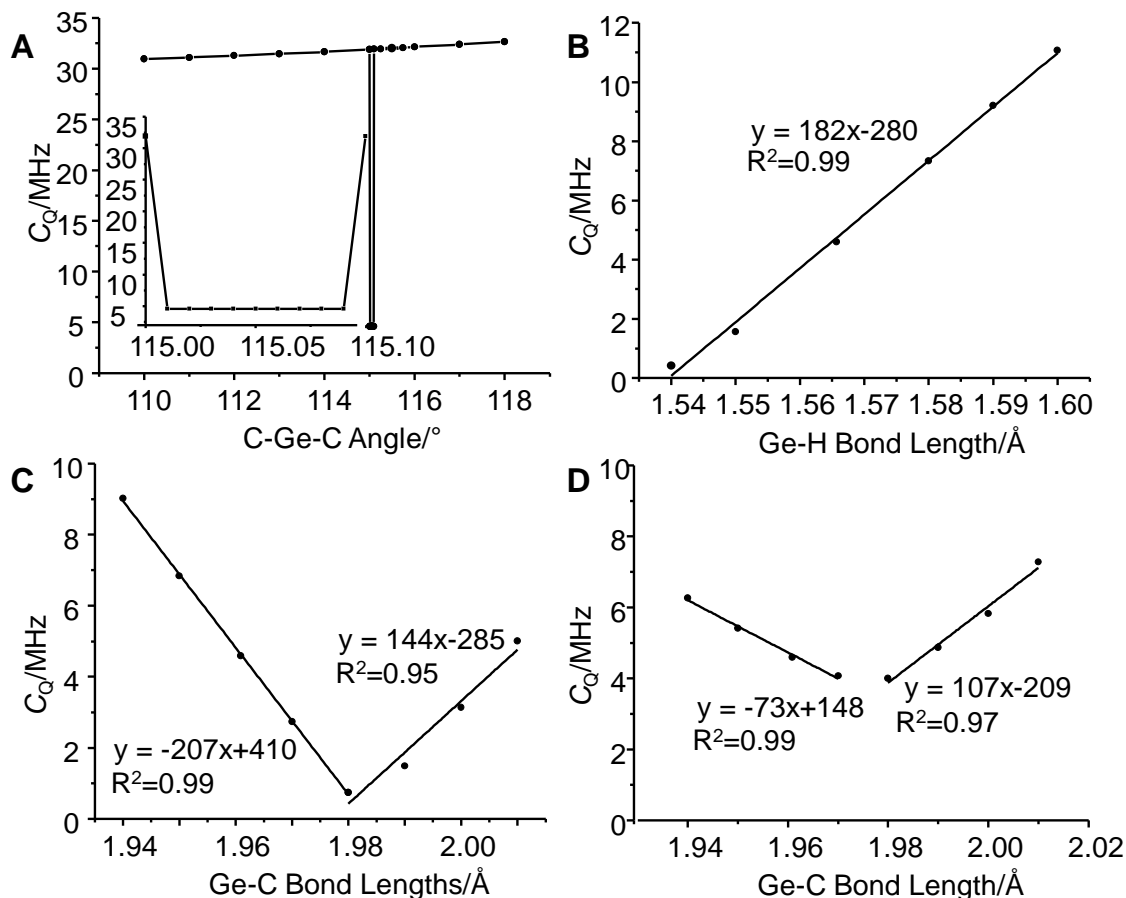


Figure 2.9 Relationship between calculated C_Q value for Mes_3GeH and A) C–Ge–C bond angle. The geometry optimized value is a notable outlier. B) Ge–H bond length C) all Ge–C bond lengths D) one Ge–C bond length with the others held at their optimized value.

There were two possible bond lengths that gave calculated values consistent with experiment: 1.97 \AA ($C_Q = 2.7$ MHz) and 2.00 \AA ($C_Q = 3.1$ MHz). In view of the large size of the mesityl group, the longer Ge–C distance appears to be more plausible and this is also consistent with the average Ge–C bond (2.045 \AA) reported in the disordered structure.²¹ The calculated η_Q value ($\eta_Q = 0$) at the same geometry does not correspond to experimental one (0.7), suggesting that the C_3 symmetry imposed on the model does not exist in the actual structure. Indeed, the inequivalence of the three mesityl groups is supported by the ^{13}C CPMAS SSNMR spectrum of Mes_3GeH which exhibits multiple

resonances for each chemically distinct carbon of mesityl group (Figure 2.11A). The fact that changing one C-Ge-C bond angle from the optimized geometry by even half of a degree caused the calculated C_Q to increase by approximately 30 MHz suggests that the deviation from axial symmetry is more likely due to non-equivalent bond lengths rather than angular distortion. When only one bond length is altered, the correlation to C_Q remains linear (Figure 2.9D) while the value of η_Q rapidly rises from zero to more reasonable values (Figure 2.10).

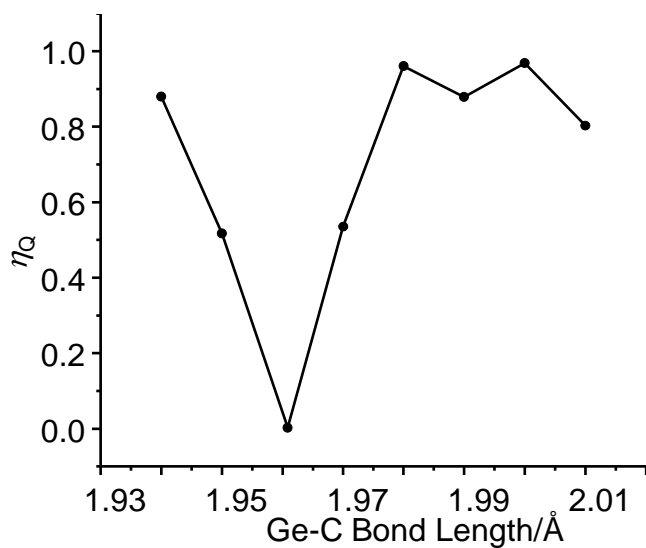


Figure 2.10 Relationship between calculated η_Q value and one Ge-C bond length in Mes_3GeH .

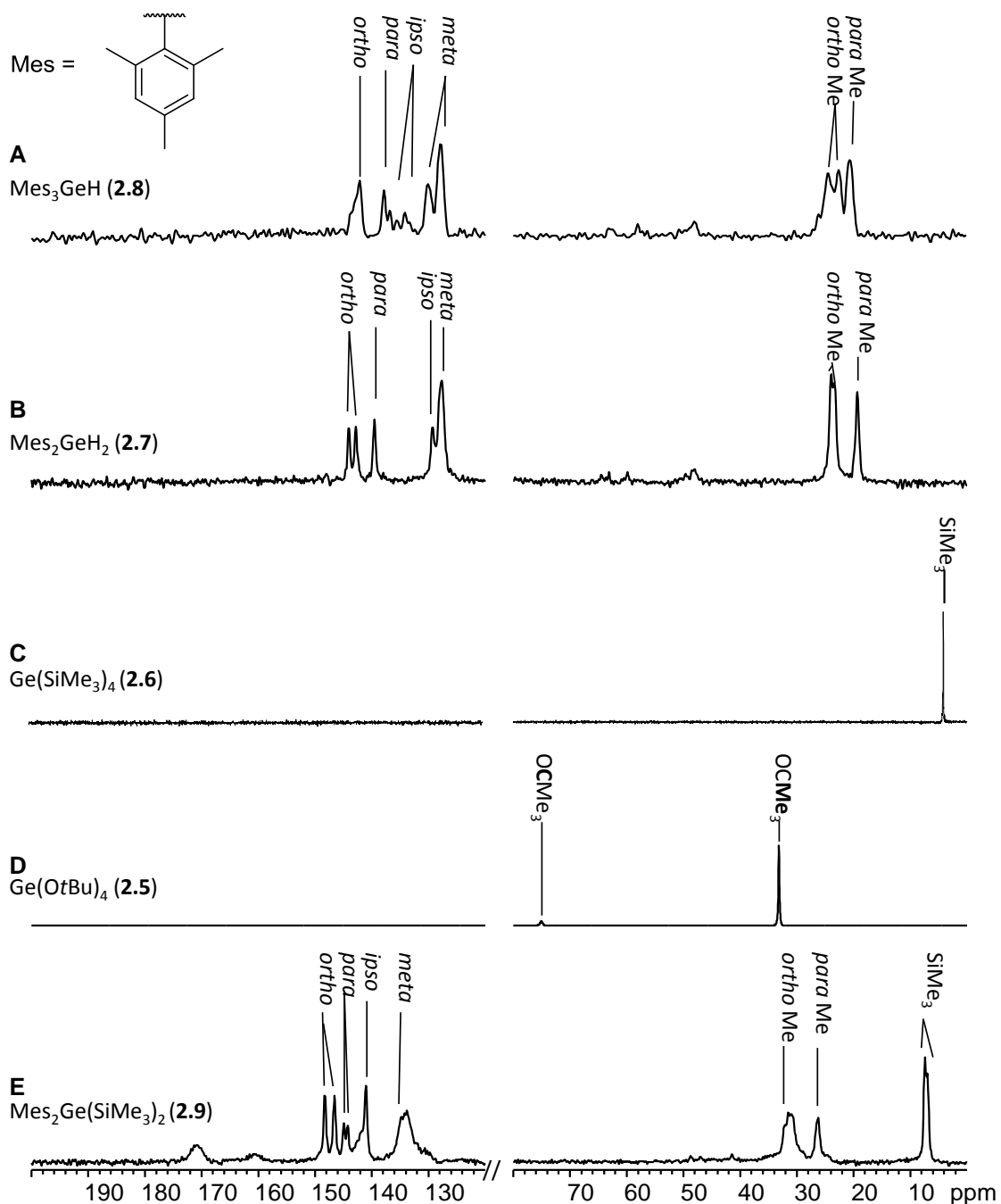


Figure 2.11 Selected ^{13}C CPMAS SSNMR spectra at 9.4 T. A) Mes₃GeH B) Mes₂GeH₂ C) Ge(SiMe₃)₄ D) Ge(OtBu)₄ E) Mes₂Ge(SiMe₃)₂ MAS spinning speed was 8 kHz in A, B and C and 10 kHz in D and E.

Taking all the factors into consideration, the following structural parameters: Ge–H = 1.55

Å; $\angle \text{C-Ge-C} = 115.06^\circ \times 3$; Ge–C₁ = 1.99 Å and Ge–C₂ = 2.00 Å $\times 2$ lead to $C_Q = 2.7$

MHz and $\eta_Q = 0.8$. The final proposed structure represents one of many possibilities as multiple combinations of Ge-C bond lengths would yield similar C_Q values. It was not possible to further refine the structure without additional constraints. However, it should be noted that the proposed structure is in fact lower in energy than the geometry optimized structure by 2 kJ/mol.

The overall structure adopts a propeller geometry due to the steric effect of the *ortho* methyl groups on the mesityl substituents. In the absence of such an interaction, all six *ortho* carbons would lie in a single plane, leading to a $C_{ipso}\text{-Ge-}C_{ipso}\text{-}C_{ortho}$ dihedral angle of 30° ; however, when the rings rotate to minimize the methyl-methyl interactions (Figure 2.12), one angle (α) becomes smaller while the other (β) becomes larger. These angles appear three times within the structure. The overall distortion can be described in terms of the average $\varphi = 0.5[(\alpha+30)+(\beta-30)]$, where α and β are the average values of the angles in a single structure. In the proposed structure, as determined by ^{73}Ge SSNMR spectroscopy and computational modeling, φ is 32° , indicating that the structure is less twisted than was observed in the X-ray structure ($\varphi = 42^\circ$). It is possible that this difference arises from slight structural changes at room temperature when compared to the low temperature at which the X-ray data were collected.

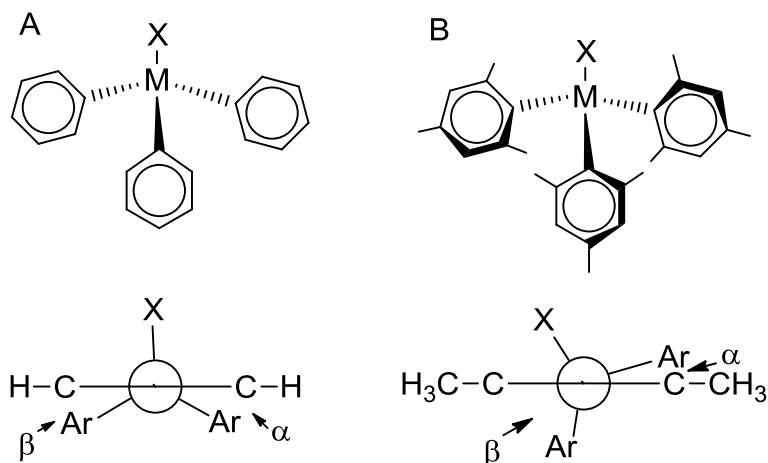


Figure 2.12 A) The stereographic structure of an untwisted metallane is shown above and its Newman projection below. B) In order to minimize interactions between ortho substituents, the aryl rings twist into a propeller geometry as shown above. The Newman projection below demonstrates the effect of this twisting on the dihedral angles α and β .

A similar approach was used to approximate the structure of Mes_2GeH_2 whose crystal structure is not known. When using the geometry optimized structure, the calculated quadrupolar coupling constant for Mes_2GeH_2 was found to be 5.4 MHz, somewhat greater than the experimental value of 2.3 MHz. As the Ge–C bond length has already been shown to considerably affect the largest EFG component, the Ge–C bond lengths of Mes_2GeH_2 were altered in an effort to approximate the experimental parameters (Figure 2.13A). Elongation of the two Ge–C bonds led to a minimum value of C_Q of 2.2 MHz at a Ge–C bond length of 1.97 Å (geometry optimized value: 1.95 Å). The Ge–H bond length once again had a dramatic (180 MHz/Å) effect on the value of C_Q (Figure 2.13B). Altering the Ge–H bond length rapidly increased C_Q well beyond the experimental value, and thus, it was left at the optimized value. While the H–Ge–H angle had a negligible impact (Figure 2.13C), the C–Ge–C angle had a small but noticeable effect (Figure 2.13D). However, the value from the geometry optimized structure proved to give the best agreement with experiment. Thus, we predict the molecular structure of Mes_2GeH_2

to have an average Ge–C bond length of 1.97 Å and a C-Ge-C bond angle of 113°. The span of the CSA tensor at the final geometry was calculated to be 124 ppm, in reasonable agreement with the experimental value of 100 ppm (Table 2.1). Once again, the geometry determined in this manner was lower in energy than the geometry optimized value, in this case by 1 kJ/mol. The ¹³C CPMAS SSNMR spectrum (Figure 2.11B) shows very sharp resonances for two distinct *ortho* methyl groups and one *para* methyl group as well as a total of five aromatic carbons. This most likely arises from the carbons within the individual mesityl groups being crystallographically inequivalent while two mesityl groups are likely related by either a C₂ axis or a mirror plan, making them equivalent or very nearly so.

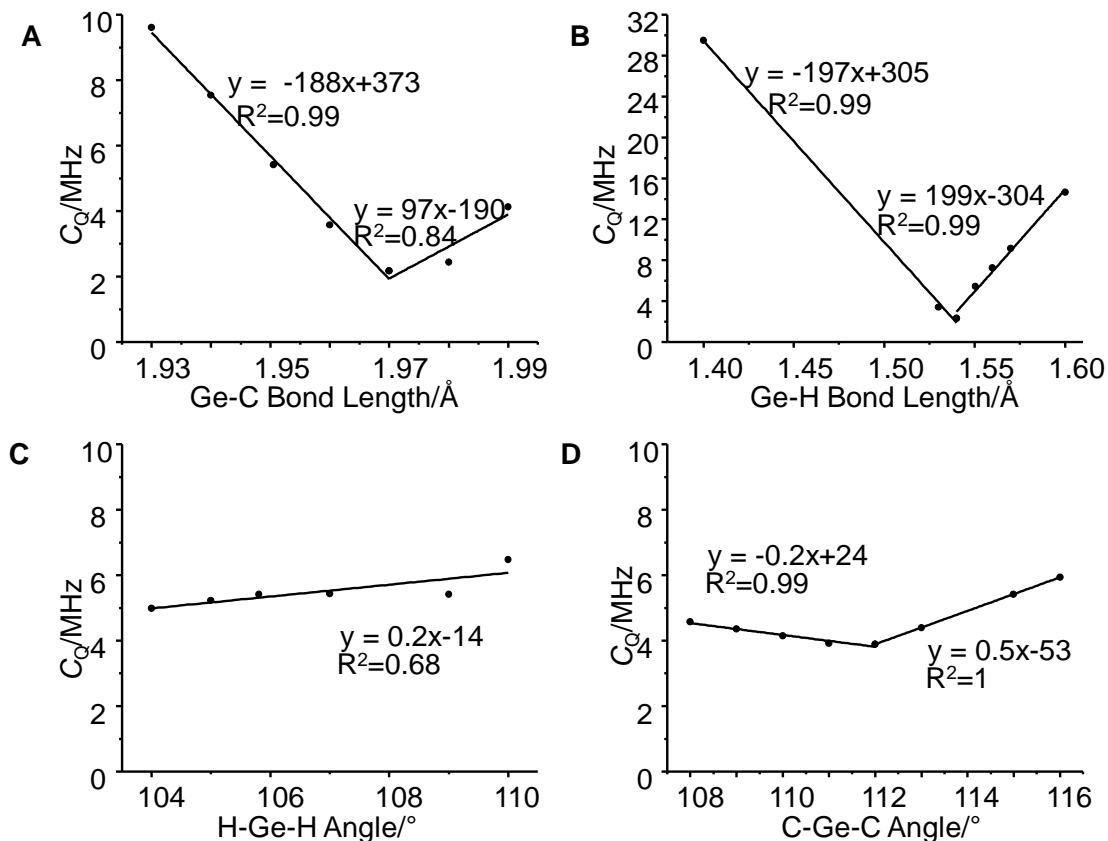


Figure 2.13 Relationship between the calculated C_Q value for Mes_2GeH_2 and A) Ge–C bond lengths, B) Ge–H bond lengths, C) H–Ge–H bond angle, and D) C–Ge–C bond angle.

2.2.3 Tetrakis(trimethylsilyl)germane and tetra(tert-butoxy)germane

For $Ge(SiMe_3)_4$ (**2.6**), the MAS and static spectra (Figure 2.17C,D) acquired at 21.1 T both exhibit sharp single resonances (FWHH \sim 65 Hz), indicating that the Ge experiences neither quadrupolar nor CSA interactions. Such observations are consistent with its crystal structure,³² which shows that the molecule adopts ideal T_d symmetry. Furthermore, the ^{13}C CPMAS SSNMR spectrum of **2.6** (Figure 2.11C) shows a single sharp resonance, suggesting that, much like in $Si(SiMe_3)_4$,³³ $Ge(SiMe_3)_4$ undergoes rapid isotropic motion about a fixed center of mass, leading to a solution-like environment around germanium, and thus, a lack of effect on lineshape from CSA and EFG. A similar

situation was observed under ^{29}Si CPMAS conditions, with a linewidth at half height of only 8.4 Hz (Figure 2.14).

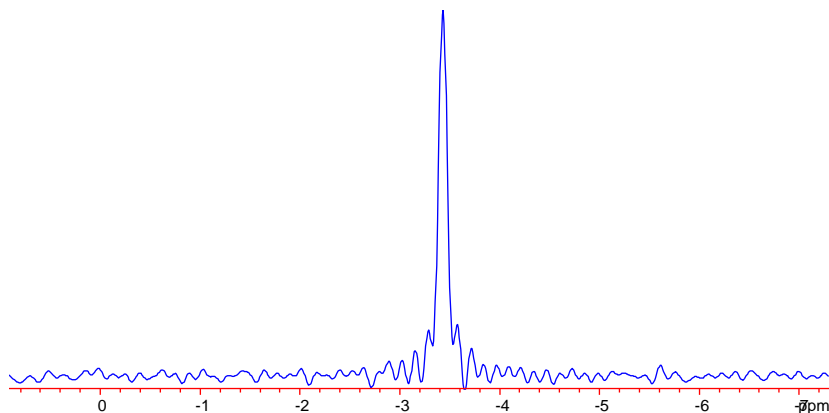


Figure 2.14 ^{29}Si CPMAS spectrum of $\text{Ge}(\text{SiMe}_3)_4$ at 9.4 T.

Differential scanning calorimetry (DSC) revealed a solid-solid phase transition at -34.6 °C ($\Delta H = 6.4 \text{ kJmol}^{-1}$), attributed to an order-disorder transition (Figure 2.15). The transition exhibits a large entropy of transition ($\Delta S = 27 \text{ JK}^{-1}\text{mol}^{-1}$) reminiscent of a solid-liquid transition, which suggests a large degree of molecular motion in the higher temperature phase consistent with a plastic crystal. The transition temperature is consistent with what has been previously observed for $\text{C}(\text{SiMe}_3)_4$ (-46 °C) and $\text{Si}(\text{SiMe}_3)_4$ (-42 °C).³⁴ There appears to be a linear ($R^2=0.99$) relationship between the atomic number and the transition temperatures, with the heavier elements attaining the ordered phase at higher temperature.

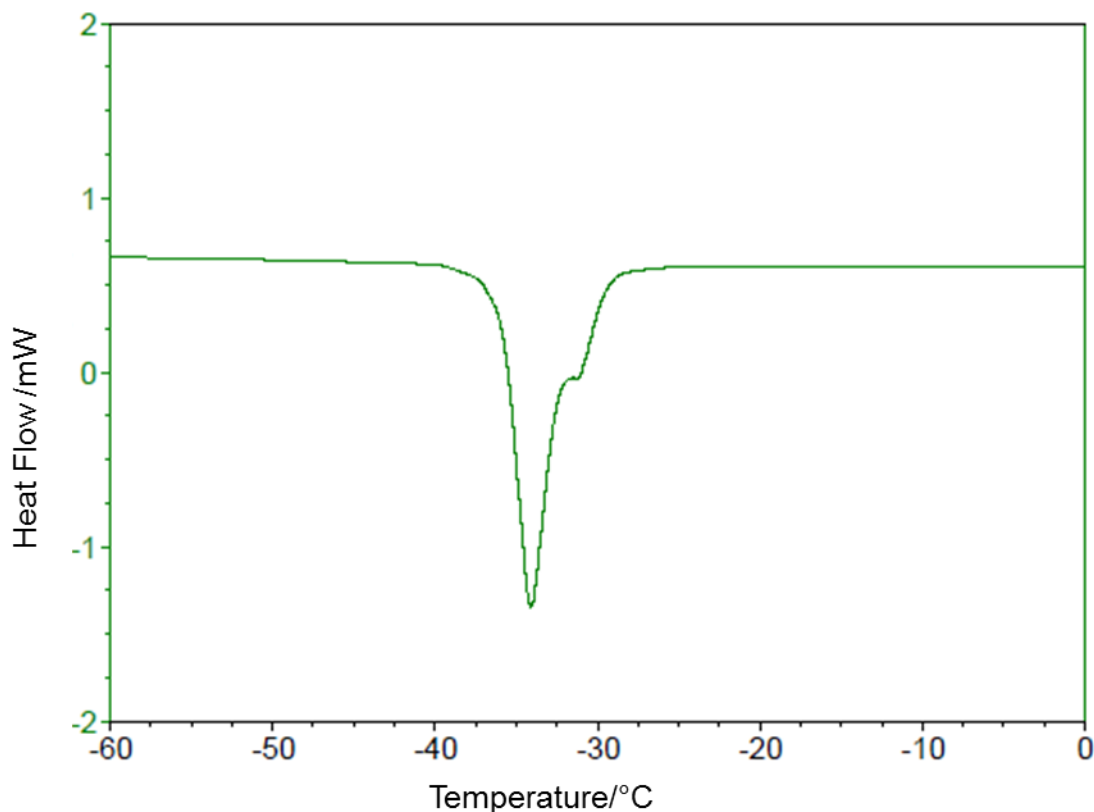


Figure 2.15 Differential scanning calorimetry plot of $\text{Ge}(\text{SiMe}_3)_4$ showing a solid-solid phase transition at $-34.6\text{ }^\circ\text{C}$.

The dynamics of the two phases were explored using variable temperature static ^{29}Si SSNMR spectroscopy (Figure 2.16). Over the course of the experiment there does not appear to be any change in the overall peak position. There is very little change at all in the spectrum until $-58\text{ }^\circ\text{C}$, with all spectra showing a single narrow (FWHM=120 Hz) resonance. The spectrum acquired at $-33\text{ }^\circ\text{C}$ exhibits a somewhat poorer signal-to-noise ratio than the higher temperature spectra, though the linewidth remains similar. The $-58\text{ }^\circ\text{C}$ spectrum is even noisier, despite having been acquired under otherwise identical conditions. Upon further cooling, the signal-to-noise ratio returns to being similar to the higher temperature spectra. It is notable that the two abnormally noisy spectra were

acquired at the temperatures closest to the phase transition as determined from the DSC data.

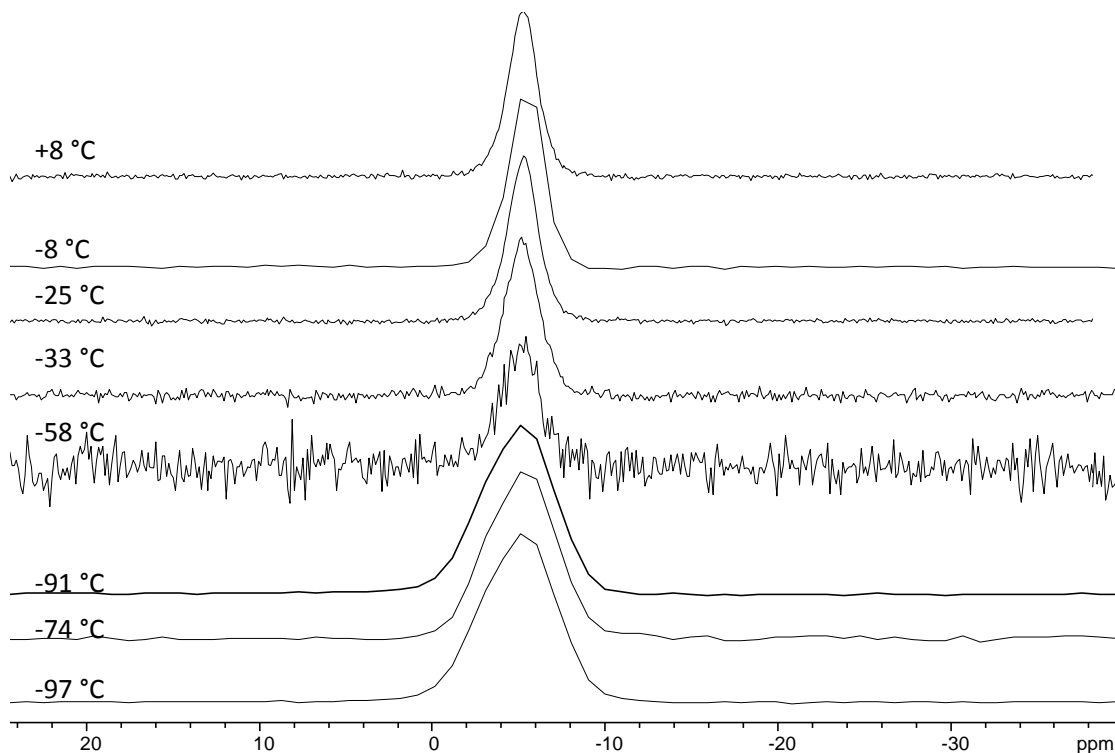


Figure 2.16 Variable temperature ^{29}Si SSNMR spectra of $\text{Ge}(\text{SiMe}_3)_4$ at 9.4 T.

The spectra recorded below the phase transition temperature exhibit much broader (FWHH > 400 Hz) linewidths than the higher temperature phase. Broader lines are consistent with slower molecular motion leading to decreased averaging of the CSA interaction. While even the peak acquired at -97°C does not exhibit a classic CSA based lineshape, there is a slight shoulder indicating a gradual loss of symmetry in the peak. However, the molecular motion appears to continue at much lower temperatures than were observed for the carbon and silicon centered analogues. While spectral changes began at the phase transition temperature, a pure CSA based pattern was not recorded for either analogue until 155 K, a temperature which could not be achieved in this study. The

general shapelessness of the lines can be attributed to the Ge–Si bond lengths being longer than Si–Si and C–Si bonds, allowing rotation to continue to lower temperatures before the energy barrier becomes prohibitive.

Similar to $\text{Ge}(\text{SiMe}_3)_4$, both MAS and static spectra of $\text{Ge}(\text{O}t\text{Bu})_4$ (**2.5**) (Figure 2.17A,B) show a relatively narrow and symmetric resonance (FWHH = 2 kHz). The fact that the FWHHs of the static and MAS spectra of **2.5** are nearly identical supports the absence of an observable electric field gradient and CSA as the molecules likely undergo fast isotropic reorientation in solids. While there is no known crystal structure for $\text{Ge}(\text{O}t\text{Bu})_4$, some information can be obtained from solid-state ^{73}Ge and ^{13}C NMR spectral parameters. The Ge spectra indicate that there is only one unique Ge site with a high symmetry in the unit cell. The ^{13}C spectrum of **2.5** exhibits one sharp resonance at 32 ppm assigned to the methyl groups and one at 75 ppm assigned to the quaternary carbon based on the chemical shifts (Figure 2.11D). The observation of a single sharp ^{13}C signal assigned to the quaternary carbons suggests that the four *Ot*Bu groups are identical, further confirming the high symmetry of $\text{Ge}(\text{O}t\text{Bu})_4$. The twelve methyl groups only produce one sharp signal, indicating rapid rotation of the *t*-butyl groups around the O–C bond leading to high molecular symmetry on the NMR time scale at room temperature.

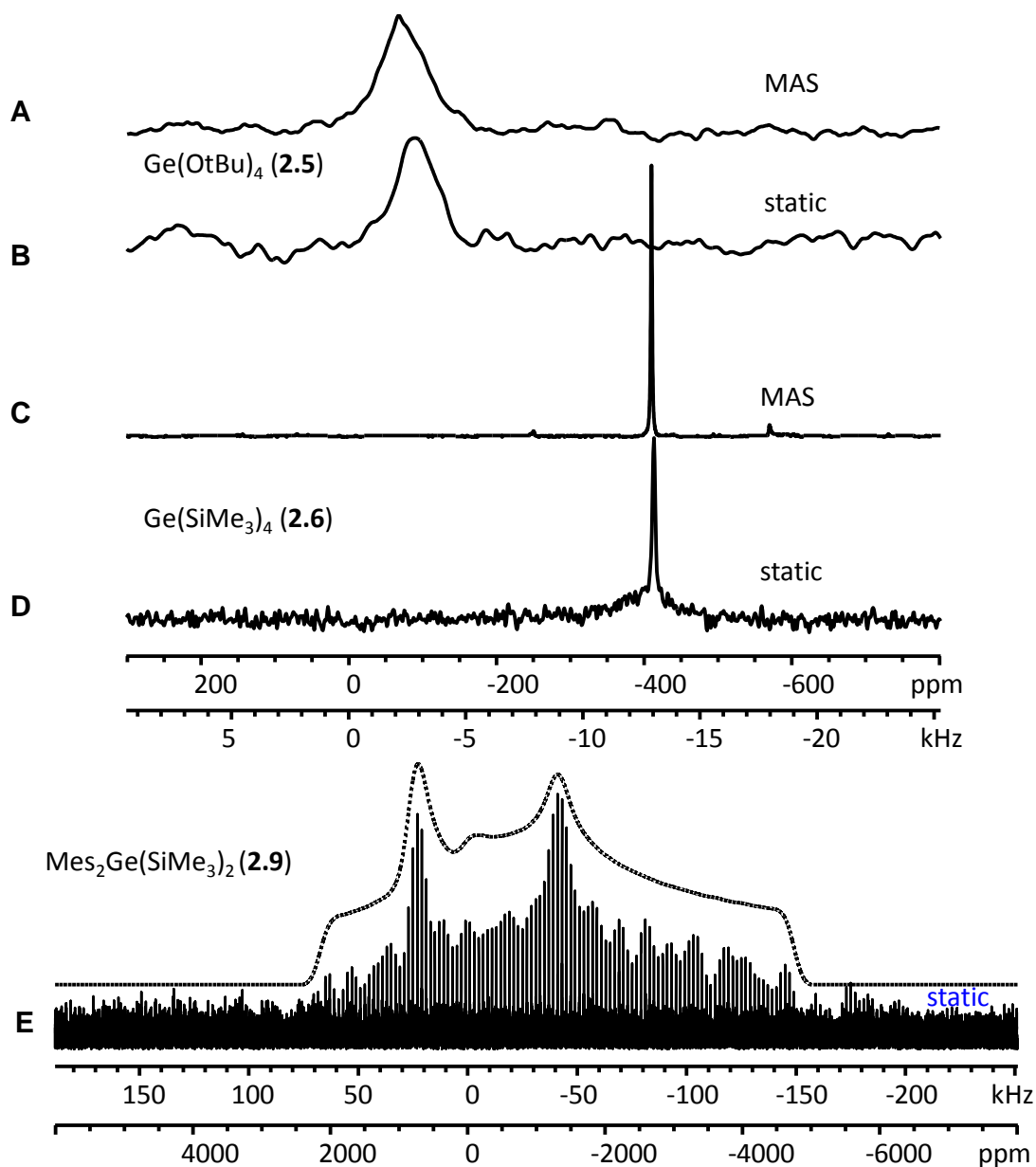


Figure 2.17 ^{73}Ge SSNMR spectra of compounds **2.5**, **2.6** and **2.9** at 21.1 T. Dotted traces represent simulations using parameters from Table 2.1. A) MAS (5 kHz) and B) static spectra of $\text{Ge}(\text{OtBu})_4$. C) MAS (5 kHz) and D) static spectra of $\text{Ge}(\text{SiMe}_3)_4$. E) Static WURST-CPMG spectrum of $\text{Mes}_2\text{Ge}(\text{SiMe}_3)_2$.

2.2.4 Dimesitylbis(trimethylsilyl)germane (2.9)

Replacing two of the trimethylsilyl ligands in $\text{Ge}(\text{SiMe}_3)_4$ with mesityl groups changes the appearance of the static ^{73}Ge SSNMR spectrum in a dramatic fashion. The signal is so

wide that the WURST-QCPMG method had to be used to acquire the spectrum. Rather than a single narrow line, $\text{Mes}_2\text{Ge}(\text{SiMe}_3)_2$ (**2.9**) exhibits the broadest signal of any observed in this study with a breadth greater than 200 kHz (Figure 2.1E). The magnitude of the quadrupolar coupling constant ($C_Q = 24.7$ MHz) is very large, which is consistent with the large EFG expected for a Ge local environment significantly deviating from spherical symmetry. The asymmetry parameter ($\eta_Q = 0.6$) indicates the absence of axial symmetry. While the quadrupolar interactions of the two dimesityl compounds are quite different, the isotropic shift (-173 ppm) is similar to that observed for Mes_2GeH_2 . The inclusion of CSA was not required for spectral simulation, due to the magnitude of the quadrupolar interaction dominating the spectrum. A CSA of 30-100 ppm such as observed in the compounds examined in this study would not have an observable impact on the overall lineshape. Due to the extreme breadth of the static spectrum, MAS experiments were not performed.

Since the crystal structure of $\text{Mes}_2\text{Ge}(\text{SiMe}_3)_2$ is not known, computational modelling was conducted to gain information on the molecular geometry in the solid state. The experimental C_Q (24.7 MHz) was somewhat underestimated at the Gaussian optimized geometry (19.3 MHz), though it did give reasonable agreement with η_Q (experimental = 0.6, calculated = 0.5). The Ge–C and Ge–Si bond distances and angles were systematically varied to explore their effect on C_Q . As previously observed, the Ge–C bond length continued to have a dramatic ($121 \text{ MHz}/\text{\AA}$) effect on the magnitude of calculated C_Q (Figure 2.18A); however, elongation of the germanium-silicon bonds also caused a non-negligible ($-85 \text{ MHz}/\text{\AA}$) decrease in C_Q (Figure 2.18B). The C–Ge–C (Figure 2.18C) bond angle caused small ($-0.5 \text{ MHz}/^\circ$) but systematic changes in the

calculated C_Q . While the effect of the Si-Ge-Si (Figure 2.18D) angle was also systematic, the overall impact was negligible ($-0.06 \text{ MHz}/^\circ$).

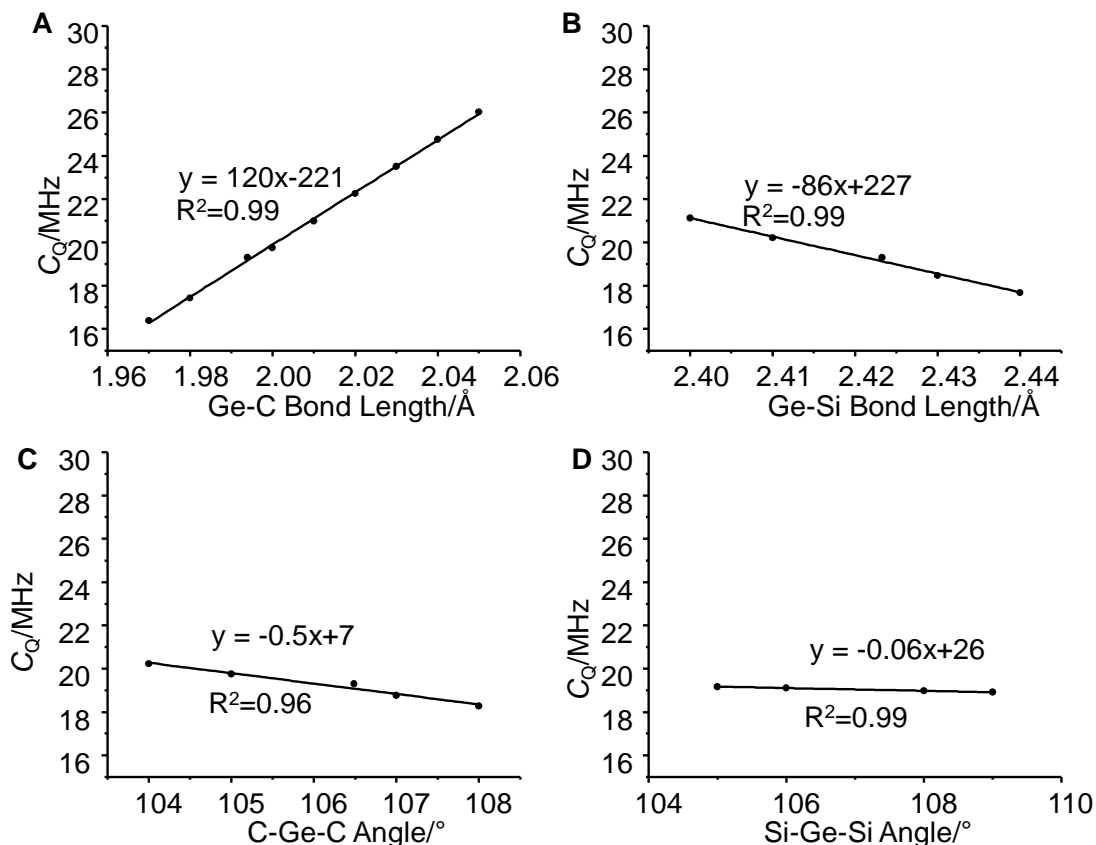


Figure 2.18 Relationship between the calculated C_Q value for $\text{Mes}_2\text{Ge}(\text{SiMe}_3)_2$ and A) Ge-C bond lengths, B) Ge-Si bond lengths, C) C-Ge-C angle, and D) Si-Ge-Si angle.

In $\text{Mes}_2\text{Ge}(\text{SiMe}_3)_2$, the predicted η_Q correlated linearly to both the Ge-C (Figure 2.19A) and the Ge-Si (Figure 2.19B) bond lengths, providing an additional constraint to approximate the structure. The C-Ge-C angle also had a small effect on the overall EFG tensor (Figure 2.19C), while the effect of the Si-Ge-Si angle was again negligible (Figure 2.19D).

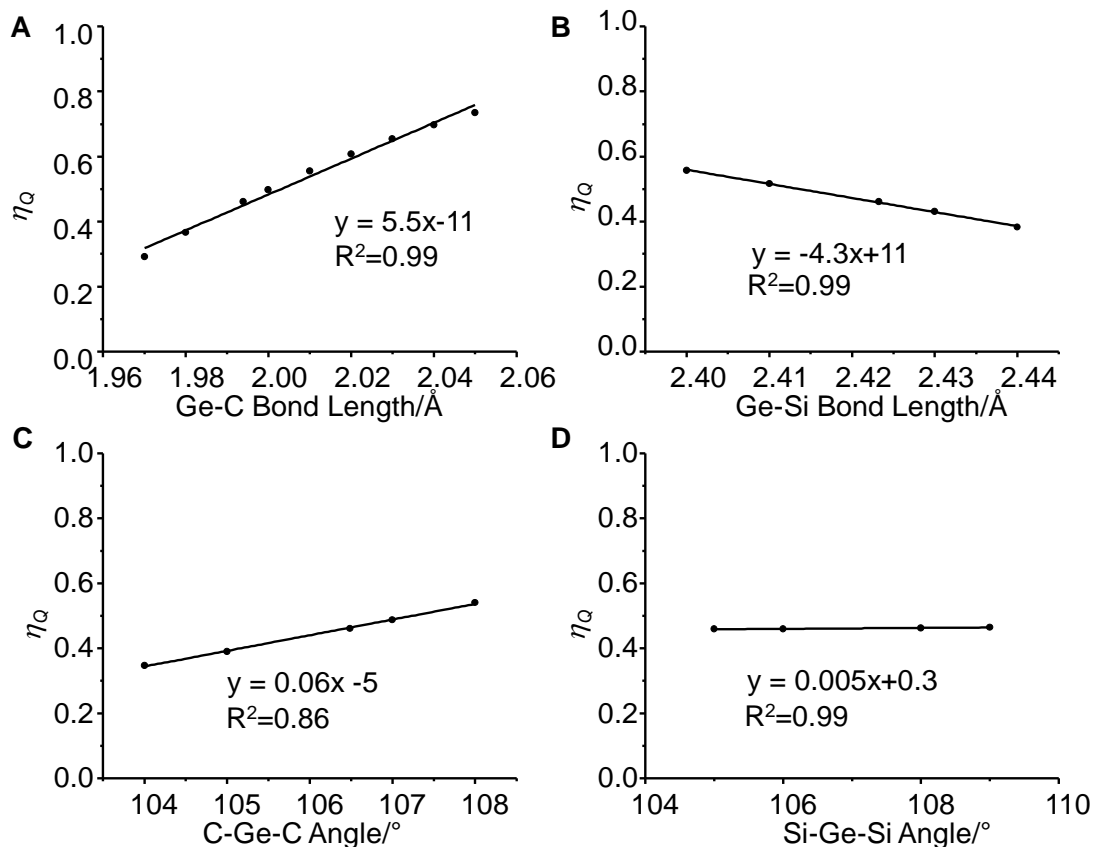


Figure 2.19 Relationship between the calculated η_Q value for $\text{Mes}_2\text{Ge}(\text{SiMe}_3)_2$ and A) Ge–C bond lengths, B) Ge–Si bond lengths, C) C–Ge–C bond angle, and D) Si–Ge–Si bond angle.

The final geometry tested was, thus, selected to give a larger C_Q than calculated for the optimized geometry while keeping η_Q close to its experimental value. The final geometry was determined by varying the Ge–C bond length to raise the calculated value of C_Q to the highest value possible without raising η_Q above its experimental value. C_Q was then further adjusted by contraction of the Ge–Si bond until the same limit was reached.

Finally, fine adjustments to the calculated value of C_Q were made by altering the C–Ge–C and Si–Ge–Si angles. With a Ge–C bond length of 2.01 Å, a Ge–Si bond length of 2.4 Å, a C–Ge–C bond angle of 104° and a Si–Ge–Si bond angle of 105°, the quadrupolar parameters were calculated to be $C_Q = 24.5$ MHz and $\eta_Q = 0.5$, which is within

experimental error of the observed values (Table 2.1). While both bond lengths (Ge–C or Ge–Si) were kept the same to minimize the number of variables, the ^{13}C CPMAS SSNMR spectrum of **2.9** indicates that neither the mesityl groups nor the trimethylsilyl groups are actually equivalent to each other (Figure 2.11E). The bond lengths obtained in this manner thus represent a predicted *average* value. The non-equivalence of the trimethylsilyl groups is further supported by the ^{29}Si CPMAS spectrum (Figure 2.20), which shows two distinct resonances which are better resolved than in the carbon spectrum. The ^{29}Si spectrum would be more sensitive to differences in Ge–Si bond length than the more distant carbon atoms, and thus this experiment provides better support for the earlier conclusion.

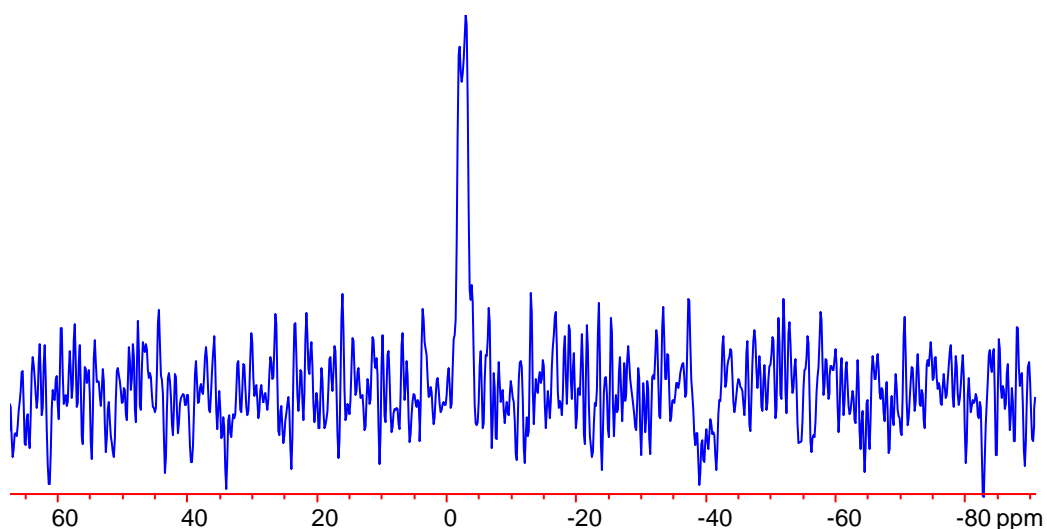


Figure 2.20 ^{29}Si CPMAS spectrum of $\text{Mes}_2\text{Ge}(\text{SiMe}_3)_2$ at 9.4 T showing two distinct silicon resonances for the trimethylsilyl groups.

One can further adjust the bond lengths to make two mesityl groups inequivalent (one of such possibility, with Ge–C bond lengths of 2.01 and 2.005 Å, is listed in Table 2.1). Since there are many possible combinations, the structure was not refined further. In this case, the final geometry is somewhat higher in energy than the geometry optimized

structure, likely due to differences between the solid and gas phases. It is notable that the higher energy corresponds to the only case in which the geometry optimized structure *underestimated* C_Q .

2.2.5 Compounds for which ^{73}Ge SSNMR Spectroscopy was Unsuccessful

Many germanium compounds were investigated for which a ^{73}Ge SSNMR spectrum could *not* be obtained (Figure 2.21). From this, it has been possible to establish general guidelines for when ^{73}Ge SSNMR spectroscopy is feasible.

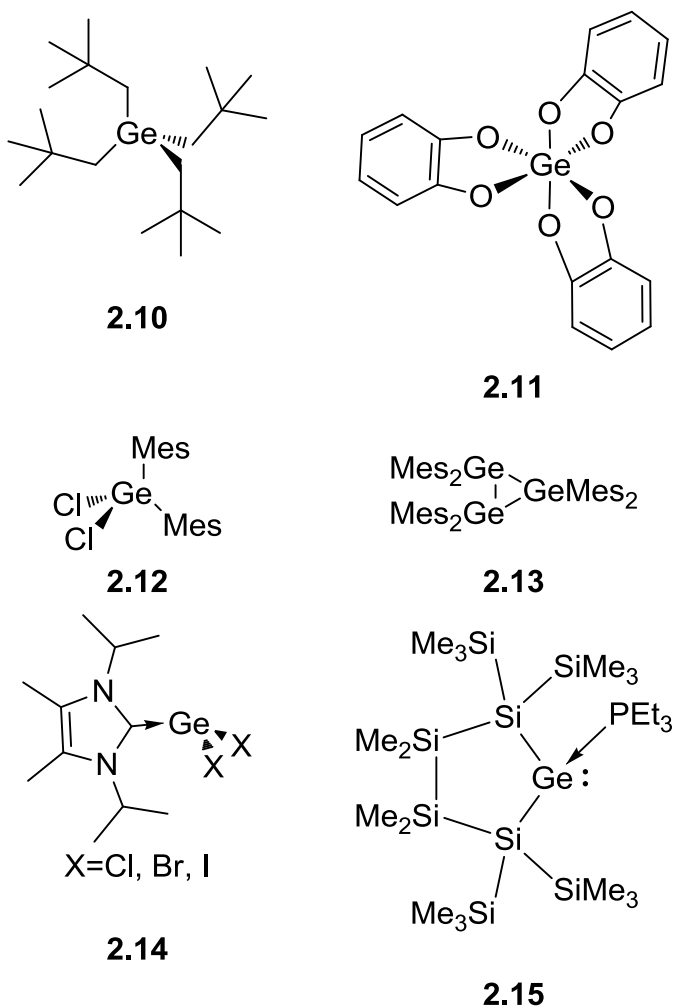


Figure 2.21 Compounds for which a ^{73}Ge SSNMR signal was not observed.

Tetraneopentylgermane (**2.10**) and triscatecholatenogermane (**2.11**) both initially appeared to be ideal candidates for ^{73}Ge SSNMR spectroscopy due to the high (tetrahedral and octahedral, respectively) symmetry at germanium. However, no ^{73}Ge signal was observed in the solid state. Examination of the ^{13}C SSNMR spectra (not shown) revealed more signals than could be accounted for from the structure. Thus, the lack of signal was attributed to multiple germanium environments present in the bulk material due to structural disorder. With multiple environments, no individual environment was present in sufficient concentration to obtain an acceptable signal-to-noise ratio.

$\text{Mes}_2\text{GeCl}_2$ (**2.12**) also appeared to be a suitable candidate after high quality spectra were obtained for Mes_2GeH_2 and $\text{Mes}_2\text{Ge}(\text{SiMe}_3)_2$. The challenge in obtaining the spectrum in this case was attributed to the attached quadrupolar chlorine atoms, which may lead to very short T_2 relaxation times. Rapid T_2 relaxation poses a considerable challenge in NMR spectroscopy for any nucleus, but is particularly problematic when attempting to employ QCPMG-based pulse sequences. The signal enhancement in these sequences is derived from the repeated refocusing of magnetization during acquisition. In the case of $\text{Mes}_2\text{Ge}(\text{SiMe}_3)_2$, it was possible to refocus 64 times over an acquisition time of 32 ms, but if T_2 is short, only an extremely limited number of refocusing pulses can be applied before the signal has completely decayed, thereby greatly limiting signal enhancement. While there is no known crystal structure for $\text{Mes}_2\text{GeCl}_2$, it should be noted that the C_Q value calculated for a geometry-optimized structure is considerably larger than that observed for $\text{Mes}_2\text{Ge}(\text{SiMe}_3)_2$, which could also explain the inability to obtain a signal.

While the germanium atoms of hexamesitylcyclotrigermane (**2.13**) are chemically equivalent, the molecular structure possesses only two-fold symmetry.³⁵ There are, thus, two crystallographically distinct germanium sites within the molecule, making **2.13** a more complicated spectroscopic target than **2.1-2.9**.

A series of germylenes complexed with N-heterocyclic carbenes (NHC) (**2.14**) were investigated. As a high quality spectrum had previously been acquired for $\text{GeCl}_2 \cdot \text{dioxane}$,¹⁸ the related compounds appeared to be promising targets. However, due to the small size of dioxane in comparison to the bulkier carbenes, $\text{GeCl}_2 \cdot \text{dioxane}$ has a much higher germanium concentration ($5.17 \text{ Ge}/1000 \text{ \AA}^3$) than the NHC derivatives (**2.14** X = Cl $2.74 \text{ Ge}/1000 \text{ \AA}^3$, X = Br $2.55 \text{ Ge}/1000 \text{ \AA}^3$, X = I $\text{Ge}/1000 \text{ \AA}^3$). This is also an additional challenge for cyclotrigermane **2.13**, as the bulky mesityl groups lead to a very low germanium concentration of $1.46 \text{ Ge}/1000 \text{ \AA}^3$ for the two equivalent germanium atoms and $0.73 \text{ Ge}/1000 \text{ \AA}^3$ for the unique germanium atom. The low germanium concentration is further complicated by the low natural abundance of the NMR active ^{73}Ge isotope. Several of the germanes for which spectra were obtained do have low germanium concentrations (**2.1** $\text{Ge}(p\text{-Me-C}_6\text{H}_4)_4$, $1.69 \text{ Ge}/1000 \text{ \AA}^3$; **2.2** $\text{Ge}(p\text{-MeO-C}_6\text{H}_4)_4$, $1.65 \text{ Ge}/1000 \text{ \AA}^3$; **2.3** GePh_4 , $2.15 \text{ Ge}/1000 \text{ \AA}^3$; **2.8** Mes_3GeH , $1.74 \text{ Ge}/1000 \text{ \AA}^3$); however, these all had very low C_Q values, and thus, an inherently higher signal-to-noise ratio. From these data, it can be determined that to observe a ^{73}Ge NMR signal in a lower symmetry environment, there must be a concentration of at least $3 \text{ Ge}/1000 \text{ \AA}^3$ in the solid state.

The phosphine-complexed germylene **2.15** was considered to be an interesting target and served as a test of the guideline established regarding the required germanium

concentration. As was expected, the attempt to obtain ^{73}Ge data was unsuccessful. We, thus, turned to silicon and phosphorus NMR spectroscopy for further investigations.

The ^{29}Si spectrum of **2.15** (Figure 2.22) consists of several sharp signals, indicating that the bulk material is a well-ordered, highly crystalline system. On the basis of chemical shift, four signals between 0 and -20 ppm are consistent with the trimethylsilyl groups of the ligand. The remaining three signals, between -120 and -130 ppm, are attributed to the backbone silicon atoms, with two signals overlapping at -120 ppm.

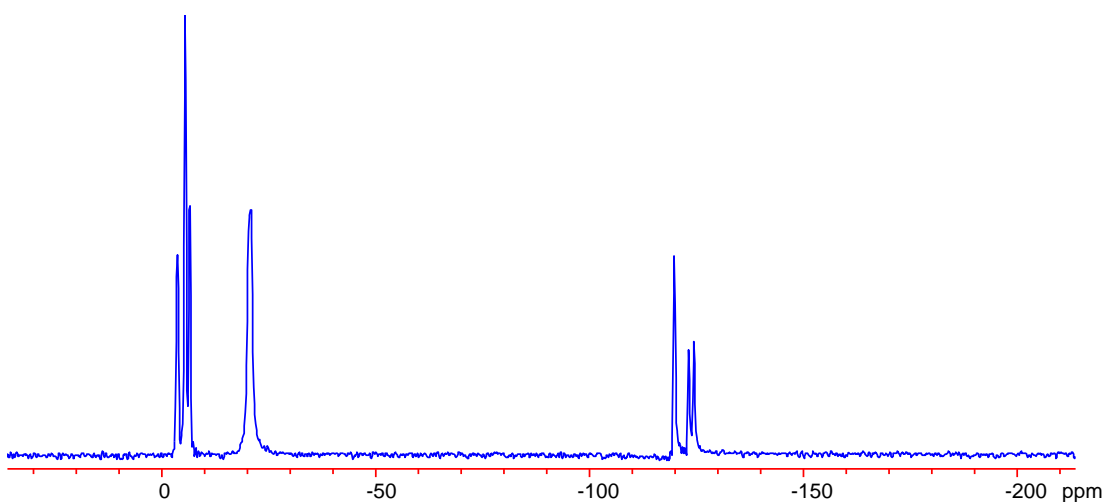


Figure 2.22 ^{29}Si CPMAS NMR spectrum of the germylene complex **2.15** at 9.4 T.

The observation of sharp lines consistent with a highly crystalline powder rules out structural disorder as an explanation for the lack of a ^{73}Ge NMR signal. A single phosphorus resonance was detected under MAS conditions (Figure 2.23), further supporting a single germanium site as seen in the crystal structure. Unfortunately, attempts to obtain a static ^{31}P spectrum resulted in a complex lineshape due to decomposition of the sample into at least three phosphorus containing products.

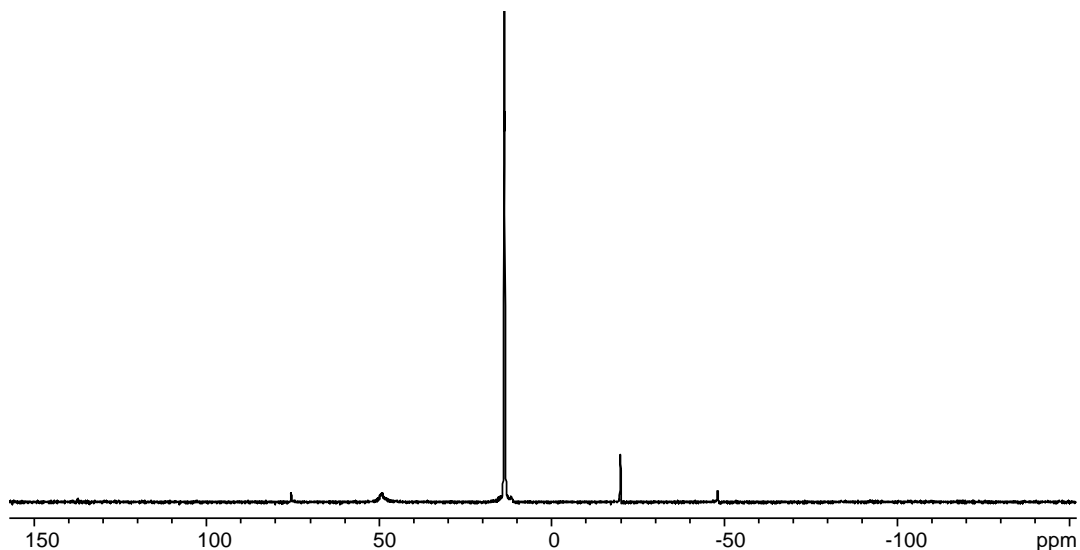


Figure 2.23 ^{31}P MAS ($\nu_{\text{rot}} = 10$ kHz) spectrum of **2.15** at 9.4 T. The spectrum was acquired over 16 transients with a 30 second pulse delay.

Given the high quality ^{29}Si and ^{31}P data, it is most likely that the lack of ^{73}Ge signal arises from the low germanium content of the sample, confirming previous observations of a relationship between the germanium concentration in a sample and the feasibility of ^{73}Ge SSNMR spectroscopy.

2.3 Conclusion

Obtaining useful ^{73}Ge SSNMR spectra of organogermanium compounds for structural analyses has been traditionally very difficult due to the extremely low sensitivity. The present work demonstrates that ^{73}Ge SSNMR spectra can now be obtained for some compounds at ultrahigh magnetic field.

We have shown through examination of the compounds with a known crystal structure that the ^{73}Ge MAS and static spectral parameters are very sensitive to the Ge local environment. The ^{73}Ge NMR tensor values correlate to structural parameters, with longer Ge–C bonds giving rise to smaller C_Q values and greater angular distortion leading to

larger C_Q values. The combination of ^{73}Ge SSNMR data and computational modelling provides insight into the local geometry around Ge for organogermanes of unknown or poorly described structures. ^{73}Ge SSNMR spectroscopy at ultrahigh magnetic field is a promising method for the characterization of organogermanium compounds.

In order to observe a germanium signal, the sample must meet several criteria. The molecule must crystallize in a single environment in the solid state. If C_Q is not predicted to be unusually small, the overall germanium concentration in the solid state must be high, as compounds with germanium concentrations lower than 3 Ge/1000 Å³ did not give rise to signals. Unfortunately, this presents a challenge for the low oxidation state compounds that represent the current area of greatest interest, as they are commonly stabilized with bulky ligands. Finally, attached quadrupolar nuclei are highly unfavourable for the acquisition of ^{73}Ge SSNMR spectral data as the shorter T_2 relaxation leads to diminished benefit from the QCPMG pulse sequence.

2.4 Experimental

2.4.1 Materials

Germylene **2.15** was prepared by Christoph Marschner. Tetrabenzylgermane,³⁶ Ge(*p*-Me-C₆H₄)₄,¹⁹ Ge(*p*-MeO-C₆H₄)₄,¹² tetra(*tert*-butoxy)germane,³⁷ tetrakis(trimethylsilyl)germane,³⁸ dimesitylgermane,³⁹ trimesitylgermane,²¹ dimesitylbis(trimethylsilyl)germane,⁴⁰ tetraneopentylgermane,⁴¹ triscatecholentogermane,⁴² dimesityldichlorogermane,³⁹ hexamesitylcyclotrigermane⁴³ and N-heterocyclic carbene complexes of GeX₂ (X = Cl,⁴⁴ Br,⁴⁵ I⁴⁴) were prepared according to literature procedures. The structure of the compounds was confirmed by

comparison of solution state ^1H NMR spectra to the literature values. Compounds **2.1**, **2.2**, **2.4**, **2.10** and **2.11** were further characterized by mass spectrometry. X-ray quality single crystals of $\text{Ge}(p\text{-MeO-C}_6\text{H}_4)_4$ were grown from dichloromethane/isopropanol.

2.4.2 Solid-State NMR Spectroscopy

^{73}Ge SSNMR spectra were acquired on a Bruker Avance 900 MHz spectrometer at the *National Ultrahigh Field NMR Facility for Solids* (www.nmr900.ca). Experimental setup and pulse calibrations were performed on neat GeCl_4 . Chemical shift referencing was also performed relative to the same sample of GeCl_4 (30.9 ppm relative to GeMe_4 at 0 ppm). Magic-angle spinning experiments were performed on a 7 mm single channel low gamma MAS probe. A one-pulse experiment was performed using a solid 90° pulse with a 1-2 second recycle delay, spinning at 4-5 kHz. Static experiments with proton decoupling were performed on a home built 7 mm H/X low gamma NMR probe for stationary samples with a dual resonator design. Quadrupolar echo experiments of the form $\pi/2$ - τ - $\pi/2$ -acquire were employed for the majority of samples. For **2.8**, a WURST-QCPMG⁷ sequence, consisting of a WURST-80 pulse followed by a series of refocusing pulses was employed. This sequence was also attempted for compound **2.2**, however, due to the relatively narrow spectrum and a short T_2 relaxation time, it did not provide signal enhancement. Complete acquisition parameters are given in Table 2.4.

Table 2.4 Detailed ^{73}Ge SSNMR experimental conditions.

Sample	Experiment	pulse length (μs)	SW (kHz)	recycle delay (s)	τ_1 (μs)	# scans
$\text{Ge}(p\text{-Me-C}_6\text{H}_4)_4$	MAS 5 kHz	4.0	50	2	---	27132
	static echo	4.0	250	2	19.6	25440
$\text{Ge}(p\text{-MeO-C}_6\text{H}_4)_4$	MAS 5 kHz	4.0	50	2	---	31512
GePh_4	MAS 4 kHz	3.0	500	1	---	1024
	static echo	3.0	100	5	19.6	10237
$\text{Ge}(\text{CH}_2\text{Ph})_4$	MAS 5 kHz	4.0	100	1	---	37833
	static echo	4.0	200	1	19.6	71680
$\text{Ge}(\text{O}t\text{Bu})_4$	MAS 5 kHz	4.0	100	1	---	10240
	static echo	4.0	200	1	19.6	64679
$\text{Ge}(\text{SiMe}_3)_4$	MAS 5 kHz	4.0	50	1	---	256
	static echo	4.0	250	1	19.6	14000
Mes_2GeH_2	MAS 5 kHz	4.0	50	2	---	2500
	static echo	4.0	250	2	19.6	29131
Mes_3GeH	MAS 5 kHz	4.0	50	2	---	2403
	static echo	4.0	250	2	19.6	40360
$\text{Mes}_2\text{Ge}(\text{SiMe}_3)_2$	static WURST-QCPMG*	50	500	1	25	131639

* $\tau_a = 132 \mu\text{s}$, M (# of loops) = 64, $\tau_2 = 26 \mu\text{s}$, $\tau_3 = 26 \mu\text{s}$, $\tau_4 = 26 \mu\text{s}$

^{13}C SSNMR spectra were acquired on a Varian Infinity 400 MHz spectrometer.

Experimental setup and pulse calibrations were performed on adamantane. Magic-angle spinning (MAS) experiments were performed on a Varian 4 mm HXY probe. Cross polarization experiments were utilized for all compounds. Signals were assigned using solution-state Heteronuclear Multiple Bond Coherence (HMBC) and Heteronuclear

Single Quantum Coherence (HSQC) experiments performed on a Varian Inova 400 MHz spectrometer on samples dissolved in C_6D_6 .

^{29}Si data were collected on a Varian Infinity 400 spectrometer. $^1H \rightarrow ^{29}Si$ CPMAS data were obtained on a Varian 4 mm HXY probe operating in dual resonance mode with high power 1H decoupling spinning at 8 kHz. Pulse width calibrations and chemical shift referencing were performed on $Si(SiMe_3)_4$.

Static CP variable temperature experiments were performed on a Varian 9 mm HXY probe operating in dual resonance mode. Samples were allowed to equilibrate at the set temperature for a minimum of twenty minutes before spectra were recorded. The temperature readings of the cryostat were calibrated using the peak maximum of static lead nitrate.⁴⁶

2.4.3 NMR Spectral Simulations

Experimental NMR parameters were determined from analytical simulations using WSolids.⁴⁷ Errors were determined by visual comparison to the experimental spectrum. Starting from the best fit value, the parameter being evaluated was varied systematically in both directions while all others were held constant until a visible change was observed.

2.4.4 Theoretical Calculations

First principles calculations were performed using Gaussian 09²⁷ on the Shared Hierarchical Academic Research Computing Network (SHARCNET, www.sharcnet.ca). Calculations were performed on a 4 core Opteron 2.4 GHz CPU with 32 GB memory or an 8 core Xeon 2.83 GHz CPU with 16 GB memory. CSA tensors were computed using the gauge-including atomic orbitals (GIAO) method. Basis sets and methods were used as

indicated in the results and discussion. As there is no absolute shielding scale known for germanium, isotropic shifts were calculated relative to $\text{Ge}(\text{CH}_3)_4$ optimized at the TPSSTPSS²⁹/6-31G* level and calculated at the TPSSTPSS/6-311+G** level. The results of the Gaussian calculations were analyzed using EFGShield.⁴⁸

2.4.5 Differential Scanning Calorimetry

DSC measurements were performed using a Thermal Analytics Q20 instrument. The sample was heated to 100 °C, cooled to -180 °C and warmed back to 20 °C at a rate of 5 °C/minute. The data reported is from the second heating run.

2.4.6 Single Crystal X-ray Diffraction

Data were collected by Dr. Guerman Popov at low temperature (150 K) on a Nonius Kappa-CCD area detector diffractometer with COLLECT. Data were corrected for absorption effects using the multi-scan method (ShADABS). The unit cell parameters were calculated and refined from the full data set.

The structure was solved and refined by Dr. Popov using the Bruker SHELXTL software package. Subsequent difference Fourier syntheses allowed the remaining atoms to be located. All of the non-hydrogen atoms were refined with anisotropic thermal parameters.

Crystallographic data are summarized in Table 2.5. CCDC-822868 contains the supplementary crystallographic information. These data can be obtained free of charge from The Cambridge Crystallographic Data Center via

www.ccdc.cam.ac.uk/data_request/cif.

Table 2.5 Crystallographic data for *Ge(p-MeO-C₆H₄)₄*.

empirical formula	C ₂₈ H ₂₈ GeO ₄
fw	501.09
cryst syst	triclinic
space group	P-1
<i>a</i> (Å)	10.525(2)
<i>b</i> (Å)	10.973(2)
<i>c</i> (Å)	11.939(2)
α (deg)	70.916(4)
β (deg)	69.605(4)
γ (deg)	77.627(4)
volume (Å ³)	1213.5(4)
<i>Z</i>	2
no. of data/restraints/params	5487 / 0 / 302
goodness-of-fit	1.005
<i>R</i> [<i>I</i> > 2σ(<i>I</i>)]	0.0475
wR ² (all data)	0.0823
largest diff peak and hole (e Å ⁻³)	0.498, -0.504

2.5 References

- (1) Wrackmeyer, B. *Annu. Rep. NMR Spectrosc.* **2006**, *57*, 1.
- (2) Liepins, E.; Zicmane, I.; Lukevics, E. *J. Organomet. Chem.* **1988**, *341*, 315.
- (3) Takeuchi, Y.; Takayama, T. *Annu. Rep. NMR Spectrosc.* **2005**, *54*, 155.
- (4) Pykko, P. *Mol. Phys.* **2008**, *106*, 1965.
- (5) Larsen, F. H.; Jakobsen, H. J.; Ellis, P. D.; Nielsen, N. C. *J. Phys. Chem. A* **1997**, *101*, 8597.
- (6) Schurko, R. W.; Hung, I.; Widdifield, C. M. *Chem. Phys. Lett.* **2003**, *379*, 1.
- (7) O'Dell, L. A.; Schurko, R. W. *Chem. Phys. Lett.* **2008**, *464*, 97.
- (8) Siegel, R.; Nakashima, T. T.; Wasylshen, R. E. *J. Magn. Reson.* **2007**, *184*, 85.
- (9) Verkhovskii, S. V.; Yakubovskii, A. Y.; Trokiner, A.; Malkin, B. Z.; Saikin, S. K.; Ozhogin, V. I.; Tikhomirov, A. V.; Ananyever, A. V.; Gerashenko, A. P.; Piskunov, Y. V. *Appl. Magn. Reson.* **1999**, *17*, 557.

- (10) Takeuchi, Y.; Nishikawa, M.; Tanaka, K.; Takayama, T.; Imanari, M.; Deguchi, K.; Fujito, T.; Sugisaka, Y. *Chem. Commun.* **2000**, 687.
- (11) Takeuchi, Y.; Nishikawa, M.; Yamamoto, H. *Magn. Reson. Chem.* **2004**, *42*, 907.
- (12) Takeuchi, Y.; Nishikawa, M.; Hachiya, H.; Yamamoto, H. *Magn. Reson. Chem.* **2005**, *43*, 662.
- (13) Stebbins, J. F.; Du, L.-S.; Kroeker, S.; Neuhoff, P.; Rice, D.; Frye, J.; Jakobsen, H. J. *Solid State Nucl. Magn. Reson.* **2002**, *21*, 105.
- (14) Michaelis, V. K.; Aguiar, P. M.; Terskikh, V. V.; Kroeker, S. *Chem. Commun.* **2009**, 4660.
- (15) Michaelis, V. K.; Kroeker, S. *J. Phys. Chem. C* **2010**, *114*, 21736.
- (16) Sen, S.; Gan, Z. *J. Non-Cryst. Solids* **2010**, *356*, 1519.
- (17) Greer, B. J.; Michaelis, V. K.; Terskikh, V. V.; Kroeker, S. *Can. J. Chem.* **2011**, *89*, 1118.
- (18) Sutrisno, A.; Hanson, M. A.; Rugar, P. A.; Terskikh, V. V.; Baines, K. M.; Huang, Y. *Chem. Commun.* **2010**, *46*, 2817.
- (19) Charissé, M.; Roller, S.; Dräger, M. *J. Organomet. Chem.* **1992**, *427*, 23.
- (20) Riedmiller, F.; Wegner, G. L.; Jockisch, A.; Schmidbaur, H. *Organometallics* **1999**, *18*, 4317.
- (21) Lambert, J. B.; Stern, C. L.; Zhao, Y.; Tse, W. C.; Shawl, C. E.; Lentz, K. T.; Kania, L. *J. Organomet. Chem.* **1998**, *568*, 21.
- (22) *NMR Crystallography*; Harris, R. K.; Wasylishen, R. E.; Duer, M. J., Eds.; Wiley: Chichester, UK, **2009**.

- (23) Yoder, C. H.; Agee, T. M.; Griffith, A. K.; Schaeffer, C. D. J.; Carroll, M. J.; DeToma, A. S.; Fleisher, A. J.; Gettel, C. J.; Rheingold, A. L. *Organometallics* **2010**, *29*, 582.
- (24) Ferguson, G.; Glidewell, C. *Acta Crystallogr., Sect. C: Cryst. Struct. Commun.* **1996**, *52*, 1889.
- (25) Kibalchenko, M.; Yates, J. R.; Pasquerello, A. *J. Phys.: Condens. Matter* **2010**, *22*, 145501.
- (26) Charpentier, T. *Solid State Nucl. Magn. Reson.* **2011**, *40*, 1.
- (27) Frisch, M. J.; Revision A1 ed.; Gaussian Inc.: Wallingford, CT, **2009**.
- (28) Stephens, P. J.; Devlin, F. J.; Chabalowski, C. F.; Frisch, M. J. *J. Phys. Chem.* **1994**, *98*, 11623.
- (29) Tao, J.; Perdew, J. P.; Staroverov, V. N.; Scuseria, G. E. *Phys. Rev. Lett.* **2003**, *91*, 146401.
- (30) Adamo, C.; Barone, V. *J. Chem. Phys.* **1999**, *110*, 6158.
- (31) Robinson, K.; Gibbs, G. V.; Ribbe, P. H. *Science* **1970**, *172*, 567.
- (32) Freitag, S.; Herbst-Immer, R.; Lamery, L.; Stalke, D. *Organometallics* **1996**, *15*, 2839.
- (33) Aliev, A. E.; Harris, K. D. M.; Apperley, D. C. *J. Chem. Soc., Chem. Commun.* **1993**, 251.
- (34) Dinnebier, R. E.; Dollase, W. A.; Helluy, X.; Kümmerlen, J.; Sebald, A.; Schmidt, M. U.; Stephens, P. W.; van Smaallen, S. *Acta Crystallogr., Sect. B: Struct. Sci.* **1999**, *55*, 1014.

- (35) Baines, K. M.; Cooke, J. A.; Payne, N. C.; Vittal, J. J. *Organometallics* **1992**, *11*, 1408.
- (36) Glockling, F.; Hooton, K. A. *J. Chem. Soc.* **1962**, 3509.
- (37) Bradley, D. C.; Kay, L. J.; Wardlaw, W. *J. Chem. Soc.* **1956**, 4916.
- (38) Brook, A. G.; Abdesaken, F.; Söllradl, H. J. *J. Organomet. Chem.* **1986**, *299*, 9.
- (39) Cooke, J. A.; Dixon, C. E.; Netherton, M. R.; Kollegger, G. M.; Baines, K. M. *Synth. React. Inorg. Met. -Org. Chem.* **1996**, *26*, 1205.
- (40) Ando, W.; Tsumuraya, T. *Organometallics* **1989**, *8*, 1467.
- (41) Davidson, P. J.; Lappert, M. F.; Pearce, R. *J. Organomet. Chem.* **1973**, *57*, 269.
- (42) Cerveau, G.; Chult, C.; Corriu, J. P.; Reyé, C. *Organometallics* **1991**, *10*.
- (43) Ando, W.; Tsumuraya, T. *J. Chem. Soc., Chem. Commun.* **1987**, 1514.
- (44) Rugar, P. A.; Staroverov, V. N.; Ragogna, P. J.; Baines, K. M. *J. Am. Chem. Soc.* **2007**, *129*, 15138.
- (45) Rugar, P. A.; Jennings, M. C.; Baines, K. M. *Organometallics* **2008**, *27*, 5043.
- (46) Beckmann, P. A.; Dybowski, C. *J. Magn. Reson.* **2000**, *146*, 379.
- (47) Eichele, K.; Wasylshen, R. E. In *WSolids1: Solid-State NMR Spectrum Simulation* **2001**.
- (48) Adiga, S.; Aebi, D.; Bryce, D. L. *Can. J. Chem.* **2007**, *85*, 496.

Chapter 3 Characterization of Germanium Monohalides by Solid-State NMR Spectroscopy and Density Functional Theory Calculations

3.1 Introduction

Nanocrystals of germanium exhibit photoluminescence properties not seen in either the bulk or molecular phases.¹ The smallest particles, with diameters less than 2 nm, are the least understood, however, exhibit the best photoluminescence efficiency.² Thus, interest in a bottom up approach to the synthesis of small clusters with known composition to obtain insight into the structural properties of such compounds represents a first step toward developing structure-property relations in the grey area between molecules and the bulk phase.³ Metalloid clusters of the general formula Ge_nR_m , where $n > m$ and R is a bulky ligand such as $\text{Si}(\text{SiMe}_3)_3$ or $\text{N}(\text{SiMe}_3)_2$ required for kinetic stabilization, are ideal model compounds in this respect as they bridge between molecular chemistry and bulk elemental material.⁴⁻⁶ The realm between bulk and molecular chemistry is the essence of nanotechnology.

The majority of germanium compounds are found in the +4 oxidation state, analogous to carbon chemistry. However, due to ease of reduction, the synthesis of metalloid clusters, where the germanium atoms exhibit an average oxidation state approaching zero,⁷ is more easily achieved starting from germanium in a lower oxidation state. Germanium nanoclusters have been synthesized in solution by the reduction of a variety of germanium(IV) precursors, yielding a distribution of particle sizes which, while narrow, was not uniform.⁸ Disproportionation represents an alternate method of synthesis. Given

the resemblance of the nanoclusters to elemental germanium, it is desirable to start from a low oxidation state. Of the lower oxidation states, germanium(II) is the most readily accessible;⁹⁻¹¹ however, the germanium(II) halides are poor starting materials for the synthesis of metalloid clusters by way of a disproportionation reaction as they only begin to disproportionate into GeX_4 and elemental germanium at high temperatures, where the isolation of metastable metalloid clusters is not feasible.¹² Hence, a different starting material is necessary that is more reactive and disproportionates at lower temperatures. Of particular note in this respect are the germanium(I) monohalides, GeCl and GeBr , compounds that disproportionate at much lower temperatures.¹³

To prepare the monohalides, elemental germanium is reacted with HX at high temperature (1600 °C) and low pressure (ca. 10^{-2} mbar). The overall reaction is: $\text{Ge} + \text{HX} \rightarrow \text{GeX} + \frac{1}{2} \text{H}_2$; $\text{X} = \text{Cl}, \text{Br}$. The resulting gas phase molecules are then rapidly condensed with a solvent at -196 °C. Only when toluene is used as solvent, is an amorphous solid of the composition GeX ($\text{X} = \text{Cl}, \text{Br}$) obtained. The monohalides have been successfully employed in the preparation of cluster compounds.^{7,14} The structure of the germanium monohalide is unknown as it is an amorphous solid which does not diffract. Thus, an alternate approach to structural characterization is required.

Solid-state NMR spectroscopy has proven to be a valuable technique for providing insight into the structure of solids even when X-ray diffraction is not feasible.¹⁵

Furthermore, *ab initio* calculations are often used as a complement to solid-state NMR spectroscopy to provide additional structural insight.¹⁶

The three elements present in GeCl and GeBr are among the less frequently studied NMR active isotopes due to their inherent challenges. The NMR properties of these nuclei are summarized in Table 3.1. ^{73}Ge is a particularly unfavourable nucleus due to its low abundance, moderate quadrupole moment and low gyromagnetic ratio.¹⁷ When the overall germanium content of a given sample is diluted by bulky ligands, the ^{73}Ge NMR sensitivity decreases even further. The germanium monohalides have an extremely high germanium content, which makes them attractive targets for ^{73}Ge SSNMR spectroscopy. ^{35}Cl and ^{79}Br possess much higher natural abundances and gyromagnetic ratios than germanium (Table 3.1); however, they remain challenging due to large quadrupole moments which give rise to very broad signals in the absence of perfect spherical symmetry. In this work, we employ solid-state ^{73}Ge , ^{35}Cl and ^{79}Br NMR spectroscopy complemented with density functional theory calculations in an effort to determine the structures of these novel main group halides.

Table 3.1 NMR properties of ^{35}Cl , ^{73}Ge and ^{79}Br .

Nucleus	I	Q (mb) ¹⁸	Natural Abundance (%)	$\gamma/10^7$ (radT ⁻¹ s ⁻¹)	Larmor Frequency at 21.1 T (MHz)
^{35}Cl	3/2	-81.65	76.78	2.624198	88.18
^{73}Ge	9/2	-196	7.76	0.9332	31.39
^{79}Br	3/2	313	50.69	6.725616	225.47

3.2 Results and Discussion

Initial investigations of the spectroscopic properties of the germanium monohalides were restricted to Raman spectroscopy (Figure 3.1) as the material does not diffract. Even recording the Raman spectra of the solids was challenging; attempts to obtain a spectrum

for GeCl were unsuccessful. The stretch at 290 cm^{-1} in the Raman spectrum of GeBr is consistent with a covalent Ge–Br bond.¹⁹ The remaining vibrations below 300 cm^{-1} can be assigned to Ge–Ge stretches, consistent with analogous assignments in Ge cluster compounds.^{20,21} While this does provide some information about the atomic connectivity of the material, the ability to deduce the structure from the Raman data alone was limited.

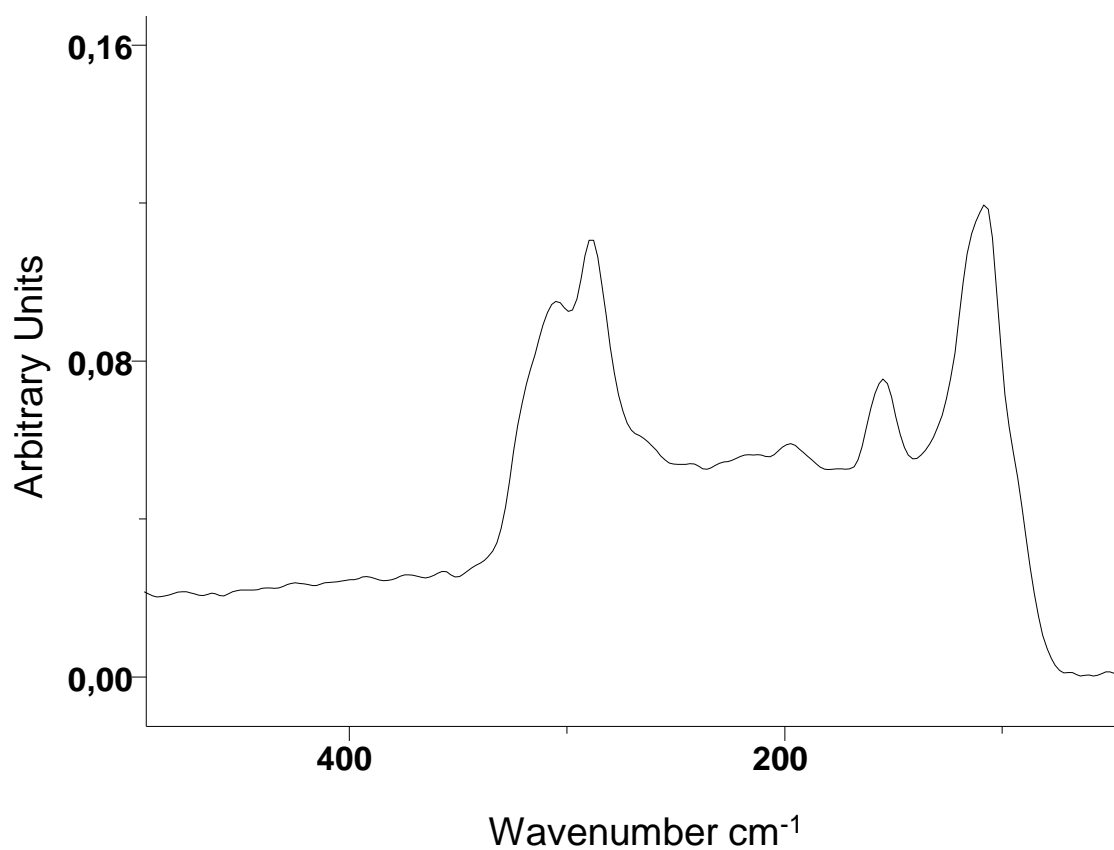


Figure 3.1 Raman spectrum of GeBr.

3.2.1 Solid-State NMR Spectroscopy

The ^{35}Cl , ^{73}Ge and ^{79}Br spectra of GeCl and GeBr all exhibit broad, featureless lines, indicating a highly disordered solid-state structure with many individual environments with slightly different NMR parameters contributing to the overall line shape. As expected from the lack of diffraction, the spectra more closely resemble those of typical

glasses rather than crystalline solids. A major challenge in the study of amorphous materials is the sensitivity of SSNMR parameters to small structural changes. A large distribution of NMR parameters will give broad, featureless lines which cannot be simulated using single values of C_Q and η_Q . As a consequence, we used QuadFit,²² a specialized program for disordered solids, to simulate the spectra with a Gaussian distribution of both parameters. Vitreous germanates are known to exhibit similarly featureless solid-state ^{73}Ge spectra.²³⁻²⁵ The experimental NMR parameters of GeCl and GeBr are summarized in Table 3.2.

Table 3.2 Summary of experimental SSNMR data of GeX X = Cl, Br.

Compound	Nucleus	C_Q Range (MHz)	η_Q Range	δ_{iso} (ppm)
GeCl	^{35}Cl	3.5-8.5	0.75-0.95	200
	^{73}Ge	6-22	0.8-1	-150
GeBr	^{79}Br	10-33	0.8-1	650
	^{73}Ge	16-26	0.8-1	-150

Even after overnight acquisition, the ^{73}Ge spectra of GeX (X = Cl, Br) were very noisy due to structural disorder combined with the inherent low NMR sensitivity of germanium. The featureless ^{73}Ge spectrum of GeCl (Figure 3.2) was fit by a Gaussian distribution of quadrupolar parameters. C_Q varied greatly, with the distribution being centred at 14 MHz and extending 8 MHz to either side. The large quadrupolar coupling constant indicates a low symmetry environment around germanium, as would be expected if GeCl contains Ge–Ge and Ge–Cl interactions. Germanium glasses doped with alkali cations exhibit quadrupolar coupling constants in a similar range (10.5-25 MHz).²⁴ Notably, in Ge–Se glasses, a similar quadrupolar interaction was observed from sites containing Ge–Ge linkages.²⁶ The monomodal nature of the distribution suggests that

while the exact structural metrics vary within the material, the overall connectivity is regular. In germanium selenide glasses, GeSe_4 units and tetrahedra containing Ge–Ge linkages gave readily resolved signals. If there was a small fraction of GeCl_4 units present, a second, sharper signal would be superimposed over the observed signal, which was not observed in the spectrum. The quadrupolar asymmetry parameter distribution ($\eta_Q = 0.9 \pm 0.1$) suggests that the symmetry is not close to axial.

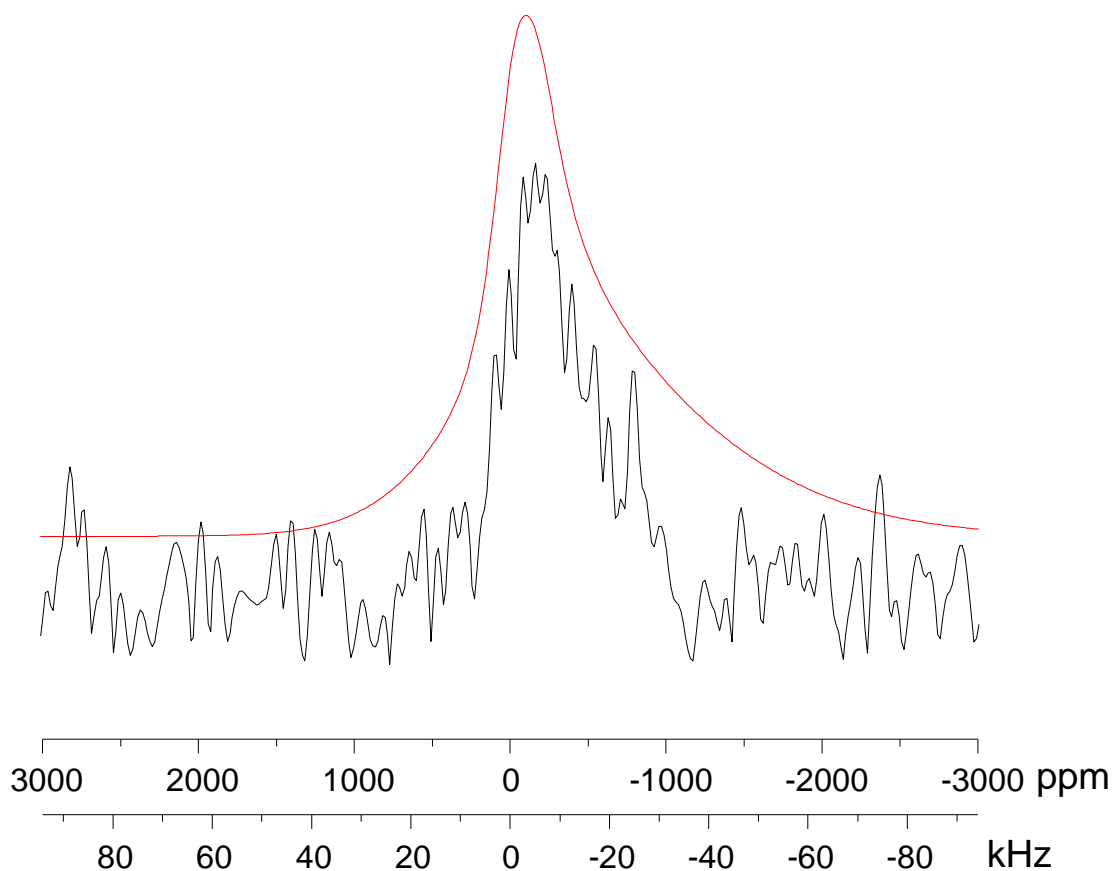


Figure 3.2 ^{73}Ge static echo NMR spectrum of GeCl . The spectrum was acquired overnight in 245670 transients with a 0.25 s recycle delay and an 8 ms acquisition time. The simulated fit is indicated by the solid trace.

While the ^{35}Cl SSNMR spectrum of GeCl exhibited a considerably better signal-to-noise ratio than the ^{73}Ge SSNMR spectrum due to the overall higher sensitivity of ^{35}Cl , it was

also featureless and monomodal (Figure 3.3). The isotropic shift, at 200 ppm, is consistent with a covalent, as opposed to an ionic chloride. Ionic chlorides tend to have a chemical shift below 150 ppm.²⁷⁻²⁹ The quadrupolar coupling constant range (3.5-8.5 MHz) is relatively small for chlorine, indicating that the chlorine centre must be sitting on a site of high symmetry. This is highly unusual for a covalently bound chloride. In ionic chlorides, such a low value corresponds to chloride in a distorted tetrahedral environment;³⁰ there are no documented cases of such a low quadrupolar coupling constant in a covalent chloride.

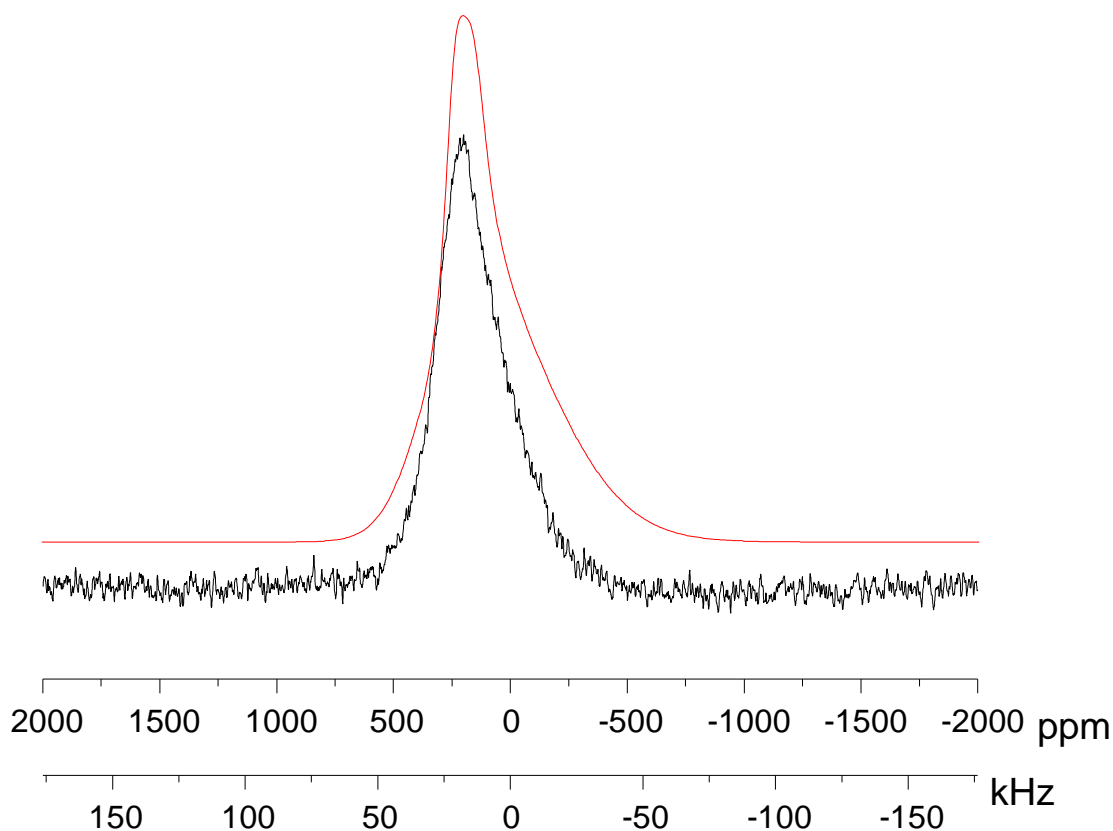


Figure 3.3 ^{35}Cl quadrupolar echo spectrum of GeCl at 21.1 T. The spectrum was acquired in 20480 transients with a recycle delay of 0.5 and an acquisition time of 16 ms. The simulated fit is indicated by a solid line.

The ^{79}Br SSNMR spectrum of GeBr (Figure 3.4) closely resembles the ^{35}Cl SSNMR spectrum of GeCl . The quadrupolar coupling constant distribution was centred at 16.5 MHz and spanned 6.5 MHz to either side. Due to the large quadrupole moment of ^{79}Br , this is considered to be a small C_Q range.²⁸ Given the relative magnitudes of the quadrupole moments of ^{35}Cl and ^{79}Br (Table 3.1), the data suggest that the environment around bromine in GeBr is very similar to that around chlorine in GeCl . The distribution of the quadrupolar asymmetry parameter ($\eta_Q = 0.9 \pm 0.1$) was also very similar to what was seen in the chloride analogue.

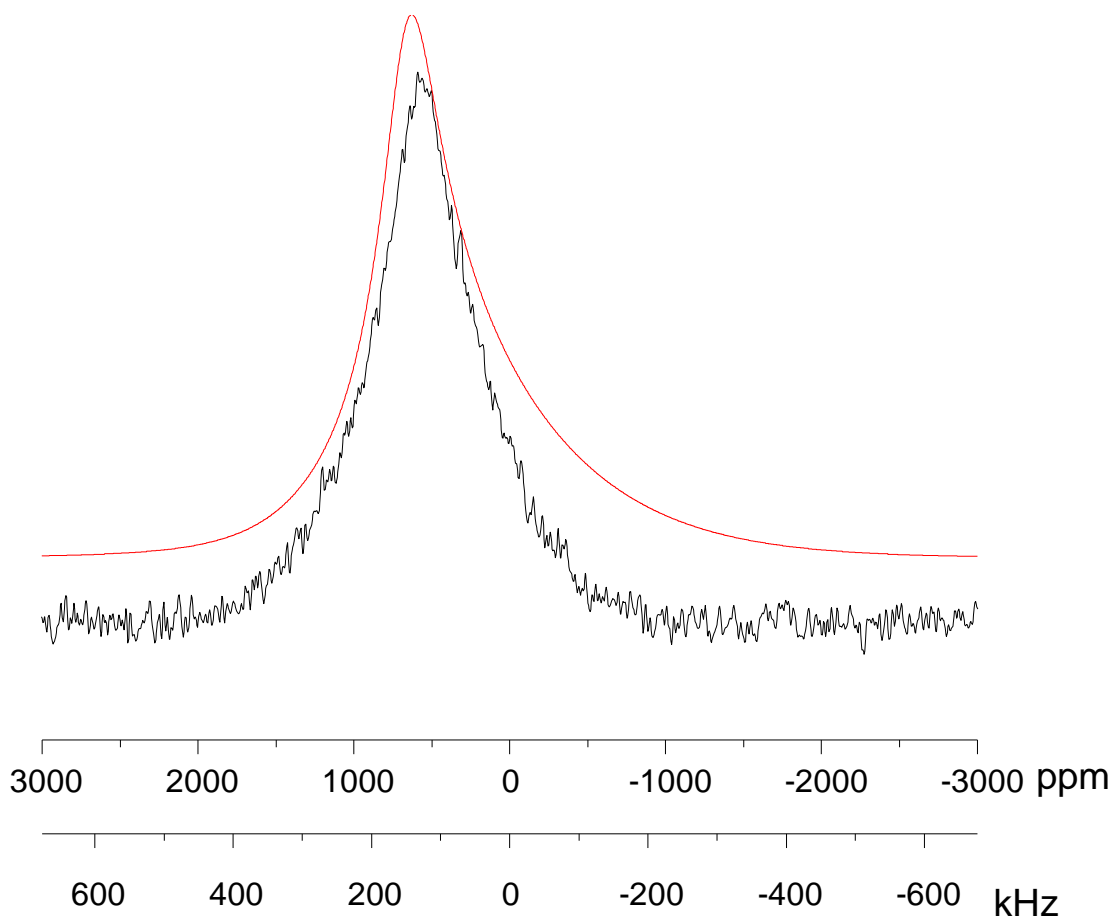


Figure 3.4 ^{79}Br quadrupolar echo spectrum of GeBr at 21.1 T. The spectrum was acquired over 20480 transients with a recycle delay of 0.25 s and an acquisition time of 1 ms. The simulated fit is indicated by a solid line.

The ^{73}Ge spectrum of GeBr (Figure 3.5) exhibited the same poor signal-to-noise ratio observed for the ^{73}Ge spectrum of GeCl . The spectrum was best fit with a C_Q distribution of 16 ± 10 MHz, which is similar to the value of 14 ± 8 MHz found for GeCl . The asymmetry distribution is once again $\eta_Q = 0.9 \pm 0.1$. The isotropic shift of 650 ppm does not offer the same insight as in the ^{35}Cl SSNMR spectrum as previous ^{79}Br SSNMR studies have only examined ionic bromides.²⁸

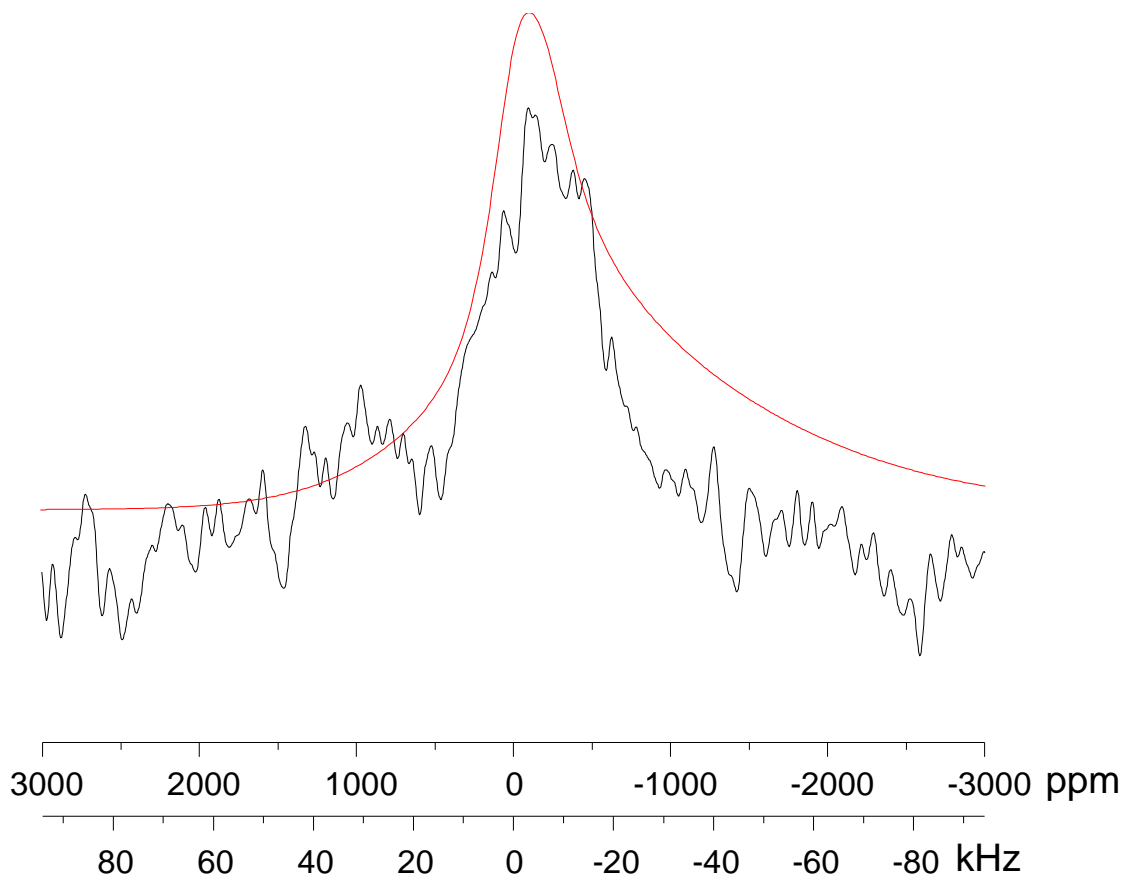


Figure 3.5 ^{73}Ge quadrupolar echo spectrum of GeBr at 21.1 T. The spectrum was acquired over 276480 transients with a 0.25 s recycle delay and an 8 ms acquisition time. The simulated fit is indicated by a solid line.

The similar ^{73}Ge distributions and the comparable parameters for the halogen spectra suggest that the two monohalides have similar structures. From the halogen spectra, it is apparent that chlorine and bromine must sit at sites of high symmetry. The isotropic shift of the ^{35}Cl signal of GeCl and the Raman spectrum of GeBr both suggest a covalent Ge-X bond rather than a simple ion pair as suggested by the GeX formula. Additionally, ion pairing is not a chemically reasonable description as it would involve a naked Ge cation. Cationic germanium is highly reactive and requires bulky ligands for isolation.³¹⁻³⁴ The broad, featureless spectra observed are consistent with a polymeric or oligomeric structure, rather than isolated small molecules.

3.2.2 Computational Investigations

Computational studies are increasingly used as a complement to spectroscopic data to obtain further structural insights. Previous studies of glasses have calculated the vibrational spectra of small clusters to reproduce the experimental Raman spectra, and thus, determine the presence or absence of various structural units in the overall glass structure.³⁵⁻³⁷ We attempted a similar approach with the ³⁵Cl and ⁷³Ge quadrupolar coupling constant to obtain a sense of the general structure of the monohalides. As GeCl and GeBr are expected to have very similar structures from the NMR data, all modelling was performed on GeCl to greatly reduce the computational time. Model clusters were built and the NMR parameters calculated in Gaussian 09.³⁸ The TPSS/6-311+G** method has previously been shown to produce good agreement with experimental ⁷³Ge and ³⁵Cl parameters and was used here. The results of the DFT calculations are summarized in Table 3.3.

Table 3.3 Summary of computational results.

Cluster	C_Q ³⁵Cl (MHz)	C_Q ⁷³Ge (MHz)
1	47.1	83.4
2	47.4	72.8
3	49.0	69.1
4	39.6	126.7
5	31.7	104.3
6	32.0	66.9
7	18.3	N/A
8	8.6	73.4
9	11.9	63.1
10	8.9	63.3
10b	6.5	53.0
Experiment	3.5-8.5	6-22

Covalently bound halides are most frequently found in a terminal position, which was used as a starting point for modelling the structure of the germanium monohalides. Possible structures (Figure 3.6) can be visualized by starting from the diamond lattice structure of the elemental material. One potential model involves cutting along the lattice and capping the dangling bonds with halogen atoms. The clusters were terminated with hydrogen atoms for computational simplicity. In the resulting structures, each germanium atom is bonded to three other germanium atoms for a final formula of GeCl . Germanium selenide glasses containing GeSe_4 tetrahedra generally have smaller (< 10 MHz) quadrupolar coupling constants.²⁶ As the C_Q values for GeCl and GeBr are greater than 10 MHz, the inclusion of Ge–Ge interactions in the clusters is logical. As further coordination spheres can have a dramatic effect on the EFG tensor, two different model clusters were derived from the diamond lattice structure. The simplest cluster (Figure 3.6, cluster **1**), containing four germanium atoms, gave a value of C_Q for the central germanium atom of 83.4 MHz, considerably greater than the experimental range (6-22 MHz). The one chlorine atom in the structure had a calculated C_Q of 47.1 MHz, also considerably larger than the experimental range ($^{35}\text{Cl } C_Q = 3.5\text{-}8.5$ MHz). The latter difference is more notable as theoretical calculations of ^{35}Cl NMR parameters are better developed than those for ^{73}Ge due to the greater variety of experimental data available for comparison. Extension into the second coordination sphere by including further branches for a total of 10 Ge atoms (Figure 3.6, cluster **2**) offers only minimal improvement, with a $^{73}\text{Ge } C_Q$ of 72.8 MHz and a similar value (47.4 MHz) for the $^{35}\text{Cl } C_Q$.

Alternately, a section of the lattice could be cut away, leaving a puckered six membered ring of germanium atoms. The dangling bonds can once again be capped with halogens

resulting in a structure consistent with the GeCl formula (Figure 3.6, cluster **3**). The puckered ring cluster does not offer an improvement in the agreement with the experimental value. While the calculated C_Q of ^{73}Ge is reduced to 69.1 MHz, the ^{35}Cl C_Q increases to 49.0 MHz. Clearly, while terminal environments are the most common for covalent chlorides, the germanium monohalides must involve a more symmetrical environment around Cl.

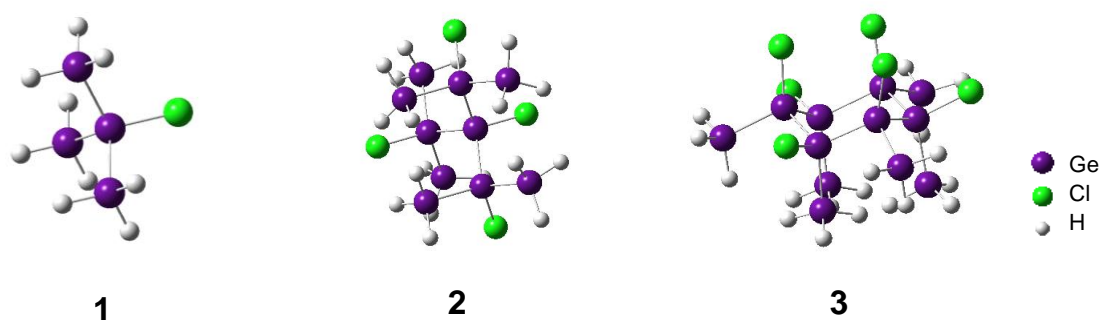


Figure 3.6 Clusters featuring chlorine in a terminal environment.

In an attempt to increase the symmetry at chlorine, three clusters of increasing complexity featuring chlorine in a bridging environment were constructed (Figure 3.7). The simplest structure (Figure 3.7, cluster **4**) features three pairs of germanium tetrahedra bridged by two Cl atoms while the more complex structures (Figure 3.7, clusters **5** and **6**) extend the chain in two dimensions. While the additional complexity did provide a modest reduction of the calculated ^{35}Cl C_Q value to 31.7 MHz in cluster **5**, the calculated value of C_Q value of ^{73}Ge increased to 104.3 MHz in the same cluster. Cluster **6** did not affect the value of the ^{35}Cl C_Q , but did reduce that of ^{73}Ge to 66.9 MHz, still in poor agreement with the experimental maximum of 22 MHz. Apparently, even greater

symmetry at chlorine is required in addition to increasing the symmetry about germanium.

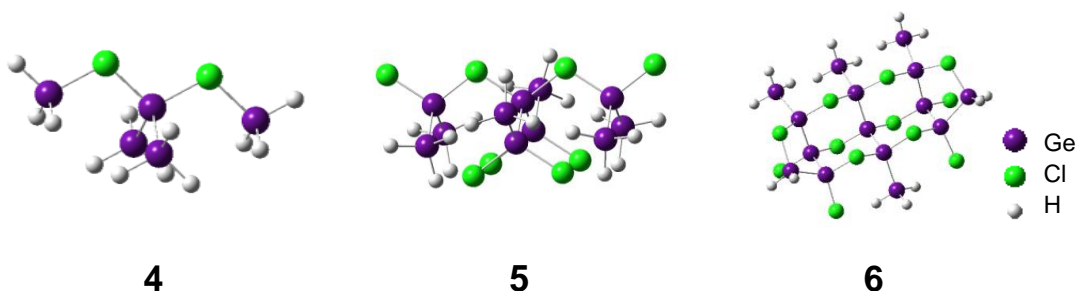


Figure 3.7 Computational clusters featuring chlorine in a bridging environment.

By building tetrahedral clusters centred around chlorine (Figure 3.8), the value of the ^{35}Cl C_Q was reduced to less than ten, suggesting that a tetrahedral environment at chlorine is the most reasonable model. There is only minimal distortion from ideal tetrahedral symmetry; hence the non-zero C_Q likely arises from variation in the higher coordination spheres. The ^{73}Ge C_Q was not calculated for the simplest cluster (Figure 3.8, cluster **7**) as the first coordination sphere of the germanium atoms were completed with hydrogen atoms not present in the experimental material. In the more complex clusters (Figure 3.8, clusters **8** and **9**), the inclusion of additional coordination spheres improved the value of the ^{73}Ge C_Q , dropping it from 73.4 to 63.1 MHz, which remains in poor agreement with experimental results.

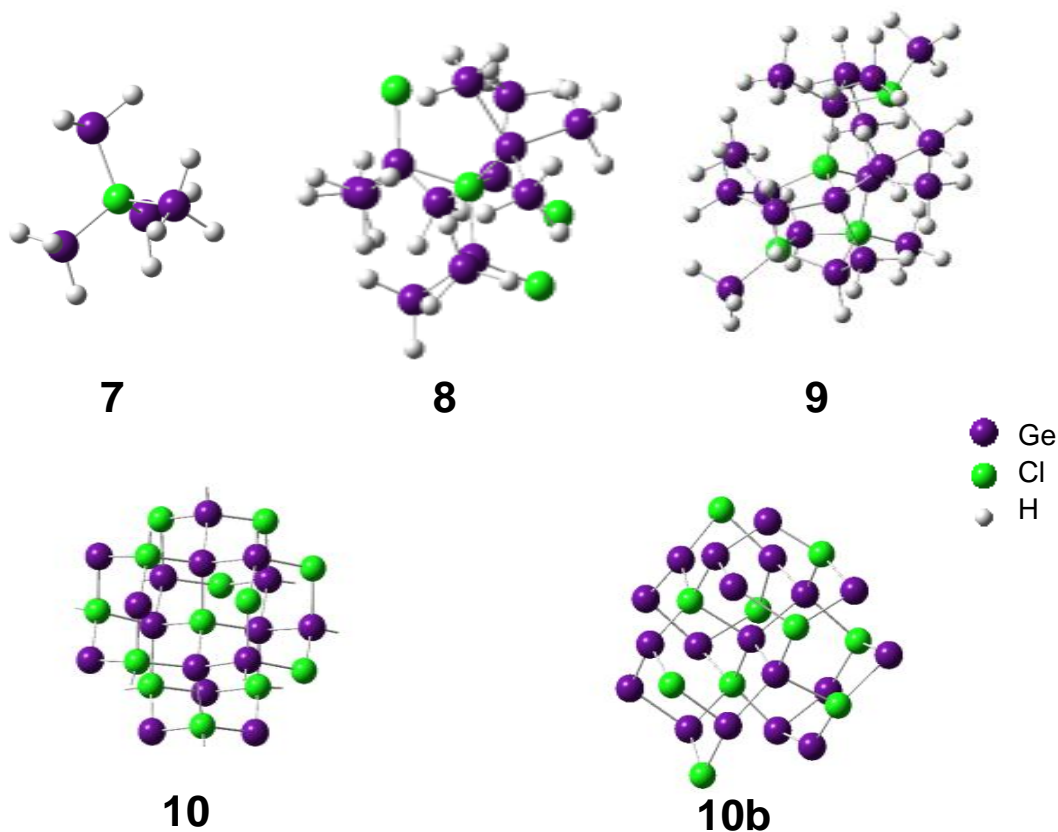


Figure 3.8 Clusters for calculations involving tetrahedral chlorine.

Full extension of the tetrahedral clusters in three dimensions leads back to the diamond lattice model. Rather than cutting into the lattice, the chlorine atoms were located in positions surrounded by germanium (Figure 3.8, cluster **10**). Germanium atoms were each bonded to two chlorine atoms and two germanium atoms, leading to an overall 1:1 ratio, and thus, an overall GeCl stoichiometry. Using an average Ge–Cl bond length of 2.5 Å, the C_Q of ^{35}Cl is 8.9 MHz, in reasonable agreement with the average experimental value of 5.5 MHz. The calculated value of the ^{73}Ge C_Q did not improve from the 63.1 MHz calculated for cluster **9**. However, if the cluster selected from the overall repeat unit places germanium rather than chlorine at the central position (Figure 3.8, cluster **10b**), the

calculated ^{73}Ge quadrupolar coupling constant drops to 53.0 MHz. While the calculated value is still not in good agreement with the experimental value, it is the best obtained in this study. The magnitude of the ^{35}Cl C_Q for cluster **10b** also dropped to its lowest calculated value at 6.5 MHz, well within the experimental range. If clusters **10** and **10b** were extended infinitely, the resulting structures would be identical as the only difference between the two is the precise section of the full lattice selected.

Previous investigations of germanium quadrupolar parameters have shown a relationship between the EFG tensor and both bond lengths and angles, with bond lengths proving to have a more dramatic effect on the magnitude of the EFG tensor.²³ The cluster was simplified to a simple germanium-centred tetrahedron due to the difficulty in altering the bond lengths of the full diamond lattice. Compression of the Ge–Cl bond length was found to decrease the magnitude of ^{73}Ge C_Q (Figure 3.9A). Elongation of the Ge–Ge bond, on the other hand, caused a similar decrease in ^{73}Ge C_Q (Figure 3.9B). When the two trends were examined together, the overall magnitude of ^{73}Ge C_Q was found to depend on the ratio between the two bond lengths (Figure 3.9C).

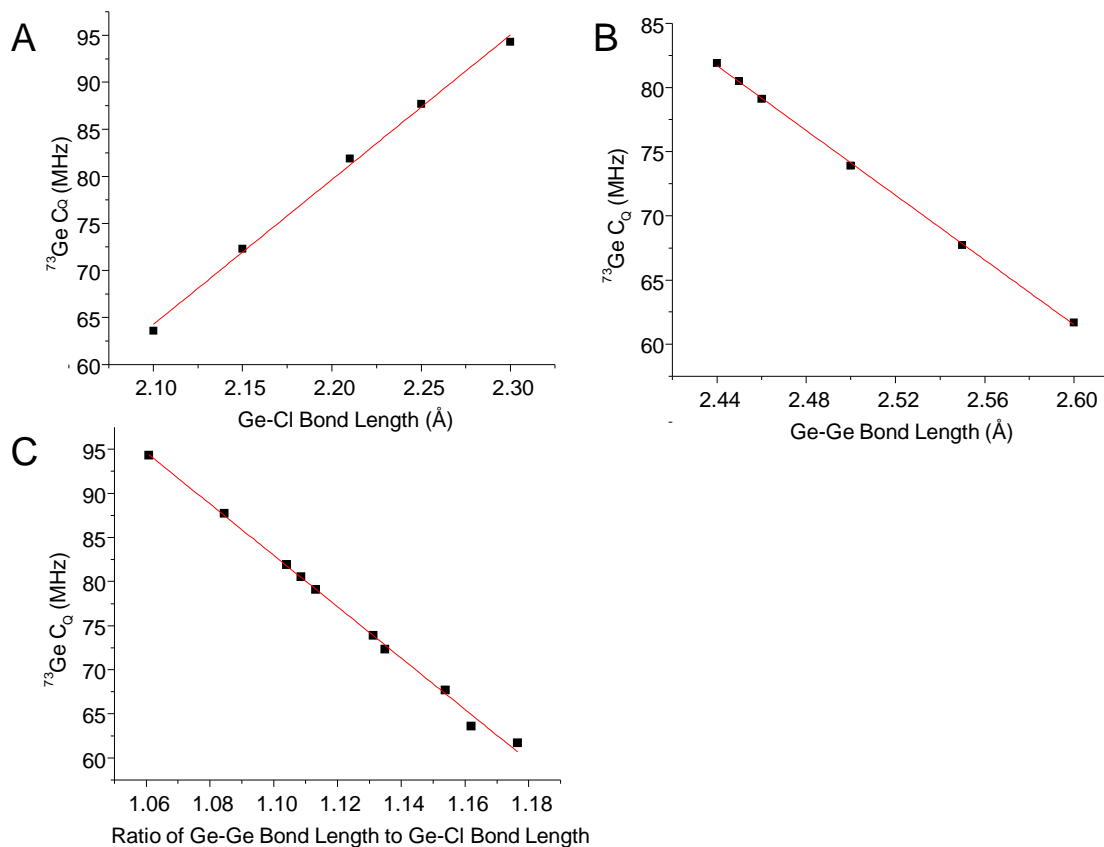


Figure 3.9 Relationships between A) Ge–Ge bond length B) Ge–Cl bond length and C) the ratio between the two bond lengths and the calculated value of C_Q for ^{73}Ge .

While the specific bond lengths must vary considerably, as demonstrated by the wide ranges found for each parameter, the calculations do suggest a general environment of a diamond lattice structure featuring one dimensional Ge–Ge chains connected by chlorine atoms. The chloride centres are surrounded on all sides by germanium. The Ge–Cl bonds are relatively short in comparison to typical bond lengths. On the other hand, the Ge–Ge bonds are considerably longer than more typical covalent bonds. While a classical Ge–Ge bond is typically 2.45 Å, in germanium(IV) chemistry,⁴⁰ we predict the Ge–Ge distances in the monohalides to be approximately 2.7 Å long, consistent with the long (>2.6 Å) bonds seen in cluster compounds.^{20,41} Further refinement of the structure was not possible due to the large number of variables with insufficient constraints.

3.3 Conclusions

As expected from the inability to obtain X-ray diffraction data, both GeCl and GeBr are amorphous, glasslike materials. From the ^{73}Ge spectra, it is apparent that the two compounds possess very similar structures. From the ^{35}Cl data, it can be concluded that the halogens are covalently bound to germanium and sit at a site of distorted tetrahedral symmetry. Density functional theory calculations on model clusters suggest that a reasonable structure for these unusual materials is a diamond lattice with linear Ge–Ge chains connected by bridging chlorine atoms. The overall GeCl stoichiometry is most readily observed by the alternation of germanium and chlorine in the six membered rings formed in the diamond lattice. The overall distribution of parameters likely arises from variations in both bond angles and bond lengths leading to individual sites being in slightly different environments.

3.4 Experimental

3.4.1 Materials

GeCl and GeBr were prepared by Andreas Schnepf according to literature procedures.¹³

3.4.2 Solid-State NMR Spectroscopy

^{73}Ge , ^{35}Cl and ^{79}Br spectra were collected on a Bruker Avance 900 MHz spectrometer at the National Ultrahigh-field NMR Facility for Solids in Ottawa, Ontario, Canada. Pulse width calibrations were performed on the reference compounds given in Table 3.4.

Spectra were acquired under static conditions on a dual channel 7 mm low gamma probe operating in single resonance mode. A quadrupolar echo experiment of the form $\pi/2-\tau-$

$\pi/2$ -acquire was employed for all spectra. Full acquisition parameters are given in Table 3.4.

Table 3.4 Solid-state NMR acquisition parameters.

Spectrum	Reference Compound	Pulse Width (μ s)	Recycle Delay (s)	# scans	τ (μ s)	Acquisition time (ms)
GeCl (^{35}Cl)	1 M KCl _(aq) ^a	6	0.5	20480	9.4	16
GeCl (^{73}Ge)	GeCl ₄ ^b	4	0.25	245670	15.6	8
GeBr (^{79}Br)	KBr ^c	2	0.25	20480	2.8	1
GeBr (^{73}Ge)	GeCl ₄ ^b	4	0.25	276480	15.6	8

^a 0 ppm relative to 0.1 M NaCl in H₂O at 0 ppm

^b 30.9 ppm relative to GeMe₄ at 0 ppm

^c 54 ppm relative to 0.1 M KBr in H₂O at 0 ppm

3.4.3 Spectral Simulations

Spectral simulations were performed using QuadFit²² with a Gaussian distribution of both the quadrupolar coupling constant and the quadrupolar asymmetry parameter. Isotropic shifts were assumed to be constant for all geometries to minimize the number of calculations required. Lines of best fit were determined by visual comparison to the experimental spectrum combined with the built in iteration algorithm.

3.4.4 Theoretical Calculations

Model clusters were constructed in GaussView 4. Theoretical calculations were performed using Gaussian 09³⁸ on the Shared Hierarchical Academic Research Computing Network (SHARCNET). Calculations were performed on an 8 core Xeon 2.83 GHz CPU with 16 GB memory. All calculations employed the TPSSSTPSS³⁹ functional with a 6-311+G** basis set on all atoms. The results of the Gaussian calculations were then analyzed using EFGShield.⁴²

3.5 References

- (1) Henderson, E. J.; Veinoit, J. G. C. *Chem. Mater.* **2007**, *19*, 1886.

- (2) Li, A. P.; Flack, F.; Lagally, M. G.; Chisholm, M. F.; Yoo, K.; Zhang, Z.; Weitering, H. H.; Wendelken, J. F. *Phys. Rev. B* **2004**, *69*, 245310.
- (3) Schnepf, A. *Coord. Chem. Rev.* **2006**, *250*, 2758.
- (4) Schnöckel, H. *Dalton Trans.* **2005**, *19*, 3131.
- (5) Schnepf, A. *Angew. Chem.* **2004**, *116*, 680.
- (6) Schnepf, A. *Angew. Chem. Int. Ed.* **2004**, *43*, 664.
- (7) Schnepf, A. *New J. Chem.* **2010**, *34*, 2079.
- (8) Warner, J. H. *Nanotechnology* **2006**, *17*, 5613.
- (9) Weidenbruch, M. *Eur. J. Inorg. Chem.* **1999**, 373.
- (10) Nagendran, S.; Roesky, H. W. *Organometallics* **2008**, *27*, 457.
- (11) Mizuhata, Y.; Sasamon, T.; Tokitoh, N. *Chem. Rev.* **2009**, *109*, 3479.
- (12) Schnepf, A. *Phosphorus, Sulfur Silicon Relat. Elem.* **2004**, *179*, 695.
- (13) Schnepf, A.; Koppe, R. *Z. Anorg. Allg. Chem.* **2002**, *628*, 2914.
- (14) Schenk, C.; Henke, F.; Schnepf, A. *Phosphorus, Sulfur Silicon Relat. Elem.* **2011**, *186*, 1370.
- (15) MacKenzie, K. J. D.; Smith, M. E. In *Multinuclear Solid-State NMR of Inorganic Materials*; MacKenzie, K. J. D., Smith, M. E., Eds.; Pergamon: Kidlington, **2002**, p 1.
- (16) Taulelle, F. In *NMR Crystallography*; Harris, R. K., Wasylishen, R. E., Duer, M. J., Eds.; John Wiley & Sons: Chichester, **2009**, p 245.
- (17) Takeuchi, Y.; Takayama, T. *Annu. Rep. NMR Spectrosc.* **2005**, *54*, 155.
- (18) Pykko, P. *Mol. Phys.* **2008**, *106*, 1965.

- (19) Nakamoto, K. In *Infrared and Raman Spectra of Inorganic and Coordination Compounds Part A*; 6 ed.; Wiley: Hoboken, **2009**, p 288.
- (20) Curda, J.; Carillo-Cabrera, W.; Schmeding, A.; Peters, K.; Somer, M.; von Schnering, H. G. *Z. Anorg. Allg. Chem.* **1997**, *623*, 929.
- (21) Somer, M.; Carrillo-Cabrera, W.; Peters, E. M.; Peters, K.; Von Schnering, H. G. *Z. Anorg. Allg. Chem.* **1998**, *624*, 1915.
- (22) Kemp, T. F.; Smith, M. E. *Solid State Nucl. Magn. Reson.* **2009**, *35*, 243.
- (23) Michaelis, V. K.; Aguiar, P. M.; Terskikh, V. V.; Kroeker, S. *Chem. Commun.* **2009**, 4660.
- (24) Michaelis, V. K.; Kroeker, S. *J. Phys. Chem. C* **2010**, *114*, 21736.
- (25) Stebbins, J. F.; Du, L.-S.; Kroeker, S.; Neuhoff, P.; Rice, D.; Frye, J.; Jakobsen, H. J. *Solid State Nucl. Magn. Reson.* **2002**, *21*, 105.
- (26) Sen, S.; Gan, Z. *J. Non-Cryst. Solids* **2010**, *356*, 1519.
- (27) Bryce, D. L.; Sward, G. D. *Magn. Reson. Chem.* **2006**, *44*, 409.
- (28) Widdifield, C. M.; Chapman, R. P.; Bryce, D. L. *Annu. Rep. NMR Spectrosc.* **2009**, *66*, 195.
- (29) Chapman, R. P.; Widdifield, C. M.; Bryce, D. L. *Prog. Nucl. Magn. Reson. Spectrosc.* **2009**, *55*, 215.
- (30) Bryce, D. L.; Bultz, E. B. *Chem.-Eur. J.* **2007**, *13*, 4786.
- (31) Rugar, P. A.; Staroverov, V. N.; Baines, K. M. *Science* **2008**, 1360.
- (32) Rugar, P. A.; Bandyopadhyay, R.; Cooper, B. F. T.; Stinchcombe, M. R.; Ragona, P. J.; Macdonald, C. L. B.; Baines, K. M. *Angew. Chem. Int. Ed.* **2009**, *48*, 5155.

- (33) Cheng, F.; Hector, A. L.; Levason, W.; Reid, G.; Webster, M.; Zhang, W. *Angew. Chem. Int. Ed.* **2009**, *48*, 5152.
- (34) Levason, W.; Reid, G.; Zhang, W. *Coord. Chem. Rev.* **2011**, *255*, 1319.
- (35) Cuisset, A.; Hindle, F.; Laureyns, J.; Bychkov, E. *J. Raman Spectrosc.* **2010**, *41*, 1050.
- (36) Grisolíá, M.; Rincón, L.; Almeida, R. *J. Mol. Struct.: THEOCHEM* **2006**, *769*, 143.
- (37) Kassim, H. A.; Jalil, I. A.; Yusof, N.; Devi, V. R.; Shrivastava, K. N. *J. Non-Cryst. Solids* **2007**, *353*, 111.
- (38) Frisch, M. J.; Trucks, G. W.; Schlegel, H. B.; Scuseria, G. E.; Robb, M. A.; Cheeseman, J. R.; Scalmani, G.; Barone, V.; Mennucci, B.; Petersson, G. A.; Nakatsuji, H.; Caricato, M.; Li, X.; Hratchian, H. P.; Izmaylov, A. F.; Bloino, J.; Zheng, G.; Sonnenberg, J. L.; Hada, M.; Ehara, M.; Toyota, K.; Fukuda, R.; Hasegawa, J.; Ishida, M.; Nakajima, T.; Honda, Y.; Kitao, O.; Nakai, H.; Vreven, T.; Montgomery, J., J. A.; Peralta, J. E.; Ogliaro, F.; Bearpark, M.; Heyd, J. J.; Brothers, E.; Kudin, K. N.; Staroverov, V. N.; Kobayashi, R.; Normand, J.; Raghavachari, K.; Rendell, A.; Burant, J. C.; Iyengar, S. S.; Tomasi, J.; Cossi, M.; Rega, N.; Millam, N. J.; Klene, M.; Knox, J. E.; Cross, J. B.; Bakken, V.; Adamo, C.; Jaramillo, J.; Gomperts, R.; Stratmann, R. E.; Yazyev, O.; Austin, A. J.; Cammi, R.; Pomelli, C.; Ochterski, J. W.; Martin, R. L.; Morokuma, K.; Zakrzewski, V. G.; Voth, G. A.; Salvador, P.; Dannenberg, J. J.; Dapprich, S.; Daniels, A. D.; Farkas, Ö.; Foresman, J. B.; Ortiz, J. V.; Cioslowski, J.; Fox, D. J.; Revision A1 ed.; Gaussian Inc.: Wallingford, CT, **2009**.

- (39) Tao, J.; Perdew, J. P.; Staroverov, V. N.; Scuseria, G. E. *Phys. Rev. Lett.* **2003**, *91*, 146401.
- (40) Weinert, C. S. In *Comprehensive Organometallic Chemistry III*; Housecroft, C. E., Ed.; Elsevier: Oxford, **2007**; Vol. 3, p 700.
- (41) Campbell, J.; Schrobilgen, G. J. *Inorg. Chem.* **1997**, *36*, 4078.
- (42) Adiga, S.; Aebi, D.; Bryce, D. L. *Can. J. Chem.* **2007**, *85*, 496.

Chapter 4 Chlorine-35 SSNMR Spectroscopy as an Indirect Probe of Germanium Compounds

4.1 Introduction

In a recent paradigm shift, low valent and cationic germanium compounds have been recognized to show greater similarity to the chemistry of transition metal complexes compared to traditional organic chemistry.¹ Within this field, there is a rich variety of neutral and cationic complexes of the divalent germanium halides to explore in this context.² Undoubtedly, the lone pair and empty p-orbital on germanium(II) compounds and the ability to isolate stable derivatives has led to an interest in these complexes. Preliminary investigation into the reactivity of low valent germanium has demonstrated reversible reaction with small molecules, leading to potential applications in catalysis without expensive transition metals. The most important tool for characterization of germanium(II) halide complexes has, thus far, been X-ray crystallography.² While single crystal diffraction provides valuable structural information, there is a continuing need to expand the range of available spectroscopic tools for the characterization of these novel compounds.

A major obstacle to the study of new germanium compounds, such as donor complexes and cations of germanium(II), is the extreme difficulty in performing ^{73}Ge NMR spectroscopic experiments. While ^{13}C , ^{29}Si , ^{119}Sn and ^{207}Pb are all relatively routine nuclei for NMR spectroscopy, germanium possesses considerably less favourable NMR properties. While the other group 14 elements possess at least one spin $\frac{1}{2}$ isotope, ^{73}Ge is quadrupolar with a spin of $\frac{9}{2}$ and has a moderate quadrupole moment of -19.6 mb .³ Germanium-73 also possesses a low natural abundance (7.76%); however, the greatest

challenge is that germanium has one of the smallest gyromagnetic ratios in the periodic table, corresponding to a Larmor frequency of only 31.4 MHz at 21.1 T.

While ^{73}Ge is a challenging nucleus, new sensitivity enhancement pulse sequences and higher field instruments have made it accessible under favourable conditions of either high symmetry at germanium or high germanium content in the sample. However, in addition to low symmetry systems being far more common, many interesting germanium compounds are kinetically stabilized by bulky ligands. Consequently, the overall germanium content in a given volume can be quite low, with lower concentrations leading to lower signal-to-noise ratios much like in solution.

Due to the prevalence of Ge–Cl bonds in low valent germanium chemistry, we are interested in exploring solid-state ^{35}Cl NMR spectroscopy as an indirect method for obtaining information about germanium. To assess chlorine as a potential source of information, we chose to undertake a systematic investigation of various compounds containing Ge–Cl bonds to determine what information about the germanium centre might be determined from the ^{35}Cl NMR parameters. To fully examine the scope of the technique, we included examples of both germanium(II) and more the prevalent germanium(IV) compounds

^{35}Cl has a spin of $3/2$ and a large quadrupole moment ($Q = -81.7 \text{ mb}$), which rapidly leads to extremely broad NMR signals in the absence of spherical symmetry.⁴ While ^{35}Cl is considered to be low gamma with a Larmor frequency of 88.1 MHz at 21.1 T, a natural abundance of 75% leads to reasonable sensitivity. Extremely broad quadrupole NMR spectra are much more easily acquired at ultrahigh ($>18.8 \text{ T}$) magnetic field due to the

inverse relationship between second order quadrupolar broadening and field strength. Additionally, the study of these nuclei has benefited greatly from the use of QCPMG⁵ and related pulse sequences.⁶⁻⁸ In particular, adiabatic WURST pulses have greatly improved the excitation profile of the QCPMG sequence.⁹ While stepwise spectral acquisition is often still required, the overall number of subspectra required is greatly reduced, thereby shortening the total acquisition time by a considerable amount. Through a combination of these two techniques, it has become increasingly more common to study chlorine in a covalent environment in addition to simple ionic inorganic chlorides. Several recent reviews on ³⁵Cl NMR spectroscopy have been published.¹⁰⁻¹² Particularly notable is an investigation by Bryce of organic chlorides featuring chlorine covalently bound to carbon, which gave rise to very large quadrupolar coupling constants ($C_Q = 66-75$ MHz).¹³ The only published example of ³⁵Cl NMR spectroscopy of a germanium compound examined GeCl₂.¹⁴ A single narrow signal was observed under static conditions with an estimated C_Q of less than 40 kHz. GeCl₂ does not have a known crystal structure, and had previously been proposed to be similar in structure to the distorted octahedral GeBr₂. However, the combined ³⁵Cl and ⁷³Ge data suggest a structure similar to the regularly octahedral GeI₂, with high symmetry at both germanium and chlorine and a single halogen site.

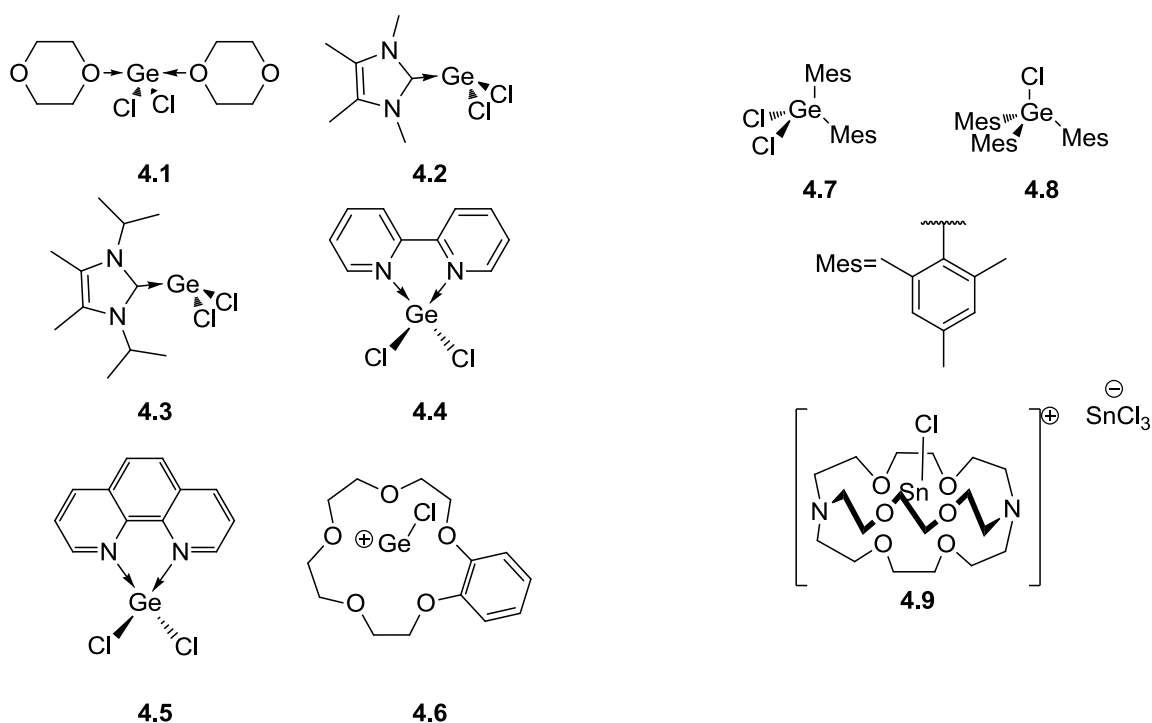


Figure 4.1 Germanium and tin chlorides examined in this study.

We have investigated a variety of germanium chlorides (Figure 4.1). The majority of the germanium(II) compounds investigated can be described as GeCl_2 stabilized by a donor. Solid-state NMR parameters are strongly influenced by structure and thus, the most prominent structural features of the germanium chlorides **4.1-4.6** are reviewed here.

While GeCl_2 is a nominally stable germylene, it is only isolated in a polymeric form.¹⁵ A more convenient starting material for the synthesis of germanium(II) compounds is germanium dichloride complexed with dioxane ($\text{GeCl}_2 \cdot \text{dioxane}$, **4.1**).¹⁶ This complex is readily synthesized from GeCl_4 ¹⁷ and is stable indefinitely under inert conditions. The complex is a coordination polymer composed of infinite chains of alternating GeCl_2 and dioxane units. There is one crystallographically unique germanium site (C_2 symmetry) and one unique chlorine site (C_s symmetry). The germanium atom has two strong covalent bonds to chlorine atoms ($\text{Ge}-\text{Cl}$ bond length = 2.281 Å) and two weak

coordinate covalent bonds to the oxygen of the dioxane (Ge–O distance = 2.3999 Å; a typical Ge–O bond length falls in the range of 1.75–1.85 Å¹⁸). Additionally, there are two non-bonded chlorine atoms found at a distance of 3.463 Å from the adjacent Ge, resulting in an overall pseudo-octahedral geometry at germanium and a pseudo-bridging environment for chlorine (Figure 4.2).

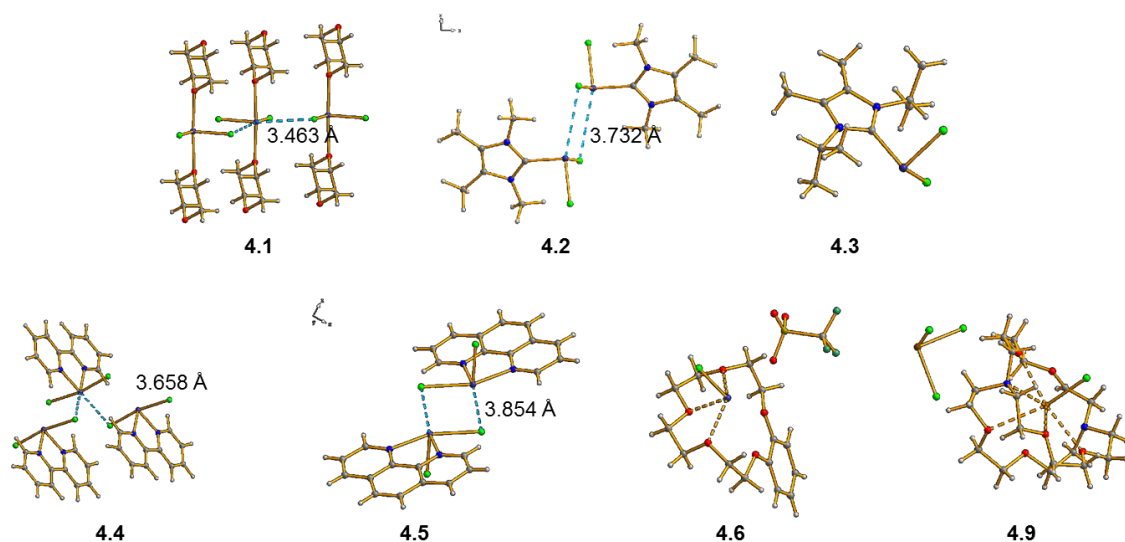


Figure 4.2 X-ray structures of compounds **4.1–4.6** and **4.9** showing the long range interactions between chlorine and germanium in **4.1**, **4.2**, **4.4** and **4.5**.

Two N-heterocyclic carbene (NHC) complexes of GeCl₂ (**4.2** and **4.3**)¹⁹ were included in the investigation. Attempts to acquire ⁷³Ge SSNMR spectra of these complexes at 21.1 T were unsuccessful even after extended acquisition times (See Chapter 2, section 2.2.5).

The difficulties in obtaining a ⁷³Ge spectrum were attributed to a combination of low molecular symmetry and low overall germanium concentration in the sample due to the size of the ligands. Complex **4.2**, with methyl groups on the nitrogen of the NHC ligand, features a long range (3.732 Å) interaction between chlorine of one complex and the germanium of the adjacent molecule (Figure 4.2). With larger isopropyl groups on

nitrogen, as in complex **4.3**, the complexes are not in close enough proximity to each other for a chloride to interact with the germanium of an adjacent complex (shortest $\text{Ge}_{(\text{adjacent})}\text{-Cl}$ distance $> 6.9 \text{ \AA}$), leading to a truly terminal environment for the chloride.

Two GeCl_2 complexes with neutral nitrogen donors, 2,-2'-bipyridine (**4.4**) and 1,10-phenanthroline (**4.5**), were also investigated.²⁰ The bipyridine complex **4.4** resembles $\text{GeCl}_2\cdot\text{dioxane}$ in that a long range Ge-Cl contact (3.6582 \AA) leads to a pseudooctahedral environment at germanium. Unlike $\text{GeCl}_2\cdot\text{dioxane}$, the covalent Ge-Cl bonds in the bipyridine complex are different lengths ($\text{Ge-Cl}(1) = 2.5428 \text{ \AA}$ and $\text{Ge-Cl}(2) = 2.7195 \text{ \AA}$) leading to two crystallographically distinct chlorine sites. By contrast, the phenanthroline complex **4.5** is a weakly associated centrosymmetric dimer with one terminal chloride site ($\text{Ge-Cl} = 2.3145 \text{ \AA}$) and the other chloride ($\text{Ge-Cl} = 2.6276 \text{ \AA}$) forming a weak bridging interaction (Figure 4.2).

The final germanium(II) complex investigated is a cationic species stabilized by benzo-15-crown-5 (**4.6**).²¹ In this case, the single chloride is in a terminal position, with a Ge-Cl bond length of 2.288 \AA and no interaction with the adjacent ions. While a series of cationic crown ether complexes is known,^{21,22} the benzo-15-crown-5 derivative was specifically selected for this study because the counterion is triflate rather than GeCl_3^- , simplifying the expected ^{35}Cl NMR spectrum.

As the +4 oxidation state is far more common in germanium chemistry, two germanium(IV) compounds were also investigated. The two related compounds, dichlorodimesitylgermane (**4.7**) and chlorotrimesitylgermane (**4.8**) are, given the large size of the mesityl group, believed to feature chlorine in a terminal environment as is

typical in germanium(IV) chemistry.¹⁸ Both compounds represent prototypical germanium(IV) chlorides. Neither of these compounds has a known crystal structure.

The final compound examined, a cationic cryptand complex of tin chloride (**4.9**) represents the beginning of a larger exploration of group 14 chlorides. While a cryptand is used instead of a crown ether, **4.9**, is in general terms, quite similar to **4.6**: a macrocyclic ether is used to stabilize a reactive group 14 cation in the +2 oxidation state. As would be expected for a larger atom, the Sn–Cl bond length (2.532 Å) is notably longer than what was observed for the germanium cation.

4.2 Results

4.2.1 Solid-State NMR Spectroscopy

A summary of the experimental results is presented in Table 4.1. The ³⁵Cl SSNMR spectra of the complexed germylenes in this study differed considerably from that of uncomplexed GeCl₂.¹⁴ While GeCl₂ gave rise to remarkably narrow lines, the spectra in this study are more typical of terminal chlorides with pronounced quadrupolar lineshapes. The environment around germanium has a clear impact on the ³⁵Cl NMR parameters, particularly those in which a substituent on germanium disrupts the symmetry at chlorine.

Table 4.1 Summary of experimental ^{35}Cl SSNMR parameters

Compound	δ_{iso} (ppm)	C_Q (MHz)	η_Q	Ω (ppm)	κ
4.1	300(50)	28.3(1)	0.055(10)	250(100)	1
4.2	200(50)	29.3(1)	0.12(2)	300(100)	1
4.3	150(50)	28.6(3)	0.23(5)	<i>n.o.</i> ^a	<i>n.o.</i> ^a
4.4	250(50)	15.0(1)	0.10	<i>n.o.</i> ^a	<i>n.o.</i> ^a
	250(50)	10.8(1)	0.20(2)	250(100)	0
4.5	250(50)	13.8(1)	0.15(2)	200(100)	0
4.6	300(50)	25.1(1)	0.10(2)	350(100)	1
4.7	200(100)	43.0(5)	0.1(1)	<i>n.o.</i> ^a	<i>n.o.</i> ^a
4.8	200(100)	41.5(5)	0	<i>n.o.</i> ^a	<i>n.o.</i> ^a
4.9	200(50)	19.0(1)	0.15(5)	<i>n.o.</i> ^a	<i>n.o.</i> ^a

^a *n.o.* = not observed

The ^{35}Cl SSNMR spectrum of **4.1** provides an excellent illustration of the advantages of the WURST-QCPMG pulse sequence over the simple QCPMG sequence. The QCPMG spectrum of **4.1** (Figure 4.3A) required the acquisition of 13 individual subspectra at 100 kHz offset over a total of nine hours. The use of the WURST-QCPMG sequence (Figure 4.3B) reduced the number of subspectra required to two and the total acquisition time to 45 minutes. Additionally, the overall lineshape of the co-added spectrum was much smoother using the WURST-QCPMG spectrum, making the central discontinuity much easier to observe.

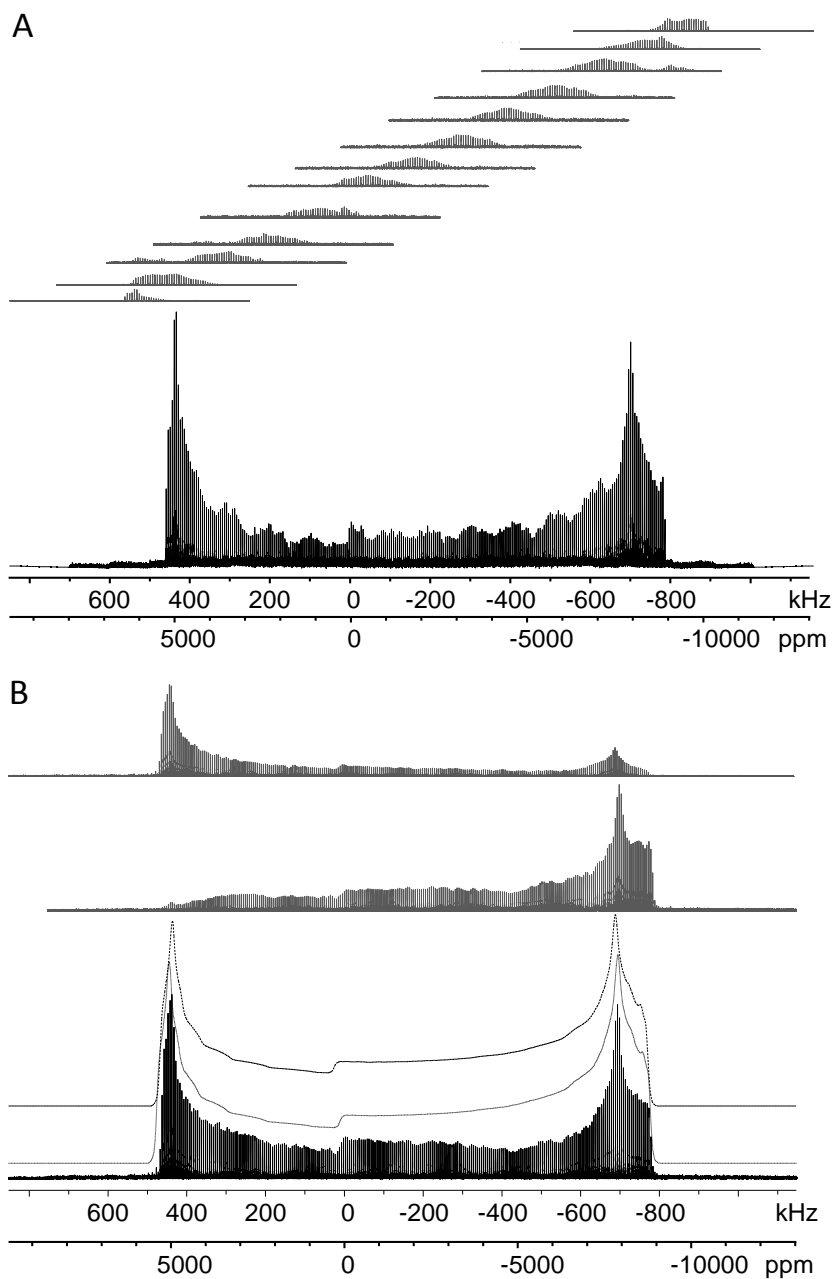


Figure 4.3 A) Individual ^{35}Cl static QCPMG subspectra (offset= 100 kHz) and co-added spectrum of GeCl_2 -dioxane. B) Individual static WURST-QCPMG subspectra (no offset, but opposite sweep directions) and coadded spectrum. of GeCl_2 -dioxane at 21.1 T. The dashed trace indicates the empirical simulation accounting for only the EFG interaction. The dotted trace indicates the simulation including CSA.

Although the quadrupolar interaction with the electric field gradient (EFG) is the dominant interaction for ^{35}Cl , it was not possible to accurately reproduce all features of

the spectrum of GeCl_2 -dioxane without including chemical shielding anisotropy (CSA) (Figure 4.3B). Proper positioning of the central discontinuity of the spectrum required a span of approximately 250 ppm ($\kappa = 1$). The quadrupolar coupling constant of 28.3 MHz is consistent with the low symmetry environment around chlorine.²³ This value falls within the range previously observed for group 13 chlorides.²⁴ The quadrupolar asymmetry parameter ($\eta_Q=0.055$) corresponds to an essentially axially symmetric environment. Terminal chlorides tend to have values of η_Q much closer to zero than bridging ligands,^{25,26} suggesting that the long range interaction observed in the X-ray structure of **4.1**²³ is not sufficient to disrupt the overall symmetry of the EFG tensor.

While the two NHC complexes of GeCl_2 (**4.2** and **4.3**) are extremely similar in structure, the ^{35}Cl SSNMR spectra exhibit distinct differences (Figure 4.4). Complex **4.2** has a somewhat broader ^{35}Cl spectrum than GeCl_2 -dioxane, with a C_Q value of 29.3 MHz. To fit the spectra of **4.2** acquired at 9.4 T (Appendix 1, Figure A1.1) and 21.1 T accurately with the same parameters, a small amount of CSA interaction ($\Omega = 300$ ppm) must be included. The sharp signal around 0 ppm in both spectra is likely the hydrochloride salt of the NHC carbene arising as a decomposition product due to the air and moisture sensitivity of these compounds. The considerably poorer signal-to-noise ratio of **4.3** can be attributed to the shorter T_2 relaxation leading to decreased signal enhancement from the WURST-CPMG pulse sequence. While echoes can be observed on the FID of **4.2** until 10 ms, the signal for **4.3** decays by 3 ms. The rapid relaxation likely arises from mobility in the isopropyl groups. The spectrum of **4.3** was fit with $C_Q = 28.6$ and $\eta_Q = 0.23$. Due to the poor signal-to-noise ratio, it was not possible to determine any contributions from CSA.

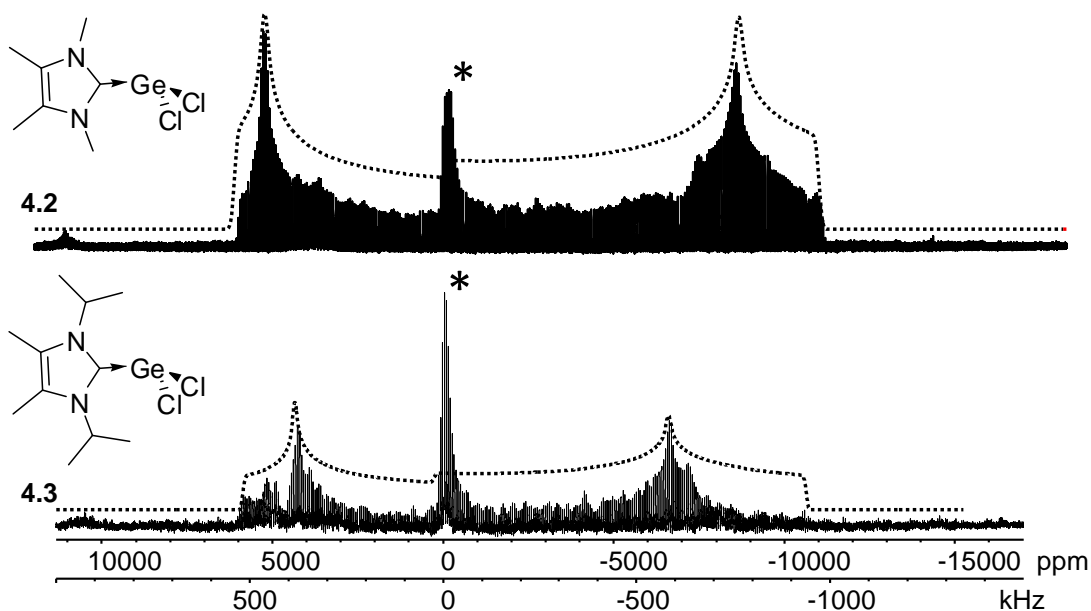


Figure 4.4 Static ^{35}Cl WURST-QCPMG spectra of **4.2** (top) and **4.3** (bottom) at 21.1 T. Dotted traces indicate empirical simulations. An impurity of the hydrochloride salt of the carbene is indicated by an asterisk.

The ^{35}Cl SSNMR spectrum of **4.4** (Figure 4.5) shows two distinct overlapping signals, one with $C_Q = 10.8$ MHz and the other with $C_Q = 15.0$ MHz. Both signals have η_Q values (0.2 and 0.1, respectively) which suggest somewhat less than axial symmetry. A small CSA ($\Omega = 250$ ppm) was required to fit the narrower signal, but the overlap of the two signals meant that the central discontinuity that has proven crucial for CSA determination in the other complexes was not visible for the broader signal in this spectrum. While both chlorides in **4.4** are found in similar pseudo-bridging environments, the Ge–Cl bond lengths in differ by 0.3 \AA ,²⁰ which leads to very different EFG tensors, a difference which was also observed at 9.4 T (Appendix 1, Figure A1.2). The resolution of the two signals is notable because earlier studies often could not resolve the signals arising from two different terminal or bridging sites. It is not clear from the spectrum alone which signal arises from which site, necessitating DFT calculations for further insight (*vide infra*). An

attempt to acquire a ^{73}Ge SSNMR spectrum of **4.4** did not yield a signal after overnight acquisition, most likely due to a combination of the low symmetry at germanium and a low germanium density of $3.6 \text{ Ge}/1000 \text{ \AA}^3$ (corresponding to a concentration of NMR active nuclei of only $0.28 \text{ }^{73}\text{Ge}/1000 \text{ \AA}^3$). This concentration lies between the previously established minimum and the concentration in **4.1**. While the germanium concentration in **4.4** is higher than in the carbene complexes **4.2** and **4.3**, it was still insufficient.

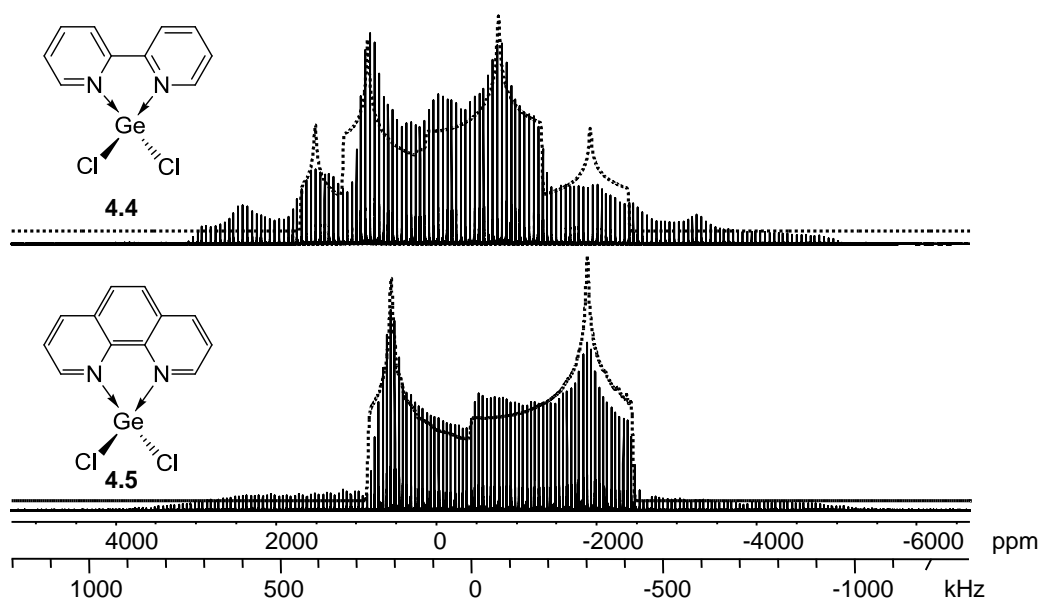


Figure 4.5 Static ^{35}Cl WURST-QCPMG spectra of **4.4** and **4.5** at 21.1 T. The dotted traces indicate empirical simulations. Both spectra exhibit partial satellite transitions, visible as lower intensity spikelets along the baseline.

The spectrum of the phenanthroline complex **4.5** is a single broad signal with $C_Q = 13.8$ MHz, which falls between the two ^{35}Cl C_Q values determined for the bipyridine complex **4.4**. Much like complex **4.4**, the η_Q value of 0.15 suggests a slight deviation from axial symmetry. The small spikelets from 4000 to 1000 ppm and -2000 to -5000 ppm in the ^{35}Cl WURST-QCPMG spectrum of **4.5** arise from a partial satellite transition; however, due to the breadth of the signal the full transition was not acquired. The intensity is not

sufficient to attribute this signal to the second non-equivalent chloride seen in the X-ray structure²⁰ unless there is a considerable difference in the magnitude of the EFG tensors. To accurately fit the central discontinuity while keeping the low field data (Appendix 1, Figure A1.3) in mind, it was necessary to include a small ($\Omega=200$ ppm, $\kappa=0$) CSA contribution. While attempts at ^{73}Ge NMR spectroscopy did yield a weak signal after overnight acquisition (Figure 4.6), it was not possible to obtain a sufficient signal-to-noise ratio to allow for spectral simulation, and thus, the determination of spectroscopic parameters. The germanium density of **4.5** ($3.4 \text{ Ge}/1000 \text{ \AA}^3$, $0.27 \text{ }^{73}\text{Ge}/1000 \text{ \AA}^3$) is comparable to **4.4**, and thus, the weak signal most likely arises from somewhat higher symmetry at germanium.

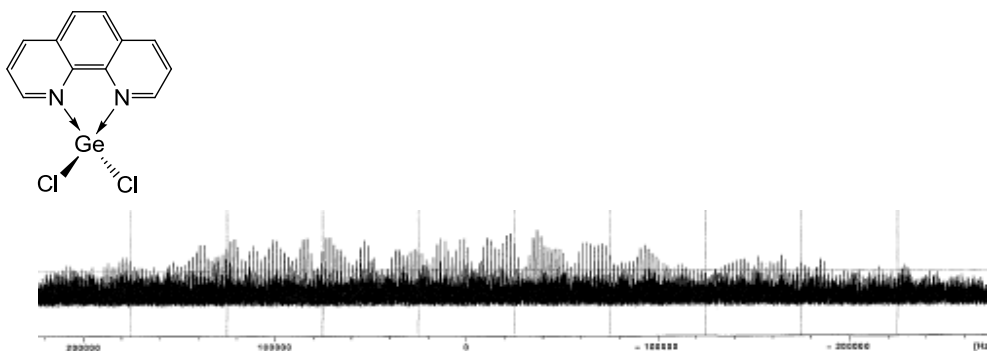


Figure 4.6 ^{73}Ge SSNMR spectrum of **4.5** at 21.1 T after overnight acquisition.

Consistent with the low symmetry of a terminal chloride, the ^{35}Cl SSNMR spectrum of [benzo-15-crown-5-GeCl][OTf], **4.6**, has a C_Q of 25.1 MHz (Figure 4.7). To completely fit the lineshape, it was necessary to include a CSA comparable to the others in this study ($\Omega= 350$ ppm, $\kappa=1$). A skew value indicative of axial symmetry was consistent with the near axial η_Q value (0.1). Due to the relatively small magnitude of the CSA in comparison to the EFG interaction, the error is quite large on the former. ^{73}Ge SSNMR spectroscopy

of **4.6** was not attempted in due to the large size of the crown ether leading to a prohibitively low germanium concentration.

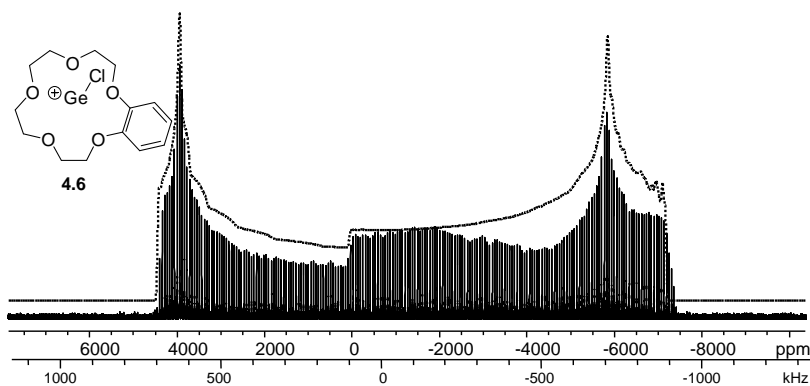


Figure 4.7 Static ^{35}Cl WURST-QCPMG spectrum of [benzo-15-crown-5 GeCl][OTf] (**4.6**) at 21.1 T. The dotted trace indicates the analytical simulation.

The ^{35}Cl SSNMR spectrum of $\text{Mes}_2\text{GeCl}_2$ (**4.7**) (Figure 4.8) differed considerably from the spectra of the germanium(II) compounds. The signal was considerably broader, spanning approximately five megahertz at 9.4 T (Appendix 1, Figure A1.4) and three megahertz at 21.1 T. The quadrupolar coupling constant of 43 MHz was the largest observed in this study, though larger are known.^{4,13,27} The ^{35}Cl SSNMR spectrum of Mes_3GeCl (**4.8**) exhibited similar features, with a C_Q value of 41.5 MHz. Despite the low germanium concentration in $\text{Mes}_2\text{GeCl}_2$, ^{73}Ge NMR spectroscopy was attempted due to the unusually small ^{73}Ge C_Q value observed for Mes_2GeH_2 . Unfortunately, no signal was observed, likely due to rapid T_2 relaxation caused by the quadrupolar chlorine atoms.

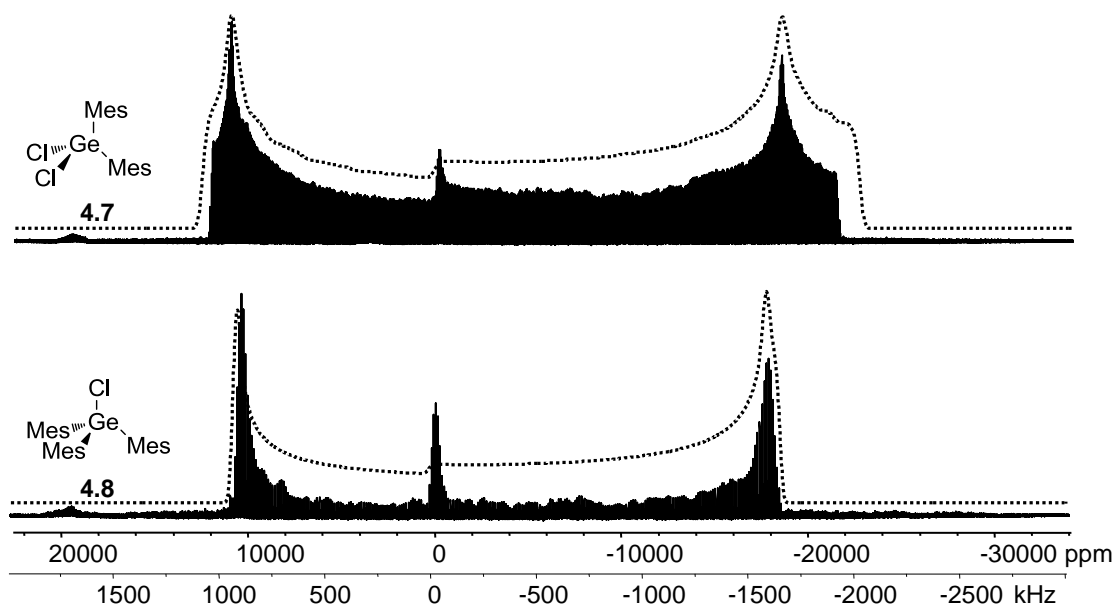


Figure 4.8 Static ^{35}Cl WURST-QCPMG spectra of **4.7** (top) and **4.8** (bottom) at 21.1 T. The dotted traces indicated analytical simulations.

The ^{35}Cl SSNMR spectrum of the tin cryptand complex **4.9** (Figure 4.9) was quite similar to that of the germanium(II) complexes. It had a similar η_Q value at 0.15 and a C_Q value of 19 MHz, which falls squarely in the middle of the range determined for the germanium(II) compounds. The quadrupolar coupling constant is somewhat smaller than that observed for the cationic crown ether complex **4.6**. Unlike the crown ether complex, the counterion for the tin cation contains chlorine, SnCl_3^- . DFT calculations (*vide infra*) were, thus, required to determine whether the signal observed arose from the cation or the anion.

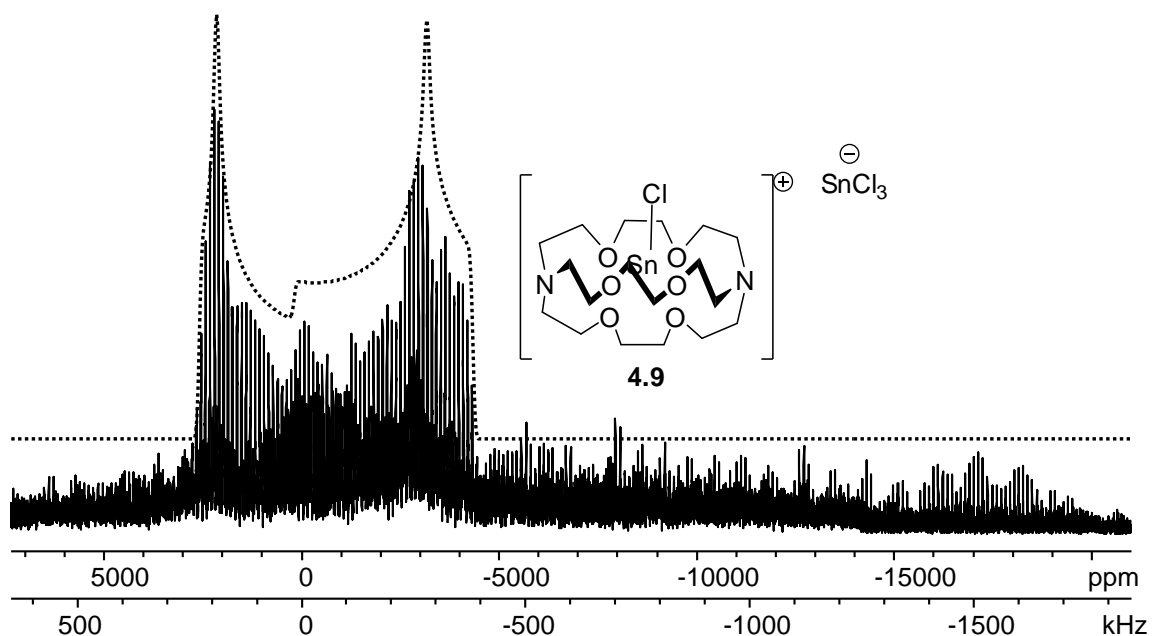


Figure 4.9 ^{35}Cl WURST-QCPMG spectrum of $[[2.2.2]\text{SnCl}][\text{SnCl}_3]$ (**4.9**) at 21.1 T. The dashed trace indicates the analytical simulation.

4.3 Discussion

Overall, the clearest trend observed is the relationship between the quadrupolar coupling constant and the oxidation state of the attached germanium (Figure 4.10). Both germanium(IV) compounds exhibit *considerably* larger ^{35}Cl C_Q values ($C_Q > 40$ MHz) than any of the germanium(II) compounds studied ($C_Q = 10\text{-}30$ MHz). This marked difference makes ^{35}Cl SSNMR spectroscopy a potentially useful tool for the study of compounds with ambiguous oxidation state. While Mössbauer spectroscopy can provide similar information, it is only commonly employed for iron, tin, antimony and iodine and many elements lack an appropriate gamma ray source.²⁸ This approach would require only that there be a chlorine atom attached to the metalloid. Notably, GeCl , the only germanium(I) chloride studied by ^{35}Cl NMR spectroscopy, had an average C_Q value of 5.5 MHz. Although the C_Q value of GeCl is larger than value observed for uncomplexed GeCl_2 (40 kHz), GeCl_2 is believed to have a regular octahedral environment at chlorine

through complexation with itself. This suggests that while there is in general a relationship between the oxidation state of germanium and the magnitude ^{35}Cl C_Q there are multiple factors at play. Specifically, highly symmetrical environments at Cl will still lead to an extremely small EFG, and thus, small C_Q values. Notably, organic chlorides of carbon(IV)¹³ also exhibit very large C_Q values. Within the germanium(II) series, complexes with related ligands had similar C_Q values. For example, the C_Q of complexes with ligands with nitrogen donor atoms at Ge (ie **4.4** and **4.5**) all fell within a 5 MHz range of each other, as did those with oxygen donors at Ge (ie **4.1** and **4.6**). The C_Q of ligands with carbon donor atoms (ie **4.2** and **4.3**) fell within an even smaller 1 MHz range.

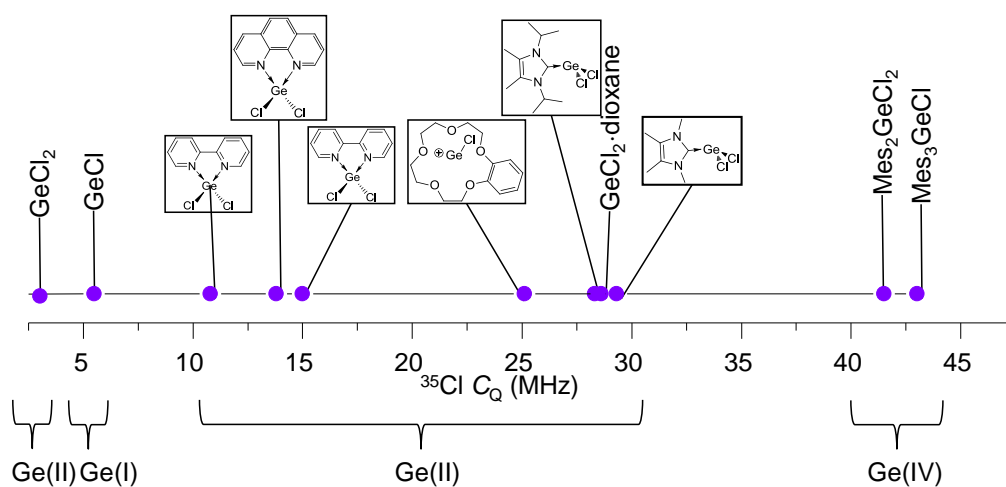


Figure 4.10 Relationship between quadrupolar coupling constant and germanium oxidation state.

The η_Q values for **4.1- 4.9** range from 0 for the axially symmetric Mes_3GeCl (**4.8**) to 0.23 for the isopropyl-substituted NHC complex of GeCl_2 (**4.3**). Such low values are generally indicative of near axial symmetry at the nucleus of interest; however, it is notable that the

largest η_Q values of compounds where the chlorine is bound to carbon was observed for an aryl chloride ($\eta_Q = 0.139$) even though there is a distinct lack of axial symmetry.¹³

To develop solid-state NMR spectroscopy as a tool for structural characterization, it is necessary to determine if spectroscopic parameters can be correlated to structural metrics. Thus, correlations between the crystallographically-determined structural metrics and the NMR spectral parameters were examined. Within the series germanium(II) complexes **4.1-4.6**, there was a quadratic relationship ($R^2=0.90$) between the Ge–Cl bond length and the magnitude of $^{35}\text{Cl } C_Q$ (Figure 4.11A), with longer bonds leading to smaller C_Q values. In the case of the cationic germanium complex **4.6** and the cationic tin complex **4.9**, it is notable that the Sn–Cl bond is considerably (0.3 Å) longer than the Ge–Cl bond. However, this is unlikely to be the sole cause of the smaller C_Q value observed for the cryptand complex, as tin and germanium would be expected to have unique effects on the electric field gradient. The trend in C_Q values may be a consequence of the covalency of the Ge–Cl bond and may also explain the low C_Q value for GeCl, as the germanium(I) halides are not expected to have traditional covalent bonds. Likewise, the high symmetry in GeCl₂ may arise from the Ge–Cl bonds having low covalent character.

The average angle between chlorine, germanium and the donor atom also correlated to C_Q (Figure 4.11B). Generally, wider bond angles correlated to larger C_Q values.

GeCl₂·dioxane (**4.1**) is notable as a significant outlier. If the data point for GeCl₂·dioxane is excluded, there is a linear ($R^2=0.94$) relationship between D-Ge-Cl angle and $^{35}\text{Cl } C_Q$ (Figure 4.11C). If the covalently bound substituents are regarded as being donors, the germanium(IV) compounds **4.7** and **4.8** fit the trend of wide angles corresponding to large C_Q values (using the geometry optimized structures). The trend may be attributed to

the degree of hybridization, with the germanium(IV) compounds having sp^3 hybridization while the germanium(II) compounds, with D-Ge-Cl angles close to 90° , are closer to sp^2 hybridization or even an unhybridized germanium centre. Indeed, Natural Bond Order calculations at the TPSS/TPSS/6-311+G** level revealed Ge-Cl bond orders well below the value of 1 expected for a traditional covalent bond.

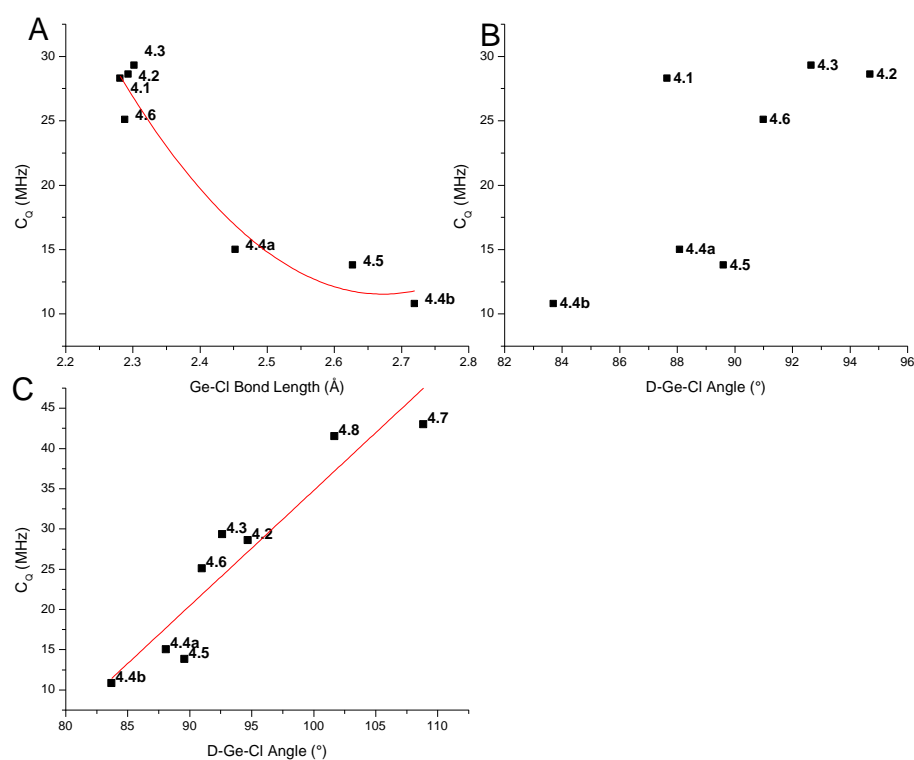


Figure 4.11 A) Relationship between ^{35}Cl quadrupolar coupling constant and crystallographically-determined Ge-Cl bond lengths. The solid line indicates a line of best fit ($y = 111x^2 - 592x + 802$, $R^2 = 0.90$). B) Relationship between ^{35}Cl quadrupolar coupling constant and crystallographically determined D-Ge-Cl angle for the germanium(II) series. C) Relationship between ^{35}Cl quadrupolar coupling constant and D-Ge-Cl angle excluding GeCl_2 -dioxane and including geometry optimized structures of 4.7 and 4.8. The solid line indicates a line of best fit ($y = 1.43x - 108.6$, $R^2 = 0.94$).

4.3.1 Computational Investigation

Previous calculations of ^{35}Cl SSNMR parameters have been performed using plane wave pseudopotentials using CASTEP.^{25,26,29} The CASTEP code is optimized for calculations on periodic inorganic solids.³⁰ Calculations model electron distribution throughout the entire unit cells, and thus, require extensive computational resources for substances with large unit cells.

Of the compounds included in this study, $\text{GeCl}_2\cdot\text{dioxane}$ (**4.1**) had a unit cell small enough for CASTEP calculations. The other complexes crystallized in unit cells which were too large ($> 1000 \text{ \AA}^3$) to model in CASTEP with the available computational resources. The ^{35}Cl NMR parameters of organic chlorides have been assessed using gas phase DFT calculations using the B3LYP/6-311+G** level of theory, reasonably reproducing η_Q values, though there was some scatter in the calculated C_Q values.¹³ As the complexes in this study are generally isolated molecules without the long range periodicity that the CASTEP code is optimized for, calculations in Gaussian 09 appeared to be more appropriate. Calculations were optimized using $\text{GeCl}_2\cdot\text{dioxane}$ (**4.1**) due to the known accuracy of the CASTEP calculations and the relative simplicity of the repeat unit. Additionally, a more accurate method for the calculation of the NMR parameters for germanium is greatly needed as CASTEP calculations greatly overestimated the C_Q of $\text{GeCl}_2\cdot\text{dioxane}$ (Calculated = 69 MHz, Experiment = 45 MHz).³¹

The calculations of NMR parameters for **4.1** using CASTEP, while inaccurate for germanium, gave values for ^{35}Cl parameters that were in excellent agreement with the

experimental results (calculated: $C_Q = 27.6$, $\eta_Q = 0.04$). To explore the validity of using Gaussian 09 to calculate NMR parameters, a series of clusters of increasing complexity were built in an attempt to simulate the long range order of $\text{GeCl}_2 \cdot \text{dioxane}$ in Gaussian 09 (Figure 4.12). Initial calculations were performed on the isolated monomer. Cluster **I** took into account the polymeric nature of the system by adding two repeat units. Cluster **II** was used to investigate the importance of long range Ge–Cl interactions by adding two adjacent GeCl_2 units. Cluster **III** is, effectively, a combination of clusters **I** and **II**, accounting for both the extended chain and the adjacent units. Finally, cluster **IV** extended the network in three dimensions. In all cases, the reported values for ^{73}Ge are for the central germanium atom and the values for ^{35}Cl are for the chlorines bound to that germanium.

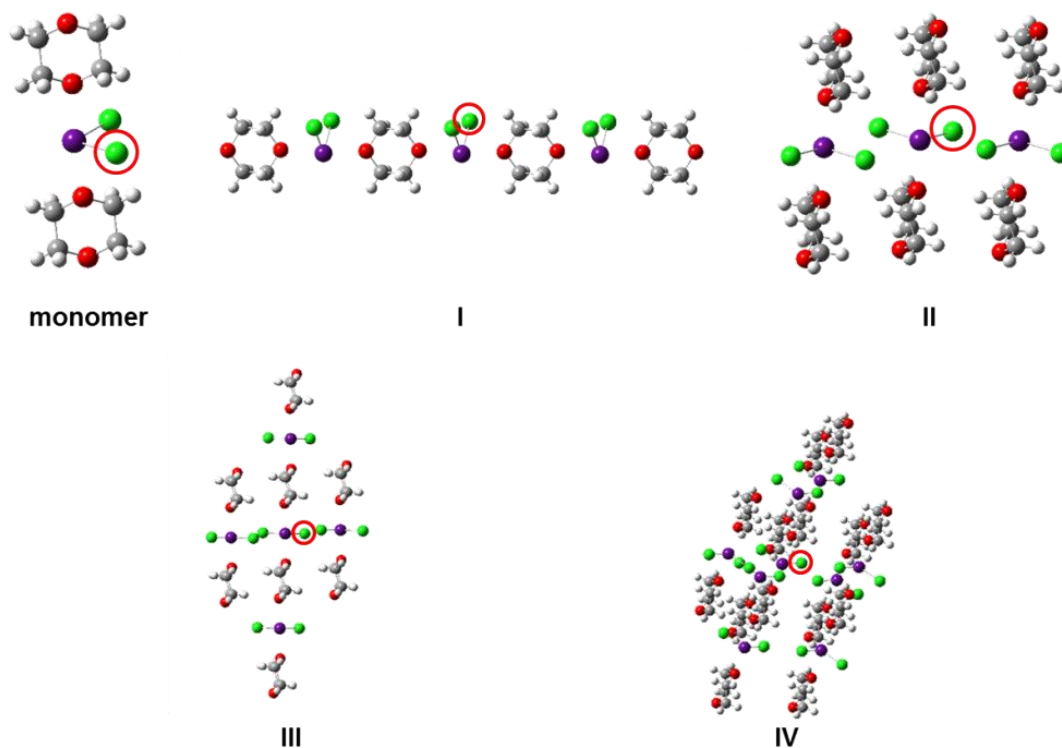


Figure 4.12 Clusters employed in the calculation of the ^{35}Cl NMR parameters for GeCl_2 -dioxane in Gaussian 09. The chlorine centre for which the parameters were determined is indicated with a circle.

As the previous work on the calculation of ^{35}Cl NMR parameters made use of the CASTEP code, there has not been a systematic investigation into the best methodology for calculating ^{35}Cl parameters in Gaussian 09. We, thus, examined several different density functionals and basis sets in order to best approximate the experimental values. The results of these calculations are summarized in Table 4.2. Although all functionals consistently overestimated the value of the ^{73}Ge C_Q , the relatively recent TPSSTPSS³² gave considerably lower values than PBE1PBE.³³ The popular B3LYP³⁴ functional was also investigated, but was abandoned when it became apparent that it overestimated C_Q by an equal or greater amount when compared to PBE1PBE. Cluster **IV** was not

calculated at the PBE1PBE/6-311+G** level as it was not possible to complete the calculation within the time constraints of the available computational resources.

Table 4.2 Assessment of computational methodology using 4.1.

Cluster	Functional	Basis Set	³⁵ Cl C _Q (MHz)	³⁵ Cl η _Q	⁷³ Ge C _Q (MHz)	⁷³ Ge η _Q
Experimental monomer			28.3	0.055	44	0.5
	PBE1PBE	6-31G*	33.1	0.13	101.1	0.7
		6-311+G**	34.2	0.11	88.4	1
	TPSSTPSS	6-31G*	32.3	0.12	93.7	0.7
		6-311+G**	33.1	0.11	79.6	1
	B3LYP	6-31G*	32.3	0.12	100.2	0.6
		6-311+G**	34.0	0.10	88.0	0.9
I	PBE1PBE	6-31G*	33.5	0.14	103.1	0.7
		6-311+G**	34.6	0.12	90.7	1
	TPSSTPSS	6-31G*	32.7	0.15	95.7	0.7
		6-311+G**	33.5	0.12	81.9	1
II	PBE1PBE	6-31G*	27.9	0.07	84.8	0.8
		6-311+G**	29.4	0.12	79.8	0.9
	TPSSTPSS	6-31G*	27.0	0.12	78.6	1
		6-311+G**	28.5	0.11	72.2	0.9
III	PBE1PBE	6-31G*	26.6	0.06	86.8	0.9
		6-311+G**	29.7	0.13	81.9	0.9
	TPSSTPSS	6-31G*	27.3	0.14	80.5	0.9
		6-311+G**	27.9	0.10	74.3	0.9
IV	PBE1PBE	6-31G*	26.6	0.06	84.7	0.9
		6-311+G**	<i>n. a.^a</i>	<i>n. a.^a</i>	<i>n. a.^a</i>	<i>n. a.^a</i>
	TPSSTPSS	6-31G*	25.8	0.05	78.4	0.9
		6-311+G**	27.8	0.10	72.3	0.9

^a *n. a.* = not applicable (job did not complete after 1 week)

Not surprisingly, the isolated monomer gave results in poor agreement with the experimental results, overestimating C_Q for both ³⁵Cl. Extending the linear chain (cluster **I**) offered very little improvement over the calculations on the monomer. However, the addition of the adjacent GeCl₂ unit on either side of the fragment (cluster **II**) offered a dramatic improvement in the calculated value of C_Q for the chlorine attached to the central germanium, bringing it into excellent agreement with the experimental results.

This suggests that the long range contact between the terminal chlorine and the adjacent germanium atom is of importance to the largest tensor component. Further elaboration (clusters **III** and **IV**) did not offer any notable improvement in the calculated values. Notably, for all clusters and functionals, the larger 6-311+G** basis set consistently gave better results than 6-31G*.

Despite the excellent agreement between the experimental and theoretical C_Q and η_Q values for ^{35}Cl , Gaussian calculations did not accurately reproduce the experimental results for ^{73}Ge . Similar to chlorine, there was poor agreement with the experimental results in the isolated monomer and cluster **I**. A dramatic drop in the calculated value of C_Q for the central germanium atom was observed upon the addition of the adjacent GeCl_2 unit in cluster **II**, though it was still considerably higher than the experimental value. This once again points to the importance of the long range Ge–Cl interaction. As with the ^{35}Cl NMR parameters, further elaboration (clusters **III** and **IV**) did not provide a significant improvement in the calculated ^{73}Ge NMR parameters.

Because the results for the second row chlorine were consistently more accurate than for the third row germanium, we suspected the difficulties might lie in the basis sets employed. While the 6-311+G** basis set was sufficient for the lighter elements, heavier atoms might require additional basis functions. As the most dramatic improvement was seen with cluster **II** and additional complexity did not offer a great benefit, we used this structure for further explorations. In the interest of keeping computational times within the limits of the resources available, we employed the 6-31G* basis set on carbon and hydrogen and 6-311+G** on chlorine. Both 6-31G* and 6-311+G** were examined on oxygen, but there was a negligible difference in the calculated parameters. As shown in

Table 4.3, use of a quadrupole zeta basis set on germanium did offer a considerable reduction in the calculated C_Q value, though 65 MHz is still 20 MHz greater than the 44 MHz found experimentally. Unfortunately, attempts to employ the still larger quintuple zeta basis set on germanium were met with the same computational time restrictions which prevented the use of the largest cluster with the PBE1PBE/6-311+G** methodology.

Table 4.3 Effect of basis set on germanium on calculated ^{73}Ge C_Q value.

C basis set	H basis set	O basis set	Cl basis set	Ge basis set	$^{73}\text{Ge } C_Q$	$^{73}\text{Ge } \eta_Q$
6-31G*	6-31G*	6-31G*	6-311+G**	VQZ	65.0	1
6-31G*	6-31G*	6-311+G**	6-311+G**	VQZ	64.8	1
6-31G*	6-31G*	6-31G*	6-311+G**	V5Z	<i>n. a.</i>	<i>n. a.</i>

As the TPSSTPSS/6-311+G** methodology proved to be the most accurate and efficient methodology for GeCl_2 -dioxane (**4.1**), it was employed for all subsequent calculations of ^{35}Cl NMR parameters. Hydrogen positions were optimized at the TPSSTPSS/6-31G* level. A summary of the computational results is presented in Table 4.4. The ^{35}Cl CSA interaction was overestimated in all cases, ranging from 300 to 600 ppm while the experimental values ranged from 100 to 300. However, the experimental values have large errors due to the large effect of EFG on lineshape compared to CSA.

Table 4.4 Summary of computational ^{35}Cl NMR parameters compounds **4.2-4.9**.^a

Compound	Donor	Calc'd C_Q (MHz)	Exp. C_Q (MHz)	Calc'd η_Q	Exp η_Q	Calc'd Ω (ppm)	Calc'd κ
4.2 ^b	C	33.2	28.6	0.10	0.12	300	-0.7
4.3	C	33.1	29.3	0.04	0.23	350	-0.6
4.4 ^b Cl(1)	N	23.6	15.0	0.25	0.1	500	0.6
4.4 ^b Cl(2)	N	14.8	10.8	0.2	0.2	600	0.4
4.5 ^b	N	18.0	13.8	0.10	0.15	400	0.04
4.6	O	27.8	25.1	0.10	0.1	550	0.6
4.7	C	44.5	43.0	0.13	0.1	310	0.5
4.8	C	43.3	41.5	0	0	120	1
4.9	O, N	22.7	19.0	0.13	0.15	1103	-0.2

^a Hydrogen positions for **4.2-4.6** and **4.9** were optimized using the TPSS/TPSS/6-31G* method. Structures for **4.7** and **4.8** were fully optimized at the TPSS/TPSS/6-31G* level.

^b Calculations included long range interactions with adjacent GeCl_2 unit

The parameters for the methyl-substituted NHC GeCl_2 complex **4.2** were calculated for both the isolated molecule and the dimeric structure apparent from the X-ray data.³⁵

Calculation on the monomer gave a C_Q value of 34.6 MHz. Inclusion of the long range interaction with the adjacent molecule offered a modest improvement in agreement with a calculated C_Q value of 33.2 MHz. The small value of η_Q was in reasonable agreement with the 0.12 observed experimentally. The similarity between the calculated C_Q values for both the monomeric and dimeric structures suggests that the long range Ge–Cl interaction is not as important for complex **4.2** as it is for GeCl_2 -dioxane, for which the difference between the monomeric and cluster structures was dramatic. A similar value ($C_Q = 34$ MHz) was calculated for the isopropyl-substituted NHC GeCl_2 complex **4.3**. Combined with the similar experimental C_Q values for **4.2** and **4.3**, the computational results support that the long range Ge–Cl interaction is not as important in the carbene complexes as it is for **4.1**. This is most likely due to the adjacent germanium atom being 0.2 Å closer in **4.1** than **4.2**.

As the results for the GeCl_2 -dioxane complex demonstrated that the inclusion of long range interactions between germanium and chlorine is vital for obtaining accurate reproduction of experimental results, calculations on the bipyridine complex **4.4** included the adjacent molecules to either side of the center of interest. The quadrupolar coupling constants were overestimated at 23.6 MHz for Cl(1) and 14.8 MHz for Cl(2). While one of the experimental C_Q values is indeed 15 MHz, it is more likely that the relative magnitudes of the calculated values are correct. The Ge–Cl(2) bond length (2.7195 Å) is considerably longer than a typical covalent Ge–Cl bond. Indeed, in the related bromine complex, the analogous bromide is fully anionic in character.²⁰ A weaker covalent bond would have a less dramatic effect on the electric field gradient, leading to a lower C_Q value. This ordering is also consistent with the general trend observed experimentally (Figure 4.10). Calculations predict similar η_Q values for both chlorine sites of roughly 0.2, which is within experimental error of the experimental values of 0.1 and 0.2. The situation was similar with the phenanthroline complex dimer **4.5**, with C_Q overestimated at 18 MHz and η_Q accurately reproduced at 0.1, in agreement with experiment.

The C_Q value for the crown ether GeCl complex **4.6** was somewhat overestimated at 27.8 MHz. A difference of 2 MHz, while greater than the experimental error, is still reasonable for such a large C_Q value. The value of η_Q was reasonably reproduced.

While there are no X-ray structures available for the two germanium(IV) compounds **4.7** and **4.8**, calculations were performed using structures optimized at the TPSS/TPSS/6-31G* level. Gaussian calculations on compound **4.7** predicted a C_Q of 44.5 MHz and η_Q of 0.13. A difference of 1.5 MHz from the experimental C_Q value of 43.0 MHz is very reasonable agreement for such a broad signal. Compound **4.8** demonstrated a similar

agreement, with a calculated C_Q value of 43.3 MHz, representing an overestimation very similar to that seen in **4.7**, and an η_Q value of 0, exactly in agreement with experiment.

The effect of the Ge–Cl bond length and the D-Ge-Cl bond angle on the value of the ^{35}Cl C_Q were investigated computationally using Mes_3GeCl (**4.8**) as a model compound. The structural metric was systematically varied to determine the effect on the calculated value of C_Q (Figure 4.13A). A linear ($R^2 = 0.99$) relationship was found between the Ge–Cl bond length and the ^{35}Cl C_Q value. In contrast to the experimental trend (Figure 4.11A), longer bonds corresponded to *larger* C_Q values. In the computational case, the longer bonds correspond to a chlorine more closely resembling *atomic* chlorine, which has a very large C_Q value due to an unpaired electron. In the experimental compounds, the longer bonds appeared to correspond to more ionic chlorine centres. As was previously seen for ^{73}Ge C_Q values, bond angles had a much smaller impact on the calculated ^{35}Cl C_Q value (Figure 4.13B). Experimentally, a considerably greater influence was observed (Figure 4.11B), which may partly be attributed to the adjustment of one C-Ge-Cl angle in Mes_3GeCl by necessity impacting the others, reducing the overall variance in the *average* angle.

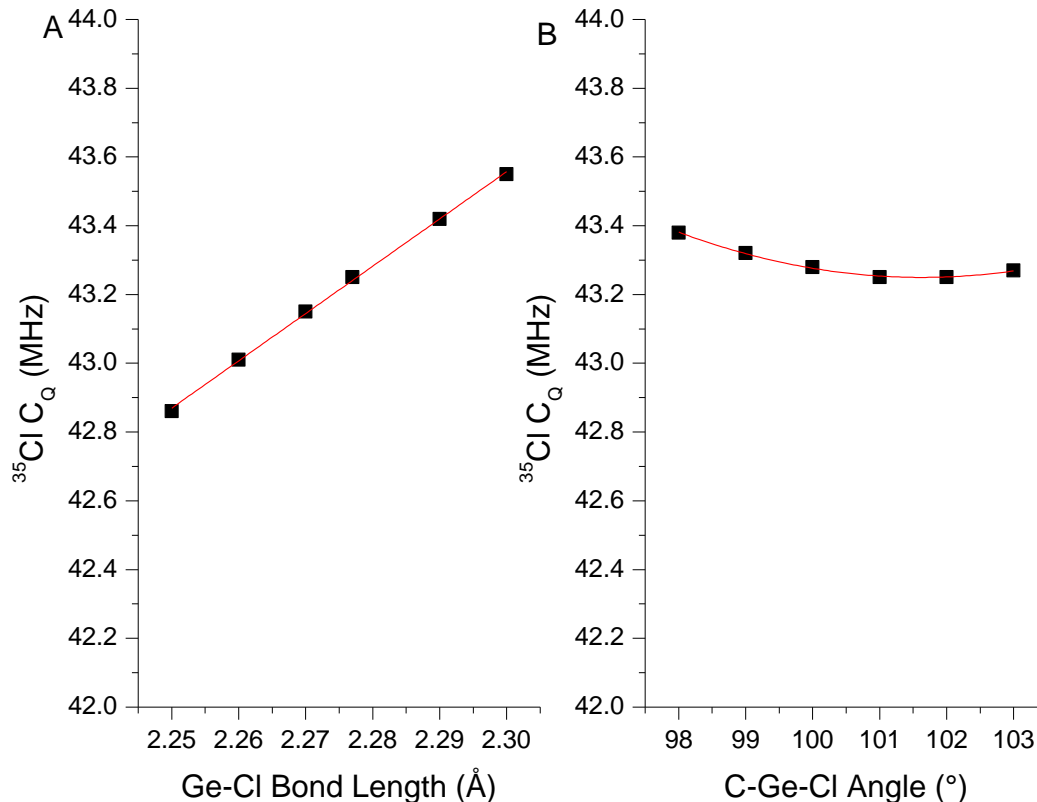


Figure 4.13 Relationship between calculated $^{35}\text{Cl } C_Q$ value and A) Ge–Cl bond length. The solid line indicates a line of best fit ($y = 13.8x + 11.9$, $R^2 = 0.99$) B) C–Ge–Cl angle. The solid line indicates a line of best fit ($y = 0.01x^2 - 2x + 147$, $R^2 = 0.99$).

For **4.9**, the Lan2DZ basis set was employed for tin, as the 6-311+G** basis set does not include fourth row elements. All other elements in the structure were still calculated using the latter basis set. Much like **4.4**, DFT calculations were necessary for **4.9** to determine why only one chlorine signal was observed when there are two distinct chlorine environments. The chloride bound to the cationic tin site was predicted to have a C_Q value of 22.7 MHz, in reasonable agreement with the 19 MHz observed experimentally. The chlorides of the SnCl_3^- anion have a calculated C_Q value of 105 MHz, confirming that the signal observed must be assigned to the cationic site. Even with

the trend towards overestimating C_Q in the DFT calculations, the anionic chlorides would be over 10 MHz broad at 21.1 T, and thus, are not observed.

The overall agreement between calculation and experiment is illustrated in Figure 4.14. In general, the complexes with oxygen donor atoms (**4.1** and **4.6**) have calculated C_Q values which agree most closely with the experimental values. While the compounds with carbon donor atoms (**4.2** and **4.3**) and those with nitrogen donor atoms (**4.4** and **4.5**) lie a similar distance from the line of 1:1 agreement, the difference is more significant for the smaller C_Q values of **4.4** and **4.5**. Overall, the correlation between the experimental values is linear, with an R^2 value of 0.95. With an ideal 1:1 correlation, the slope of the line of best fit would be 1; it is instead 0.87, suggesting that the overall agreement between theory and experiment is reasonable. It is not clear why the agreement is considerably better for the complexes with oxygen donor atoms when compared to the other complexes with first row donor atoms. The C_Q values of the germanium(IV) compounds **4.8** and **4.9** were reasonably reproduced using geometry optimized structures.

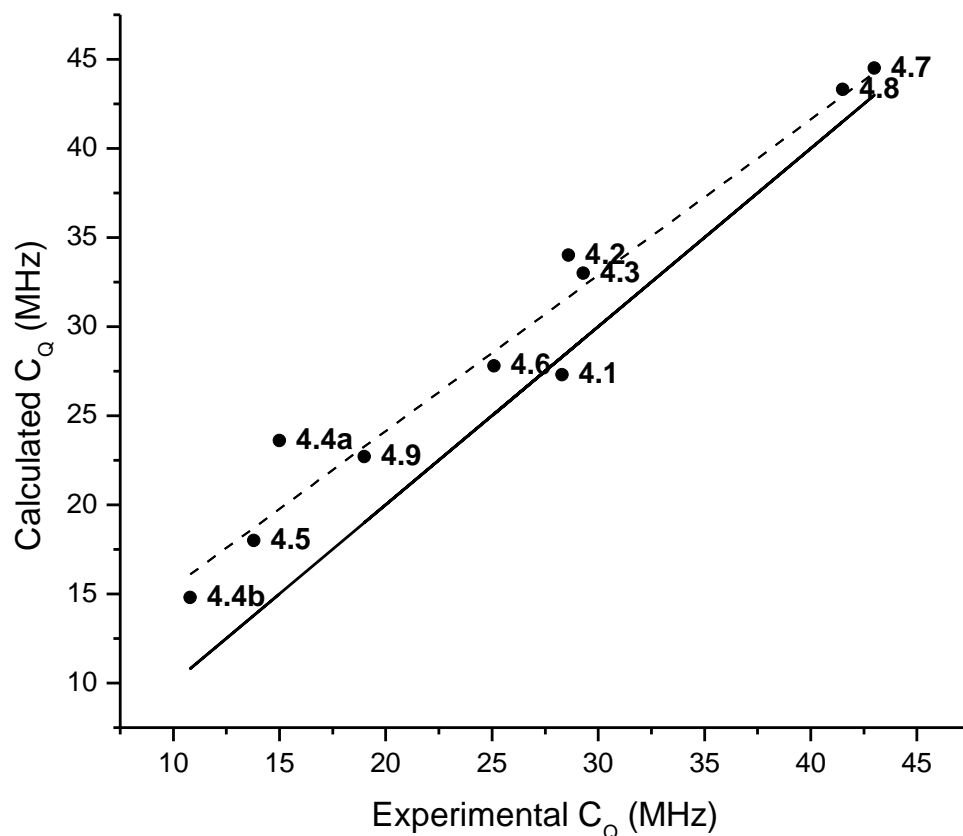


Figure 4.14 Agreement between calculated and experimental C_Q values. The solid line represents an ideal 1:1 correlation, while the dashed line represents a line of best fit ($y = 0.87x + 6.7$, $R^2 = 0.95$).

The orientation of the EFG tensor components (Figure 4.15) can often provide insight into the specific structural effects on the NMR parameters. In the majority of the germanium(II) complexes, the largest tensor component (V_{33}) was oriented along the Ge–Cl bond, with the remaining components oriented perpendicular. This likely explains the general relationship seen between the Ge–Cl bond length and the magnitude of C_Q .

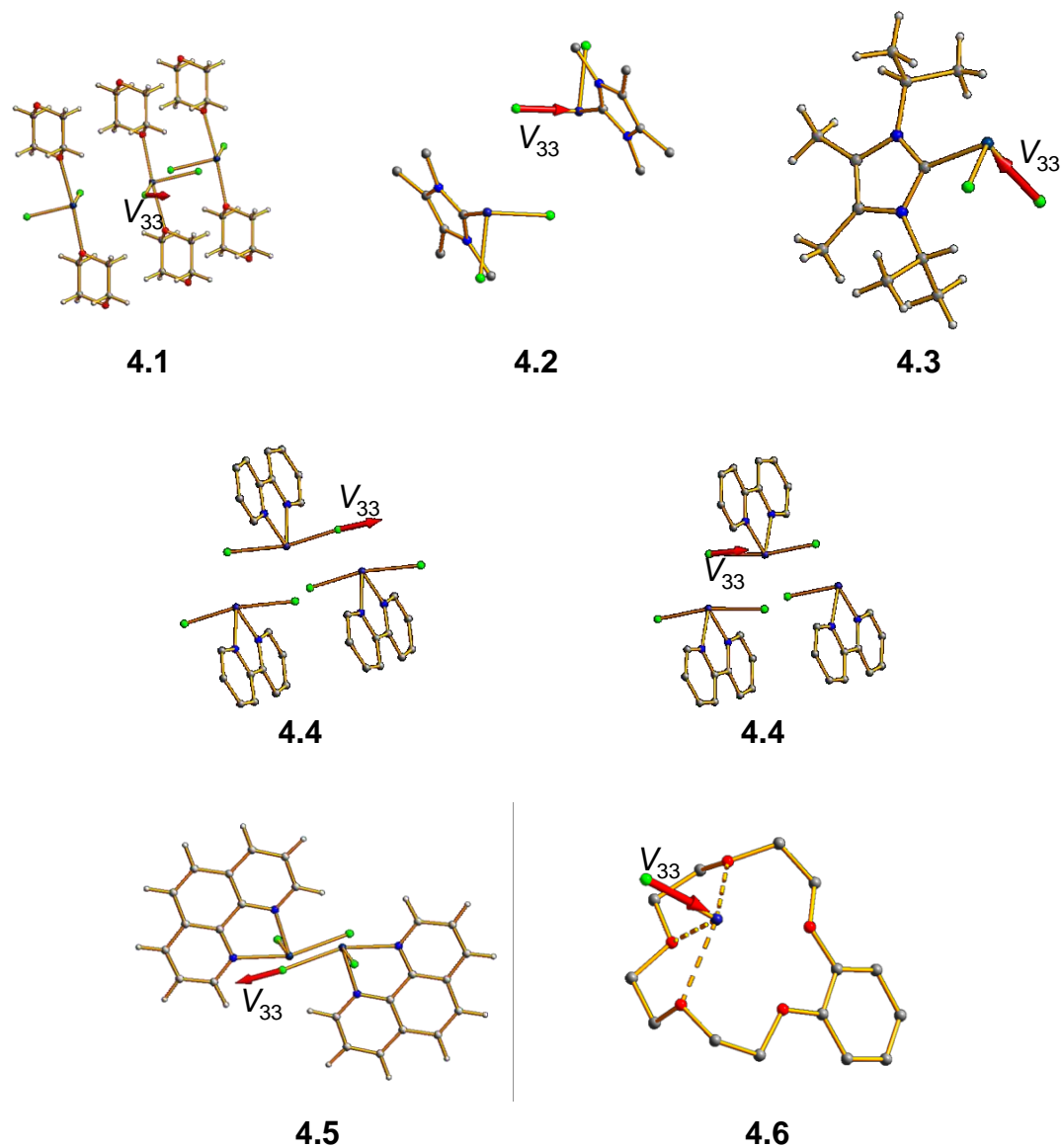


Figure 4.15 Orientation of the V_{33} component for compounds **4.1-4.6** calculated at the TPSS/TPSS/6-311+G** level. Hydrogen atoms have been omitted for clarity.

The V_{22} and V_{11} components of **4.2-4.6** are not orientated towards any particular structural feature, providing a possible explanation for the similar η_Q values observed for all compounds. Notably, the situation is somewhat different for GeCl_2 -dioxane (**4.1**), with the intermediate component (V_{22}) being orientated along the Ge–Cl bond and the largest component (V_{33}) being orientated toward the adjacent germanium atom. This was not seen

in any of the other complexes which feature a long range Ge–Cl contact (4.2, 4.4 and 4.5), offering a possible explanation for why $\text{GeCl}_2 \cdot \text{dioxane}$ is an outlier in the structural trends relating C_Q to both bond length and bond angle (Figure 4.11). The greater influence of the long range contact may be attributed to the adjacent germanium atom being 0.2 Å closer in $\text{GeCl}_2 \cdot \text{dioxane}$ than in 4.4, with 4.3 having an even more distant contact.

The same tensor orientation pattern is observed in the germanium(IV) compounds (Figure 4.16). While the geometry optimized Ge–Cl bond lengths (2.224 Å for $\text{Mes}_2\text{GeCl}_2$ and 2.277 Å for Mes_3GeCl) are the shortest Ge–Cl bond lengths in this study, the bond lengths are not sufficiently different from those of the germanium(II) complexes to reasonably be the only explanation for the dramatic difference observed in C_Q values. The oxidation state at germanium, thus, appears to be the most important influence on the value of C_Q ; however it is likely bond length will play a role in determining ^{35}Cl C_Q within the subcategory of germanium(IV) compounds.

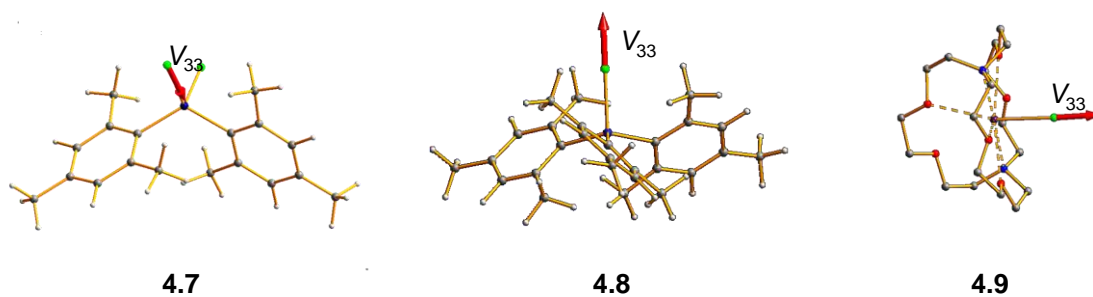


Figure 4.16 Orientation of the V_{33} component for compounds 4.7-4.9. Compounds 4.7 and 4.8 were geometry optimized at the TPSS/TPSS/6-31G* level. Hydrogen atoms and the SnCl_3^- anion were omitted for clarity.

Finally, the same tensor orientation pattern, with the V_{33} component aligned with the E–Cl bond, is also observed for the tin complex **4.9**. While this is a single example, it points to the possibility that the same trends might be observed for other group 14 compounds.

4.4 Conclusions

All the compounds examined in this study gave rise to broad spectra as is expected for chlorine in a low symmetry environment. Through the use of the WURST-QCPMG pulse sequence and piecewise acquisition, it was possible to obtain high quality spectra suitable for extraction of quadrupolar parameters through spectral simulation. This is a marked contrast to attempts to obtain ^{73}Ge SSNMR spectra for the same compounds. While ^{73}Ge NMR spectroscopy was attempted for the majority of the selected compounds, it was only possible to obtain a reasonable ^{73}Ge SSNMR spectrum for $\text{GeCl}_2 \cdot \text{dioxane}$. Examples of cationic and low valent species were studied, demonstrating a new source of structural information about exciting new compounds.

Examination of the ^{35}Cl parameters revealed apparent relationships to several properties of germanium. The most dramatic observation is the distinct relationship between the oxidation state of germanium and the ^{35}Cl quadrupolar coupling constant.

Germanium(IV) compounds exhibit considerably broader ($C_Q > 40$ MHz) signals than germanium(II) compounds ($C_Q = 10\text{-}30$ MHz), providing a useful indicator of the oxidation state at germanium. If this trend persists in additional examples, ^{35}Cl SSNMR spectroscopy could prove to be a useful diagnostic tool. In tin chemistry, oxidation states are often determined by Mössbauer spectroscopy; however, there is no appropriate gamma ray source for the Mössbauer spectroscopy of germanium compounds, adding to the value of the oxidation state information available from ^{35}Cl SSNMR spectroscopy. To

make ^{35}Cl SSNMR spectroscopy a truly reliable indicator of oxidation state, the oxidation states of the compounds included in this study should be confirmed by an independent method.

Given the observed relationship between the donor-germanium-chlorine angle and the value of the ^{35}Cl C_Q , the dependence on oxidation state could also arise from the covalency of the Ge–Cl bond, with more ionic bonds exhibiting smaller C_Q values. This is consistent with larger trends seen in chlorine chemistry, with the bulk of the existing material focusing on the ionic chlorides,⁴ which have considerably narrower spectra than covalent organic chlorides.¹³

Within the germanium(II) complexes, ligands with common donor atoms gave rise to signals with similar C_Q values, most likely due to the similar environment at germanium. The largest EFG tensor component of the majority of the germanium(II) complexes was oriented along the Ge–Cl bond, as determined by TPSSTPSS/6-311+G** model chemistry. This suggests that the general trend noted in related donors is likely due to similar germanium chlorine bond lengths due to similar overall structures. GeCl_2 -dioxane is a notable exception as the V_{33} component is instead orientated toward the adjacent germanium atom, which explains why the long range Ge–Cl interaction (which is the closest such interaction seen in this study) has the largest influence on C_Q . Similar tensor orientations were also observed for the germanium(IV) compounds, suggesting that there may be a similar relationship between C_Q and Ge(IV)–Cl bond length. Finally, the cationic tin complex also has an EFG tensor with the largest component oriented along the E–Cl bond, leading to the possibility of extending this study into the rest of group 14.

4.5 Experimental

4.5.1 Materials

GeCl₂·dioxane (**4.1**),¹⁷ **4.2**,³⁵ **4.3**,¹⁹ **4.4**,²⁰ **4.5**,²⁰ **4.6**,²¹ Mes₂GeCl₂ (**4.7**)³⁶ and Mes₃GeCl (**4.8**)³⁶ were all prepared according to literature procedures. The structure and purity of the materials were confirmed by comparison of solution state ¹H NMR spectra to the literature values. After the SSNMR experiments were complete, the ¹H NMR spectra of **4.2-4.6** were re-measured to determine that no decomposition had occurred during the experiment.

4.5.2 Solid-State NMR Spectroscopy

³⁵Cl SSNMR spectra were acquired on a Bruker Avance 900 MHz spectrometer at the *National Ultrahigh Field NMR Facility for Solids* (www.nmr900.ca). ³⁵Cl experimental setup and pulse calibrations were performed on 1 M KCl in H₂O and chemical shift referencing was performed relative to this sample (0 ppm relative to 0.1 M NaCl in H₂O at 0 ppm). Spectra were acquired under static conditions on a dual channel 7 mm low gamma probe operating in single resonance mode. With the exception of one spectrum of **4.1** (Figure 4.3) acquired using the QCPMG⁵ pulse sequence, all spectra were acquired using a WURST-QCPMG⁹ sequence with a 50 μs WURST-80 pulse for both excitation and refocusing and τ₁ = 25 μs, τ₂ = τ₃ = τ₄ = 26 μs. In those cases where piecewise acquisition was required, WURST-QCPMG subspectra were acquired at 200 kHz offset. Specific acquisition parameters for individual compounds are given in Table 4.5.

Table 4.5 ³⁵Cl SSNMR acquisition parameters for 4.1-4.9.

Compound	# of Subspectra	Transients per Subspectrum	# Loops	Recycle Delay (s)
4.1 (QCPMG)	13	512	64	5
4.1 (WURST-QCPMG)	2	256	64	5
4.2	9	1024	128	2
4.3	9 ^a	4096	128	2
4.4	1	1024	128	4
4.5	1	128	128	5
4.6	1	12288	96	2
4.7	17	512	128	2
4.8	8	2048	64	1
4.9	2	81920	32	1

^a An additional subspectrum was acquired over 28762 transients to confirm the position of the low frequency edge of the spectrum

Low field data were acquired on a Varian Infinity 400 spectrometer. WURST-QCPMG experimental setup and optimization were performed on solid CaCl₂·2H₂O and chemical shift referencing was performed relative to solid KCl (-3 ppm relative to 0.1 M NaCl in H₂O at 0 ppm). Spectra were acquired in a piecewise manner with a 150 kHz offset between subspectra. A 50 μs WURST-80 pulse was used for both excitation and refocusing.

4.5.3 NMR Spectral Simulations

Experimental NMR parameters were determined from analytical simulations using WSolids.³⁷ Errors were determined by visual comparison to the experimental spectrum. Starting from the best fit value, the parameter being evaluated was varied systematically in both directions while all others were held constant until a visible change was observed.

4.5.4 Theoretical Calculations

First principles calculations were performed using Gaussian 09³⁸ on the Shared Hierarchical Academic Research Computing Network (SHARCNET, www.sharcnet.ca).

Calculations were performed on a 4 core Opteron 2.4 GHz CPU with 32 GB memory or an 8 core Xeon 2.83 GHz CPU with 16 GB memory. CSA tensors were computed using the gauge-including atomic orbitals (GIAO) method. For structures with available X-ray structures, atom coordinates were taken directly from the CIF file and hydrogen positions optimized at the TPSS/TPSS/6-31G* level. The compounds without available crystal structures were fully geometry optimized at the same level. Basis sets and methods were used as indicated in the results and discussion. The results of the Gaussian calculations were analyzed using EFGShield.³⁹

Plane wave-pseudo potential calculations on compound **4.1** were performed using CASTEP through the Materials Data Studio interface on a single core Pentium 2.6 GHz CPU with 4 GB of memory. The NMR module was used to calculate the ⁷³Ge and ³⁵Cl EFG and CSA parameters. The gauge-including projector augmented-wave (GIPAW) method, which uses pseudo potentials and plane wave basis sets to simulate 3 dimensional lattices in crystalline materials, was employed. Unit cell parameters and atomic coordinates were taken directly from the crystal structure. Calculations were performed using ultra-soft pseudopotentials generated using the “on the fly” method included in CASTEP. The Generalized Gradient Approximation (GGA) with Perdew, Becke and Ernzhof (PBE) functional was used. A plane wave energy cutoff of 450 eV (coarse basis set accuracy) was used.

4.6 References

- (1) Power, P. P. *Nature* **2010**, *463*, 171.
- (2) Levason, W.; Reid, G.; Zhang, W. *Coord. Chem. Rev.* **2011**, *255*, 1319.
- (3) Pykko, P. *Mol. Phys.* **2008**, *106*, 1965.

- (4) Widdifield, C. M.; Chapman, R. P.; Bryce, D. L. *Annu. Rep. NMR Spectrosc.* **2009**, *66*, 195.
- (5) Larsen, F. H.; Jakobsen, H. J.; Ellis, P. D.; Nielsen, N. C. *J. Phys. Chem. A* **1997**, *101*, 8597.
- (6) Schurko, R. W.; Hung, I.; Widdifield, C. M. *Chem. Phys. Lett.* **2003**, *379*, 1.
- (7) O'Dell, L. A.; Rossini, A. J.; Schurko, R. W. *Chem. Phys. Lett.* **2009**, *468*, 330.
- (8) Siegel, R.; Nakashima, T. T.; Wasylshen, R. E. *J. Magn. Reson.* **2007**, *184*, 85.
- (9) O'Dell, L. A.; Schurko, R. W. *Chem. Phys. Lett.* **2008**, *464*, 97.
- (10) MacKenzie, K. J. D.; Smith, M. E. In *Multinuclear Solid-State NMR of Inorganic Materials*; 1st ed.; Pergamon: New York, **2002**, p 461.
- (11) Bryce, D. L.; Sward, G. D. *Magn. Reson. Chem.* **2006**, *44*, 409.
- (12) Butler, B. J.; Hook, J. M.; Harper, J. B. *Annu. Rep. NMR Spectrosc.* **2011**, *73*, 63.
- (13) Perras, F. A.; Bryce, D. L. *Angew. Chem. Int. Ed.* **2012**, *51*, 4227.
- (14) Greer, B. J.; Michaelis, V. K.; Terskikh, V. V.; Kroeker, S. *Can. J. Chem.* **2011**, *89*, 1118.
- (15) Nefedov, O. M.; Manokov, M. N. *Angew. Chem. Int. Ed.* **1966**, *5*, 1021.
- (16) Khulishov, V. I.; Bokii, N. G.; Struchkov, Y. T.; Nefedov, O. M.; Kolesnikov, S. P.; Perl'mutter, B. M. *Zh. Strukt. Khim.* **1970**, *11*, 71.
- (17) Leigh, W. J.; Harrington, C. R.; Vargas -Baca, I. *J. Am. Chem. Soc.* **2004**, *126*, 16105.
- (18) Baines, K. M.; Stibbs, W. G. *Coord. Chem. Rev.* **1995**, *145*, 157.
- (19) Rugar, P. A.; Jennings, M. C.; Baines, K. M. *Organometallics* **2008**, *27*, 5043.

- (20) Cheng, F.; Dyke, J. M.; Ferrante, F.; Hector, A. L.; Levason, W.; Reid, G.; Webster, M.; Zhang, W. *Dalton Trans.* **2010**, 39, 847.
- (21) Rupar, P. A.; Bandyopadhyay, R.; Cooper, B. F. T.; Stinchcombe, M. R.; Ragogna, P. J.; Macdonald, C. L. B.; Baines, K. M. *Angew. Chem. Int. Ed.* **2009**, 48, 5155.
- (22) Cheng, F.; Hector, A. L.; Levason, W.; Reid, G.; Webster, M.; Zhang, W. *Angew. Chem. Int. Ed.* **2009**, 48, 5152.
- (23) Denk, M. K.; Khan, M.; Lough, A. J.; Shuchi, K. *Acta Crystallogr., Sect. C* **1998**, C54, 1830.
- (24) Chapman, R. P.; Bryce, D. L. *Phys. Chem. Chem. Phys.* **2009**, 11, 6987.
- (25) Bryce, D. L.; Bultz, E. B. *Chem.-Eur. J.* **2007**, 13, 4786.
- (26) Rossini, A. J.; Mills, R. W.; Briscoe, G. A.; Norton, E. L.; Geier, S. J.; Hung, I.; Zheng, S.; Autschbach, J.; Schurko, R. W. *J. Am. Chem. Soc.* **2009**, 131, 3317.
- (27) Chapman, R. P.; Widdifield, C. M.; Bryce, D. L. *Prog. Nucl. Magn. Reson. Spectrosc.* **2009**, 55, 215.
- (28) Bancroft, G. M. *Mössbauer Spectroscopy: An Introduction for Inorganic Chemists and Geochemists*; Wiley: New York, **1973**.
- (29) Chapman, R. P.; Bryce, D. L. *Phys. Chem. Chem. Phys.* **2007**, 9, 6219.
- (30) Segall, M. D.; Lindan, P. J. D.; Probert, M. J.; Pickard, C. J.; Hasnip, P. J.; Clark, S. J.; Payne, M. C. *J. Phys.: Condens. Matter* **2002**, 14, 2717.
- (31) Sutrisno, A.; Hanson, M. A.; Rupar, P. A.; Terskikh, V. V.; Baines, K. M.; Huang, Y. *Chem. Commun.* **2010**, 46, 2817.

- (32) Tao, J.; Perdew, J. P.; Staroverov, V. N.; Scuseria, G. E. *Phys. Rev. Lett.* **2003**, *91*, 146401.
- (33) Adamo, C.; Barone, V. *J. Chem. Phys.* **1999**, *110*, 6158.
- (34) Stephens, P. J.; Devlin, F. J.; Chabalowski, C. F.; Frisch, M. J. *J. Phys. Chem.* **1994**, *98*, 11623.
- (35) Ruddy, A. J.; Rupar, P. A.; Bladek, K. J.; Allan, C. J.; Avery, J. C.; Baines, K. M. *Organometallics* **2010**, *29*, 1362.
- (36) Cooke, J. A.; Dixon, C. E.; Netherton, M. R.; Kollegger, G. M.; Baines, K. M. *Synth. React. Inorg. Met.-Org. Chem.* **1996**, *26*, 1205.
- (37) Eichele, K.; Wasylshen, R. E. In *WSolids1: Solid-State NMR Spectrum Simulation* **2001**.
- (38) Frisch, M. J.; Trucks, G. W.; Schlegel, H. B.; Scuseria, G. E.; Robb, M. A.; Cheeseman, J. R.; Scalmani, G.; Barone, V.; Mennucci, B.; Petersson, G. A.; Nakatsuji, H.; Caricato, M.; Li, X.; Hratchian, H. P.; Izmaylov, A. F.; Bloino, J.; Zheng, G.; Sonnenberg, J. L.; Hada, M.; Ehara, M.; Toyota, K.; Fukuda, R.; Hasegawa, J.; Ishida, M.; Nakajima, T.; Honda, Y.; Kitao, O.; Nakai, H.; Vreven, T.; Montgomery, J., J. A.; Peralta, J. E.; Ogliaro, F.; Bearpark, M.; Heyd, J. J.; Brothers, E.; Kudin, K. N.; Staroverov, V. N.; Kobayashi, R.; Normand, J.; Raghavachari, K.; Rendell, A.; Burant, J. C.; Iyengar, S. S.; Tomasi, J.; Cossi, M.; Rega, N.; Millam, N. J.; Klene, M.; Knox, J. E.; Cross, J. B.; Bakken, V.; Adamo, C.; Jaramillo, J.; Gomperts, R.; Stratmann, R. E.; Yazyev, O.; Austin, A. J.; Cammi, R.; Pomelli, C.; Ochterski, J. W.; Martin, R. L.; Morokuma, K.; Zakrzewski, V. G.; Voth, G. A.; Salvador, P.; Dannenberg, J. J.; Dapprich, S.;

Daniels, A. D.; Farkas, Ö.; Foresman, J. B.; Ortiz, J. V.; Cioslowski, J.; Fox, D. J.; Revision A1 ed.; Gaussian Inc.: Wallingford, CT, **2009**.

(39) Adiga, S.; Aebi, D.; Bryce, D. L. *Can. J. Chem.* **2007**, *85*, 496.

Chapter 5 Solid-State ^{119}Sn NMR Studies of Cationic Tin Cryptand Complexes[†]

5.1 Introduction

In recent years, there has been considerable interest in the chemistry of the heavier group 14 cations.¹ While the chemistry of carbocations is well established, the structure and reactivity of the heavier congeners can be strikingly different. While the +4 oxidation state is strongly preferred by carbon, the +2 oxidation state becomes increasingly stable as one descends the group.

Complex **5.1**, a germanium(II) dication encapsulated in a cryptand, is notable as the first example of a non-metal cation stabilized by a cryptand.² Direct observation of the germanium centre in this unusual species could potentially provide insight into the bonding situation at germanium. However, due to the inherent challenges of ^{73}Ge NMR spectroscopy, it was desirable to first assess the information available from SSNMR spectroscopy by examining a more accessible nucleus. As the rest of the group 14 elements possess NMR active isotopes with more favourable properties than ^{73}Ge , we also investigated the NMR spectroscopy of analogues containing other elements.

[†] A version of this chapter has been published. Jessica C. Avery, Margaret A. Hanson, Rolfe H. Herber, Kamila J. Bladec, Paul A. Rugar, Israel Nowik, Yining Huang, Kim M. Baines. Cationic Cryptand Complexes of Tin(II). *Inorg. Chem.* **2012**, *51*, 7306. Reproduced with permission from the American Chemical Society.

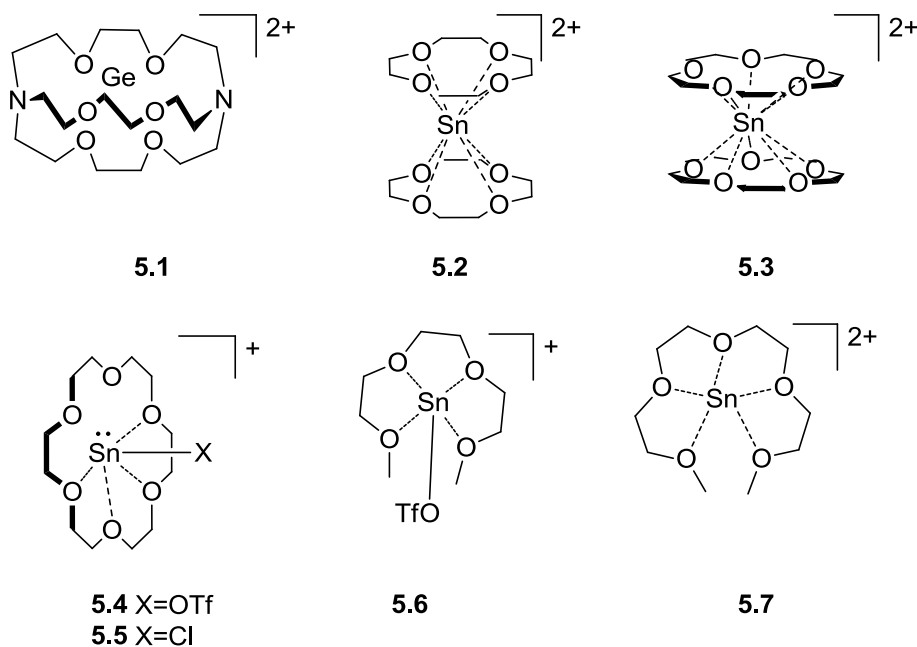


Figure 5.1 A germanium cryptand complex and examples of macrocyclic tin complexes. Counterions are ^-OTf , with the exception of **5.5** for which the counterion is $SnCl_3^-$.

In contrast to germanium, tin possesses three spin $\frac{1}{2}$ isotopes (^{115}Sn , ^{117}Sn and ^{119}Sn).³ Of these, ^{115}Sn is generally not studied due to the extremely low (0.32%) natural abundance. The other two isotopes have more reasonable abundances of 7.86% (^{117}Sn) and 8.59% (^{119}Sn). In addition to the higher abundance, ^{119}Sn also has a slightly higher gyromagnetic ratio ($\nu_L = 142.5$ MHz and 149.1 MHz, respectively, at 9.4 T), making it the preferred nucleus for tin NMR spectroscopy.

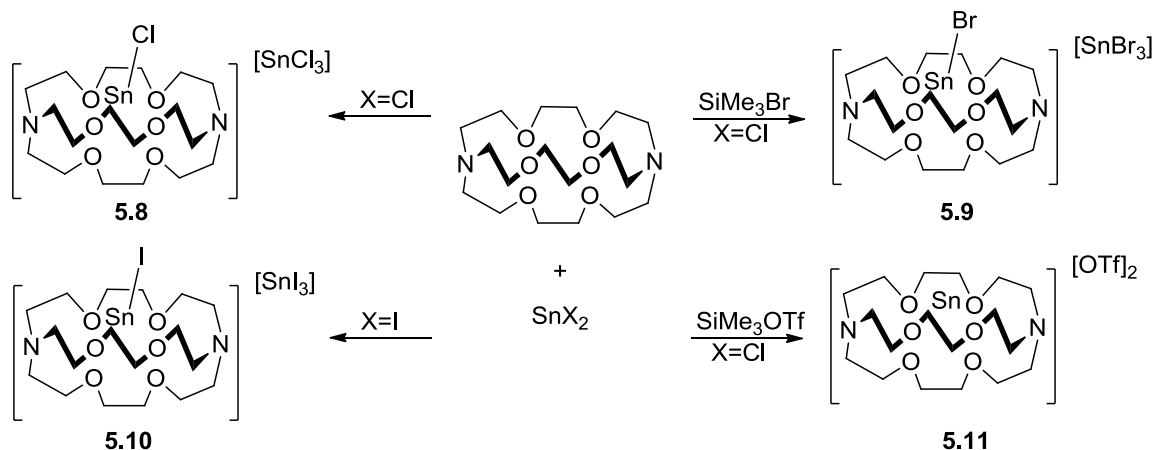
Related complexes stabilized by crown ethers (**5.2-5.5**)⁴ and glymes (**5.6** and **5.7**)⁵ (Figure 5.1) have been previously studied by X-ray crystallography, Mössbauer spectroscopy, solid-state NMR spectroscopy and density functional theory (DFT) calculations. Solid-state ^{119}Sn NMR spectroscopy proved to be a powerful structural probe. The experimental parameters of **5.2-5.7** are summarized in Table 5.1. In general, the dicationic triflate complexes (**5.2**, **5.3** and **5.7**) yielded narrow signals with very

shielded chemical shifts. The monocationic chloride complex **5.5** and **5.6** gave rise to a broader signal at a higher frequency,^{4,5} while **5.4**, described as monocationic, exhibited NMR parameters more closely resembling those of the dicationic complexes.

Table 5.1 Experimental ^{119}Sn SSNMR parameters for crown ether and glyme complexes of tin(II).⁵

Compound	δ_{iso} (ppm)	Ω (ppm)	κ
5.2	-1405	267	0.09
5.3	-1721	140	0.85
5.4	-1578	325	0.15
5.5 (cation)	-840	1700	1
5.5 (anion)	-58	814	1
5.6	-1436	375	0.27
5.7	-1448	283	-0.26

The reactivity of tin with cryptand[2.2.2] was explored in our lab.⁶ The addition of tin dichloride to cryptand[2.2.2] (Scheme 5.1) yielded a monocationic complex with one chlorine atom still bound to tin [(CryptSnCl)SnCl₃] (**5.8**) as determined by X-ray crystallography (Figure 5.2A).⁷ The complex featured a tin atom encapsulated within the distorted cryptand with a covalent bond to chloride. The charge was balanced by a SnCl₃⁻ anion. The chloride was replaced by bromide (**5.9**) by the addition of trimethylsilyl bromide to the reaction mixture. Complex **5.10** was prepared using an analogous route from SnI₂. Attempts to synthesize **5.10** from SnCl₂ using trimethylsilyl iodide resulted in the formation of a solid with a different Raman spectrum (**5.10'**). The use of the weakly coordinating triflate anion (**5.11**) was also investigated by adding cryptand[2.2.2] to a solution of Sn(OTf)₂. An X-ray structure was obtained for the bromide derivative, revealing the structure to be similar to that of the chloride compound (Figure 5.2B). Attempts to grow X-ray quality single crystals of the iodide derivative were unsuccessful.



Scheme 5.1 Synthesis of tin cryptand derivatives.

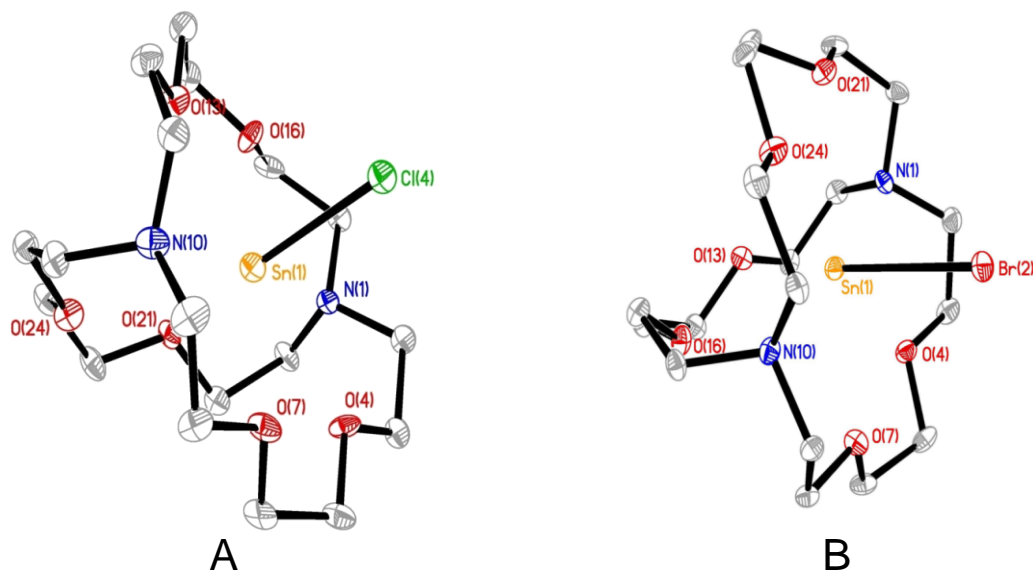


Figure 5.2 X-ray structures of A) $[\text{CryptSnCl}][\text{SnCl}_3]$ and B) $[\text{CryptSnBr}][\text{SnBr}_3]$. Anions and hydrogen atoms have been omitted for clarity.

Crystallographic examination of the triflate derivative indicated two different tin sites, one monocationic and the other a dicationic species (Figure.5.3).⁷ However, it was not clear from these data whether the triflate was actually covalently bound and whether the tin was best described as being mono- or dicationic.

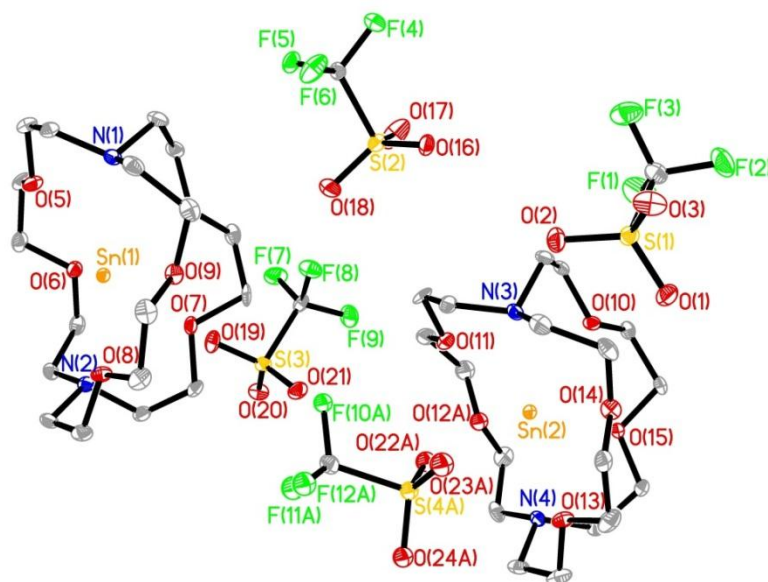


Figure.5.3 X-ray structure of the triflate complex showing two distinct tin sites.

The cryptand complexes **5.8-5.11** were also characterized by ^1H and ^{13}C solution state NMR spectroscopy, electrospray ionization mass spectrometry (ESI-MS), Raman spectroscopy and Mössbauer spectroscopy. However, despite the extensive characterization, there remained several questions about the compounds. There was no X-ray structure determined for **5.10** and even the nature of the anion was ambiguous. While we were able to obtain a crystal structure for **5.11**, the degree of interaction between the triflate and the tin, and thus, whether the complex was mono- or dicationic, was ambiguous. ^1H and ^{13}C solution state NMR spectroscopy revealed only that the cryptand remained intact after the formation of the complex and nothing about the encapsulated metal. It was possible to confirm the structure of the anions through Raman spectroscopy, but the Sn–X stretch of the cation was not observed. The ESI-MS spectrum of **5.11**

showed isotopic clusters consisted with both a monocation and a dication. It was hoped that ^{119}Sn NMR spectroscopy would be able to provide additional insight into these structures; however, it was not possible to obtain a solution state spectrum of any of the complexes, most likely due to rapid CSA relaxation. In light of the recent work with cationic tin(II) crown ether complexes,^{4,5} the cryptand complexes were examined in the solid state by NMR spectroscopy.

5.2 Results and Discussion

5.2.1 Halide Complexes

^{119}Sn solid-state NMR data for **5.8-5.10** were collected using both magic angle spinning (MAS) and static conditions. Isotropic shifts were determined by acquiring MAS spectra at two different spinning speeds, except in the case of the iodide complex **5.10** which was determined by spectral simulation. The parameters are summarized in Table 5.2. The overall tin concentration in these complexes is low due to the large size of the encapsulating cryptand, leading to noisy spectra even after acquisition of the data overnight. However, due to the more favourable NMR properties of ^{119}Sn in comparison to ^{73}Ge , the low concentration did not prove to be an insurmountable barrier.

Table 5.2 Spectral ^{119}Sn SSNMR parameters of **5.8-5.11** and various stannates.

Complex	Anion			Cation		
	δ_{iso} (ppm)	Ω (ppm)	κ	δ_{iso} (ppm)	Ω (ppm)	κ
5.8	5(1)	880(100)	1	-980(1)	1060(100)	0.75(10)
5.9	165(1)	890(100)	0.95(5)	-920(1)	1180(100)	0.7(1)
5.10	50(50)	700(100)	0.75(10)	-810(50)	1400(200)	0.8(1)
5.11	---	---	---	-1533(1)	165(10)	0.2(1)
[NBu ₄][SnCl ₃]	2(5)	805(50)	1	---	---	---
[NBu ₄][SnBr ₃]	125(1)	790(100)	0.8(1)	---	---	---
[NBu ₄][SnI ₃]	250(50)	900(100)	0.8(1)	---	---	---
[NBu ₄][SnCl ₂]	130(50)	1000(100)	0.45(10)	---	---	---

The MAS spectrum of **5.8** (Figure 5.4) is composed of two signals with isotropic shifts of 5 ppm and -980 ppm. An isotropic shift of 5 ppm for the SnCl₃⁻ anion is consistent with solution state data for the SnCl₃⁻ anion;⁸ however, it differs from that reported for crown ether complex **5.5** (Table 5.1, -58 ppm). The MAS SSNMR spectrum of **5.5** was recorded at a much lower spinning speed (11 kHz versus 17 kHz), leading to the possibility of temperature effects, which could account for the difference in isotropic shift.

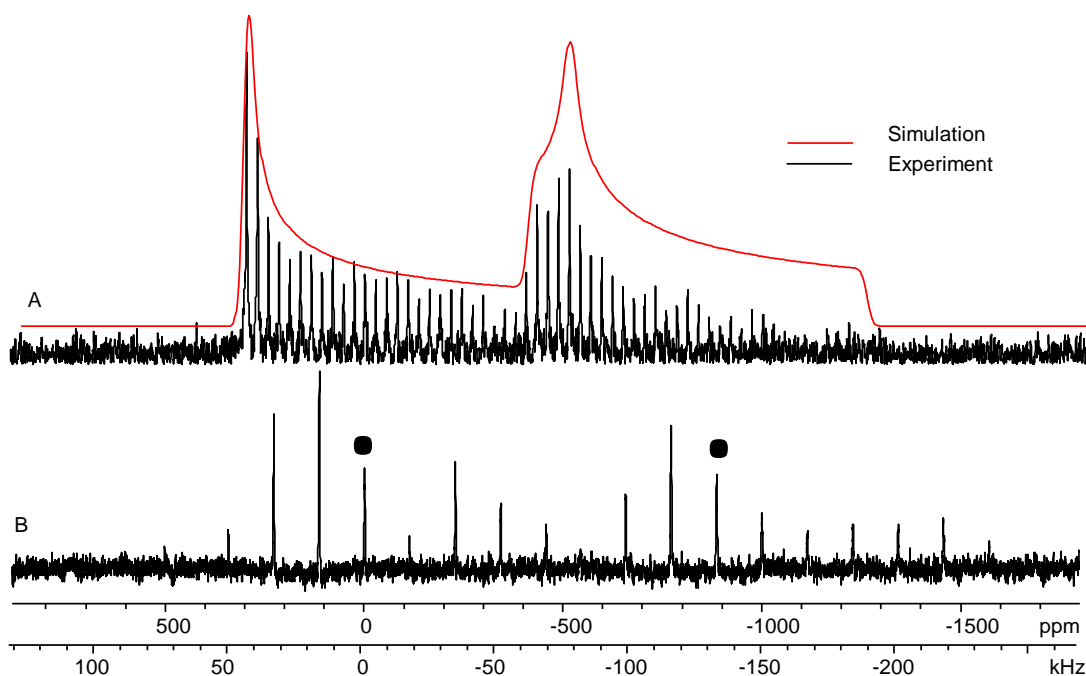


Figure 5.4 A) Static ^{119}Sn WURST-CPMG spectrum of **5.8** at 9.4 T. The solid trace indicates the simulated spectrum. B) ^{119}Sn MAS spectrum ($\nu_{\text{rot}} = 17$ kHz) of **5.8** at 9.4 T. The solid dots indicate the isotropic shifts of the signals.

The assignment was confirmed by preparing the anion independently as the $[\text{NBu}_4][\text{SnCl}_3]$ salt.⁹ The ^{119}Sn SSNMR spectrum of the ammonium salt closely resembles the less shielded signal of the complex **5.8** (Figure 5.5). The more shielded signal must, therefore, arise from the cationic portion of **5.8**. While not consistent with the expected chemical shift of a stannylum ion,¹⁰ the chemical shift of the tin(II) cationic crown ether complexes **5.2-5.7** were also considerably shielded.^{4,5} This has been attributed to the high s-character of the tin lone pair leading to a relatively small paramagnetic shielding term. The more negative isotropic shift value for **5.8** when compared to the cationic portion of crown ether complex **5.5** suggests that there may be greater s character in the lone pair on Sn in **5.8**.

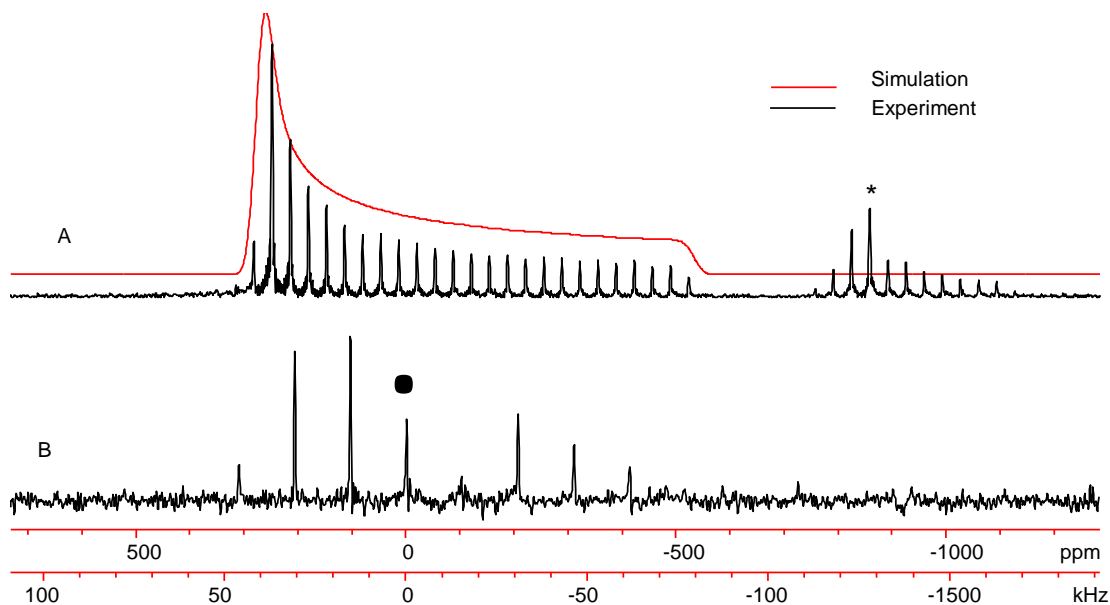


Figure 5.5 A) Static ^{119}Sn WURST-CPMG spectrum of $[\text{NBu}_4][\text{SnCl}_3]$ at 9.4 T. The solid trace indicates the simulated spectrum. An impurity of SnCl_2 is marked with an asterisk. B) ^{119}Sn MAS spectrum at 9.4 T ($\nu_{\text{rot}}=15.4$ kHz).

Due to the large CSA pattern observed in the MAS spectrum of **5.8**, the WURST-CPMG pulse sequence was employed for the acquisition of the static spectrum. The WURST-CPMG sequence is based on the Carr-Purcell-Meiboom-Gill pulse sequence; however, rather than hard $\pi/2$ and π pulses, adiabatic WURST (Wideband Uniform Rate Smooth Truncation) pulses are used for both excitation and refocusing purposes. By using these shaped pulses, it is possible to excite a larger region than would be possible with a hard pulse. Additionally, the use of refocusing pulses enhances the signal-to-noise ratio of the spectrum.

From the static spectrum of **5.8** (Figure 5.4A), it is apparent that the signal attributed to the SnCl_3^- anion arises from Sn in an axially symmetric environment ($\kappa = 1$), consistent with the C_3 axis through the trichlorostannate anion as observed crystallographically.

The skew value of the low frequency signal (0.75) is consistent with the absence of

specific site symmetry about tin in the cation in the structure. Both signals exhibit considerable chemical shielding anisotropy ($\Omega = 880$ ppm and 1060 ppm, respectively) consistent with the absence of spherical symmetry about both tin atoms in the complex differing from what was observed in the crown ether complexes **5.2** and **5.3**,²⁴ which have a small span and a near zero skew due to the spherical arrangement of the oxygen atoms in the sandwich complexes. In the case of **5.8**, the attached chloride disrupts both spherical and axial symmetry leading to a greater orientation dependence. The ^{119}Sn spectrum of **5.4** more closely resembles the dicationic complexes, in contradiction to the covalent bond to the triflate. The smaller span of **5.8**, when compared to the crown ether analogue **5.5**, suggests that the lone pair has lower p-character, and thus **5.8** is expected to be less reactive than **5.5**.

While the MAS spectrum of **5.9** (Figure 5.6) exhibits a considerably poorer signal-to-noise ratio attributed to the observed shorter T_2 relaxation as well as the lower overall tin concentration in the same sample volume compared to **5.8**, it bears an overall resemblance to the spectrum of the chloride derivative. The spectrum once again consists of two broad signals. The less shielded signal, with an isotropic shift of 165 ppm, is assigned to the tribromostannate anion.⁸ In this case, the anion site falls slightly short of perfect axial symmetry ($\kappa = 0.95$), consistent with slight deviations from C_{3v} symmetry observed in the X-ray structure of this anion.⁹ The isotropic shift of the lower frequency signal is similar to that of **5.8** ($\delta_{\text{iso}} = -920$ ppm) and exhibits no specific symmetry ($\kappa = 0.7$).

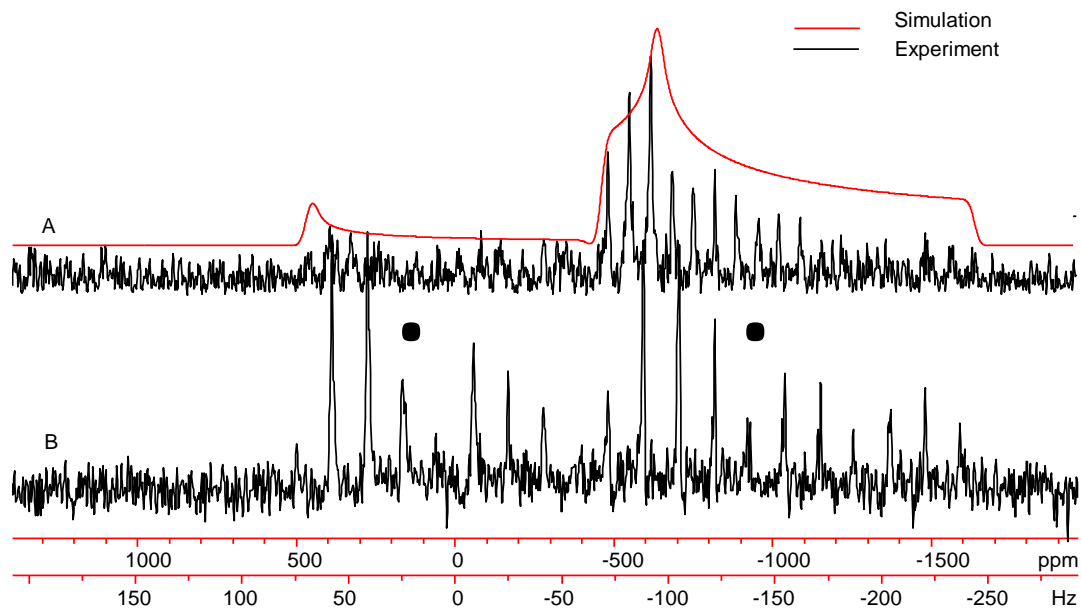


Figure 5.6 A) Static ^{119}Sn WURST-CPMG spectrum of **5.9** at 9.4 T. The solid trace indicates the simulated spectrum. B) ^{119}Sn MAS spectrum at 9.4 T ($\nu_{\text{rot}} = 15.5$ kHz).

The nature of the anionic site was once again confirmed by comparison to the ^{119}Sn SSNMR spectrum of the tetrabutylammonium salt (Figure 5.7). While the isotropic shift of $[\text{NBu}_4][\text{SnBr}_3]$ ($\delta_{\text{iso}} = 125$ ppm) differed from that seen in **5.9**, the overall lineshape was within experimental error. The difference in isotropic shift suggests some degree of interaction between the cation and anion in complex **5.9**.

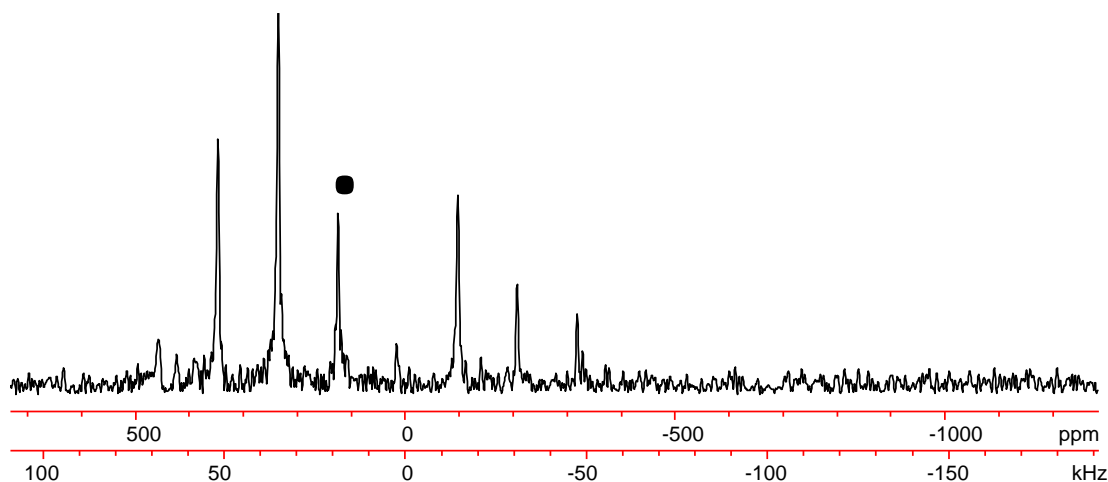


Figure 5.7 ^{119}Sn MAS spectrum of $[\text{NBu}_4][\text{SnBr}_3]$ at 9.4 T ($\nu_{\text{rot}}=15.5$ kHz).

The static WURST-CPMG spectrum of **5.9** (Figure 5.6A), at first, appears to consist of only one signal. However, a second, considerably weaker signal is present in the region expected for the signal derived from the anion in **5.9** after extended (3 days) acquisition. Likely, the anion in **5.9** relaxes more rapidly than the cation due to the large quadrupole moment of the three covalently bound bromine atoms. With a much shorter T_2 , the signal receives considerably less signal enhancement than the cation as the signal is only refocused a limited number of times before true decay. Examination of the FID of the MAS spectrum of $[\text{NBu}_4][\text{SnBr}_3]$ reveals that the signal decays within 0.6 ms, while the FID of $[\text{NBu}_4][\text{SnCl}_3]$ continues for 1 ms. The major signal in the WURST-CPMG spectrum of **5.9**, as expected from the MAS spectrum of **5.9**, very closely resembles the cationic portion of **5.8**. As the ^{119}Sn spectra of **5.8** and **5.9** very closely resembled each other, it was hoped that ^{119}Sn SSNMR spectroscopy would also offer insight into the unknown structure of **5.10**.

Attempts to obtain an MAS spectrum of **5.10** were ultimately unsuccessful, most likely due to the longer Sn–I bond lengths leading to a lower tin density in this sample compare

to **5.8** and **5.9**. However, it was possible to acquire a static WURST-CPMG spectrum (Figure 5.8). The signal at $\delta_{\text{iso}} = -810$ ppm exhibited a similar lineshape ($\Omega = 1400$ ppm, $\kappa = 0.8$) to the cationic sites in the ^{119}Sn SSNMR spectra of **5.8** and **5.9**. The isotropic shift of the signal is not as shielded as those of **5.8** and **5.9**, possibly due to a smaller positive charge on the nucleus or less s-character in the tin lone pair. Either phenomenon would lead to a greater paramagnetic shielding term. However, the larger span of the signal suggests that lower s-character in the lone pair is the more likely explanation, as greater p-character in the HOMO lone pair has been shown to lead to larger spans in tin(II) compounds.^{11,12} Due to the absence of an MAS spectrum, the standard uncertainties in the parameters of **5.10** are much greater, but the overall lineshape is undeniably similar to the cationic signals of **5.8** and **5.9**. Similar to **5.9**, the signal attributed to the anion ($\delta_{\text{iso}} = 50$ ppm) is less intense than that attributed to the cation. The signal at $\delta_{\text{iso}} = 50$ ppm has the expected lineshape ($\Omega = 700$ ppm, $\kappa = 0.75$) for a system distorted from axial symmetry.

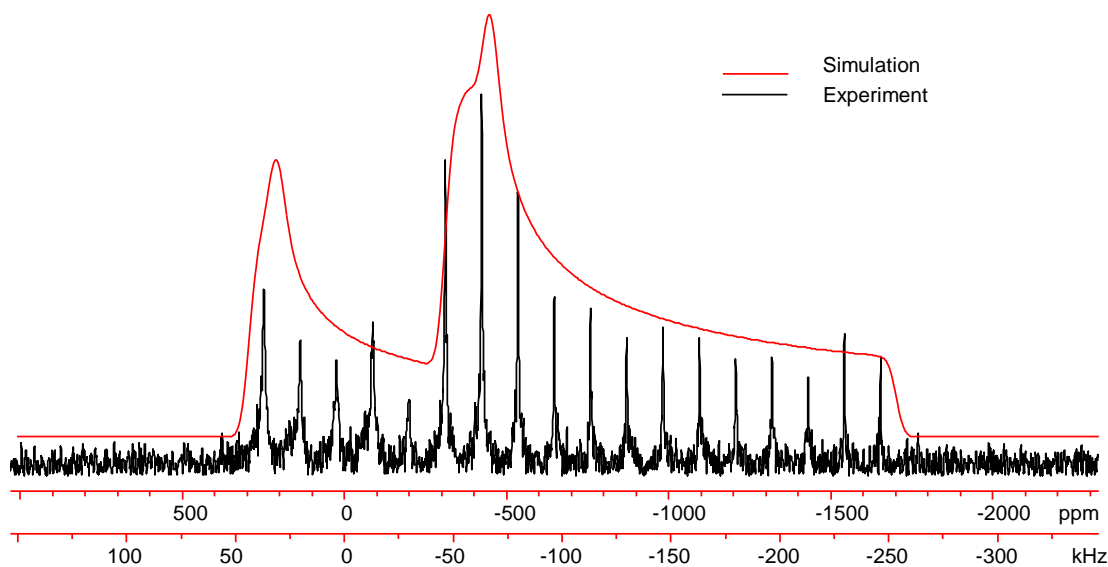


Figure 5.8 Static ^{119}Sn WURST-CPMG spectrum of **5.10** at 9.4 T. The solid trace indicates the simulated spectrum.

The triiodostannate anion was prepared independently as the $[\text{NBu}_4][\text{SnI}_3]$ salt.⁹ The ^{119}Sn static WURST-CPMG spectrum of the salt (Figure 5.9) resembled the deshielded signal of **5.10**, although the isotropic shift was considerably less shielded ($\delta_{\text{iso}} = 250$ ppm, $\Omega = 900$ ppm, $\kappa = 0.8$).

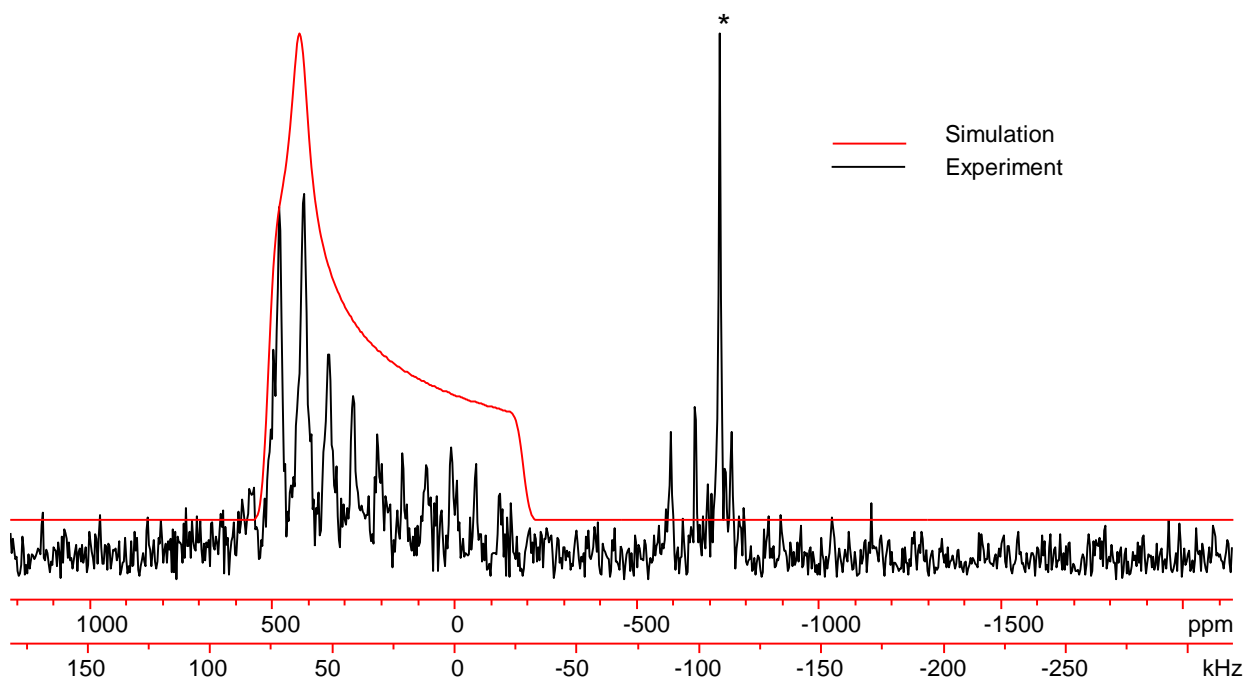


Figure 5.9 Static ^{119}Sn WURST-CPMG spectrum of $[\text{NBu}_4][\text{SnI}_3]$ at 9.4 T. The solid trace indicates the simulated spectrum. An impurity of SnI_2 is indicated with an asterisk.

An attempt was made to prepare **5.10** by the addition of trimethylsilyl iodide to a solution of SnCl_2 and cryptand[2.2.2] (analogous to the synthesis of **5.9**), rather than by the addition of cryptand[2.2.2] to SnI_2 . A yellowish solid was obtained (**5.10'**) that had virtually identical ^1H NMR and Raman data to those of **5.10** but significantly different ^{119}Sn SSNMR and ESI-MS spectra. The ^{119}Sn SSNMR WURST-CPMG spectrum of the solid contained two apparent signals (Figure 5.10). While the lineshape of the upfield

signal at $\delta_{\text{iso}} -945$ resembles that of the analogous signal in the ^{119}Sn SSNMR spectrum of **5.10**, the apparent isotropic shift is more shielded, closer to the values observed for the cations in **5.8** and **5.9**. The downfield signal differed considerably from the analogous signal assigned to the anion of **5.10**. While the isotropic shift of the downfield signal initially appeared reasonable ($\delta_{\text{iso}} = 0$ ppm), the overall lineshape ($\Omega = 880$ ppm, $\kappa = -0.3$) was not consistent with the distorted axially symmetric geometry expected for the triiodostannate anion,⁹ leading to the conclusion that the anion in this solid cannot be SnI_3^- .

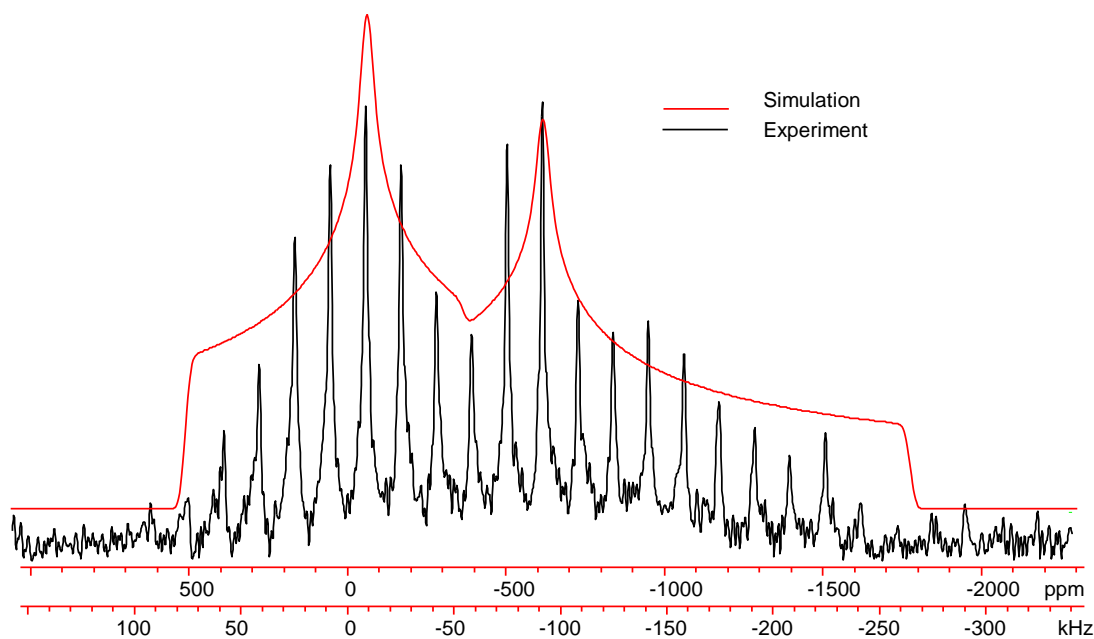


Figure 5.10 Static ^{119}Sn WURST-CPMG spectrum at 9.4 T of **5.10'** prepared from SnCl_2 via halogen exchange. The solid trace indicates the simulated spectrum.

A signal, assigned to the SnClI_2^- , was observed in the ESI negative mode mass spectrum of **5.10'**, and thus, the tetrabutylammonium salt of SnClI_2^- was prepared and its ^{119}Sn SSNMR WURST-CPMG spectrum recorded (Figure 5.11). As expected from the lower symmetry, the skew value does not correspond to any specific site symmetry ($\kappa = 0.45$).

These data suggest that **5.10** is a mixture of different anions and cations. The experimental ^{119}Sn SSNMR spectrum of **5.10** (Figure 5.12) was reproduced using a combination of the parameters for both the cation of **5.8** and **5.9** and a combination of the parameters for the SnI_3^- and SnClI_2^- anions plus the parameters for a small amount of SnO_2 . This is a clear example of SSNMR spectroscopy providing information that was not available from other analytical techniques. While mass spectrometry did suggest the presence the $[\text{CryptSnCl}]^+$ and $[\text{CryptSnI}]^+$ cations and the SnClI_2^- anion, this was not conclusive as there was the possibility of halogen exchange occurring *in situ*. However, the signals observed in the NMR spectrum could only arise from species after the initial reaction. On the basis of the ^{119}Sn NMR data, we conclude that the attempted preparation of **5.10** via halogen exchange was not successful. The halide exchange in both the cation and anion apparently did not go to completion, and thus, the preparation of **5.10** from SnI_2 is the preferred method.

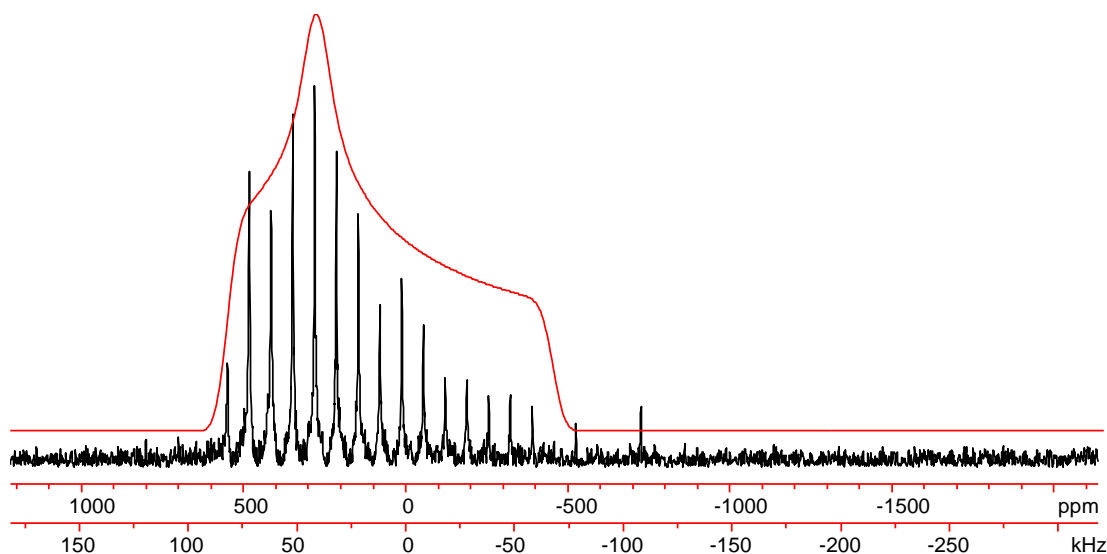


Figure 5.11 Static ^{119}Sn WURST-CPMG spectrum of $[\text{NBu}_4][\text{SnClI}_2]$ at 9.4 T. The solid trace indicates the simulated spectrum.

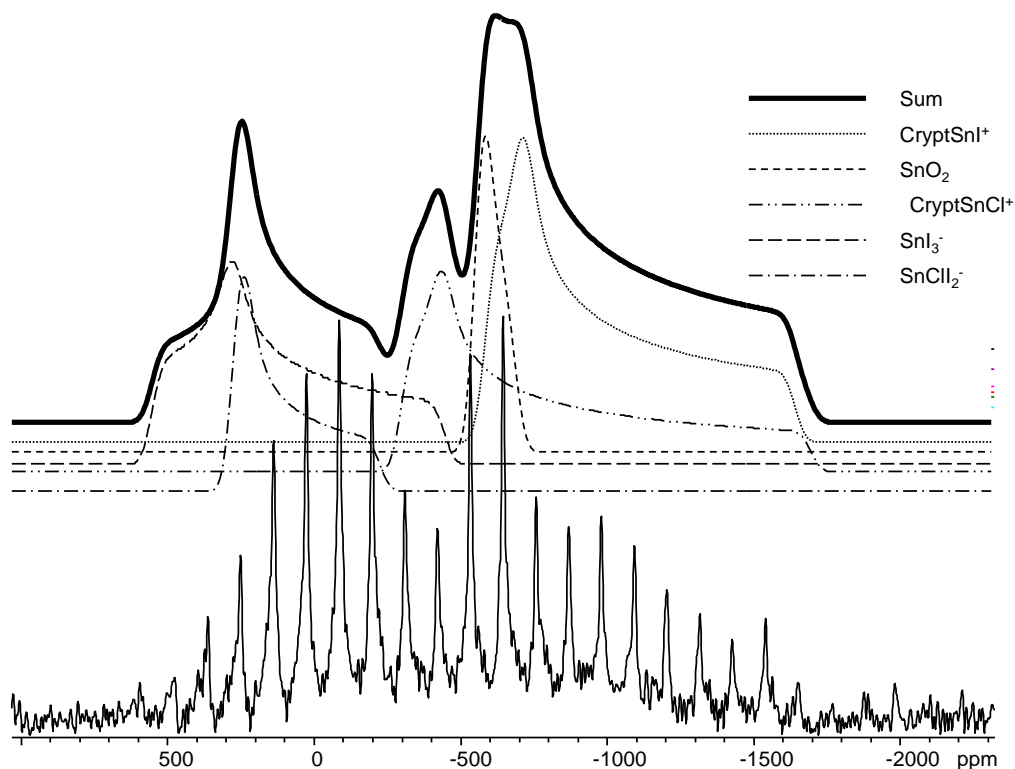


Figure 5.12 Simulation of the ^{119}Sn spectrum of **5.10'** using parameters from multiple cations and anions.

DFT calculations of the ^{119}Sn NMR shieldings of **5.8-5.10** were performed using the Amsterdam Density Functional (ADF)¹³ software package using the VWN-BP functional. The all electron quadruple zeta basis set plus polarization (Q4ZP) was employed for tin, while the triple zeta doubly polarized (T2ZP) basis set was used for all other atoms. The Zeroth Order Regular Approximation (ZORA) was employed to account for relativistic effects, including the spin orbit term. This methodology was selected as it provided good agreement with the experimental NMR parameters of the crown ether complexes **5.2-5.5**.^{4,5} While ^{119}Sn chemical shieldings have historically been challenging to determine computationally, the inclusion of relativistic effects in computational modelling offers considerable improvement. A previous study of tin halides has shown that the zeroth order regular approximation (ZORA) method included in ADF and the specifically

optimized basis sets allows for calculation of the spin orbit term, and thus, accurate reproduction of experimental chemical shifts.¹⁴

Geometry optimizations of unknown structures were carried out in Gaussian 09¹⁵ using the TPSS/PSS functional and the Lan2DZ basis set on all atoms. Shielding values were converted to chemical shifts relative to the calculated shielding of SnMe₄.

In general, the parameters of the anionic sites were more closely reproduced by theory than the cationic sites in complexes **5.8-5.10**. In the case of the trichlorostannate of **5.8**, the skew value was exactly reproduced, with both theory and experiment giving an exactly axially symmetric value of 1. The calculated span for SnCl₃⁻, 855 ppm, is within experimental error of the experimental value of 880 ppm. The cationic site of **5.8** was predicted to be much closer to axial symmetry with a skew value of 0.9 versus the 0.75 determined experimentally. The span of the cationic signal, **5.8**⁺, is overestimated ($\Omega = 1535$ ppm vs 1060 ppm) considerably.

A similar situation is observed in the case of **5.9**. The experimental parameters for the anion ($\Omega = 890$ ppm, $\kappa = 0.95$) are reproduced ($\Omega = 806$ ppm, $\kappa = 0.89$) within experimental error. Once again the cationic site of **5.9** is not quite as closely reproduced, with an overestimated span ($\Omega = 1801$ ppm vs 1180 ppm) and a more axial geometry ($\kappa = 0.89$ vs 0.7).

Calculations for the iodide complex, **5.10**, were carried out using a geometry-optimized structure which closely resembled **5.8** and **5.9**. The predicted skew for the signal assigned to [SnI₃]⁻ ($\kappa = 0.94$) was much closer to what would be expected for an anion with axially symmetric geometry ($\kappa = 1$) than the experimentally observed value for the

[NBu₄][SnI₃] salt ($\kappa = 0.8$), most likely because the gas-phase optimization of the anion produces a more symmetrical structure than what exists in the solid state. The overestimated span can, similarly, be attributed to the difficulties in reproducing the experimental parameters exactly without an X-ray structure. Of the theoretical parameters for the cationic site of **5.10** ($\Omega = 1377$ ppm, $\kappa = 0.58$), the span is within experimental error ($\Omega = 1400(200)$ ppm, $\kappa = 0.8(1)$), confirming that the structure of the cationic site is very similar to that of the chloride and bromide derivatives. The skew value is underestimated, but does correctly reflect the lack of specific site symmetry at time. Geometry optimization of the complex containing the SnClI₂⁻ anion rather than the SnI₃⁻ anion gives rise to almost no difference in the NMR parameters calculated for the cation. The parameters of the anion ($\Omega = 845$ ppm, $\kappa = 0.38$) are in reasonable agreement with those observed for the [NBu₄][SnClI₂] salt, with the skew falling within experimental error and the span being within 1.5 times the experimental error.

5.2.2 Triflate Complex

The ¹¹⁹Sn SSNMR static spectrum (Figure 5.13A) of **5.11** differed considerably from the analogous spectra of the halide complexes, **5.8-5.10**. The signal was considerably narrower with a width at half height of only 30 kHz, and therefore, the spectrum was acquired using a static echo sequence. The much narrower spectrum, with $\kappa = 0.2$ and $\Omega = 165$ ppm, is consistent with what was observed for the tin crown ether complexes.^{4,5} The skew is consistent with the glyme complexes **5.6** and **5.7** ($\kappa = 0.27, -0.26$), which lack specific site symmetry, much like the environment presented by the distorted cryptand. Additionally, the isotropic shift ($\delta_{\text{iso}} = -1533$ ppm) of **5.11** is within the range of the dicationic complexes **5.2** ($\delta_{\text{iso}} = -1405$ ppm), **5.3** ($\delta_{\text{iso}} = -1721$ ppm) and **5.7** ($\delta_{\text{iso}} =$

1448 ppm).⁴ The more negative isotropic shift value and smaller span when compared to the halide complexes both suggest that the lone pair of **5.11** has greater s-character than the lone pairs of the halide complexes **5.8-5.10**. Among the crown ether and glyme complexes, only **5.3** exhibits a span consistent with greater s-character.

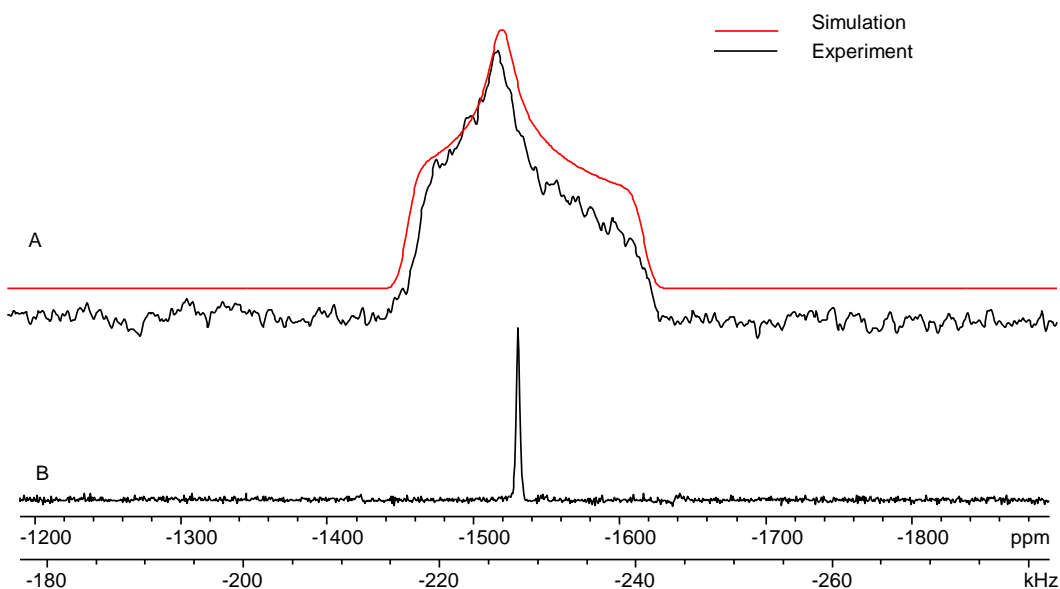


Figure 5.13 A) Static ^{119}Sn spin echo spectrum of **5.11** at 9.4 T. The solid trace indicates the simulated spectrum. B) ^{119}Sn MAS spectrum ($\nu_{\text{rot}} = 16$ kHz) of **5.11** at 9.4 T.

In contradiction to the two crystallographically distinct tin sites observed in the X-ray structure, only one ^{119}Sn signal was observed under MAS and static conditions (Figure 5.13B). This is further supported by the solid state ^{19}F NMR spectrum of **5.11** (Figure 5.14), which features two fluorine resonances rather than the four expected on the basis of the crystal structure. Both fluorine resonances possess isotropic shifts ($\delta_{\text{iso}} = -78.3$ ppm and -80.5 ppm) consistent with ionic triflates,¹⁶ despite the appearance in the X-ray structure that one of the triflates was covalently bound to tin.

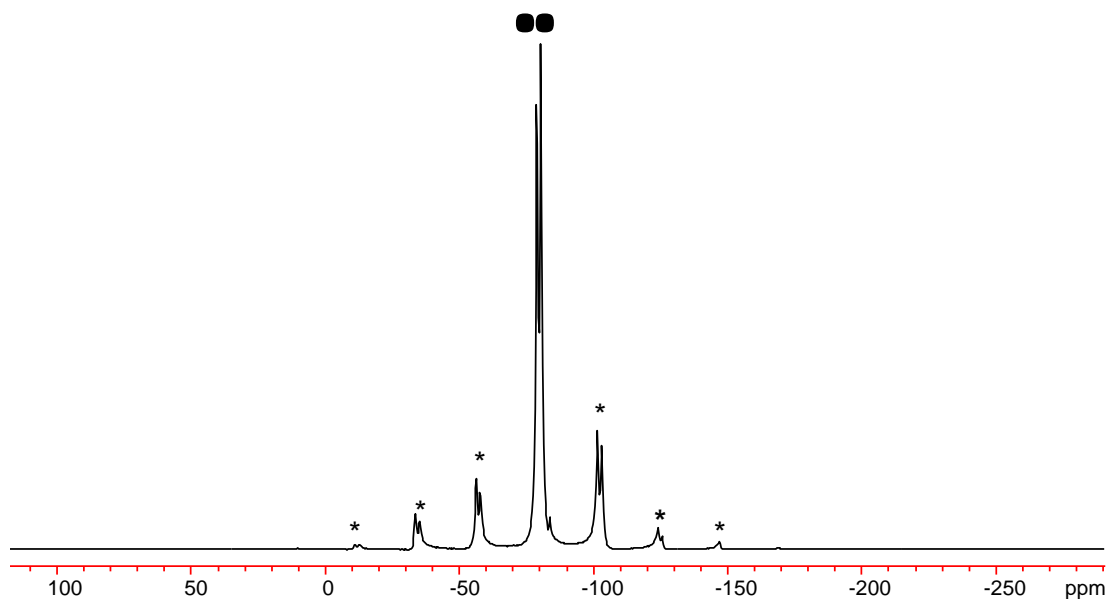


Figure 5.14 ^{19}F MAS spectrum ($\nu_{\text{rot}} = 10$ kHz) of **5.5** at 9.4 T. Isotropic shifts are designated with solid dots, while the asterisks indicate spinning sidebands.

Theoretical parameters for both crystallographically distinct tin atoms, Sn(1) (dicationic) and Sn(2) (monocationic), from the X-ray structure were determined using the same computational techniques as the halide derivatives. While neither set of parameters exactly matched experiment ($\delta_{\text{iso}} = -1533$ ppm, $\Omega = 165$ ppm, $\kappa = 0.2$), as illustrated in Figure 5.15, the calculated parameters for Sn(1) ($\delta_{\text{iso}} = -1520$ ppm, $\Omega = 275$ ppm, $\kappa = -0.05$) more closely resembled the experimental data for **5.11** than the calculated parameters for Sn(2) ($\delta_{\text{iso}} = -1165$ ppm, $\Omega = 531$ ppm, $\kappa = 0.11$). The theoretical parameters for Sn(2) more closely resemble those observed experimentally for **5.8-5.10**, with a more deshielded isotropic shift and a larger span. While they do exhibit the largest spans of the crown ether and glyme complexes, these calculations predict that a covalently bound triflate would introduce greater broadening and deshielding than seen in

these complexes. On the basis of the spectroscopic data, it is thus more likely that **5.4** and **5.6** are actually dicationic complexes with very little interaction with the nearby triflate.

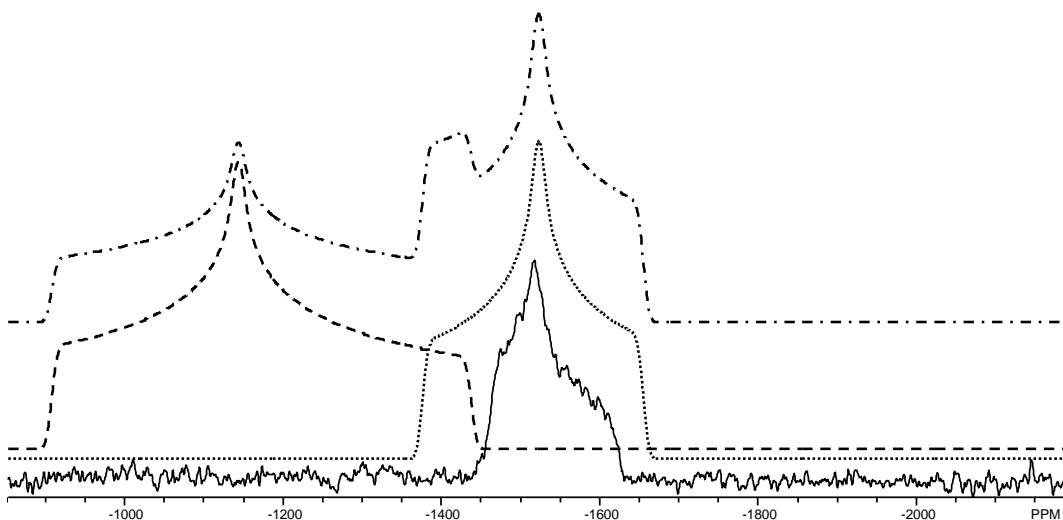


Figure 5.15 Comparison between the experimental ^{119}Sn static spectrum of **5.11** and the calculated spectrum based on the X-ray structure (dash-dot line). The monocationic site is shown by the dashed line and the dicationic site by the dotted line.

The theoretical parameters further support the MAS data which suggests that there is only one tin site present in the bulk sample. In addition to providing an example of how SSNMR spectroscopy can be used to interpret a crystal structure, complex **5.11** also illustrates that a single crystal does not always accurately reflect that bulk sample. The dramatic difference in predicted lineshape between the monocationic and dicationic sites from the X-ray structure also call into question the assignment of **5.4** and **5.6** as monocationic species.

5.2.3 Calculation of Isotropic Shifts

Isotropic shifts were overestimated for all compounds, **5.8-5.11**, suggesting that the difficulty may partially lie with the calculated value for the shielding of the standard. There is a linear ($R^2 = 0.96$) correlation between the experimental and calculated shifts

(Figure 5.16). If there were perfect 1:1 agreement between the experimental and theoretical isotropic shifts, the slope of the line in Figure 5.16 would be exactly 1; however, the slope is 1.25, suggesting that while there is a systematic overestimation, the overall agreement between the experimental and theoretical shifts remains reasonable. While the span and skew were generally better reproduced in the anions, the opposite appears to be true for the isotropic shift. The theoretical shifts of the cations lie much closer to the 1:1 line than those of the anions.

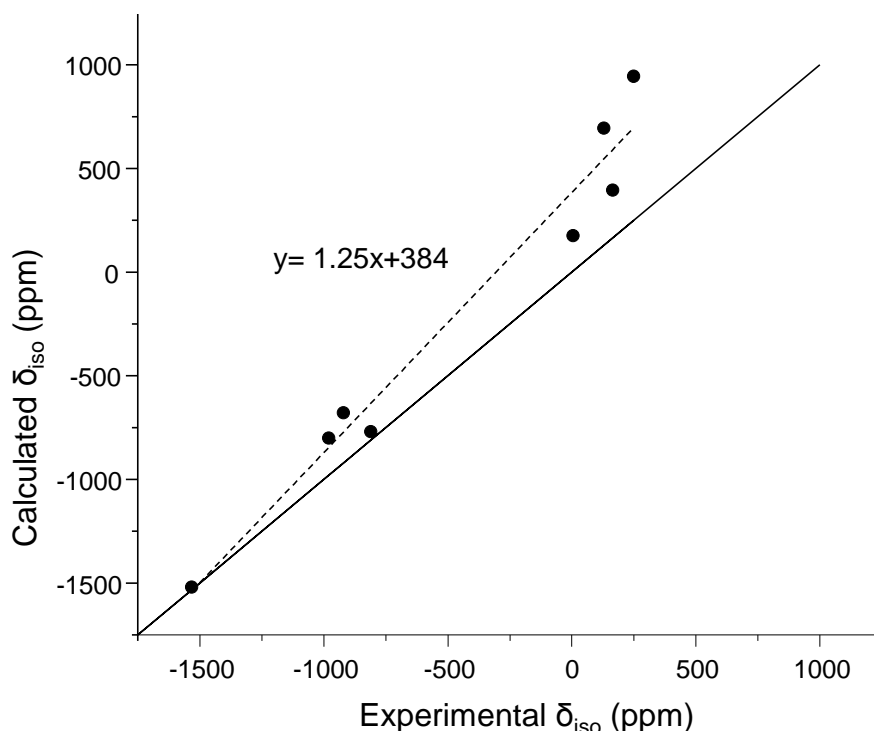


Figure 5.16 Experimental vs. Calculated ^{119}Sn SSNMR isotropic shifts for complexes **5.8-5.11**. The solid line indicates a 1:1 correlation between theory and experiment while the dashed line represents the line of best fit.

5.2.4 Natural Bond Order Calculations

To assess the extent of interaction between the heteroatoms of the cryptand and the tin centres and to better understand the electronic structures of these systems, Natural Bond

Order (NBO) analyses and Natural Population Analyses (NPA)¹⁷ were carried out on all complexes. The results of these analyses are summarized in Table 5.3.

Table 5.3 Summary of natural bond order calculations and natural population analysis.^a

Compound	E Charge	Sn–X Bond Order	E–O Bond Order Range	Sn lone pair % s character	Sn lone pair % p character
5.1 ² E = Ge	+1.38	N/A	0.10	---	---
5.8 X = Cl	+1.26	0.54	0.06 – 0.11	98.62	1.38
5.9 X = Br	+1.19	0.61	0.07 – 0.11	99.04	0.96
5.10 X = I	+1.10	0.71	0.07 – 0.11	98.38	1.62
5.11 Sn(1)	+1.44	0.11	0.10 – 0.11	99.41	0.59
5.11 Sn(2)	+1.24	0.14	0.10 – 0.13	99.52	0.48

^a Calculations for **5.8**, **5.9** and **5.11** were performed at the TPSS/TPSS/Lan2DZ level. The structure of **5.10** was first geometry optimized at the TPSS/TPSS/Lan2DZ and then NBO calculations carried out at the same level.

As was observed in the germanium complex **5.1**,² the Wiberg bond indices (WBI) between the tin atom and the cryptand oxygen atoms range from 0.06 to 0.13, well below the value of 1.0 expected for a single covalent bond. The corresponding values for nitrogen and tin range from 0.09 to 0.13, also suggesting that there is no significant interaction. In contrast, there is a stronger bonding interaction with the halogen in **5.8-5.10**. The Sn–Cl bond is the weakest with a Wiberg bond index of only 0.54. While this is not as large as would be expected for a classical single bond, it is clearly more significant compared to the WBI between the tin and the heteroatoms of the cryptand. The WBI of the Sn–Br bond is 0.61 while the interaction with I is 0.71. The tin–iodide bond exhibits the highest bond order presumably due to the superior orbital overlap between the similarly sized tin and iodine atoms. From the NPA data for these complexes, the positive charge remains centred on tin. The monocationic halide complexes (**5.8-5.10**) feature charges on tin ranging from +1.10 to +1.25. The lower Sn–X bond orders correspond to a higher residual positive charge on tin.

Calculations on the triflate complex were performed for Sn(1) and Sn(2) separately. The Wiberg bond index of the Sn(2)–O (triflate) interaction, which was close enough in the X-ray structure to potentially be considered a covalent bond, is only 0.14, which is not significantly greater than the bond index between the tin centre and the cryptand oxygens, which range from 0.10 to 0.13. The value of 0.14 is also not significantly greater than the value between the Sn(1) centre and the nearest triflate oxygen (0.10), suggesting that there is no significant bonding present. While the calculated bond orders of the two tin atoms did not differ significantly, the calculated residual positive charge on each tin centre gave significantly different results. The Sn(2) atom has a calculated charge of +1.24. While this is greater than the expected +1 charge for a generic monocation, it is very similar to the value calculated for **5.8** (+1.26). The Sn(1) atom, in contrast, has a calculated charge of +1.44, very similar to the +1.38 calculated for **5.1**,² although not as large as the NBO charges reported for the crown ether (**5.2-5.5**) and glyme (**5.7** and **5.8**) complexes of Sn(OTf)₂ (+1.64),⁵ possibly due to the larger number of donor atoms in the cryptand diffusing the charge.

Consistent with the more negative isotropic shift and narrow span, the lone pair on **5.11** is essentially a pure s-orbital with 99.5% s-character, second only to **5.2**⁵ in s-character.

While the corresponding orbital on the halide derivatives still has considerable s-character, there is also p-character. The bromide derivative has the least p-character (0.98%), consistent with it having the smallest span. The less negative isotropic shift is, thus, likely due to the smaller positive charge. The chloride derivative possesses 1.38% p-character. Finally, the iodide derivative, which has the largest span and least negative isotropic shift, has 1.69% p-character. It can, thus, be predicted that the iodide derivative

will be the most reactive of the cryptand complexes. However, **5.10** still exhibits considerably less p-character than **5.3-5.7**, suggesting that in general the cryptand complexes will be less reactive than any of the crown ether and glyme complexes. This is consistent with the smaller span and more shielded isotropic shifts seen for all the halide cryptand complexes when compared to the chloride crown ether complex **5.5**.

5.2.5 Investigation of the Germanium Dication 5.1

Given the high symmetry (D_{3h}) at germanium in complex **5.1**,² it appeared to be an extremely promising target for ^{73}Ge SSNMR spectroscopy. Given the major role ^{119}Sn SSNMR spectroscopy played in characterizing the tin analogues, it was hoped that ^{73}Ge SSNMR spectroscopy would also provide useful information. Initial attempts to acquire a ^{73}Ge SSNMR spectrum were completely unsuccessful. Examination of the ^{13}C CPMAS spectrum of **5.1** as precipitated from tetrahydrofuran (Figure 5.17A) revealed a molecule of THF associated with the complex in a 1:1 ratio, likely distorting the symmetry. This is supported by the difference in ^{13}C peak positions between this spectrum and the ^{13}C CPMAS spectrum of **5.1** recrystallized from acetonitrile (Figure 5.17B). The most notable difference is the peak found at 51 ppm in the spectrum of the recrystallized material being shifted to 50 ppm in the spectrum of the precipitated material, which is not within experimental error.

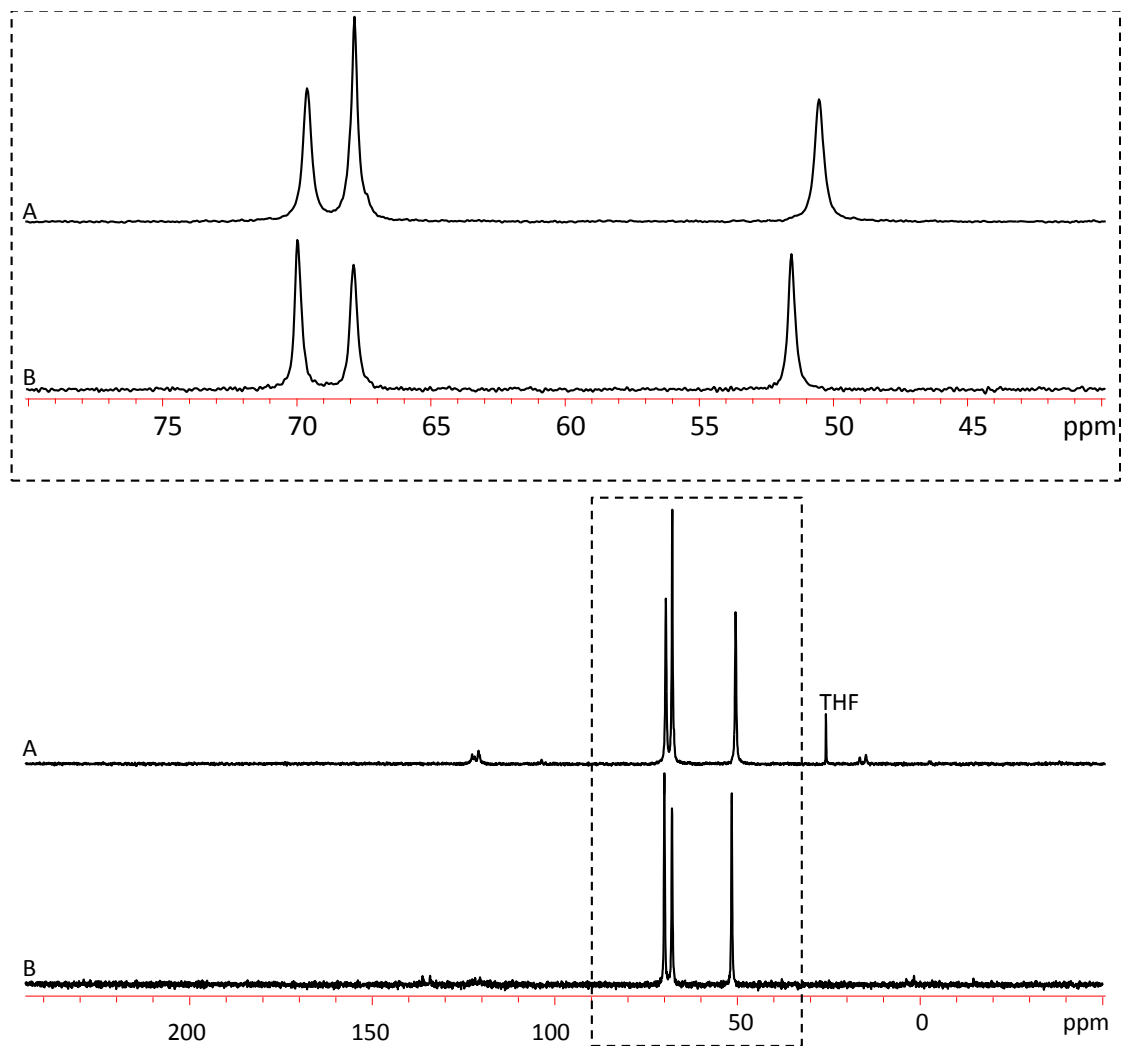


Figure 5.17 ^{13}C CPMAS spectrum at 21.1 T of A) **5.1** precipitated from THF B) **5.1** recrystallized from CH_3CN .

After recrystallizing the sample from acetonitrile, a weak ^{73}Ge SSNMR signal was obtained (Figure 5.18). Unfortunately, it was not possible to obtain a spectrum with an acceptable signal-to-noise ratio in a reasonable acquisition time. This is most likely due to the large size of the cryptand which leads to an extremely low germanium concentration in the sample ($1.34 \text{ Ge}/1000 \text{ \AA}^3$, resulting in a concentration of NMR active ^{73}Ge nuclei of only $0.1 \text{ }^{73}\text{Ge}/1000 \text{ \AA}^3$). A similar effect can be seen in the tin halide

series, with the signal-to-noise ratio decreasing as one descends the group due to the longer Sn–X bond leading to poorer packing.

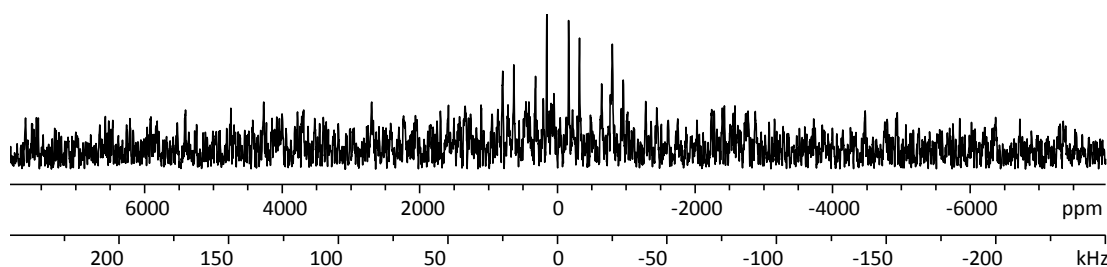


Figure 5.18 Static ^{73}Ge WURST-QCPMG spectrum of **5.1** at 21.1 T.

5.3 Conclusions

Through the use of solid-state NMR spectroscopy, we were able to address two major questions about the structure of the tin cryptand complexes **5.8-5.11**. The ^{119}Sn SSNMR spectrum of **5.10** closely resembled those of **5.8** and **5.9**, indicating that the structure of the iodide derivatives is very similar to the crystallographically-characterized chloride and bromide derivatives. While mass spectrometry provided stoichiometric information, SSNMR spectroscopy allowed for firm conclusions about the structure of **5.10** and the bonding in **5.11**. This conclusion is further supported by the close reproduction of the experimental NMR parameters through DFT calculations on the geometry-optimized structure. Additionally, it was possible to determine from these data that the preparation of **5.10** directly from tin diiodide is preferable to preparation from tin dichloride followed by halogen exchange. Spectral simulation of **5.10'** indicated that there was incomplete halogen exchange in both the anion and cation. While it was possible to determine the incomplete halogen exchange in the case of the anion from Raman spectroscopy, SSNMR spectroscopy was the only characterization technique that provided evidence for the incomplete exchange in the cationic portion of the complex.

The ^{119}Sn and ^{19}F SSNMR spectra of **5.11** made it apparent that the single crystals which were used to determine the X-ray structure did *not* accurately reflect the bulk powder. While the X-ray structure indicated that there were two crystallographically distinct tin sites, only one tin signal was observed under MAS conditions. This also clarified that observation of both dicationic and monocationic species in the mass spectrum arose from aggregation of the dicationic species with the counterion rather than two distinct species as DFT calculations indicate that the bulk sample most closely resembled the site free of covalent interaction with the triflate. This was further supported by the resemblance of the SSNMR parameters of **5.11** to those of the dicationic crown ether and glyme complexes **5.2**, **5.3** and **5.7**.

This work clearly demonstrates the vital role ^{119}Sn SSNMR spectroscopy can play in the characterization of novel tin compounds. Even without an X-ray structure, we were able to determine the structure of **5.10** unambiguously as well as assess the effectiveness of two different synthetic preparations. Furthermore, the structure of **5.11** was *not* definitive based on diffraction experiments alone. Through the use of SSNMR spectroscopy, we were able to resolve the ambiguity and get a clear picture of the structure of the *bulk* material. Unfortunately, due to the lower sensitivity of ^{73}Ge combined with the low germanium density in the spectrum, it was not possible to obtain a spectrum of **5.1** to seek similar insights.

5.4 Experimental

5.4.1 Materials

The cationic cryptand complexes were prepared by Jessica Avery according to the published procedure.⁷ The tetrabutylammonium stannate salts were prepared according to literature procedures.⁹ Compound **5.1** was prepared by Paul Rugar according to the published procedure.² The solution state ¹H spectra were verified after acquisition of SSNMR spectra to determine that decomposition had not occurred over the course of the experiment.

5.4.2 ¹¹⁹Sn SSNMR Spectroscopy

All solid-state NMR spectra were acquired on a Varian Infinity 400 MHz spectrometer. Specific experimental parameters are given in Table 5.4. Experimental setup and pulse width calibration for one pulse and spin echo experiments were performed on solid tetracyclohexyltin. Chemical shift referencing was performed relative to this sample (-97.3 ppm relative to SnMe₄). Optimization of the WURST-CPMG¹⁸ sequence was carried out on tin(II) oxide.

MAS experiments were carried out using a 4 mm HXY MAS probe in dual resonance mode. A one pulse sequence with proton decoupling with a pulse width corresponding to a 30 degree pulse was employed. Recycle delays were selected to allow full relaxation. Static experiments were carried out using an HX static probe in dual resonance mode. The majority of these experiments employed a WURST-CPMG sequence consisting of a 50 μs WURST-80 pulse followed by a series of identical refocusing pulses. For the

triflate complex, a standard ($\pi/2$ - τ - π - τ -acquisition) spin echo experiment was employed.

Full acquisition parameters are given in Table 5.4.

Table 5.4 Experimental ^{119}Sn acquisition parameters.

Compound	Experiment	# transients	# Loops	ν_{rot} (kHz)	Pulse delay (s)
5.8	Static	5728	32	---	15
	MAS	2804	---	17	30
5.9	Static	15304	30	---	15
	MAS	7828	---	16.5	30
5.10	Static	5976	35	---	10
5.10'	Static	23880	100	---	10
5.11	Static	2096	---	---	60
	MAS	2352	---	16	30

5.4.3 SSNMR Spectral Simulations

Experimental parameters were determined by analytical simulations using WSolids.¹⁹

MAS spectra were analyzed using the Herzfeld-Berger analysis package included with WSolids. Errors were determined by visual comparison to the experimental spectrum.

Starting from the best fit value, the parameter being evaluated was varied systematically in both directions while all others were held constant until a visible change was observed.

5.4.4 Theoretical Calculations

Geometry optimizations and Natural Bond Order calculations were performed in

Gaussian 09¹⁵ using the TPSSSTPSS²⁰ functional and the Lan2DZ basis set on all atoms.

Calculation of ^{119}Sn CS parameters was carried out in ADF¹³ using the BPVWN

functional and a Q4ZP basis set on tin with T2ZP employed on all other atoms. All

electron basis sets were optimized for the ZORA method. All calculations were

performed on the Shared Hierarchical Academic Research Computing Network

(SHARCNET). Calculations were performed on an 8 core Xeon 2.83 GHz CPU with 16 GB memory.

5.5 References

- (1) Lee, V. Y.; Sekiguchi, A. *Acc. Chem. Res.* **2007**, *40*, 410.
- (2) Rupar, P. A.; Staroverov, V. N.; Baines, K. M. *Science* **2008**, 1360.
- (3) Wrackmeyer, B. In *Tin Chemistry: Fundamentals, Frontiers, and Applications*; Davies, A. G., Gielen, M., Pannel, K. H., Tiekink, E. R., Eds.; Wiley: West Sussex, **2008**, p 17.
- (4) Bandyopadhyay, R.; Cooper, B. F. T.; Rossini, A. J.; Schurko, R. W.; Macdonald, C. L. B. *J. Organomet. Chem.* **2010**, *695*, 1012.
- (5) Macdonald, C. L. B.; Bandyopadhyay, R.; Cooper, B. F. T.; Friedl, W. W.; Rossini, A. J.; Schurko, R. W.; Eichhorn, S. H.; Herber, R. H. *J. Am. Chem. Soc.* **2012**, *134*, 4332.
- (6) Avery, J. C., The University of Western Ontario, **2011**.
- (7) Avery, J. C.; Hanson, M. A.; Herber, R. H.; Bladec, K. J.; Rupar, P. A.; Nowik, I.; Huang, Y.; Baines, K. M. *Inorg. Chem.* **2012**, *51*, 7306.
- (8) Coddington, J. M.; Taylor, M. J. *J. Chem. Soc. Dalton Trans.* **1989**, 2223.
- (9) Goldstein, M.; Tok, G. C. *J. Chem. Soc. (A)* **1971**, 2303.
- (10) Lambert, J. B. In *Tin Chemistry: Fundamentals, Frontiers, and Applications*; Davies, A. G., Gielen, M., Pannel, K. H., Tiekink, E. R., Eds.; Wiley: West Sussex, **2008**, p 152.
- (11) Eichler, B. E.; Philips, B. L.; Power, P. P.; Augustine, M. P. *Inorg. Chem.* **2000**, *39*, 5450.

- (12) Spikes, G. H.; Giuliani, J. R.; Augustine, M. P.; Nowik, I.; Herber, R. H.; Power, P. P. *Inorg. Chem.* **2006**, *45*, 9132.
- (13) Te Velde, G.; Bickelhaupt, F. M.; Baerends, E. J.; Fonseca Guerra, C.; van Gisbergen, S. J. A.; Snijders, J. G.; Ziegler, T. *J. Comput. Chem.* **2001**, *22*, 931.
- (14) Bagno, A.; Casello, G.; Saielli, G. *J. Chem. Theory Comput.* **2006**, *2*, 37.
- (15) Frisch, M. J.; Trucks, G. W.; Schlegel, H. B.; Scuseria, G. E.; Robb, M. A.; Cheeseman, J. R.; Scalmani, G.; Barone, V.; Mennucci, B.; Petersson, G. A.; Nakatsuji, H.; Caricato, M.; Li, X.; Hratchian, H. P.; Izmaylov, A. F.; Bloino, J.; Zheng, G.; Sonnenberg, J. L.; Hada, M.; Ehara, M.; Toyota, K.; Fukuda, R.; Hasegawa, J.; Ishida, M.; Nakajima, T.; Honda, Y.; Kitao, O.; Nakai, H.; Vreven, T.; Montgomery, J., J. A.; Peralta, J. E.; Ogliaro, F.; Bearpark, M.; Heyd, J. J.; Brothers, E.; Kudin, K. N.; Staroverov, V. N.; Kobayashi, R.; Normand, J.; Raghavachari, K.; Rendell, A.; Burant, J. C.; Iyengar, S. S.; Tomasi, J.; Cossi, M.; Rega, N.; Millam, N. J.; Klene, M.; Knox, J. E.; Cross, J. B.; Bakken, V.; Adamo, C.; Jaramillo, J.; Gomperts, R.; Stratmann, R. E.; Yazyev, O.; Austin, A. J.; Cammi, R.; Pomelli, C.; Ochterski, J. W.; Martin, R. L.; Morokuma, K.; Zakrzewski, V. G.; Voth, G. A.; Salvador, P.; Dannenberg, J. J.; Dapprich, S.; Daniels, A. D.; Farkas, Ö.; Foresman, J. B.; Ortiz, J. V.; Cioslowski, J.; Fox, D. J.; Revision A1 ed.; Gaussian Inc.: Wallingford, CT, **2009**.
- (16) Huang, L.; Huang, X. In *Electronic Encyclopedia of Reagents in Organic Synthesis*; Wiley: New York, **2005**; Vol. 226.
- (17) Weinhold, F. In *Encyclopedia of Computational Chemistry*; von Ragué Schleyer, P., Ed.; Wiley: Chichester, UK, **1998**; Vol. 3, p 1792.

- (18) MacGregor, A. W.; O'Dell, L. A.; Schurko, R. W. *J. Magn. Reson.* **2011**, *208*, 103.
- (19) Eichele, K.; Wasylshen, R. E. In *WSolidsI: Solid-State NMR Spectrum Simulation* **2001**.
- (20) Tao, J.; Perdew, J. P.; Staroverov, V. N.; Scuseria, G. E. *Phys. Rev. Lett.* **2003**, *91*, 146401.

Chapter 6 Summary, Conclusions and Future Work

6.1 Summary

Several approaches and applications of solid-state NMR spectroscopy for the characterization of group 14 compounds have been examined. The major goal was to obtain structure and bonding information about germanium through direct and indirect means.

In Chapter 2, a series of simple organogermanium compounds were examined directly by ^{73}Ge SSNMR spectroscopy. While it was not possible to acquire spectra for all the compounds examined, high quality spectra for systems of varying symmetry were obtained. Through available structural data, we were able to draw relationships between the quadrupolar coupling constant and both the distortion from ideal tetrahedral symmetry and Ge–C bond length. DFT calculations provided further support for these relationships. Additionally, these relationships were used to build model structures for compounds of unknown structure. Through calculation of NMR parameters at varying geometries, we were able to propose potential structures for Mes_2GeH_2 , Mes_3GeH and $\text{Mes}_2\text{Ge}(\text{SiMe}_3)_2$. The compounds for which we were unable to acquire ^{73}Ge NMR spectra led to a better understanding of the factors required to obtain high quality ^{73}Ge spectra in the solidstate. The most important factors appear to be a high degree of order in the solid state as well as high germanium content in the sample. The former is required to have a sufficient amount of signal originating from a given germanium site while the latter reflects the effect of concentration on the signal-to-noise ratio in NMR spectroscopy.

The principles established in Chapter 2 were applied to an open research question in Chapter 3. The germanium monohalides are highly novel germanium(I) species used as precursors for nanoclusters. However, due to their amorphous nature they could not be structurally characterized. Consistent with the amorphous nature of these compounds, the ^{73}Ge , ^{35}Cl and Br spectra featured a distribution of NMR parameters due to the multiple environments present in an amorphous, glasslike material. In most cases, this degree of structural disorder would be prohibitive for ^{73}Ge NMR spectroscopy; however, due to the extremely high germanium content of the samples it was possible to obtain spectra. The spectra of GeCl and GeBr indicated that the structures of the two compounds were largely similar, with slightly lower symmetry in GeBr. The quadrupolar coupling constants predicted a highly symmetrical environment around the halogen and lower symmetry around germanium. Additionally, the ^{35}Cl isotropic shift indicated that the chlorine atom was covalently bound, as expected from the Raman spectrum of GeBr. The ^{73}Ge quadrupolar coupling constants were consistent with what has been seen previously for germanium selenide glasses containing Ge–Ge bonds;¹ however, this relationship is not yet well established. Computational modelling was carried out on a series of model clusters to determine that the best agreement with experimental NMR parameters was obtained with a diamond lattice structure consisting of one dimensional Ge–Ge chains connected by bridging chlorine atoms. The chlorine atoms are surrounded on all sides by germanium. In light of the trends noted in Chapter 2, the influence of Ge–Ge and Ge–Cl bond lengths were also examined computationally and it was determined that the average environment of this material involves short Ge–Ge bonds and long Ge–Cl bonds.

Chapter 4 further explored the utility of ^{35}Cl SSNMR spectroscopy for cases where there is a chlorine atom covalently bonded to germanium in compounds for which we were not able to obtain ^{73}Ge NMR spectra. The study examined a series of six germanium(II) complexes as well as two germanium(IV) compounds and a cationic tin(II) complex. With the exception of the monocationic complex, the germanium(II) compounds could be described as GeCl_2 complexed with a base. The addition of the ligand considerably altered the environment around both chlorine and germanium, causing much lower symmetry as reflected by the large quadrupole coupling constant in the complexed species. Within the germanium(II) series, the magnitude of the quadrupole coupling constant was correlated to the length of the Ge–Cl bond due to the largest component of the EFG tensor being aligned along this bond. The exception was $\text{GeCl}_2 \cdot \text{dioxane}$, where the most important interaction was the long range contact between chlorine and the adjacent germanium atom. Additionally, the germanium(IV) compounds both had considerably larger C_Q values than the germanium(II) compounds, which could not be rationalized by bond lengths alone. If the relationship between ^{35}Cl C_Q value and the oxidation state of germanium proves to be consistent, ^{35}Cl SSNMR spectroscopy could be used as an alternative to Mössbauer spectroscopy for compounds containing covalent Ge–Cl bonds.

Finally, a series of cationic tin(II) cryptand complexes were examined by ^{119}Sn SSNMR spectroscopy. It was not possible to obtain ^{119}Sn NMR spectra in solution, prompting us to examine the complexes in the solid state. The cryptand complexes consisted of tin bound to a halogen ($X = \text{Cl}, \text{Br}$ and I) as well as a derivative with a weakly coordinating triflate anion. The chloride and bromide derivatives had clear crystal structures and thus

served as benchmarks for the NMR parameters of these species. It was not possible to obtain X-ray quality crystals of the iodide derivative. Additionally, it was not clear in the X-ray structure of the triflate derivative whether the triflate was covalently bound to tin.

^{119}Sn SSNMR spectroscopy proved to be a vital technique in determining the structure of the iodide derivative. Additionally, two different synthetic methodologies for the iodide derivative were examined, with ^{119}Sn SSNMR spectroscopy revealing that preparation from SnCl_2 via halogen exchange did not go cleanly. Direct preparation from SnI_2 yielded a sample that had a very similar ^{119}Sn SSNMR spectrum to the chloride and bromide derivatives. The ambiguity of the X-ray structure of the triflate derivative was resolved. While there were two crystallographically unique tin sites in the X-ray structure, the bulk material only contained one. By comparison to the work of McDonald *et al.*^{2,3} as well as DFT calculation of the NMR parameters for both species, we were able to determine that the triflate derivative was a dication without any covalent interaction with the counterion. Furthermore, it was possible to conclude that some of MacDonald's complexes were likely dications rather than monocations as initially reported.

6.2 Future Work

Given the guidelines we have determined for successful ^{73}Ge SSNMR spectroscopy, future investigations should focus on samples possessing high germanium concentrations. Unfortunately, this restriction eliminates many of the currently exciting low valent and cationic species due to the necessity of bulky substituents to isolate the sample.

However, many such samples do contain an attached chloride, making ^{35}Cl NMR spectroscopy very promising. If the chloride remains attached to a low valent species

during a catalytic reaction, the ^{35}Cl NMR spectrum could be monitored to determine if a change in oxidation state is occurring analogous to catalytic cycles of transition metals. While ^{35}Cl NMR spectroscopy requires too many scans to be effective in situ, it would be beneficial to study isolated intermediates on the reaction pathway. Dissociation of the attached chloride, a common step in catalytic cycles of transition metals, would be particularly distinctive by ^{35}Cl SSNMR spectroscopy.

It would also be beneficial to further expand the ^{35}Cl investigation into other group 14 species. If the relationship between ^{35}Cl C_Q and oxidation state proves to be more universal, it has potential utility in tin and silicon chemistry. Despite having nuclei much more amenable to NMR spectroscopy, the actual oxidation state is not always readily determined. ^{35}Cl NMR spectroscopy could, thus, provide a new probe. This is particularly promising for silicon chemistry, as there is not an effective source for Mössbauer spectroscopy.

Given the observations of the degree of p-character in the lone pair of the cationic tin complexes, we expect the iodide derivative to be the most reactive. While preliminary studies have been performed, they have thus far focused exclusively on the chloride and triflate complexes. These studies should thus be expanded to include the iodide derivative in order to determine if the p-character is in fact the most important factor in reactivity. The cryptand complexes in general are expected to be much less reactive than the corresponding crown ethers. However, as cationic tin species, it remains worthwhile to investigate their reactivity for reversible reactions that could potentially be employed in catalysis.

6.3 Conclusions

From this study, it has been possible to determine guidelines for what makes ^{73}Ge NMR spectroscopy feasible. Ultrahigh magnetic fields (21.1T) are vital in order to counteract the inherently low sensitivity of ^{73}Ge , with only one spectrum being successfully obtained at 9.4 T. While narrow spectra for high symmetry compounds can be obtained using the standard quadrupolar echo sequence, broader spectra require the QCPMG⁴ and, ideally, the WURST-QCPMG⁵ sequence.

To benefit from the WURST-QCPMG sequence, the T_2 relaxation time must be relatively long. Compounds with very short relaxation times can only be refocused a minimal number of times and, thus, do not experience notable signal enhancement. This problem often arises when examining nuclei covalently bonded to halogens, as was seen with Me_2GeCl_2 and SnBr_3^- , due to quadrupolar relaxation.

In cases without unusually high symmetry, one of the most important factors is the actual germanium content of the sample in the solid state. In cases involving large ligands, the actual amount of germanium in the rotor is quite low, giving rise to the same low signal-to-noise ratio seen in solution state spectroscopy with low concentrations. With the exception of the symmetrical germanes with narrow spectra discussed in Chapter 2, it was not possible to obtain a ^{73}Ge spectrum with a sufficiently high signal-to-noise ratio to determine spectroscopic parameters in any sample with a germanium content less than 4 Ge/1000 Å³.

Related to the importance of germanium concentration, the sample must also be well ordered in the solid state. If there is structural disorder, the concentration of each

individual environment is quite low. The only samples with solid-state disorder for which it was possible to obtain ^{73}Ge data were the monohalides GeCl and GeBr , due to the anomalously high germanium content due to the diatomic formulae, and even these compounds had very noisy spectra. The structural order of a compound can be verified using ^{13}C or ^{29}Si SSNMR spectroscopy so long as the relevant nuclei are present in the compound of interest. If more signals are observed than can be accounted for from the molecular structure, there are multiple crystallographically distinct molecules with unique germanium environments. Similarly, broad ^{29}Si or ^{13}C signals indicate structural disorder. In either case, ^{73}Ge NMR spectroscopy is likely to be much more challenging. Even in cases of high symmetry, structural disorder proved to be prohibitive.

DFT calculations of NMR parameters proved to be an effective way of examining compounds without known crystal structures. In general, there is a linear relationship between the bond lengths around germanium and the ^{73}Ge quadrupolar coupling constant. There is also a less dramatic correlation to angles which can be used as a fine adjustment of the structure. The value of η_Q is a useful assessment of symmetry. While it is not possible to determine the *exact* structure as is possible with diffraction method, DFT calculations of NMR parameters do offer valuable insight in cases where diffraction is not possible. Additional spectroscopic investigation through ^{13}C and ^{29}Si SSNMR spectroscopy was valuable in guiding the symmetry of the structures used in the calculations.

The magnitudes of the solid-state NMR parameters have exhibited a strong correlation to structure within related series for both ^{73}Ge and ^{35}Cl . In many cases a correlation was observed to bond lengths, which is particularly promising for future applications in

structure elucidation. The distinctive grouping of ^{35}Cl quadrupolar coupling constants by oxidation state is particularly promising as a diagnostic tool. Even with an NMR active nucleus, the ability to discern oxidation state without using specialized techniques such as Mössbauer spectroscopy would be of great value. The trend in relation to D-Ge-Cl angle suggests that both relationships may be related to the covalency of the Ge-Cl bond. Greater covalency would have a stronger effect on the electric field gradient, explaining the generally smaller EFG interaction observed for ionic chlorides and the extremely large C_Q values for organic chlorides.

In addition to establishing basic trends for both ^{73}Ge and ^{35}Cl SSNMR spectroscopy in organogermanium species, this work also demonstrated the very real role the technique can play in structural elucidation. With the support of DFT calculations, we were able to examine amorphous materials and obtain a reasonable depiction of the solid state structure. Furthermore, the tin triflate complex illustrated that an X-ray structure does not always fully reflect the nature of the bulk powder. Solid-state NMR spectroscopy can thus provide a much clearer picture. In addition to being an illustration of the power for SSNMR in structural elucidation, the tin iodide complex also demonstrates the ability to use SSNMR to assess a synthetic pathway. This is a frequent application of NMR spectroscopy in the solution state; however, solid-state studies are useful in cases such as the cationic tin complexes where a solution state signal could not be obtained due to CSA based relaxation, which is common in heavy spin 1/2 nuclei.

6.4 References

- (1) Sen, S.; Gan, Z. *J. Non-Cryst. Solids* **2010**, *356*, 1519.

- (2) Bandyopadhyay, R.; Cooper, B. F. T.; Rossini, A. J.; Schurko, R. W.; Macdonald, C. L. B. *J. Organomet. Chem.* **2010**, *695*, 1012.
- (3) Macdonald, C. L. B.; Bandyopadhyay, R.; Cooper, B. F. T.; Friedl, W. W.; Rossini, A. J.; Schurko, R. W.; Eichhorn, S. H.; Herber, R. H. *J. Am. Chem. Soc.* **2012**, *134*, 4332.
- (4) Larsen, F. H.; Jakobsen, H. J.; Ellis, P. D.; Nielsen, N. C. *J. Phys. Chem. A* **1997**, *101*, 8597.
- (5) O'Dell, L. A.; Schurko, R. W. *Chem. Phys. Lett.* **2008**, *464*, 97.

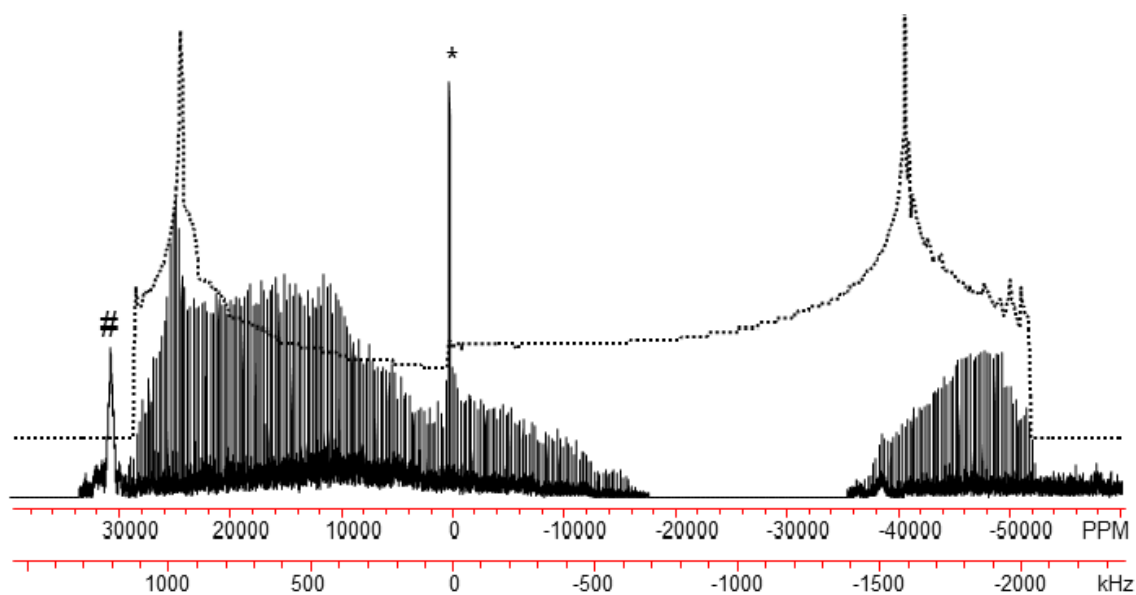
Appendix 1: Low Field ^{35}Cl SSNMR Data

Figure A1.1 Partial ^{35}Cl WURST-QCPMG spectrum of methyl-substituted NHC complex **4.2** at 9.4 T. * indicates an impurity of the hydrochloride salt of the carbene while # indicates a spectrometer artefact.

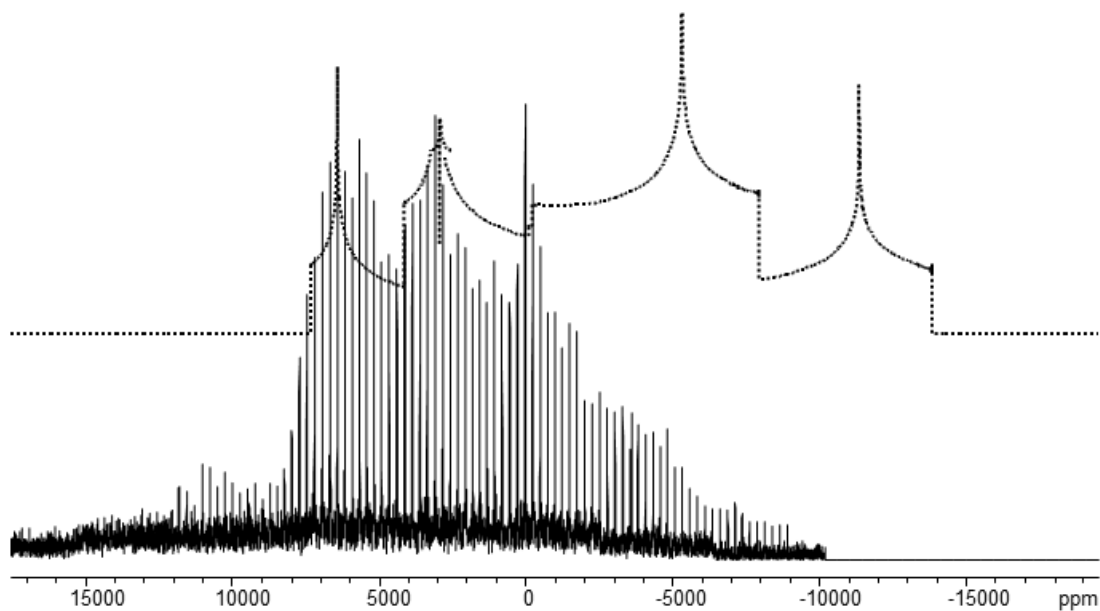


Figure A1.2 Partial ^{35}Cl WURST-QCPMG spectrum of **4.4** at 9.4 T.

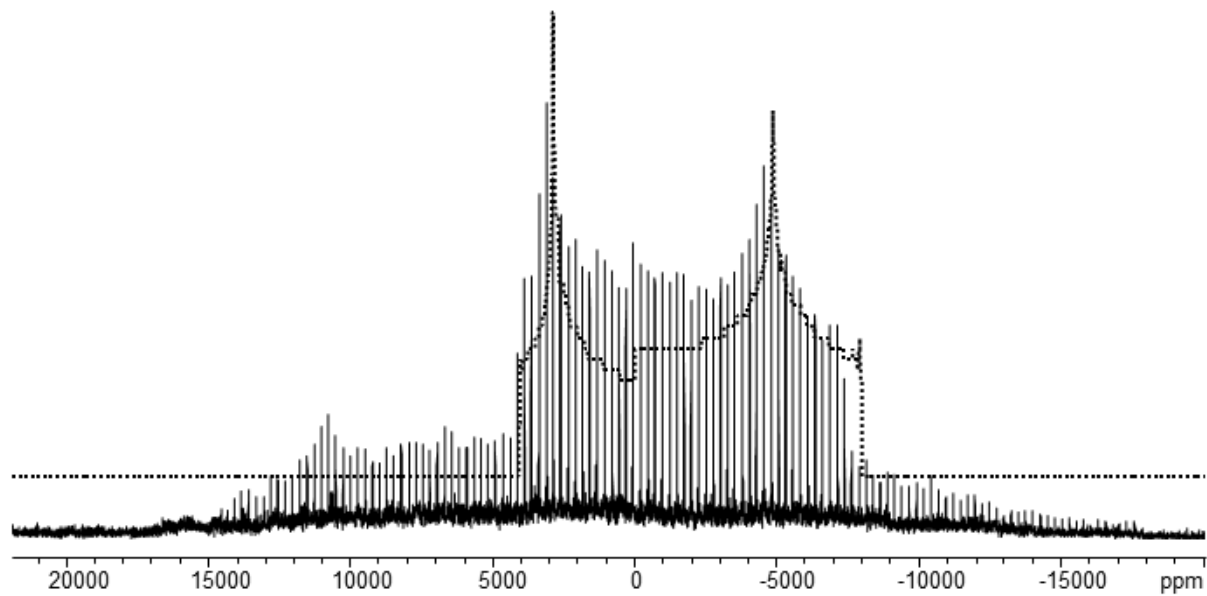


Figure A1.3 ^{35}Cl WURST-QCPMG spectrum of **4.5** at 9.4T.

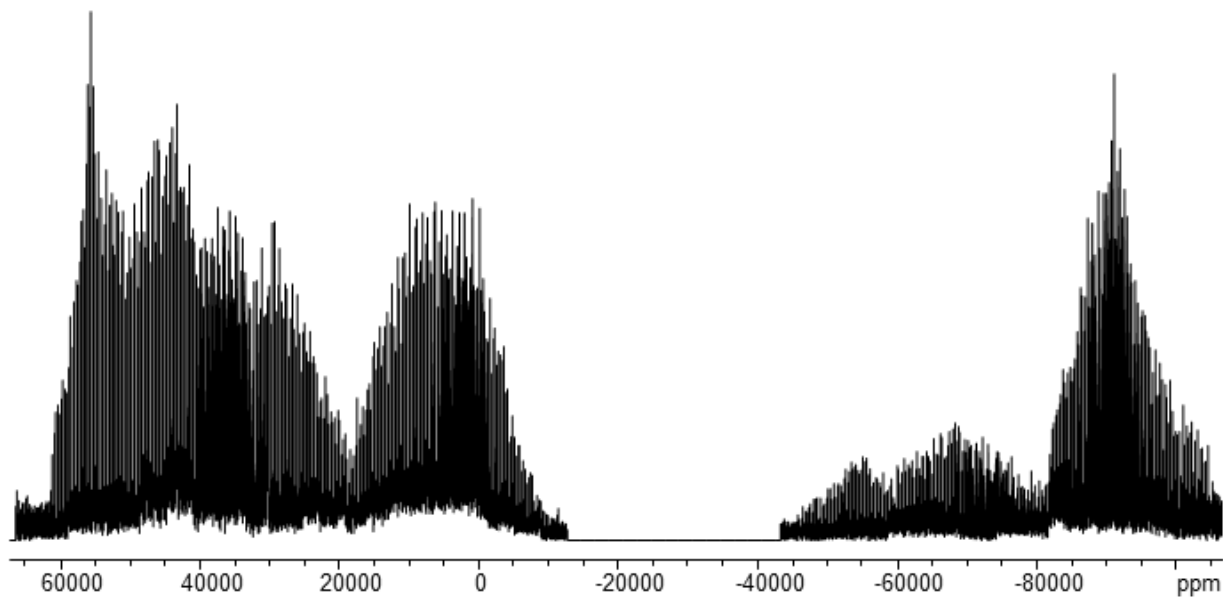


Figure A1.4 Partial ^{35}Cl WURST-QCPMG spectrum of **4.7** at 9.4 T.

Appendix 2: Copyrighted Material and Permissions

A2.1 John Wiley and Sons License Agreement

This is a License Agreement between Margaret A Hanson ("You") and John Wiley and Sons ("John Wiley and Sons") provided by Copyright Clearance Center ("CCC"). The license consists of your order details, the terms and conditions provided by John Wiley and Sons, and the payment terms and conditions.

All payments must be made in full to CCC. For payment instructions, please see information listed at the bottom of this form.

License Number 3014320834388

License date Oct 22, 2012

Licensed content
publisher John Wiley and Sons

Licensed content
publication Chemistry - A European Journal

Book title

Licensed content author Margaret A. Hanson, Andre Sutrisno, Victor V. Terskikh, Kim M.
Baines, Yining Huang

Licensed content date Sep 28, 2012

Start page	13770
End page	13779
Type of use	Dissertation/Thesis
Requestor type	Author of this Wiley article
Format	Print
Portion	Full article

A2.2 American Chemical Society's Policy on Theses and Dissertations

This is regarding request for permission to include your paper(s) or portions of text from your paper(s) in your thesis. Permission is now automatically granted; please pay special attention to the implications paragraph below. The Copyright Subcommittee of the Joint Board/Council Committees on Publications approved the following:

Copyright permission for published and submitted material from theses and dissertations

ACS extends blanket permission to students to include in their theses and dissertations their own articles, or portions thereof, that have been published in ACS journals or submitted to ACS journals for publication, provided that the ACS copyright credit line is noted on the appropriate page(s).

Publishing implications of electronic publication of theses and dissertation material

Students and their mentors should be aware that posting of theses and dissertation material on the Web prior to submission of material from that thesis or dissertation to an ACS journal may affect publication in that journal. Whether Web posting is considered prior publication may be

evaluated on a case-by-case basis by the journal's editor. If an ACS journal editor considers Web posting to be "prior publication", the paper will not be accepted for publication in that journal. If you intend to submit your unpublished paper to ACS for publication, check with the appropriate editor prior to posting your manuscript electronically.

Reuse/Republication of the Entire Work in Theses or Collections: Authors may reuse all or part of the Submitted, Accepted or Published Work in a thesis or dissertation that the author writes and is required to submit to satisfy the criteria of degree-granting institutions. Such reuse is permitted subject to the ACS' "Ethical Guidelines to Publication of Chemical Research" (<http://pubs.acs.org/page/policy/ethics/index.html>); the author should secure written confirmation (via letter or email) from the respective ACS journal editor(s) to avoid potential conflicts with journal prior publication*/embargo policies. Appropriate citation of the Published Work must be made. If the thesis or dissertation to be published is in electronic format, a direct link to the Published Work must also be included using the ACS Articles on Request author-directed link – see <http://pubs.acs.org/page/policy/articlesonrequest/index.html>

* Prior publication policies of ACS journals are posted on the ACS website at

<http://pubs.acs.org/page/policy/prior/index.html>

If your paper has not yet been published by ACS, please print the following credit line on the first page of your article: "Reproduced (or 'Reproduced in part') with permission from [JOURNAL NAME], in press (or 'submitted for publication'). Unpublished work copyright [CURRENT YEAR] American Chemical Society." Include appropriate information.

If your paper has already been published by ACS and you want to include the text or portions of the text in your thesis/dissertation, please print the ACS copyright credit line on the first page of

your article: "Reproduced (or 'Reproduced in part') with permission from [FULL REFERENCE CITATION.] Copyright [YEAR] American Chemical Society." Include appropriate information.

Submission to a Dissertation Distributor: If you plan to submit your thesis to UMI or to another dissertation distributor, you should not include the unpublished ACS paper in your thesis if the thesis will be disseminated electronically, until ACS has published your paper. After publication of the paper by ACS, you may release the entire thesis (not the individual ACS article by itself) for electronic dissemination through the distributor; ACS's copyright credit line should be printed on the first page of the ACS paper.

Curriculum Vitae

Name: Margaret A. Hanson

Post-secondary Education and Degrees: Mount Allison University
Sackville, New Brunswick, Canada
2003-2007, BSc (Hon)

The University of Western Ontario
London, Ontario, Canada
2007-2012 Ph.D.

Honours and Awards: Western Graduate Research Scholarship
2012

Poster Prize
44th Inorganic Discussion Weekend
2011

Student Travel Grant
16th International Symposium on Silicon
2011

Student Travel Grant
13th International Conference on the Coordination of Germanium,
Tin and Lead
2010

Student Travel Grant
National Ultrahigh Field NMR Facility for Solids
2010

Poster Prize
42nd Inorganic Discussion Weekend
2009

Entrance Scholarship
Mount Allison University
2003-2006

Related Work Experience Teaching Assistant
The University of Western Ontario
2007-2012

Teaching Assistant
Mount Allison University
2006-2007

Research Assistant
Mount Allison University
2005-2006

Publications:

M. A. Hanson, A. Sutrisno, V. V. Terskikh, K. M. Baines, Y. Huang “Solid-State ^{73}Ge NMR Spectroscopy of Simple Organogermanes” *Chem.- Eur. J.* **2012**, *18*, 13770-13779.

J.C. Avery, M. A. Hanson, R. H. Herber, K. J. Bladec, P. A. Rugar, I. Nowik, Y. Huang, K. M. Baines “Cationic cryptand complexes of tin(II)” *Inorg. Chem.* **2012**, *51*, 7306-7316.

A. Sutrisno, M. A. Hanson, P. A. Rugar, V. Terskikh, K. M. Baines, Y. Huang “Exploring the limits of ^{73}Ge solid-state NMR spectroscopy at ultrahigh magnetic field” *Chem. Commun.* **2010**, *46*, 2817-2819.

F. E. Appoh, M. J. Manning, T. J. Gullon, M. A. Hansen, E. C. Bevans, K. D. M. Hogan, C. S. Turner, C. M. Vogels, A. Decken, S. A. Westcott “Ugi products containing boronate esters” *Cent. Eur. J. Chem.* **2008**, *6*, 359-364.

M. A. Hanson, A. Schnepf, V. V. Terskikh, Y. Huang, K. M. Baines “Characterization of Germanium Monohalides by Solid-State NMR Spectroscopy and DFT Calculations” *Manuscript in preparation*

Presentations (Oral):

M. A. Hanson, Y. Huang, K. M. Baines *Solid State ^{35}Cl NMR Spectroscopy as an Indirect Probe of Germanium Compounds* 43rd Silicon Symposium, St. Catharines, Ontario, June 15-16, 2012

M. A. Hanson, J. C. Avery, K. M. Baines, Y. Huang *Solid State ^{119}Sn NMR Spectroscopy of Cationic Tin(II) Complexes* 16th International Symposium on Silicon, Hamilton, Ontario, August 14-18, 2011

M. A. Hanson, K. M. Baines, Y. Huang *Solid State ^{73}Ge NMR of Organogermanium Compounds* 43rd Inorganic Discussion Weekend, Windsor, Ontario, November 7-9, 2010

M. A. Hanson, K. M. Baines, Y. Huang *Solid State ^{73}Ge NMR of Organogermanium Compounds* 93rd Canadian Chemistry Conference and Exhibition, Toronto, Ontario, May 29-June 2, 2010

Presentations (Poster):

M. A. Hanson, A. Schnepf, V. V. Tersikh, K. M. Baines, Y. Huang *Solid State NMR Spectroscopy of Low Valent Germanium Halides* 44th Inorganic Discussion Weekend, Niagara Falls, Ontario, August 19-21, 2011

M. A. Hanson, K. M. Baines, Y. Huang *Solid State ⁷³Ge NMR of Organogermanium Compounds*
13th International Conference on the Coordination and Organometallic Chemistry of Germanium, Tin and Lead, Graz, Austria, July 11-15, 2010

M. A. Hanson, A. Sutrisno, Y. Huang and K. M. Baines *A combined ultrahigh field ⁷³Ge solid state NMR spectroscopic and computational study of GePh₄ and GeCl₂·dioxane* 42nd Inorganic Discussion Weekend, Guelph, Ontario, November 27-29th, 2009

M. A. Hanson, A. Sutrisno, Y. Huang and K. M. Baines *Solid State ⁷³Ge Nuclear Magnetic Resonance Spectroscopy of Simple Germanium Compounds* 42nd Silicon Symposium, Long Branch, NJ, June 9-12, 2009

M. A. Hanson, A. Sutrisno, Y. Huang and K. M. Baines *Solid State ⁷³Ge Nuclear Magnetic Resonance Spectroscopy of Simple Germanium Compounds* 92nd Canadian Chemistry Conference and Exhibition, Hamilton, ON, May 30-June 3, 2009